Polymer Materials in Sensors, Actuators and Energy Conversion

Edited by

Jung-Chang Wang

MDPI

Polymer Materials in Sensors, Actuators and Energy Conversion

Polymer Materials in Sensors, Actuators and Energy Conversion

Editor

Jung-Chang Wang

MDPI

Editor
Jung-Chang Wang
Department of Marine
Engineering (D.M.E.)
National Taiwan Ocean
University (NTOU)
Keelung
Taiwan

This is a reprint of articles from the Special Issue published online in the open access journal *Polymers* (ISSN 2073-4360) (available at: www.mdpi.com/journal/polymers/special_issues/ Polymer_Materials_in_Sensors_Actuators_and_Energy_Conversion).

For citation purposes, cite each article independently as indicated on the article page online and as indicated below:

LastName, A.A.; LastName, B.B.; LastName, C.C. Article Title. *Journal Name* **Year**, *Volume Number*, Page Range.

Contents

About the Editor

Jung-Chang Wang

Jung-Chang Wang (J.-C. Wang) is a full Professor and Dean in the School of Marine Engineering (DME), National Taiwan Ocean University (NTOU), Keelung, Taiwan, and is also the Director of the Thermal-Fluid Illumination Laboratory. He received his Bachelor's and Master's degrees from National Cheng Kung University (NCKU) and his Mechanical PhD from National Taiwan University (NTU) in Taiwan in 2007. He has been teaching on and researching electronic heat transfer and renewable energy for more than ten years. He has published more than 100 research papers in international journals, conferences and patents, and edited seven book chapters. His main research interest includes applied and software engineering in thermal-fluid science.

Preface to "Polymer Materials in Sensors, Actuators and Energy Conversion"

Polymer-based materials applications in sensors, actuators, and energy conversion are playing a key role in these recent developing areas of smart matter and electronic devices. These areas cover the synthesis, structures, and properties of polymers and composites, including energy-harvesting devices and energy-storage devices for electromagnetic (electrical to mechanical energy conversion) and magneto-mechanical (magnetic to mechanical energy conversion), light-emitting devices, and electrically driving sensors. Therefore, the modulation of the polymer-based materials and devices for controlling the detection, actuation, and energy with functional relative device can be achieved.

Jung-Chang Wang
Editor

NOA61-Polymer Fiber Fizeau Interferometer with a Flexible NOA65-Polymer Taper for Simultaneous Measurement of Tilt Angle and Temperature

Cheng-Ling Lee *[ID]**, Chi-Shiang Chen, Chun-Ren Yang and Rui-Cheng Zeng**

Department of Electro-Optical Engineering, National United University, No. 2 Lien-Da,
Miaoli City 36003, Taiwan; U0723013@gm.nuu.edu.tw (C.-S.C.); alanboy927@gmail.com (C.-R.Y.);
watermelon5424@gmail.com (R.-C.Z.)
* Correspondence: cherry@nuu.edu.tw; Tel.: +886-37-382568; Fax: +886-37-382555

Abstract: This study proposes and experimentally demonstrates a NOA61-polymer fiber Fizeau interferometer (PFFI) connected to a flexible NOA65-polymer taper (PT) for simultaneous measurement of tilt angle and temperature (T). The PT/PFFI fiber sensor consists of a taper-shaped flexible NOA65 polymer and single-mode fiber with an endface that is attached to a NOA61-polymer. The NOA61-polymer of PFFI is highly sensitive to variations of T with high repeatability and enables the simultaneous measurement of tilt angle by connecting with the highly flexible NOA65-PT. the interference fringe visibility of optical spectra in the PFFI can be highly controlled by the tilt angle of the PT and is thus capable of measuring tilt angles with high sensitivity. On the other hand, wavelength shifts of the spectra in the PFFI only occur when T varies. The proposed PT/PFFI can simultaneously detect the tilt state and the variation of surrounding T by measuring the optical spectral responses and eliminating cross sensitivity. Experimental results demonstrate the PT/PFFI can simultaneously measure tilt angles and T with good sensitivities and obtain averages of 0.4 dB/° and 0.17 nm/°C, respectively.

Keywords: fiber tilt sensor; NOA61; NOA65; polymer; simultaneous measurement; fiber Fizeau interferometer; taper

1. Introduction

Distributed and multiplexed capability of fiber optic sensors are the most important advantages that can integrate various passive optics sensors for multiple parameters and region-sensing applications. Therefore, advanced fiber optic sensors with the ability of simultaneously sensing multi-parameters have recently received much attention. These sensors can simultaneously measure any of the following parameters, pressure [1], temperature [1–16], displacement [2], strain [3,4,8], tilt angle [13–16], refractive index (RI) [5–7,9,11] and humidity [10,12]. Among the sensing parameters mentioned above, the tilt angle (ϕ) of structure and temperature (T) of the surroundings have important utility values in green buildings and health bridges, and therefore, attract much research interest. In achieving multiplex sensing capability, the key issue for practical applications of fiber optic sensors is not only cross sensitivity but also the complexity of sensing configurations. Thus far, several fiber optical sensors for simultaneous measurement of the tilt angle and temperature are proposed and investigated, but most are incorporated with well-known fiber Bragg gratings (FBG)-based devices [13–15]. For example, a simple fiber optic inclinometer is developed based on linearly chirped FBG written in both fused taper transitions [13]. Similarly, the tilt fiber sensor based on a taper-shaped polymer incorporating a FBG is proposed [14]. Simultaneous measurement of 2D tilt angles and temperature by a fiber optic sensor is also proposed and experimentally demonstrated. The sensing head consists of two FBGs to achieve various sensing performances [15]. The experimental results of the

above tilt angle fiber sensors show that their proposed sensing configuration responds well to the tilt angles, but the sensitivity and resolution of T responses may not be sufficiently recognizable due to the low thermal expansion coefficient of the fused fibers. In 2016, Feng et al. reported a fiber inclinometer that consists of a micro-fiber taper followed by an air-gap microcavity. The fringe contrast of the interferometer is highly sensitive to fiber bending and is thus capable of measuring tilt angles. However, the proposed fiber sensor cannot simultaneously measure T, to which the fused silica fiber is T insensitive [16]. In 2020, a novel, highly sensitive, and simple structure based on a tapered polymer as a tilt fiber sensor is developed to sensitively measure tilt angles [17]. The fiber-optic tilt sensor consists of a tapered polymer fabricated by a flexible adhesive NOA65-polymer with low modulus (20,000 psi) from Norland Products Inc. (Cranbury, NJ, USA) [18]. The NOA65-polymer taper easily generates a bend in the fiber sensor that is strongly correlated with tilt angles. Experimental results of the above sensors show that the sensing configuration responds well to the tilt angles, but the sensitivity and resolution of the T responses may be not sufficiently recognizable.

In this study, we connect a T-sensitive NOA61-polymer fiber Fizeau interferometer (PFFI) with a flexible adhesive NOA65-polymer taper (PT) for simultaneous sensing of tilt (ϕ) and temperature (T). The proposed PT/PFFI consists of a tapered polymer made with NOA65 and the endface of a single mode fiber (SMF) attached to a UV-cured NOA61-polymer to form an ultracompact microcavity. The NOA61-polymer in the PFFI is highly sensitive to T variations with high repeatability, and achieve an instantaneous measurement of ϕ by connecting a flexible NOA65-PT [19]. The NOA65-PT polymer is also T-sensitive with a thermal expansion coefficient (TEC) of 2.2×10^{-4} ($°C^{-1}$) is similar to that of the NOA61 [20]. However, the NOA65-PT is the part of the inclinometer that merely controls the light into the NOA61-PFFI for creating interference. Therefore, the thermal expansion effect on the NOA65 is ignorable for the optical interference from NOA61-PFFI. Variation of fringe visibility (FV) and wavelength shifts ($\Delta\lambda$) of the spectral interference of the sensor correspond to responses of the ϕ and T, respectively. The interference fringe always remains unshifted during the fiber tilts, but optical power and FV showed considerable changes. On the other hand, the interference fringe shifts when T varies while the optical power of reflection is almost unchanged at a fixed ϕ. Thus, the proposed PT/PFFI fiber sensor can detect the tilt states and discriminate the variation of surrounding T by monitoring the FV and $\Delta\lambda$ removing the cross-sensitivity of ϕ and T. The experimental results demonstrate that the developed sensor can measure ϕ and T simultaneously with good measurement sensitivities and averages of 0.4 dB/° and 0.17 nm/°C, respectively.

2. Sensor Fabrication and Principle

The configuration of the PT/PFFI sensor is based on a PFFI formed by a T-sensitivity NOA61-polymer combined with a NOA65-polymer taper (PT) with good flexibility, as presented in Figure 1.
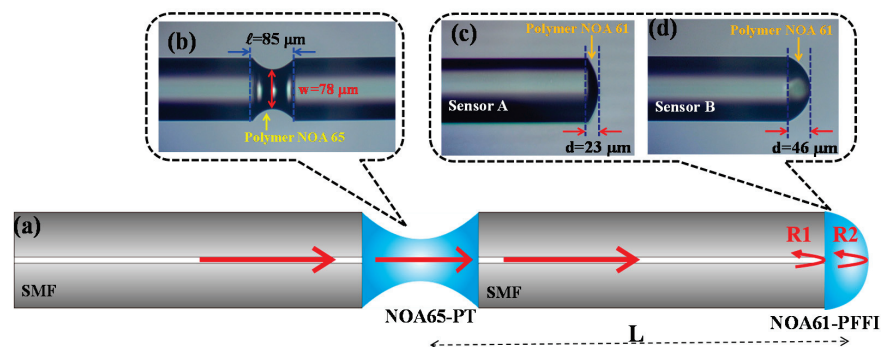
Figure 1. (**a**) Configuration of the proposed sensor with (**b**) taper-shaped NOA65-polymer with L/d = 85 μm/78 μm and (**c**) sensor A with d = 23 μm or (**d**) sensor B with d = 46 μm NOA61-PFFI.

The taper-shaped NOA65 polymer is the main part of the inclinometer that controls the light into the NOA61-PFFI for generating low-finesse interference. Here, the NOA65 (n_D = 1.52) [18,19] polymer materials used are based on a type of optical adhesive, ultraviolet (UV)-cured polymer, with good elongation and is more elastic than conventional fiber taper-based tilt sensors [14,15]. In addition, the NOA61-polymer with the high refractive index of n_D = 1.56 can produce high FV that is more suitable for this study [10]. The fabrication is monitored by a charge-coupled device (CCD) microscope. Figure 2 shows the fabrication steps of the PFFI combined with PT. The NOA65-polymer taper is simply fabricated with the assistance of three-axis translation stages at exact alignment [17]. After accomplishing the desired taper shape of the PT, the monitored translation stages are used to attach a thick film of NOA61-polymer onto the endface of the SMF (Corning@ SMF-28e) to form the PFFI (Figure 2e). The thickness of NOA61 can be carefully controlled by the number of attachment times, as plotted in Figure 2c,d. Here, Figure 1b shows the structure of the NOA65-PT with the tapered region (L)/waist diameter (w) of L/w = 85 µm/78 µm and Figure 1c,d shows the NOA61-PFFI with a cavity length of d = 23 and 46 µm for sensor A and B, respectively.
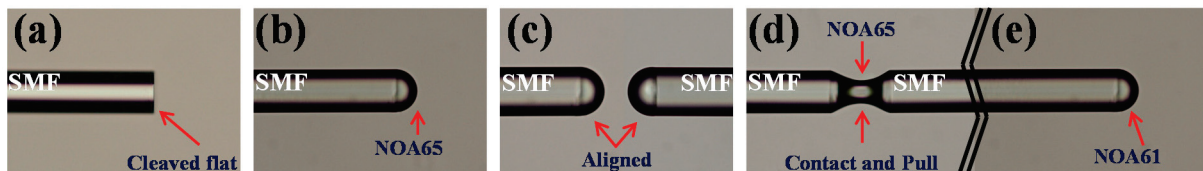
Figure 2. Fabrication of the PT/PFFI by the processes of (**a**) cleaving fiber flat, (**b**) NOA65 attached to fiber endface, (**c**) two fiber-NOA65 aligned, (**d**) contact and pull into a tapered shape to form the NOA65-PT, and (**e**) sensor endface with NOA61 attached to form the NOA61-PFFI.

Figure 1a also illustrates the principle of the proposed PT/PFFI. When the NOA65-PT is bent due to the tilt, light propagating into the NOA61-PFFI intensely decreases with deviation from the center of the fiber axis to instantly weaken the FV of the optical interferences. Figure 3 displays the experimental setup with a broadband light source (BLS, BLS-GIP Technology) and a 2 × 1 optical coupler, which reflects off the endfaces of the PFFI, and returns to the coupler. Finally, the spectral response readouts are directly measured by an optical spectrum analyzer (OSA, Advantest Q8381 A). The PT/PFFI is located inside a temperature and humidity controlling chamber (THCC, LABSON, No. LA-85R) for varying the T and ϕ with fixed humidity.
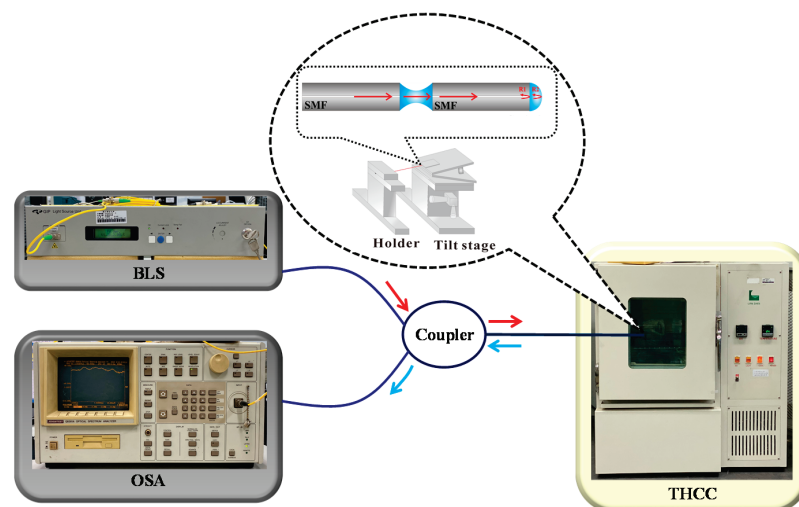
Figure 3. Experimental setup for simultaneously measuring ϕ and T.

The used THCC with temperature (T) accuracy of ~0.2 °C and relative humidity (RH) accuracy of ~2% that are applied to control the T and RH. Since the used polymer device can affected by the surrounding humidity [10], all the measurements are accomplished under a fixed RH = 50%. Therefore, reactions of tilt sensing results can be readily obtained by monitoring FV values or optical power of the reflective interference only from signals of the NOA61-PFFI. If the proposed sensor tilts at a fixed T, then the interference power and FV can considerably decay. Moreover, when the sensor is under T variation at a fixed ϕ, the interference spectra are red-shifted as T increases and are blue-shifted as T decreases. In the reflection spectra, interference signals of two cavities of the NOA65-PT and NOA61-PFFI are superimposed and collected by the OSA. However, the interference signal of NOA65-PT is much weaker than that of the NOA61-PFFI. Analyses of the optical responses from the combined interferences are accomplished using the fast Fourier transform (FFT) method, which is used to separate multiple interferences in spatial frequency into two individual spatial frequencies for the NOA65-PT and NOA61-PFFI. Figure 4 shows the optical responses of the superimposed interference, separating into the spectra through the simple FFT method. The superimposed interference plotted in Figure 4a is processed by the FFT to obtain the spatial frequency spectra, as shown in Figure 4b, indicating that the signal of NOA61-PFFI is higher than that of the NOA65-PT. Subsequently, the spatial frequencies for the NOA65-PT and NOA61-PFFI can be individually separated by the inverse FFT with signal processing, as plotted in Figure 4c,d respectively. In this study, only the interference signals of NOA61-PFFI must be measured to achieve multiple parameters sensing.
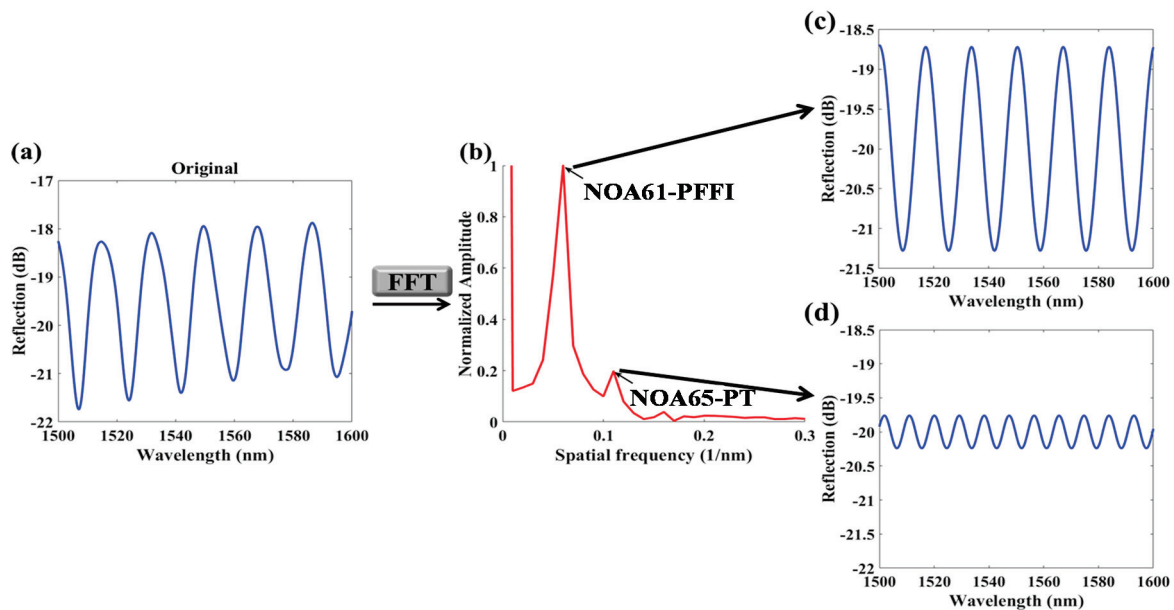
Figure 4. (**a**) Optical response of superimposed interference measured by the OSA; (**b**) superimposed spectra processed by FFT; separated optical spectra of (**c**) NOA61-PFFI and (**d**) NOA65-PT.

3. Experimental Results and Discussion

In the experiment, the proposed PT/PFFI device is placed inside the THCC, a closed space in which the tilt angle is operated from $\phi = -10° \sim +10°$ with a step of 1° under fixed T and fixed relative humidity of 50%. Figure 5 shows the results. For the sensor with d = 46 µm, Figure 5a,b show the spectral responses to positive ϕ and negative ϕ, respectively. These experimental results are almost similar due to the central symmetry of the PT structure. Figure 5c displays variations of FV of reflection for sensors A and B as the ϕ changes from $-10° \sim +10°$. When the ϕ of the sensor increases, the FV has high attenuation. Moreover, at high angles, the FV gradually weakens and then vanishes because the optical light almost leaks out in the great bending of PT. When different sensing structures of sensors A and B are used (as shown in Figure 1), the responses and sensitivities of ϕ

variation from $-10° \sim +10°$ are obtained and shown in Figure 5c,d, respectively. Sensor A (d = 23 μm) with thinner PT seems to be more sensitive than sensor B (d = 46 μm). However, the tilt measurement range is relatively small for sensor A. The tilt sensitivity S is defined as:

$$S = \frac{d(FV)}{d\phi} \tag{1}$$
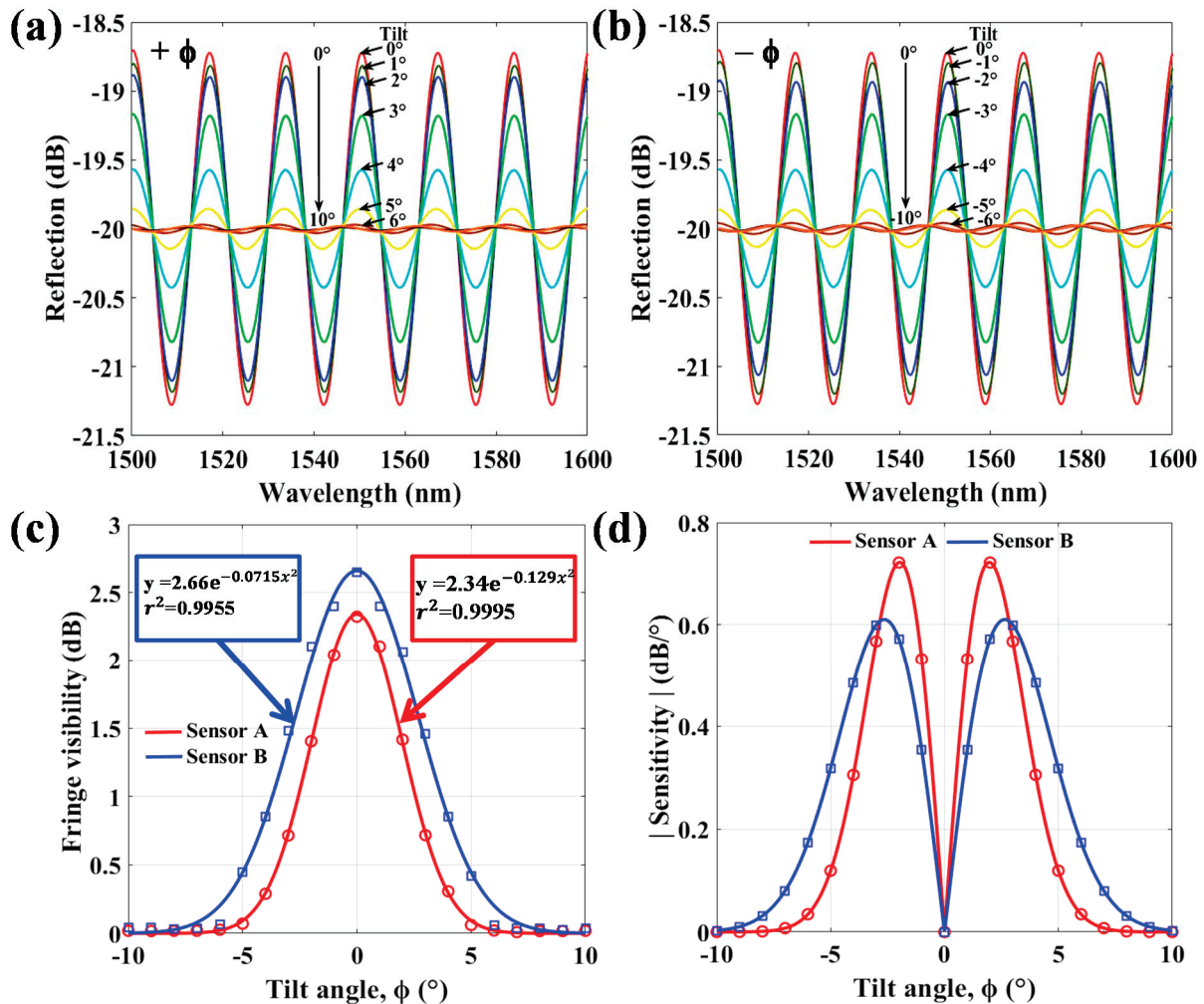
Figure 5. Optical responses for the variations of tilt angle (φ) by (**a**) positive φ and (**b**) negative φ; (**c**) Responses of FV to tilt angles by sensor A with d = 23 μm and sensor B with d = 46 μm; (**d**) φ-related sensitivities of the tapered polymer sensors for sensors A and B.

Figure 5d shows that high responses are achieved from tilt angles of φ = $-10° \sim +10°$ and sensors A and B obtain the highest sensitivities of 0.72 dB/° at φ of ±2° and 0.6 dB/° at φ of ±2.7°, respectively. It is worth mentioning that in the tilt sensing, the interference power and FV highly vary but the wavelength peaks of optical interferences are nearly unshifted, as shown in Figure 6a. The inset of Figure 6a displays the detailed optical interference spectra for the variations of corresponding parameters φ at T = 25 °C. On the other hand, when the sensor is heating and cooling with T, the range is 20 ~ 45 °C at a fixed φ = 0°. The interference is red-shifted as T increases and vice versa. Figure 6b plots the T-sensitivity of the proposed PT/PFFI sensor. The detailed optical interference spectra for heating and cooling are shown in the Figure 6c,d, respectively. The results indicate that the optical responses have high repeatability, and the sensitivity is linearly proportional to T with 0.17 nm/°C. The obtained results of the T sensitivity may not be high; however, the optical power of the spectral responses almost does not

decay that can easily distinguish non-tilt variations. Based on the above sensing results, the proposed PT/PFFI can demonstrate the superiority of sensing characteristics to avoid the cross-sensitivity of the measured parameters.
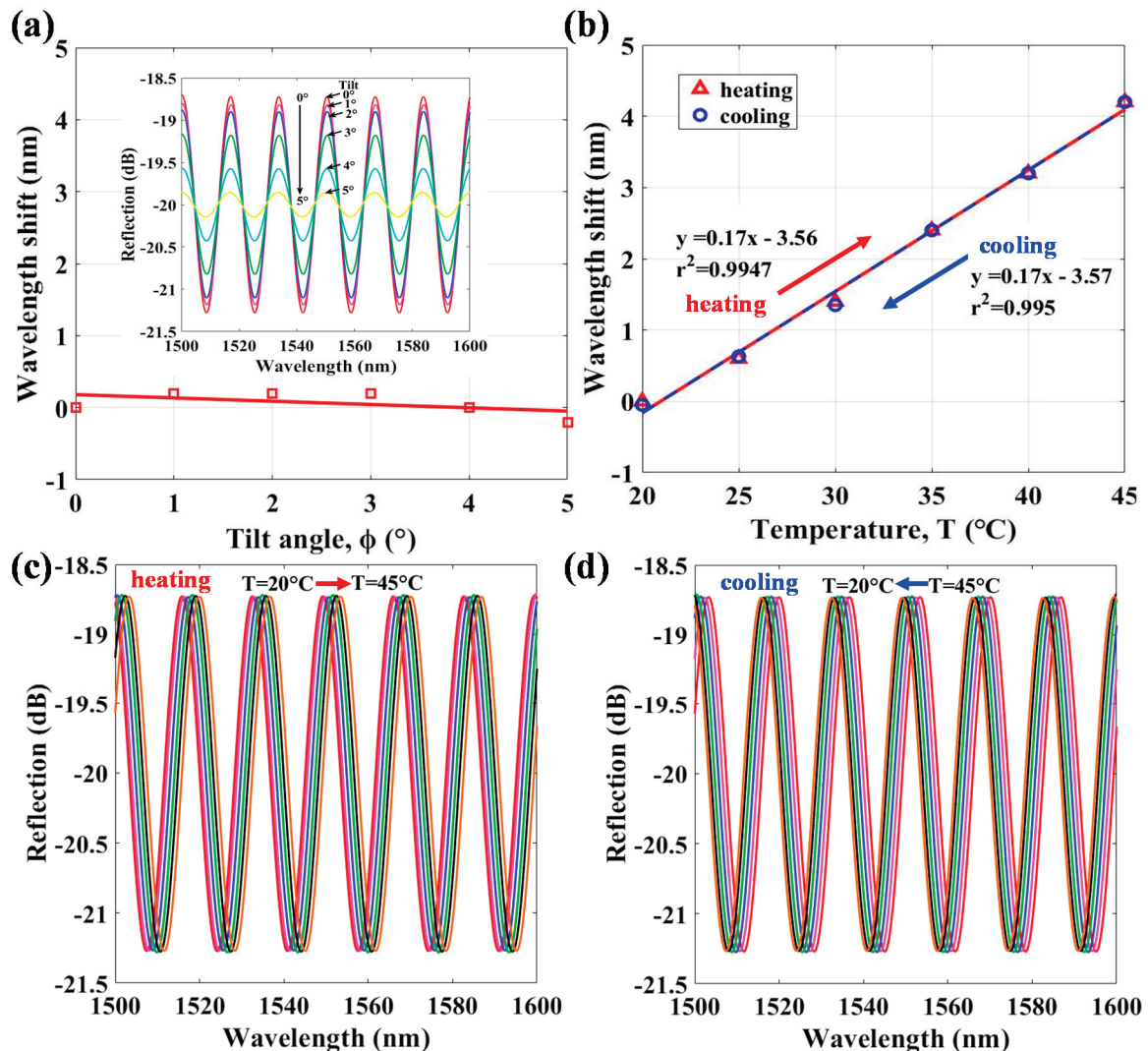
Figure 6. Wavelength shift responses for the variations of (**a**) tilt angle, ϕ at fixed T = 25 °C and (**b**) temperature, T by (**c**) heating and (**d**) cooling with fixed ϕ = 0°.

The effectiveness for the developed sensing configuration is examined by simultaneously varying ϕ and T from their reference values of ambient (set as $\phi_0 = 0°$ and $T_0 = 20$ °C) to various conditions, as shown in Figures 7 and 8, respectively. The optical spectra of the initial condition of $\phi_0 = 0°$ and $T_0 = 20$ °C as the reference for the test sensor B are recorded at the beginning of the experimental investigations (as blue-dashed lines of Figures 7 and 8). Figure 7 presents the simultaneous measurement of the arbitrarily chosen ϕ and T for many cases. Clearly, the variation of the FV is only due to changes of ϕ and the wavelength shift (Δλ) is merely affected by T variation. The parameters of ϕ and T can be respectively estimated by using the experimental relations of FV = 2.66·exp($-0.0715·\phi^2$) and Δλ = 0.17·T − 3.565 when these two factors are measured.

Figure 8 shows the individual interference spectra of every case to compare with that of the initial ϕ_0 and T_0. The arbitrary conditions are: (a) T = 20 °C, ϕ = 4°; (b) T = 25 °C, ϕ = 1°; (c) T = 30 °C, ϕ = 2°; (d) T = 35 °C, ϕ = 0°; (e) T = 40 °C, ϕ = 2°; and (f) T = 45 °C, ϕ = 5°. The measured values of the ϕ and T can be estimated by the measured FV and Δλ in the optical interference spectra by using the experimental

relations of FV = 2.66·exp($-0.0715 \cdot \phi^2$) and $\Delta\lambda = 0.17 \cdot T - 3.56$. The measured FV and $\Delta\lambda$ of each case are: (a) $\Delta\lambda = -0.1$ nm, FV = 0.847 dB (b) $\Delta\lambda = 0.73$ nm, FV = 2.399 dB, (c) $\Delta\lambda = 1.48$ nm, FV = 1.488 dB, (d) $\Delta\lambda = 2.42$ nm, FV = 2.654 dB, (e) $\Delta\lambda = 3.28$ nm, FV = 2.094 dB, and (f) $\Delta\lambda = 4.11$ nm, FV = 0.471 dB for determining every case of the measured T and ϕ, as shown in Figure 8 and also listed in the following Table 1. Here, the second decimal point for the measured $\Delta\lambda$ is an artificial estimation value, so that the accuracy of the measured $\Delta\lambda$ as well as the obtained T is one decimal point.

Table 1. Evaluating the simultaneous measurement of ϕ and T in different conditions by measuring the $\Delta\lambda$ and FV.

Measurement	Setting Conditions					
	(a) T = 20 °C, $\phi = 4°$	(b) T = 25 °C, $\phi = 1°$	(c) T = 30 °C, $\phi = 3°$	(d) T = 35 °C, $\phi = 0°$	(e) T = 40 °C, $\phi = 2°$	(f) T = 45 °C, $\phi = 5°$
Measured $\Delta\lambda$ (nm)	-0.1	0.73	1.48	2.42	3.28	4.1
Measured FV (dB)	0.847	2.399	1.488	2.654	2.094	0.471
Measured T (°C), ϕ (°)	T = 20.38, $\phi = 4$	T = 25.26, $\phi = 1.2$	T = 29.68, $\phi = 2.85$	T = 35.21, $\phi = 0.18$	T = 40.26, $\phi = 1.83$	T = 45.09, $\phi = 4.92$
Measured errors of T (°C), ϕ (°)	$T_{error} = 0.38$, $\phi_{error} = 0$	$T_{error} = 0.26$, $\phi_{error} = 0.2$	$T_{error} = -0.32$, $\phi_{error} = -0.15$	$T_{error} = 0.21$, $\phi_{error} = 0.18$	$T_{error} = 0.26$, $\phi_{error} = -0.17$	$T_{error} = 0.09$, $\phi_{error} = -0.08$
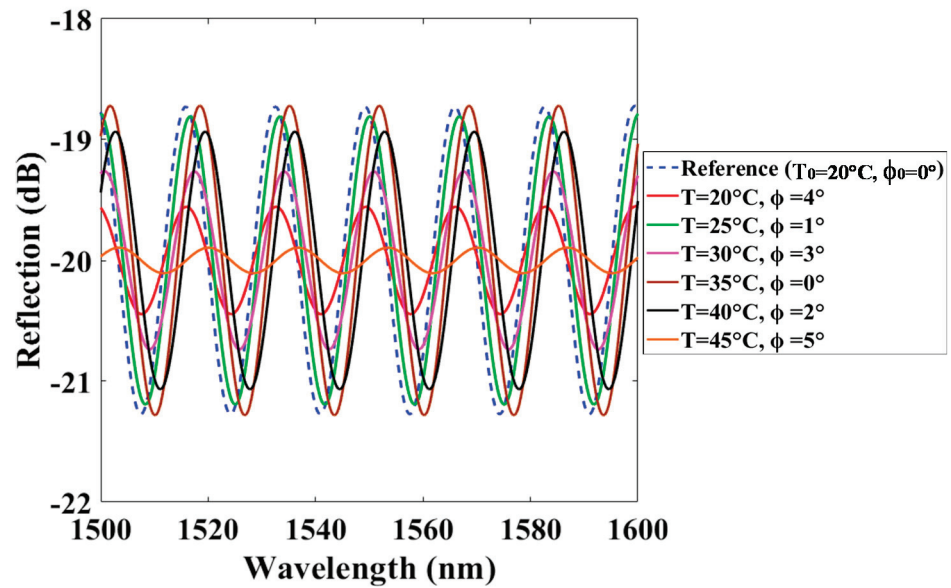
Figure 7. Interference spectra of the sensor when ϕ and T simultaneously change at different conditions.
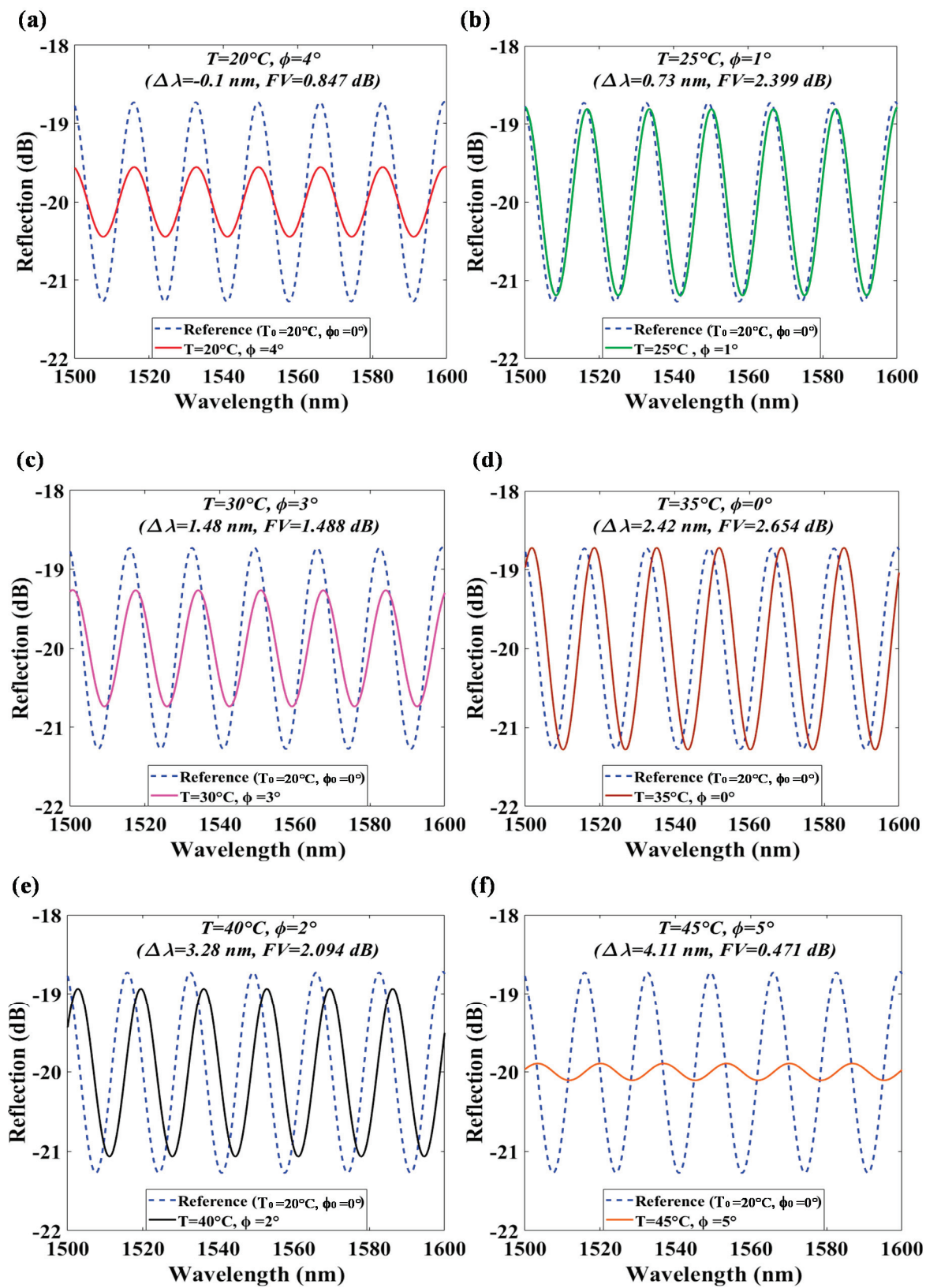
Figure 8. Interference spectra individually compared with the reference spectrum for (**a**) T = 20 °C, φ = 4°; (**b**) T = 25 °C, φ = 1°; (**c**) T = 30 °C, φ = 2°; (**d**) T = 35 °C, φ = 0°; (**e**) T = 40 °C, φ = 2°; and (**f**) T = 45 °C, φ = 5°.

The results in Figures 7 and 8 and Table 1 show that the simultaneous sensing of φ and T is accomplished. The simultaneously measured values of φ and T are very close

to the setting values displayed in the THCC and tilt stages. The six setting conditions of (a) T = 20 °C, φ = 4°; (b) T = 25 °C, φ = 1°; (c) T = 30 °C, φ = 2°; (d) T = 35 °C, φ = 0°; (e) T = 40 °C, φ = 2°; and (f) T = 45 °C, φ = 5° can achieve the measured T and φ with (a) T = 20.38 °C, φ = 4°; (b) T = 25.26 °C, φ = 1.2°; (c) T = 29.68 °C, φ = 2.85°; (d) T = 35.21 °C, φ = 0.18°; (e) T = 40.26 °C, φ = 1.83°; and (f) T = 45.09 °C, φ = 4.92°, respectively. The measured errors in T and φ are also shown in Figure 9 with (a) T_{error} = 0.38 °C, $φ_{error}$ = 0°; (b) T_{error} = 0.26 °C, $φ_{error}$ = 0.2°; (c) T_{error} = −0.32 °C, $φ_{error}$ = −0.15°; (d) T_{error} = 0.21 °C, $φ_{error}$ = 0.18°; (e) T_{error} = 0.26 °C, $φ_{error}$ = −0.17°; and (f) T_{error} = 0.09 °C, $φ_{error}$ = −0.08°, respectively. Based on the above data, the average errors of the measured φ and T of the six simultaneous measurements are approximately 0.253 °C and 0.13°, respectively. The above results demonstrate the effectiveness of the proposed PT/PFFI sensor for simultaneous measurement of φ and T. The small errors of the measurements are attributable to the deviations of operating the instruments. Moreover, non-flat endface of the fibers caus20ed by the mechanical fiber cleaver is another reason. The flat surface would be effectively cleaved by using a femtosecond laser to improve the measured accuracy [21].
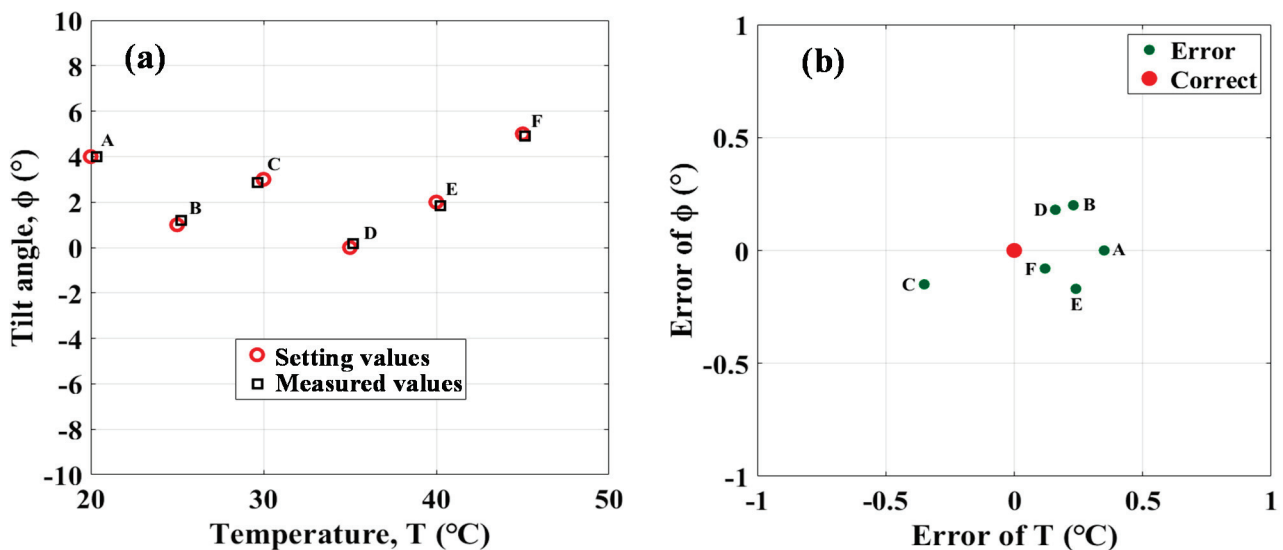
Figure 9. (**a**) Sample data for measurement comparison; (**b**) Error analysis of the sample measurement.

4. Conclusions

This study proposes a new sensing configuration combining the high T sensitivity and repeatability NOA61-PFFI to the flexible NOA65-PT. Thus, the sensor can achieve the simultaneous measurement of φ and T. The experimental results show that the interference FV of the optical spectra is only correlated with φ and the wavelength shifts (Δλ) of the interference spectra are only affected by T variations. Consistent results illustrate that by using the proposed sensing scheme with the specific characteristics of the used materials (NOA61 and NOA65 polymers), the fiber device can simultaneously and effectively measure T and φ with small errors. Furthermore, the proposed PT/PFFI can independently discriminate the tilt angle state and the surrounding T variations from the measured spectra. The sensing results demonstrate that the PT/PFFI can measure φ and T simultaneously with good sensitivities and averages of 0.4 dB/° and 0.17 nm/°C, respectively. The obtained results of the T and φ sensitivities may not be high but are comparable with those based on the FBG sensors, however, the advantages of this solution are that it is simple, flexible, easy to fabricate, and does not require an expansive laser system for writing the FBGs.

Author Contributions: This work was carried out in collaboration between all authors. The first author and corresponding author C.-L.L., proposed the sensing concept, verified the mathematical method, analyzed the data, wrote and revised the manuscript. Author, C.-S.C., an undergraduate student in the Department of EOE, finished the experiments, managed figures and data. Authors, C.-R.Y. and R.-C.Z., the graduated students in the Department of EOE, performed the first stage experiments, managed figures, and data. All authors have read and agreed to the published version of the manuscript.

Conflicts of Interest: The authors declare no conflict of interest.

References

1. Yin, J.; Liu, T.; Jiang, J.; Liu, K.; Wang, S.; Qin, Z.; Zou, S. Batch-producible fiber-optic fabry—Pérot sensor for simultaneous pressure and temperature sensing. *IEEE Photon. Technol. Lett.* **2014**, *26*, 2070–2073. [CrossRef]
2. Wu, Q.; Hatta, A.M.; Wang, P.; Semenova, Y.; Farrell, G. Use of a bent single SMS fiber structure for simultaneous measurement of displacement and temperature sensing. *IEEE Photon. Technol. Lett.* **2010**, *23*, 130–132. [CrossRef]
3. Wang, L.; Zhang, W.; Wang, B.; Chen, L.; Bai, Z.; Gao, S.; Li, J.; Liu, Y.; Zhang, L.; Zhou, Q.; et al. Simultaneous strain and temperature measurement by cascading few-mode fiber and single-mode fiber long-period fiber gratings. *Appl. Opt.* **2014**, *53*, 7045–7049. [CrossRef] [PubMed]
4. Zhou, J.; Liao, C.; Wang, Y.; Yin, G.; Zhong, X.; Yang, K.; Sun, B.; Wang, G.; Li, Z. Simultaneous measurement of strain and temperature by employing fiber Mach-Zehnder interferometer. *Opt. Express* **2014**, *22*, 1680–1686. [CrossRef] [PubMed]
5. Velázquez-González, J.S.; Monzón-Hernández, D.; Martinez-Pinon, F.; Hernández-Romano, I. Simultaneous measurement of refractive index and temperature using a SPR-based fiber optic sensor. *Sens. Actuators B Chem.* **2017**, *242*, 912–920. [CrossRef]
6. Pevec, S.; Donlagic, D. MultiParameter fiber-optic sensor for simultaneous measurement of thermal conductivity, pressure, refractive index, and temperature. *IEEE Photon. J.* **2017**, *9*, 2500114. [CrossRef]
7. Hu, D.J.J.; Lim, J.L.; Jiang, M.; Wang, Y.; Luan, F.; Shum, P.P.; Wei, H.; Tong, W. Long period grating cascaded to photonic crystal fiber modal interferometer for simultaneous measurement of temperature and refractive index. *Opt. Lett.* **2012**, *37*, 2283–2285. [CrossRef] [PubMed]
8. Ferreira, M.S.; Baptista, J.; Roy, P.; Jamier, R.; Février, S.; Frazão, O. Highly birefringent photonic bandgap Bragg fiber loop mirror for simultaneous measurement of strain and temperature. *Opt. Lett.* **2011**, *36*, 993–995. [CrossRef] [PubMed]
9. Pevec, S.; Donlagic, D. High resolution, all-fiber, micro-machined sensor for simultaneous measurement of refractive index and temperature. *Opt. Express* **2014**, *22*, 16241–16253. [CrossRef] [PubMed]
10. Lee, C.-L.; You, Y.-W.; Dai, J.-H.; Hsu, J.-M.; Horng, J.-S. Hygroscopic polymer microcavity fiber Fizeau interferometer incorporating a fiber bragg grating for simultaneously sensing humidity and temperature. *Sens. Actuators B Chem.* **2016**, *222*, 339–346. [CrossRef]
11. Choi, H.Y.; Mudhana, G.; Park, K.S.; Paek, U.-C.; Lee, B.H. Cross-talk free and ultra-compact fiber optic sensor for simultaneous measurement of temperature and refractive index. *Opt. Express* **2009**, *18*, 141–149. [CrossRef] [PubMed]
12. Ma, C.-T.; Chang, Y.-W.; Yang, Y.-J.; Lee, C.-L. A dual-polymer fiber fizeau interferometer for simultaneous measurement of relative humidity and temperature. *Sensors* **2017**, *17*, 2659. [CrossRef]
13. Osuch, T.; Markowski, K.; Manujło, A.; Jędrzejewski, K. Coupling independent fiber optic tilt and temperature sensor based on chirped tapered fiber Bragg grating in double-pass configuration. *Sens. Actuators A Phys.* **2016**, *252*, 76–81. [CrossRef]
14. Guo, J.-Y.; Wu, M.-S.; Lee, C.-L.; Liu, W.-F.; Lin, C.-F. Simultaneous measurement of tilt angle and temperature based on a taper-shaped polymer incorporating a fiber bragg grating. In Proceedings of the Conference on Lasers and Electro-Optics/Pacific Rim, Hong Kong, China, 29 July–3 August 2018; p. Th4L.4. [CrossRef]
15. Yang, R.; Bao, H.; Zhang, S.; Ni, K.; Zheng, Y.; Dong, X. Simultaneous measurement of tilt angle and temperature with pendulum-based fiber bragg grating sensor. *IEEE Sens. J.* **2015**, *15*, 6381–6384. [CrossRef]
16. Feng, Z.; Gang, T.; Hu, M.; Qiao, X.; Liu, N.; Rong, Q. A fiber inclinometer using a fiber microtaper with an air-gap microcavity fiber interferometer. *Opt. Commun.* **2016**, *364*, 134–138. [CrossRef]
17. Lee, C.L.; Zeng, R.C.; Yang, C.R.; Lin, C.F.; Ma, C.T.; Liu, W.F. Tapered polymer fiber inclinometers. *IEEE Photon. J.* **2020**, *12*, 7100910. [CrossRef]
18. Adhesive Index. Available online: https://www.norlandprod.com/adhesiveindex2.html (accessed on 24 July 2021).
19. Norland Optical Adhesive 65. Available online: https://www.norlandprod.com/adhesives/NOA%2065.html (accessed on 10 August 2021).
20. Norland Optical Adhesive 61. Available online: https://www.norlandprod.com/adhesives/NOA%2061.html (accessed on 10 August 2021).
21. Al Mamun, A.; Cadusch, P.J.; Katkus, T.; Juodkazis, S.; Stoddart, P.R. Quantifying end-face quality of cleaved fibers: Femtosecond laser versus mechanical scribing. *Opt. Laser Technol.* **2021**, *141*, 107111. [CrossRef]

Article

Preparation of Electrochemical Supercapacitor Based on Polypyrrole/Gum Arabic Composites

Rizwan Ullah [1,*], Nadia Khan [1], Rozina Khattak [2,*], Mehtab Khan [1], Muhammad Sufaid Khan [3] and Omar M. Ali [4]

[1] National Center of Excellence in Physical Chemistry, University of Peshawar, Peshawar 25120, Pakistan; Khannadia@uop.edu.pk (N.K.); mehtabk324@uop.edu.pk (M.K.)

[2] Department of Chemistry, Shaheed Benazir Bhutto Women University, Peshawar 25000, Pakistan

[3] Department of Chemistry, University of Malakand, Chakdara 18800, Pakistan; sufaidkhan1984@uom.edu.pk

[4] Department of Chemistry, Turabah University College, Turabah Branch, Taif University, P.O. Box 11099, Taif 21944, Saudi Arabia; om.ali@tu.edu.sa

* Correspondence: drrizwan@uop.edu.pk (R.U.); rznkhattak@sbbwu.edu.pk (R.K.)

Abstract: The current research focused on the super capacitive behavior of organic conducting polymer, i.e., polypyrrole (PPy) and its composites with gum arabic (GA) prepared via inverse emulsion polymerization. The synthesized composites material was analyzed by different analytical techniques, such as UV-visible, FTIR, TGA, XRD, and SEM. The UV-Vis and FTIR spectroscopy clearly show the successful insertion of GA into PPy matrix. The TGA analysis shows high thermal stability for composites than pure PPy. The XRD and SEM analysis show the crystalline and amorphous structures and overall morphology of the composites is more compact and mesoporous as compared to the pure PPy. The electrochemical properties of modified solid state supercapacitors established on pure polypyrrole (PPy), polypyrrole/gum arabic (PPy/GA) based composites were investigated through cyclic voltammetry (CV), electrochemical impedance spectroscopy (EIS) and galvanostatic charge–discharge (GCD). The specific capacitance of the PPy modified gold electrode is impressive (~168 F/g). The specific capacitance of PPy/GA 1 electrode has been increased to 368 F/g with a high energy density and power density (~73 Wh/kg), and (~599 W/kg) respectively.

Keywords: polypyrrole; gum arabic; supercapacitors; EIS; GCD

1. Introduction

In the modern era, an integral part of human life is smart technology. Accordingly, advanced technologies are always searching for smart and well-fabricated materials to satisfy the growing demand [1–3]. The development of novel materials with improved electrochemical performance is required to address the critical issue of pollution. There is a growing need for sustainable and renewable energy storage solutions in hybrid automobiles and portable electronic devices [4], necessitating the development of innovative materials with better electrochemical capabilities, such as electrochemical capacitors or supercapacitors [5]. A supercapacitor is a type of energy storage system that combines both battery and conventional capacitor properties [6,7]. Electrochemical capacitors, or supercapacitors, have been extensively used in high-power energy storage materials. As such, supercapacitors are one of the most promising candidates among the various systems that lead the state-of-the-art electrical energy storage systems due to their environmental friendliness, sustainable cycle stability, low cost [8], excellent cycling life [9], high power density, and fast charging/discharging rate [5,10]. Supercapacitors are classified as electrochemical double-layer capacitors (EDLCs) or pseudosupercapacitors based on their charge storage mechanism [11,12]. The electrostatic separation of ionic and electronic charges at the electrode and electrolyte interfaces provides energy storage in EDLCs, and the efficiency of such devices is dictated by the surface area involved in the charge accumulation process

between the electrodes and electrolyte [13]. However, a faradaic (redox) reaction happens at the electrode surfaces in the pseudocapacitor process, resulting in energy storage effects. The behavior of pseudocapacitors is determined by the electrode material, which exhibits electrochemical signatures, and the charge storage is mostly determined by the applied voltage [14,15]. Conducting polymers (CPs) are the best choice for these two types of electrochemical devices because they possess both ionic and electronic conductivities. Doping various ionic or non-ionic materials or fillers into CPs can further increase their conductivities [16].

Among the various CPs, PPy is extensively studied because of its ease of preparation, stabilized oxide form, good oxidation and reduction properties [17], and the capability to provide high conductivity [18], commercially easily available monomers [19], as well as optical and good electrical properties [20]. PPy consists of alternate single and double-bonded macromolecular chain structures. PPy excellent performance is due to its structure, but it also has some drawbacks, such as lower capacitance and poor cycling stability, which limit its use in high-performance supercapacitors [21]. It is well known that biodegradable polymers are preferable to non-biodegradable polymers. Some of the biodegradable polymers that are used as supercapacitorsare chitosan (CS) [22], PVA [23], and glycerol [24]. On the other hand, gum arabic (GA) in the composite form can be used to alleviate the pure PPy problem. The insertion of GA into the PPy matrix can be a promising choice due to its high contact area, chemical stability, thermal stability, and mechanical stability, as well as its high energy storage capabilities at the electrode/electrolyte interface.

In this research work, an electrode for a supercapacitor based on PPy/GA composites was fabricated by inverse emulsion polymerization. The electrochemical characteristics, cyclic voltammetry (CV), electrochemical impedance spectroscopy (EIS), and galvanometric charging–discharging (GCD) properties of the fabricated PPy/GA composites based supercapacitor devices were investigated. The synthesized materials could be promising electrode materials for high-performance supercapacitor applications, which have not been previously reported.

2. Materials and Methods

2.1. Materials

All the chemicals were of Analytical grade. Pyrrole monomer (Fluka Chemie AG, Buchs, Switzerland) was distilled twice before use. Toluene, 2-propanol, benzoyl peroxide (BPO) ($\geq$ 98% Sigma-Aldrich Inc., ST. Louis, MO, USA), N-methyl-2-pyrrolidone (NMP) (RCI Labscan limited Pathumwan, Bangkok, Thailand), dodecylbenzene sulphonic acid (DBSA) and acetone > 98%, Sigma-Aldrich Inc., ST. Louis, MO, USA),were used as received. Double-distilled water was used for solution preparation and for washing glassware.

2.2. Synthesis of Polypyrrole (PPy)

PPy was synthesized by using a pyrrole monomer via inverse emulsion polymerization. The procedure was carried out in a three-necked round bottom flask holding 35 mL toluene and 10 mL 2-propanol that was stirred for 15 min. After that, 200 μL of pyrrole was added and stirred for another 15 min, followed by drop wise addition of 0.5 mL of DBSA and 0.303 g of benzoyl peroxide (dissolved in 5 mL of water) to the reaction mixture. To get the precipitate, the mixture was vigorously stirred for 24 h. The precipitate was washed three times with distilled water and 50 mL of acetone to separate the pure product that was dried in an oven at 50 °C for 24 h. The representative procedure of the synthesis of polypyrrole has been sketched in Figure 1.
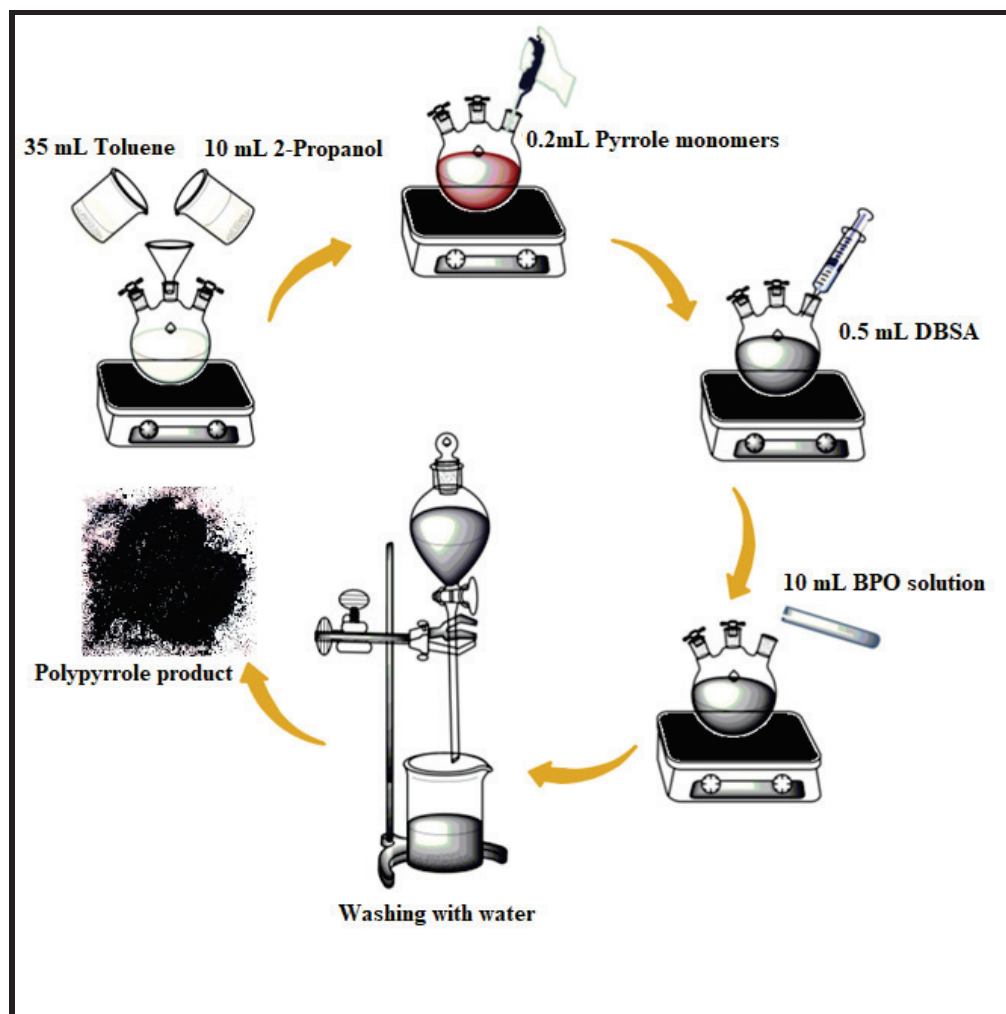
Figure 1. Synthesis route followed for polypyrrole.

2.3. Synthesis of Polypyrrole/Gum Arabic (PPy/GA) Composites

PPy/GA composites were synthesized by inverse emulsion polymerization using monomer pyrrole and gum arabic (GA). The procedure was the same as for polypyrrole synthesis, except in composite production, different weight percent's of GA, such as 0.125%, 0.25%, 0.75% and 1% were added before the addition of benzoyl peroxide (BPO). To get the precipitate, the mixture was vigorously stirred for 24 h. To separate the pure product, the precipitate was washed three times with distilled water and 50 mL of acetone, then dried in an oven at 50 °C for 24 h. Table 1 shows the composition of PPy/GA composites and Scheme 1 shows the structural representation of the reactants.

Table 1. The designation and composition of the PPy/GA composites.

Sample Designation	DBSA (mL)	BPO (g)	GA (wt%)
PPy/GA 1	0.5	0.303	0.125
PPy/GA 2	0.5	0.303	0.25
PPy/GA 3	0.5	0.303	0.5
PPy/GA 4	0.5	0.303	0.75
PPy/GA 5	0.5	0.303	1
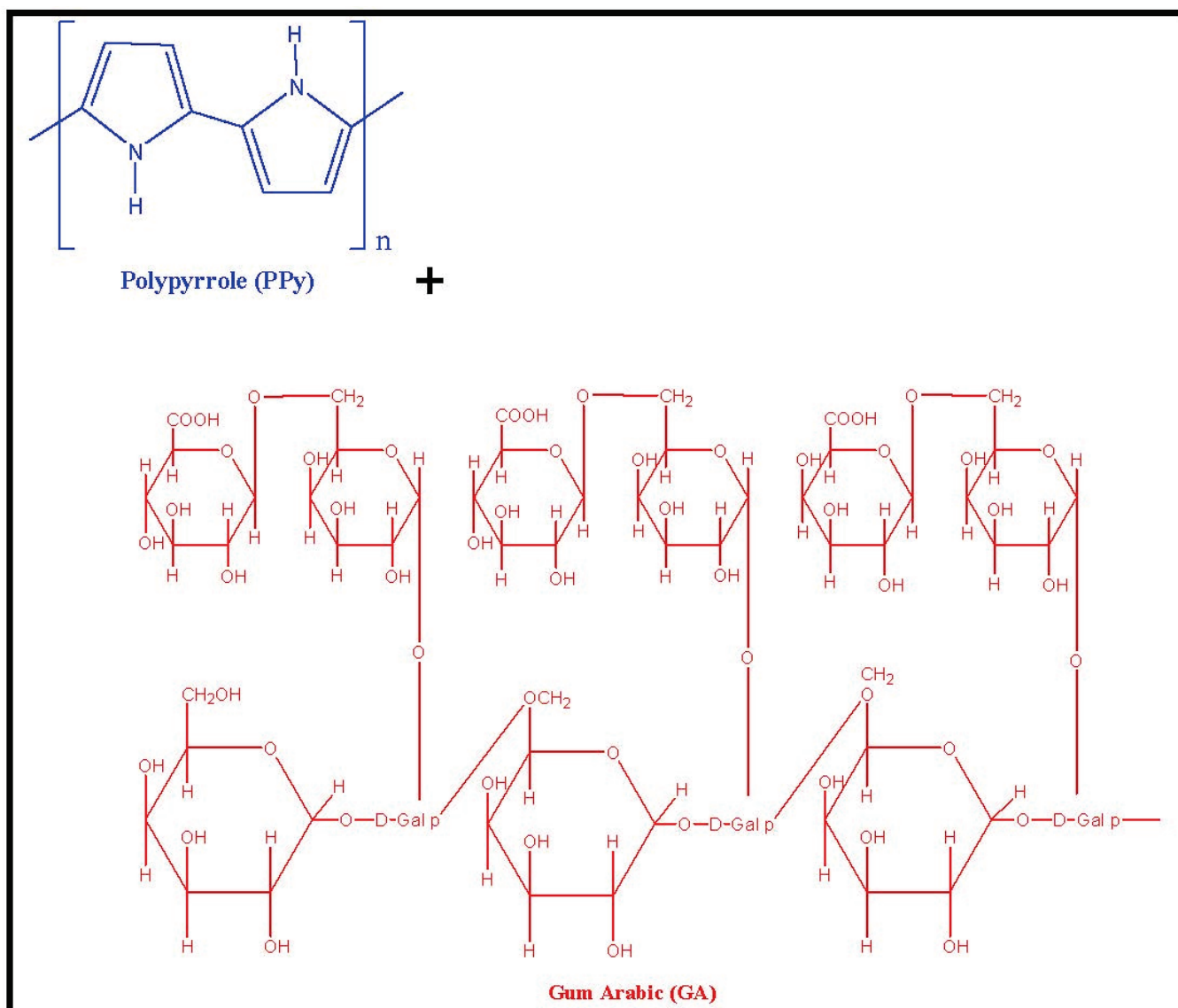
Scheme 1. Structural representation of reactants, i.e., polypyrrole and gum arabic.

2.4. Characterization of the Synthesized Polymer and its Composites with Gum Arabic

The UV/visible spectrophotometer (UV752PC) (Citi Scientific Supply, Ltd. Karachi, Pakistan) was employed to identify the electronic transitions from lower to higher energy levels in the UV-visible range of radiation. To detect functional groups and the interaction of PPy and PPy/GA composites, we employed Fourier-transform infrared (FTIR) spectroscopy (model 783 PerkinElmer Inc., Waltham, MA, USA). The crystallinity of the conducting polymers (CPs) was measured using X-ray diffractometry. The XRD spectra of the synthesized material were taken by using {Cu Kα radiations (λ = 1.5405 A°) JEOL JDX-3532, X-ray diffractometer, JEOL Ltd., Tokyo, Japan}. Scanning electron microscopy (SEM JSM-IT-100 JEOL Ltd., Tokyo, Japan) helped to scan the surface of the synthesized materials. The thermogravimetric analysis of the synthesized materials was carried out at TGA SDT Q600 (PerkinElmer Inc., Waltham, MA, USA). The electrochemical properties such as cyclic voltammetry (CV), electrochemical impedance spectroscopy (EIS), and galvanostatic charge–discharge (GCD) were performed on the electrochemical workstation (PGSTAT302, Metrohm AUTOLAB B.V. Ltd., KM Utrecht, Netherlands). The CV tests were performed at the scan rate of 100 mV/s in the potential window of −0.4 to 0.8 V. The GCD tests were

conducted under current densities from 1 to 2.5 A/g by holding the cut-off voltage between −0.4 and 0.8 V.

2.5. Fabrication of Solid-State Supercapacitors

The surface of the gold electrode (GE) was modified to evaluate the electrochemical activity of pure PPy and PPy/GA composites. Before using the GE, it was meticulously polished with 0.3 µm alumina (Al_2O_3) powder, rinsed with deionized water, then ethanol, and then sonicated for 10 min. After that, the material was ultrasonically dispersed for 5 min to prepare an effective and uniform chloroform solution of any specified composition of PPy/GA. The surface of the GE was modified using the 5 µL PPy/GA composite solution to obtain the PPy/GA/GE. The electrode was kept at room temperature for 10 min to dry completely. The surface of the electrode was activated by cycling the voltage from −0.4 to 0.8 V at a scan rate of 100 mV/s in a 1 M solution of H_2SO_4. The modified electrode was carefully cleaned with distilled water before and after the experiment, then reactivated using the method described above (Figure 2).
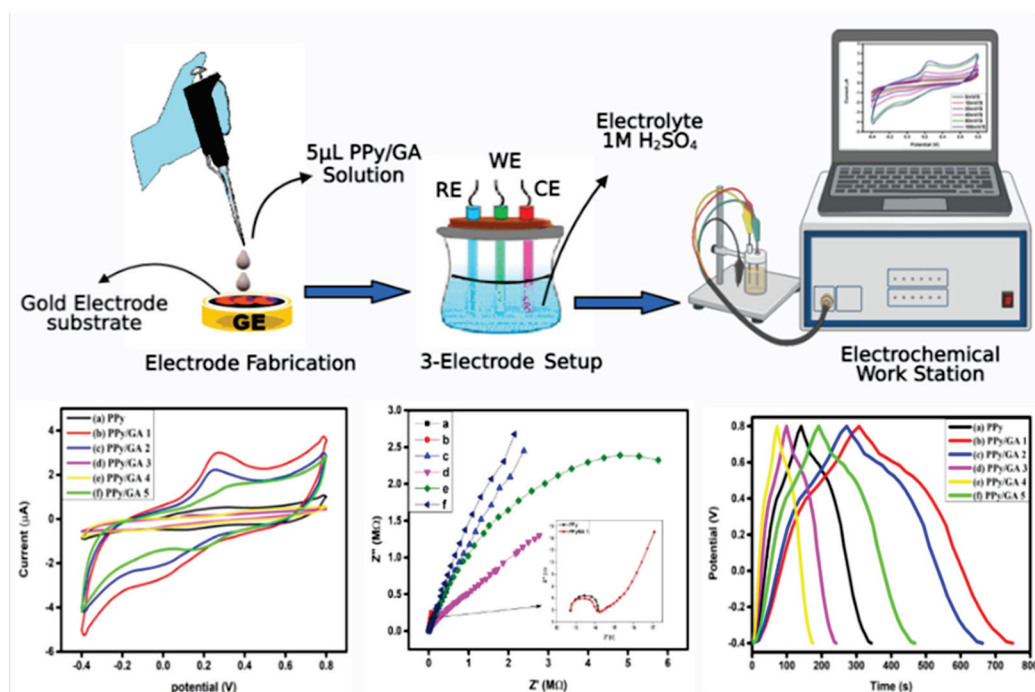
Figure 2. Schematic illustration of the electrode fabrication towards electrochemical properties.

3. Results and Discussion

3.1. UV-Visible Analysis of the Synthesized PPy and PPy/GA Composites

Figure 3a shows the UV-visible spectra of pure PPy and PPy/GA composites. Two significant absorption peaks can be seen in the spectra. At 312–319 nm and 445–480 nm, the first and second absorption peaks were found, respectively. The transition of electrons from the lowest occupied molecular orbital (LOMO) to the highest unoccupied molecular orbital (HUMO), which corresponds to the π–π* electronic transition of the aromatic ring in the polymer chain, is responsible for the first absorption band [25]. The sum of polarons and bipolarons is assigned to the second absorption band, which serves to determine that the PPy component of the composites is made up of free carriers (mainly polarons) [26], suggesting the CPs in their oxidized and conducting state [27]. The difference in peak intensities is related to the difference in composite concentration in the solvent, whereas the difference in peak position is due to the length of the polymer chain. There is a change in the absorption spectra when GA is added to the PPy matrix. The first absorption band exhibited a small rise as GA concentrations increased. Both intensity and peak shifting

were detected in the second absorption peak. The absorption peak for PPy/GA 1 shifts toward a longer wavelength (red shift). The shift of peaks towards lower wavelengths was noted in the PPy/GA 2 through PPy/GA 5 composites. The absorption shift is caused by the blocking of ions or free radicals or the active site of the PPy by GA.
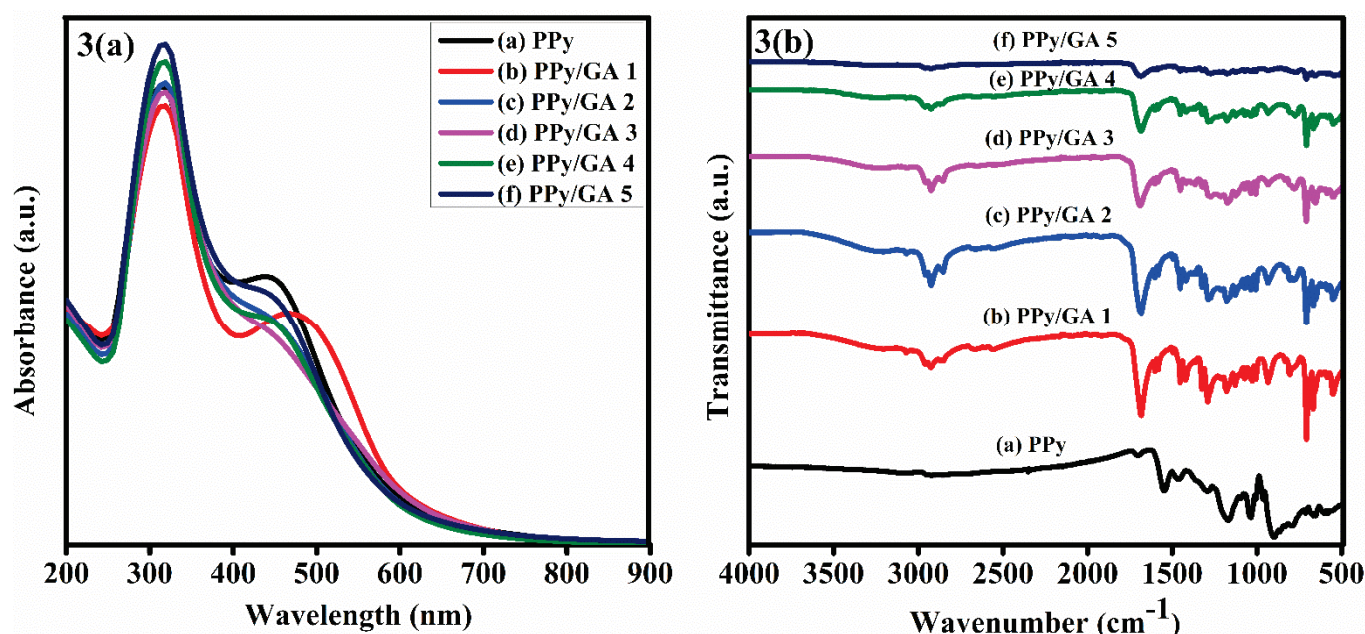
Figure 3. (**a**) UV-visible spectra of neat polypyrrole and its composites with gum arabic. (**b**) FTIR spectra of neat polypyrrole and its composites with gum arabic.

3.2. FTIR Analysis of the Synthesized PPy and PPy/GA Composites

The FTIR analysis of PPy and PPy/GA composites was performed in the range of 500 to 4000 cm^{-1} to investigate the atomic and molecular vibrations and the types of bonding states in the synthesized materials. The low-intensity peak in the PPy spectrum in the region of 2954–2851 cm^{-1} is attributable to the C–H and S=O stretching modes, which clearly reveals the existence of the benzenoid ring of DBSA in the polymer matrix in Figure 3b [28]. Sulfonate anions, –SO$_3$$^-$, have a stretching vibration of S=O at 1170 cm^{-1}, which compensates for the cation in the polypyrrole chains. The DBSA displays the distinctive signal at 652 cm^{-1} in the PPy sample [29]. The stretching vibration of C=C can be seen at 1548 cm^{-1}, whereas the stretching vibration of C–N in the Py ring can be seen at 1454–1471 cm^{-1}. The signal at 1703 cm^{-1} is due to the out-of-plane wagging of the carbonyl group. At 1035 cm^{-1}, the stretching vibration of C–H of the Py ring can be noticed [30,31]. The peak at 1291 cm^{-1} is connected to C–N in a plane.

All of the typical peaks of PPy are seen in the FTIR spectra of PPy/GA composites, as explained above and shown in Figure 3b. The stretching vibration of the O–H bond is responsible for the wide and low-intensity peak at 3209 cm^{-1}. The stretching vibration of the C=O bond of the carboxylate group of the GA molecule is responsible for the high peak intensity at 1683 cm^{-1} [32,33]. The asymmetric stretching causes the strongest band at 1602 cm^{-1}, whereas the symmetric stretching vibration of the carboxylic acid salt –COO$^-$ [34] causes the weaker band at 1422 cm^{-1}. Some of the GA peaks are superimposed over the PPy in the composites, indicating that the GA particles have been effectively incorporated into the PPy matrix.

3.3. SEM Analysis of PPy and PPy/GA Composites

Figure 4 shows SEM images of pure PPy and PPy/GA 1–5 composites. As can be seen, the synthesized PPy appears to have a uniform granular structure that is agglomerated and

homogeneous in shape and size [35]. The pure PPy powder has an average grain size of ~0.72 μm. Pure PPy has a weakly porous morphology with a non-uniform pore size.

Figure 4. SEM images of (**A**) PPy, (**B**) PPy/GA 1, (**C**) PPy/GA 2, (**D**) PPy/GA 3, (**E**) PPy/GA 4, and (**F**) PPy/GA 5.

The morphology of PPy/GA 1 composite is radically different. The particles are irregular in size and shape at lower concentrations (0.125 percent) of GA in composites, as seen in Figure 4B. By raising the GA content to 0.75 percent, wool morphologies with elongated and linked particles were found in the micrometric range. The particles aggregate and form large-sized particles with no discernible morphology when the GA concentration is raised even further to 1% [36]. As a result, the presence of GA has a significant effect on the size and morphology of the resulting composite materials. The overall morphology of the composites appears to be more compact and mesoporous as compared to the pure PPy. Figure 4F shows that the surface of the synthesized nanocomposite is smoother than that of

PPy, which is most likely due to the hydration behavior effect of GA on PPy structure. As a result, their intrinsic viscosity and particles size are affected [36,37].

3.4. X-ray Diffraction

The most efficient method for analyzing the structure and nature of materials is XRD. The XRD spectrum of PPy is shown in Figure 5a. A broad peak can be seen at 2θ = 29.73°. This is PPy characteristic peak. The scattering of X-rays from PPy chains at interplaner spacing causes the peak to expand [36]. Broad peaks in the CPs are normally thought to suggest a semicrystalline structure. The PPy average chain separation from the maxima may be calculated using Equation (1) below [38].

$$S = \frac{5\lambda}{8 sin\theta} \tag{1}$$

where *S* denotes the polymer chain separation, λ is the wavelength of the X-ray that was used, and θ is the angle of diffraction at the amorphous halo's maximum intensity. The average separation of the polymer chains was found to be 1.4 Å in the case of PPy. The Debye–Scherrer Equation (2) [39] was used to calculate the average crystallite size of PPy.

$$D = \frac{k\lambda}{\beta cos\theta} \tag{2}$$

Figure 5. (**a**) XRD peaks of neat polypyrrole and its composites with gum arabic. (**b**) TGA of neat polypyrrole and its composites with gum arabic.

D stands for the average crystallite size, while *k* stands for the dimensionless shape factor, which has a value of 0.9, which is close to unity. It varies depending upon the crystallite's shape, λ is the wavelength of X-ray that was used, and β is the angle of diffraction at full width and at half maximum. PPy has a crystallite size of 0.627 nm. Peaks were found at 2θ = 23.82°, 25.97°, 27.57°, 30.41°, and 34.99° in the PPy/GA 1 composite as shown in Figure 5a. The PPy/GA composites are partially amorphous and also partially crystalline in nature. The sharp and narrow peaks show the crystalline nature of the composites, whereas the halo and broad peaks show the amorphous nature of the composites. According to the previous discussion, increasing the quantity of GA in the composites to PPy/GA 2, where

the amount of GA is 0.25 percent, enhances the crystallinity of PPy [40]. By further increasing the amount of GA in the composite materials, the composites become less crystalline at PPy/GA 5. GA is mostly amorphous in nature. The crystallinity of PPy/GA 1 increases due to the formation of composites of GA with PPy, which is not an unexpected result. However, at higher concentration of GA in the composites (PPy/GA 5) the amorphous nature becomes dominant as clearly seen in Figure 5a, which is attributed to the mostly amorphous nature of GA.

3.5. Thermal Gravimetric Analysis (TGA)

The thermal stability of pure PPy and PPy/GA composites was investigated by thermal gravimetric analysis (TGA). The TGA curves of pure PPy and PPy/GA composites are shown in Figure 5b. The thermograms were recorded in the nitrogen atmosphere by heating the samples at a temperature ranging from 25 to 800 °C. The TGA of PPy shows weight loss at three stages. The first stage of weight loss (10%) from 35 to 150 °C is attributed to the volatilization of water molecules from the polymer. The second stage of weight loss, from 150 to 400 °C, is attributed to the decomposition of the dopant molecule DBSA. The PPy backbone is completely decomposed in the third stage of weight loss from 440 to 800 °C [41].

All the composites show the same thermogram and also show weight loss at three stages. Water molecules are removed during the first stage of weight loss, which occurs at low temperatures ranging from 35 to 150 °C. At temperatures ranging from 300 to 480 °C, the degradation of GA components causes the second readily apparent weight loss. The third and final weight loss occurred at a high temperature of 500 °C, which is attributed to the decomposition of the PPy backbone. During the polysaccharide degradation process, there is no significant difference, and at high temperatures, approximately the same amount of residue is obtained [42]. The degradation of the PPy chain has been pushed to 500 °C in the composite form. This indicates that the GA has been integrated into the PPy matrix, and it also improves the composites' thermal stability at 500 °C. The degradation of the pure PPy chain begins at 450 °C, whereas the degradation of the main polymer chain in composites begins at around 500 °C. This implies that the PPy/GA composite has good thermal stability. At 800 °C, the overall stability of PPy is greater than that of PPy/GA composites. Pure PPy causes less overall weight loss than the PPy/GA composite.

3.6. Electrochemical Properties

3.6.1. Cyclic Voltammetry

Figure 6a shows the CV curves of PPy and PPy/GA 1 to PPy/GA 5 at the scan rate of 100 mV/s in the potential window of −0.4 to 0.8 V. PPy shows the oxidation peak at 0.31 V with a current 0.539 μA and the reduction peak at 0.107 V with −0.481 μA current. However, the PPy/GA 1 shows the oxidation peak at 0.266 V and 2.99 μA, and the reduction peak at 0.014 V and −2.59 μA. Meanwhile, the PPy/GA 2 shows the oxidation peak at 0.24 V and 2.21 μA, and the reduction peak at 0.017 V and −2.12 μA. Similarly, the PPy/GA 3/4/5 show the oxidation peak at 0.13 V/0.52 V/0.35 V with current 0.164 μA/0.47 μA/1.55 μA and the reduction peak at 0.11 V/0.12 V/0.16 V with current −0.48 μA/−0.51 μA/−1.3 μA, respectively.

Figure 6. (**a**) CV of neat polypyrrole and its composites with gum arabic. (**b**) CV of PPy/GA 1 on gold electrode in 1 M H_2SO_4 at different scan rates. (**c**) Plot of square root of scan rates versus current for PPy/GA 1 in 1 M H_2SO_4.

Figure 6a shows that pure PPy, PPy/GA 2, and PPy/GA 5 composites have a rectangular shape, indicating that the material has a high capacitance characteristic. The shape of the PPy/GA 3 and PPy/GA 4 is similar to that of a banana. In comparison to pure PPy, the PPy/GA 1, PPy/GA 2, and PPy/GA 5 composites demonstrate high current. However, the PPy/GA 3 and PPy/GA 4 display low current as compared to pure PPy. The increase in current in case of PPy/GA 1 is due to the addition of 0.125% GA. The current reduces when further content, i.e., 0.25% of GA is added to the PPy, as seen in Figure 6a in sample PPy/GA 2. This is due to the blockage of the active site(s) of PPy. In addition, the inclusion of 0.5% and 0.75% GA, as in PPy/GA 3 and PPy/GA 4, respectively, resulted in higher active sites' blocking. The addition of 1% GA (PPy/GA 5) causes an increase in current, which is attributable to the alcoholic group and carboxylate ion of the GA [37].

3.6.2. Effect of Scan Rate on CV Curves of PPy/GA 1 Composite

To investigate the influence of scan rate, i.e., 5 to 100 mV/s, on the PPy/GA 1 composite or charge storage mechanism of the fabricated electrode can be determined by power law, where current is directly proportional to scan rate. Ip = a v^b, where a and b are adjustable parameters, Ip is current densities and v is scan rate. The b-value is calculated from slope of straight line equation. There are two kinds of behavior battery type (b = 0.5) and capacitive types (b = 1) [43]. When the scan rate was raised, the anodic and cathodic peak currents

rose, and the Ipa peaks moved slightly to the right as shown in Figure 6b,c shows a linear relationship between square root of scan rate and anodic and cathodic peaks current. Form straight line equation both Ipa and Ipc, the linear plots of current versus square root of scan rate exhibit regression values of 0.988 and 0.990 and slope values (0.5 Ipa) and (−0.2 Ipc) as shown in Figure 6c. Therefore, the reaction mechanism is suggesting that the reaction is diffusion controlled.

3.6.3. EIS Study of PPy and PPY/GA Composites

Impedance spectroscopy is very beneficial for obtaining information about the electrode materials' resistive and capacitance properties. At a constant DC potential of 0.5 V with an AC of 0.01 V, a potentiostatic EIS study was performed from 0.1 Hz to 100 kHz. Figure 7a depicts a Nyquist plot of pure PPy and various PPy/GA composites. However, Figure 7b shows an equivalent circuit for EIS. The Nyquist plot of pure PPy reveals a distorted semicircle at a high-frequency region [44]. This semicircle is followed by a 45° slanted or sloped line, which is followed by a straight line in the low-frequency region. The intercepts on the *X*-axis and the real axis are termed solution resistance (Rs), and the diameters of semicircles indicate electrode resistance (Rct) in the high-frequency area because of charge transfer resistance in the active compounds. When compared to pure PPy, the PPy/GA 1 composite had a somewhat narrower semicircle, indicating a low Rct value. In the low-frequency region, the PPy/GA 2, PPy/GA 3, and PPy/GA 5 display a straight line with an angle of 45° to 65°, which resembles an ideal capacitor and fast ion diffusion in electrode materials. In the high-frequency region shown in Figure 7a, as the GA loading in the composite increases from 0.125 to 1 wt%, Rs increases from 12.8 to 2682 ohm, and the diameter of the semicircle (Rct) grows. Despite the composites' 0.5 wt% GA content, the high Rct suggests that as GA content increases, the number of surface electrochemical reaction sites decreases. When the GA loading in the composite is increased to 1 wt%, the number of bulk electrochemical reaction sites increases relative to the number of surface electrochemical reaction sites and the Rs again decrease. Because of the non-homogeneity of samples, porosity, and non-uniform distribution of current, a constant phase element (CPE) is used in the equivalent circuit instead of a capacitor. PPy/GA 4 indicates poor contact between the current collector and active materials, as well as high intrinsic resistance of the active material. The high resistance to ion transport between the electrolyte solution and the electrode interface causes the semi-circle or Rct value to rise. The data is summarized in Table 2.

Table 2. Solution resistance of the PPy/GA 1–5 composites.

S. No	Samples	Solution Resistance (Rs) (Ω)
1	PPy/GA 1	12.75
2	PPy/GA 2	279
3	PPy/GA 3	2682
4	PPy/GA 4	1456
5	PPy/GA 5	98

Figure 7. (**a**) EIS spectra of (a) PPy, (b) PPy/GA 1, (c) PPy/GA 2, (d) PPy/GA 3, (e) PPy/GA 4, and (f) PPy/GA 5. (**b**) Equivalent circuit for EIS.

3.6.4. Galvanostatic Charge-Discharge (GCD) Study of PPy and PPY/GA Composites

GCD has also described the electrochemical performance of the produced electrodes [45] as well as the galvanostatic charge-discharge curves of PPy/GA 1 for the supercapacitors device at varied current densities of 1, 1.5, 2, and 2.5 A/g Figure 8a. The GCD curves for the fabricated electrodes PPy and PPy/GA 1 to PPy/GA 5 at various loading concentrations of gum arabic and at a fixed current density of 1 A/g are shown in Figure 8b. The shape of the curves depicts optimal capacitor behavior for supercapacitors. The charge curves are symmetric to discharge curves between potential intervals indicating feasibility of PPy/GA surface for supercapacitor [46].

The following equations were used to determine various parameters such as specific capacitance (Cs), energy density (E), and power density (P) from the GCD curves of modified supercapacitor electrodes [46].

The specific capacitance (Cs) of the modified supercapacitor electrodes was calculated by using Equation (3) [47].

$$Cs = \frac{I \times \Delta t}{m \times \Delta V} \tag{3}$$

where "I" is the charge-discharge current (A), Δt is the discharge time, "m" is the mass deposited on the electrode, and ΔV is the voltage difference in the discharge segment. The total energy density E (Wh kg^{-1}) and power density P (Wkg^{-1}) of the supercapacitor device were calculated using Equations (4) and (5) [48].

$$E = \frac{1}{2 \times 3.6} \times Cs \times \Delta V^2 \tag{4}$$

$$P = \frac{E}{\Delta t} \times 3600 \tag{5}$$
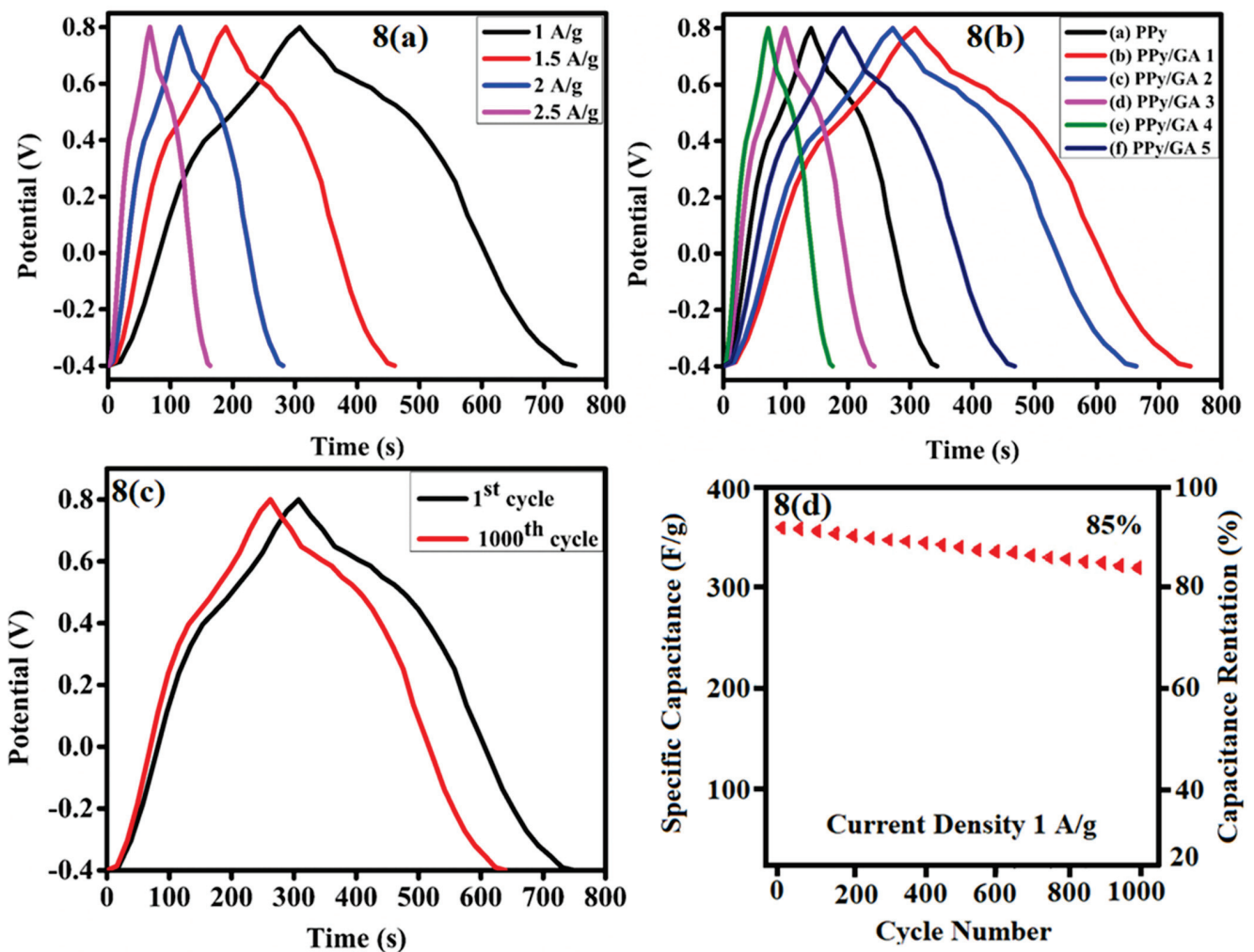
Figure 8. (**a**) GCD curves of PPy/GA 1 composite at different current densities. (**b**) GCD curves of neat PPy and PPy/GA composites at 1 A/g current density. (**c**) GCD curves of PPy/GA 1 for 1st and 1000th cycles at 1 A/g current density. (**d**) Plot of specific capacitance and capacitance retention versus cycle number.

In Equations (4) and (5) of energy density (E, Wh/kg) and power density (P, W/kg), Cs is the specific capacitance, ΔV is the potential window, and Δt is the discharge time as mentioned previously. The values of Cs, E, and P are tabulated for PPy and PPy/GA composites in Table 3.

Table 3. The specific capacitance, energy density, and power density of PPy and PPy/GA 1–5.

Sample	Current Density (A/g)	Specific Capacitance (F/g)	Energy Density (Wh/kg)	Power Density(W/kg)
PPy	1	168.6	33.698	599.37
PPy/GA 1	1	368.57	73.667	599.609
PPy/GA 2	1	325.83	65.12	599.607
PPy/GA 3	1	118.83	23.75	599.579
PPy/GA 4	1	86.25	17.238	599.582
PPy/GA 5	1	230	45.97	599.608

Table 4 compares the specific capacitance of PPy/biodegradable polymers-based electrodes to that of a PPy/GA composite developed in this study. Table 4 demonstrates that PPy/GA has a relatively high specific capacitance.

Table 4. Comparison of specific capacitance of PPy/biodegradable polymers-based electrodes.

Electrode Material	Specific Capacitance	Current Density	Reference
PPy/lignin	11.42	$2.0A\ g^{-1}$	[49]
PPy/Nanocellulose	$35\ F\ g^{-1}$	$0.27\ A\ g^{-1}$	[50]
PPy/Cotton	$225\ F\ g^{-1}$	$0.6\ mA\ cm^{-2}$	[51]
PPy/BC	$316\ F\ g^{-1}$	$0.2\ A\ g^{-1}$	[52]
PPy/SFC	$367\ F\ g^{-1}$	$0.2\ A\ g^{-1}$	[53]
PPy/GA	$368.57\ F\ g^{-1}$	$1.0\ A\ g^{-1}$	This work

The apparent behavior of the GCD curves is well-adapted to the typical behavior of supercapacitors, which reveals that specific capacities have a declining nature and an increase in current density. The PPy/GA-based electrode proved its characteristic double-layer capacitance behavior as well as good electrochemical reversibility with a highly symmetric triangular-shaped charge/discharge curve [54]. The addition of 0.125% GA to the PPy matrix increases the charge and discharge time, which demonstrates the increase in the specific capacitance. The incorporation of GA in the PPy matrix may result in a mesoporous structure, which increases surface area and ionic conductivity. Figure 8c demonstrates the cyclic stability of the modified electrode, which was evaluated for 1000 charge–discharge cycles at a current density of 1 A/g and still had an 85% specific capacitance [2] Figure 8d. The ohmic drop in the GCD curves can be attributed the solution resistance.

4. Conclusions

In the current study, the pure polypyrrole (PPy) and its composites with gum arabic (GA) have been successfully prepared by inverse emulsion polymerization method using toluene and 2-propanol as a solvent media. UV-visible and the FTIR spectroscopy confirmed the formation of PPy/GA composites. The XRD result shows that GA has both natures crystalline and amorphous. When the concentration of GA is less it shows crystalline nature, by increasing the concentration of GA the amorphous nature become dominant. The SEM morphologies demonstrate porous morphology for pure PPy and compact and mesoporous morphology for PPy/GA 1 composites. PPy/GA composites show high thermal stability up to 800 °C. The synthesized material shows good electrochemical properties in terms of using cyclic voltammetry, galvanostatic charging–discharging, and EIS tests. PPy has the lowest specific capacitance, energy density, and power density, with values of 168.6 F/g, 33.698 Wh/kg, and 599.37 W/kg respectively. With a 0.125 wt% loading of gum arabic in polypyrrole, these values were enhanced to 368.57 F/g, 73.667 Wh/kg, and 599.609 W/kg, at a current density of 1 A/g.

Author Contributions: Conceptualization, R.U., N.K. and M.K.; methodology, R.U., N.K. and M.K.; software, R.U., N.K., M.K. and M.S.K.; validation, R.U., N.K., M.K. and M.S.K.; formal analysis, R.U., N.K. and R.K.; investigation, R.U., N.K., R.K., M.K. and M.S.K.; resources, R.U., R.K., M.S.K. and O.M.A.; writing—original draft preparation, R.U. and N.K.; writing—review and editing, R.K. and O.M.A. All authors have read and agreed to the published version of the manuscript.

Data Availability Statement: Not applicable.

Conflicts of Interest: The authors declare no conflict of interest. The funders had no role in the design of the study; in the collection, analyses, or interpretation of data; in the writing of the manuscript, or in the decision to publish the results.

References

1. Zhang, X.; Gao, M.; Tong, L.; Cai, K. Polypyrrole/nylon membrane composite film for ultra-flexible all-solid supercapacitor. *J. Mater.* **2020**, *6*, 339–347. [CrossRef]
2. Liu, X.; Yang, J.; Li, X.; Li, Q.; Xia, Y. Fabrication of polypyrrole (PPy) nanotube electrode for supercapacitors with enhanced electrochemical performance. *J. Mater. Sci. Mater. Electron.* **2019**, *31*, 581–586. [CrossRef]
3. Du, X.; Wang, C.; Chen, M.; Jiao, Y.; Wang, J. Electrochemical performances of nanoparticle Fe_3O_4/activated carbon supercapacitor using KOH electrolyte solution. *J. Phys. Chem. C* **2009**, *113*, 2643–2646. [CrossRef]
4. Sarno, M.; Baldino, L.; Scudieri, C.; Cardea, S.; Reverchon, E. A one-step $SC-CO_2$ assisted technique to produce compact PVDF-HFP MoS_2 supercapacitor device. *J. Phys. Chem. Solids* **2020**, *136*, 109132. [CrossRef]
5. Wu, W.; Yang, L.; Chen, S.; Shao, Y.; Jing, L.; Zhao, G.; Wei, H. Core–shell nanospherical polypyrrole/graphene oxide composites for high performance supercapacitors. *RSC Adv.* **2015**, *5*, 91645–91653. [CrossRef]
6. Chen, G.Z. Understanding supercapacitors based on nano-hybrid materials with interfacial conjugation. *Prog. Nat. Sci. Mater. Int.* **2013**, *23*, 245–255. [CrossRef]
7. Liao, Q.; Jin, S.; Wang, C. Novel graphene-based composite as binder-free high-performance electrodes for energy storage systems. *J. Mater.* **2016**, *2*, 291–308. [CrossRef]
8. Simon, P.; Gogotsi, Y. Materials for electrochemical capacitors. In *Nanoscience and Technology: A Collection of Reviews from Nature Journals*; Nature Publishing Group: Berlin, Germany, 2010; pp. 320–329.
9. Lu, Q.; Chen, J.G.; Xiao, J.Q. Nanostructured Electrodes for High-Performance Pseudocapacitors. *Angew. Chem. Int. Ed.* **2013**, *52*, 1882–1889. [CrossRef]
10. Sowmiya, G.; Velraj, G. Designing a ternary composite of PPy-PT/TiO_2 using TiO_2, and multipart-conducting polymers for supercapacitor application. *J. Mater. Sci. Mater. Electron.* **2020**, *31*, 14287–14294. [CrossRef]
11. Winter, M.; Brodd, R.J. What Are Batteries, Fuel Cells, and Supercapacitors? *Chem. Rev.* **2004**, *104*, 4245–4270. [CrossRef]
12. Candelaria, S.L.; Shao, Y.; Zhou, W.; Li, X.; Xiao, J.; Zhang, J.-G.; Wang, Y.; Liu, J.; Li, J.; Cao, G. Nanostructured carbon for energy storage and conversion. *Nano Energy* **2012**, *1*, 195–220. [CrossRef]
13. Zhang, L.L.; Zhao, X.S. Carbon-based materials as supercapacitor electrodes. *Chem. Soc. Rev.* **2009**, *38*, 2520–2531. [CrossRef] [PubMed]
14. Conway, B.E.; Pell, W.G. Double-layer and pseudocapacitance types of electrochemical capacitors and their applications to the development of hybrid devices. *J. Solid State Electrochem.* **2003**, *7*, 637–644. [CrossRef]
15. Huang, J.; Sumpter, B.G.; Meunier, V. A Universal Model for Nanoporous Carbon Supercapacitors Applicable to Diverse Pore Regimes, Carbon Materials, and Electrolytes. *Chem.-A Eur. J.* **2008**, *14*, 6614–6626. [CrossRef] [PubMed]
16. Pal, R.; Goyal, S.L.; Gupta, V.; Rawal, I. MnO_2-Magnetic Core-Shell Structured Polyaniline Dependent Enhanced EMI Shielding Effectiveness: A Study of VRH Conduction. *ChemistrySelect* **2019**, *4*, 9194–9210. [CrossRef]
17. Cevik, E.; Gunday, S.T.; Bozkurt, A.; Amine, R.; Amine, K. Bio-inspired redox mediated electrolyte for high performance flexible supercapacitor applications over broad temperature domain. *J. Power Sources* **2020**, *474*, 228544. [CrossRef]
18. Eisazadeh, H. Studying the characteristics of polypyrrole and its composites. *World J. Chem.* **2007**, *2*, 67–74.
19. Jang, K.S.; Lee, H.; Moon, B. Synthesis and characterization of water soluble polypyrrole doped with functional dopants. *Synth. Met.* **2004**, *143*, 289–294. [CrossRef]
20. Roy, S.; Mishra, S.; Yogi, P.; Saxena, S.K.; Sagdeo, P.R.; Kumar, R. Synthesis of Conducting Polypyrrole-Titanium Oxide Nanocomposite: Study of Structural, Optical and Electrical Properties. *J. Inorg. Organomet. Polym. Mater.* **2017**, *27*, 257–263. [CrossRef]
21. Malinauskas, A.; Malinauskiene, J.; Ramanavicius, A. Conducting polymer-based nanostructurized materials: Electrochemical aspects. *Nanotechnology* **2005**, *16*, R51–R62. [CrossRef]
22. Aziz, S.B.; Hadi, J.M.; Dannoun, E.M.A.; Abdulwahid, R.T.; Saeed, S.R.; Marf, A.S.; Karim, W.O.; Kadir, M.F. The Study of Plasticized Amorphous Biopolymer Blend Electrolytes Based on Polyvinyl Alcohol (PVA): Chitosan with High Ion Conductivity for Energy Storage Electrical Double-Layer Capacitors (EDLC) Device Application. *Polymers* **2020**, *12*, 1938. [CrossRef]
23. Cevik, E.; Bozkurt, A.; Dirican, M.; Zhang, X. High performance flexible supercapacitors including redox active molybdate incorporated Poly (*vinylphosphonic acid*) hydrogels. *Int. J. Hydrogen Energy* **2020**, *45*, 2186–2194. [CrossRef]
24. Aziz, S.; Nofal, M.; Abdulwahid, R.; Ghareeb, H.O.; Dannoun, E.; Abdullah, R.M.; Hamsan, M.; Kadir, M. Plasticized Sodium-Ion Conducting PVA Based Polymer Electrolyte for Electrochemical Energy Storage—EEC Modeling, Transport Properties, and Charge-Discharge Characteristics. *Polymers* **2021**, *13*, 803. [CrossRef]
25. Sidhu, G.K.; Kumar, R. Study the Structural and Optical behaviour of Conducting Polymer based nanocomposites: ZrO2-Polypyrrole Nanocomposites. In *Proceedings of the IOP Conference Series: Materials Science and Engineering*; IOP Publishing: Lima, Peru, 2018; Volume 360, p. 012038.
26. Vasilyeva, S.V.; Vorotyntsev, M.A.; Bezverkhyy, I.; Lesniewska, E.; Heintz, O.; Chassagnon, R. Synthesis and Characterization of Palladium Nanoparticle/Polypyrrole Composites. *J. Phys. Chem. C* **2008**, *112*, 19878–19885. [CrossRef]

27. Habelhames, F.; Nessark, B.; Bouhafs, D.; Cheriet, A.; Derbal, H. Synthesis and characterisation of polypyrrole–indium phosphide composite film. *Ionics* **2010**, *16*, 177–184. [CrossRef]

28. John, J.; Saheeda, P.; Sabeera, K.; Jayalekshmi, S. Doped polypyrrole with good solubility and film forming properties suitable for device applications. *Mater. Today Proc.* **2018**, *5*, 21140–21146. [CrossRef]

29. Bilal, S.; Shah, A.A.; Shah, A.U.H.A.; Gul, H.; Ullah, W.; Gul, S. Dodecylbenzenesulphonic Acid Doped Polypyrrole/Graphene Oxide Composite with Enhanced Electrical Conductivity. *J. Sci. Innov. Res.* **2020**, *9*, 54–62.

30. Bilal, S.; Perveen, F.; Shah, A.A. Chemical synthesis of polypyrrole doped with dodecyl benzene sulfonic acid. *J. Sci. Innov. Res.* **2015**, *4*, 33–42.

31. Li, Y.; Yu, C. One-Step Electrosynthesis of Graphene Oxide-Doped Polypyrrole Nanocomposite as a Nanointerface for Electrochemical Impedance Detection of Cell Adhesion and Proliferation Using Two Approaches. *J. Nanomater.* **2016**, *2016*, 8932908. [CrossRef]

32. Ruhi, G.; Dhawan, H.C.K.; Sambyal, P.; Bhandari, H. Corrosion protection of mild steel by environment friendly Polypyrrole/Gum Acacia Composite Coatings. *Adv. Mater. Lett.* **2018**, *9*, 158–168. [CrossRef]

33. Khan, M.; Shah, L.A.; Khan, M.A.; Khattak, N.S.; Zhao, H. Synthesis of an un-modified gum arabic and acrylic acid based physically cross-linked hydrogels with high mechanical, self-sustainable and self-healable performance. *Mater. Sci. Eng. C* **2020**, *116*, 111278. [CrossRef] [PubMed]

34. Vasile, F.E.; Martinez, M.J.; Ruiz-Henestrosa, V.M.P.; Judis, M.A.; Mazzobre, M.F. Physicochemical, interfacial and emulsifying properties of a non-conventional exudate gum (Prosopis alba) in comparison with gum arabic. *Food Hydrocoll.* **2016**, *56*, 245–253. [CrossRef]

35. Advincula, A.O.; Maquiling, J.T. Morphology, Conductivity, and Mechanical Properties of Electropolymerized Polypyrrole/Silver-Coated Granular Microsphere Composite Films. *Braz. J. Phys.* **2021**, *51*, 698–721. [CrossRef]

36. Mohammed, A.M.E. Estimation of the active components in gum Arabic collected from western Sudan. *Int. J. Sci. Res.* **2015**, *80*, 9.

37. Darzi, H.H.; Larimi, S.G.; Darzi, G.N. Synthesis, characterization and physical properties of a novel xanthan gum/polypyrrole nanocomposite. *Synth. Met.* **2012**, *162*, 236–239. [CrossRef]

38. Bhadra, S.; Khastgir, D. Determination of crystal structure of polyaniline and substituted polyanilines through powder X-ray diffraction analysis. *Polym. Test.* **2008**, *27*, 851–857. [CrossRef]

39. Choudhary, R.B.; Nayak, D. Tailoring the properties of 2-DrGO-PPy-ZnS nanocomposite as emissive layer for OLEDs. *Optik* **2021**, *231*, 166336. [CrossRef]

40. Barik, P.; Bhattacharjee, A.; Roy, M. Characterization of dielectric properties of developed CdS-gum arabic composites in low frequency region. *Polym. Compos.* **2016**, *37*, 108–114. [CrossRef]

41. Ramesan, M.T.; Greeshma, K.P.; Parvathi, K.; Anilkumar, T. Structural, electrical, thermal, and gas sensing properties of new conductive blend nanocomposites based on polypyrrole/phenothiazine/silver-doped zinc oxide. *J. Vinyl Addit. Technol.* **2020**, *26*, 187–195. [CrossRef]

42. Sulaiman, M.G.; Ammar, A.F. Synthesis of Gum Arabic-g-polyaniline using diode laser. *Int. J. Biol. Macromol.* **2020**, *161*, 848–853. [CrossRef]

43. Arunachalam, S.; Kirubasankar, B.; Pan, D.; Liu, H.; Yan, C.; Guo, Z.; Angaiah, S. Research progress in rare earths and their composites based electrode materials for supercapacitors. *Green Energy Environ.* **2020**, *5*, 259–273. [CrossRef]

44. Wang, W.; Sadak, O.; Guan, J.; Gunasekaran, S. Facile synthesis of graphene paper/polypyrrole nanocomposite as electrode for flexible solid-state supercapacitor. *J. Energy Storage* **2020**, *30*, 101533. [CrossRef]

45. Kulandaivalu, S.; Azahari, M.N.M.; Azman, N.H.N.; Sulaiman, Y. Ultrahigh specific energy of layer by layer polypyrrole/graphene oxide/multi-walled carbon nanotube | polypyrrole/manganese oxide composite for supercapacitor. *J. Energy Storage* **2020**, *28*, 101219. [CrossRef]

46. Yağan, A. Investigation of Polypyrrole-Based Iron Electrodes as Supercapacitors. *Int. J. Electrochem. Sci.* **2019**, *14*, 3978–3985. [CrossRef]

47. Oliveira, R.D.; Santos, C.S.; Ferreira, R.T.; Marciniuk, G.; Marchesi, L.F.; Garcia, J.; Vidotti, M.; Pessoa, C.A. Interfacial characterization and supercapacitive properties of polyaniline—Gum arabic nanocomposite/graphene oxide LbL modified electrodes. *Appl. Surf. Sci.* **2017**, *425*, 16–23. [CrossRef]

48. Khati, K.; Joshi, I.; Zaidi, M.G.H. Electro-capacitive performance of haemoglobin/polypyrrole composites for high power density electrode. *J. Anal. Sci. Technol.* **2018**, *9*, 24. [CrossRef]

49. Bober, P.; Gavrilov, N.; Kovalcik, A.; Mičušík, M.; Unterweger, C.; Pašti, I.A.; Šeděnková, I.; Acharya, U.; Pfleger, J.; Filippov, S.K.; et al. Electrochemical properties of lignin/polypyrrole composites and their carbonized analogues. *Mater. Chem. Phys.* **2018**, *213*, 352–361. [CrossRef]

50. Nyström, G. Nanocellulose and Polypyrrole Composites for Electrical Energy Storage. Ph.D. Thesis, Acta Universitatis Upsaliensis, Uppsala, Sweden, 2012.

51. Xu, J.; Wang, D.; Yuan, Y.; Wei, W.; Gu, S.; Liu, R.; Wang, X.; Liu, L.; Xu, W. Polypyrrole-coated cotton fabrics for flexible supercapacitor electrodes prepared using CuO nanoparticles as template. *Cellulose* **2015**, *22*, 1355–1363. [CrossRef]

52. Wang, H.; Bian, L.; Zhou, P.; Tang, J.; Tang, W. Core–sheath structured bacterial cellulose/polypyrrole nanocomposites with excellent conductivity as supercapacitors. *J. Mater. Chem. A* **2013**, *1*, 578–584. [CrossRef]

53. Mo, H.; Zang, L.; Yang, C.; Wei, C.; Zhang, F.; Lu, S.; Wang, Z.; Huang, X. Polypyrrole/sisal fiber composites for energy storage. In *Proceedings of the 2015 International Conference on Power Electronics and Energy Engineering*; Atlantis Press: Amsterdam, The Netherlands, 2015.
54. Jyothibasu, J.P.; Chen, M.-Z.; Lee, R.-H. Polypyrrole/Carbon Nanotube Freestanding Electrode with Excellent Electrochemical Properties for High-Performance All-Solid-State Supercapacitors. *ACS Omega* **2020**, *5*, 6441–6451. [CrossRef]

Review

An Overview on the Novel Core-Shell Electrodes for Solid Oxide Fuel Cell (SOFC) Using Polymeric Methodology

Rong-Tsu Wang [1], Horng-Yi Chang [2],* and Jung-Chang Wang [2],*

[1] Department of Marketing and Logistics Management, Yu Da University of Science and Technology, Miaoli County 36143, Taiwan; rtwang@ydu.edu.tw
[2] Department of Marine Engineering (DME), National Taiwan Ocean University (NTOU), Keelung 202301, Taiwan
* Correspondence: hychang@mail.ntou.edu.tw (H.-Y.C.); jcwang@ntou.edu.tw (J.-C.W.);
Tel.: +886-2-24622192 (ext. 7109/7139) (J.-C.W.)

Abstract: Lowering the interface charge transfer, ohmic and diffusion impedances are the main considerations to achieve an intermediate temperature solid oxide fuel cell (ITSOFC). Those are determined by the electrode materials selection and manipulating the microstructures of electrodes. The composite electrodes are utilized by a variety of mixed and impregnation or infiltration methods to develop an efficient electrocatalytic anode and cathode. The progress of our proposed core-shell structure pre-formed during the preparation of electrode particles compared with functional layer and repeated impregnation by capillary action. The core-shell process possibly prevented the electrocatalysis decrease, hindering and even blocking the fuel gas path through the porous electrode structure due to the serious agglomeration of impregnated particles. A small amount of shell nanoparticles can form a continuous charge transport pathway and increase the electronic and ionic conductivity of the electrode. The triple-phase boundaries (TPBs) area and electrode electrocatalytic activity are then improved. The core-shell anode SLTN-LSBC and cathode BSF-LC configuration of the present report effectively improve the thermal stability by avoiding further sintering and thermomechanical stress due to the thermal expansion coefficient matching with the electrolyte. Only the half-cell consisting of 2.75 μm thickness thin electrolyte iLSBC with pseudo-core-shell anode LST could provide a peak power of 325 mW/cm^2 at 700 °C, which is comparable to other reference full cells' performance at 650 °C. Then, the core-shell electrodes preparation by simple chelating solution and cost-effective one process has a potential enhancement of full cell electrochemical performance. Additionally, it is expected to apply for double ions (H$^+$ and O^{2-}) conducting cells at low temperature.

Keywords: intermediate temperature solid oxide fuel cell; interface charge transfer impedance; diffusion impedance; core-shell structure; triple-phase boundaries; electrode electrocatalytic activity

1. Introduction

The fuel cell (FC) belongs to an electrochemical reactor that straightly converts the chemical potential of a fuel into electrical energy. Therefore, the FC capability is not restricted by the Carnot cycle count, which is the regulation for some mechanical facilities (e.g., steam turbine or internal cumbustion engine). The power conversion efficiency of a fuel cell is about 45% principally such as proton exchange membrane fuel cell (PEMFC). Taner's group [1,2] has studied hydrogen gas that entered the PEMFC anode through the catalyst anode to form the proton. The protons pass through electrolyte membrane to generate electricity due to the released electrons passing through external circuit to the cathode side underwent reduction interactions of the oxygen gas. This experimental study proves that the H$_2$ pressure drop and water management at cathode side are the important factors to affect the fuel cell performance. If combining the heat recovery system, a solid oxide fuel cell (SOFC) can reach the high power efficiency of 80% [3] with no water treatment issues because of higher 100 °C operation temperatures. Thus, fuel cells possess

characteristics of high performance of energy conversion, environment-friendly, multiple choices of fuels and high waste heat recovery rate. Figure 1 displays that the SOFC has the supreme efficiency of power conversion among various fuel cells and demonstrates the SOFC-combined cycle system achieving the highest power generation efficiency, which can be employed in a wide range of power outputs (large-scale power generation of kW~MW). It is indicated in Figure 1 marked with red circles. High power output lets SOFC suite to large power generation capacity systems, for example, various power plants and container ships. The SOFC is also a good candidate for large distributed energy systems [4,5].
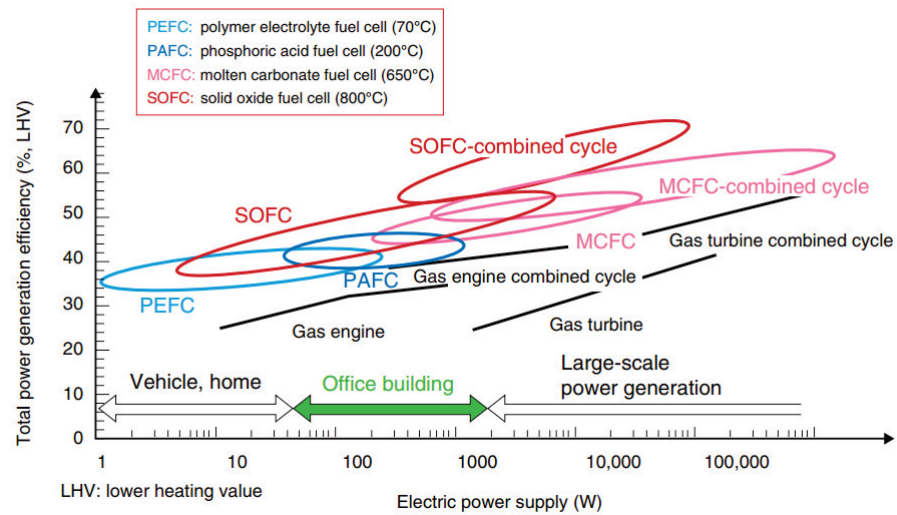
Figure 1. Total power generation efficiency of various fuel cells for the electric power output [4].

There are three consisting parts in a SOFC that are anode, electrolyte and cathode. A schematic diagram of a general planar design of SOFC is shown in Figure 2. The planar cells can be electrolyte-supported, electrode-supported and metal-supported types. Planar patterns provide a number of potential benefits, containing easier and cheaper fabricating procedures and higher power densities than tubular devices [6,7]. Thus, the planar SOFC is an excellent candidate for high power requirement such as power plant, cargo and container ships [8]. The operation of a planar fuel cell stack requires bipolar plates to connect the membrane electrode assembly (MEA) and external circuit or to combine another MEA. The bipolar plates allow fuel and oxidant flow through their channels [9]. The electrochemical capability and performance of planar SOFCs is extremely based on the materials of components, the microstructure of the electrodes and the geometric parameters of the cell [10].
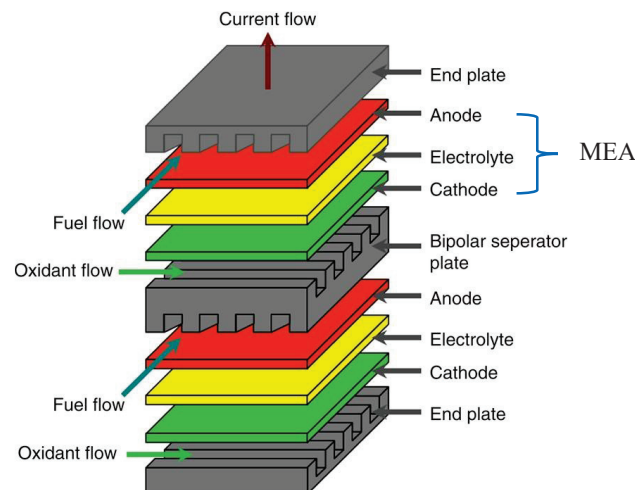
Figure 2. Planar solid oxide fuel cell stack with MEA indication [9].

The typical oxygen ion conducting SOFC is Ni/YSZ cermet for anode, 8 mol% Y_2O_3 stabilized ZrO_2 (YSZ) for electrolyte and perovskite $La_{1-x}Sr_xMnO_3$ (LSM) for cathode. Such a schematic diagram of SOFC is shown in Figure 3 [11]. The operation mechanism is that the cathode material receives the electrons from the external circuit to reduce oxygen molecules into oxygen ions ($O_2 + 4e^- \rightarrow 2O^{2-}$) at triple-phase boundaries (TPBs) of cathode/electrolyte; then the O^{2-} is conveyed into electrolyte, the electrolyte material transports the oxygen ions to the TPBs of anode/electrolyte to oxidize the fuel H_2 ($O^{2-} + H_2 \rightarrow H_2O + 2e^-$), which comes from the anode side, then the electrons are transported to the current collector and further to external circuit, which is indicated in left picture of Figure 3. The reaction products are pure water and heat. The electrolyte material also plays a role to prohibit the electrons from the anode through electrolyte into the cathode.

$$\frac{1}{2}O_2(g) + 2e^- \rightarrow O^{2-} \ (cathode)$$

$$O^{2-} + H_2(g) \rightarrow H_2O(g) + 2e^- \ (anode)$$
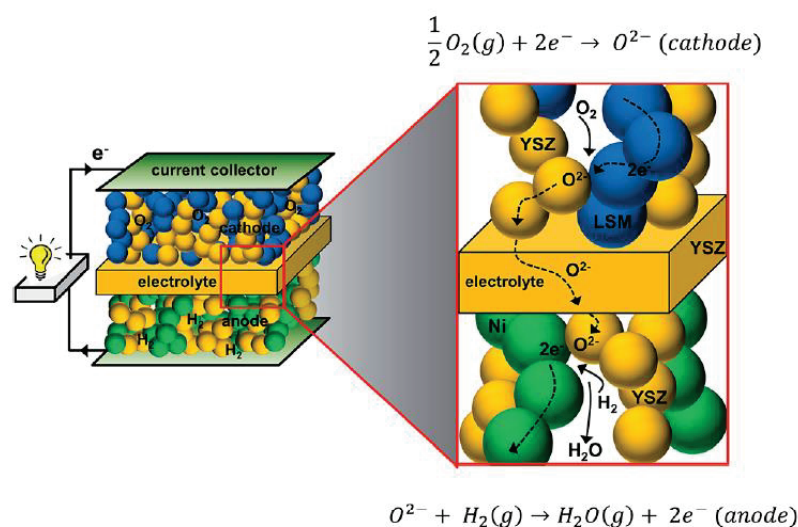
Figure 3. Schematic diagram for SOFC structure (left) and operation mechanism (right) [11].

Generally, the operation temperatures are in the range of 800–1000 °C for ZrO_2-based electrolyte [12], which is known as high temperature solid oxide fuel cell (HTSOFC). In the Ni-YSZ anode system, the reduced Ni metal network acts as electron conducting path and the YSZ can decrease the thermal expansion mismatch between Ni metal and YSZ ceramic electrolyte. The agglomeration and coarsening of Ni particles during SOFC operation at high temperature of 800–1000 °C is a major concern, since Ni particles sintering results in loss of active surface area and decreased conductivity of the anode. When using hydrocarbon fuels in a Ni-based anode of SOFCs, the major concerns are the anode catalyst coking and sulfur poisoning since H_2S exists in most of fossil fuels. The Ni-based anode catalyst can be easily deactivated by carbon deposits and suffers irreversible sulfur poisoning [13].

Decreasing the operating temperature to below 800 °C (under 600 °C is even better) permits the application of fuels involving methane and butane without pre-forming a hydrogen fuel. The advantages of a lower operating temperature incorporate the wide selections of materials, interface matching and long-term stability of the cell system and cost-effective operation and fabrication [14].

1.1. Polarizations of Fuel Cells

The energy conversion efficiency of a SOFC is mainly controlled by interface charge transfer, ohmic and diffusion impedances (or polarizations), a well-known electrochemical performance presented in Figure 4. General SOFC consists of two porous electrodes and an electrolyte assembled as the micrograph shown in the inset of Figure 4. Well-controlled gas diffusion, electron and ion conduction/diffusion are all considered key points in a SOFC operation to obtain a high peak power.
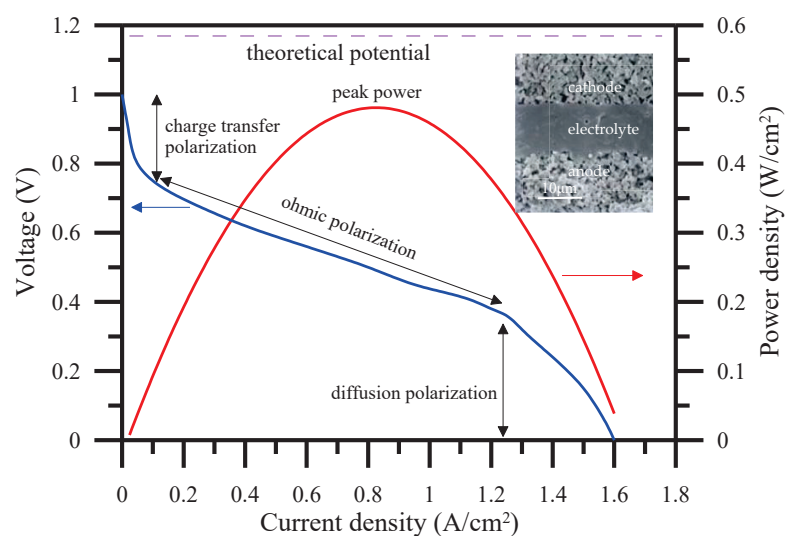
Figure 4. Typical electrochemical performance of a SOFC with I-V and I-P curves. The insect is a general microstructure of full cell (SOFC).

The electrochemical performance of SOFC is greatly determined by the species of H_2 and O_2 reaction processes in the porous electrode, such as oxygen adsorption, dissociation, surface diffusion to the TPB, ionization and incorporation into the electrolyte and bulk paths. Fewer TPBs exist at the electrode/electrolyte interfaces. The electrochemically active interface region is expected to extend a few micrometers from the electrolyte to the electrode and plays essential role in terms of the performance and durability of SOFCs [15,16].

Due to the significance of the electrode/electrolyte interface and electrocatalytic activity enhancement required, many studies pay efforts on the extension and enlargement of the TPB area [17,18]. The electrochemical reactions mainly proceed at the TPB sites of gas (H_2 or O_2), electrode and electrolyte. Theoretical calculations and experimental results have showed that a composite electrode should exhibit low charge transfer polarization by spreading the electrochemically active area within the volume of the electrode [17,19,20]. For example, the TPB length was measured by multiplying the average length of the cathode particle at the interface with the number of particles per unit area. The results suggested a three-dimensional distribution of TPB in LSM-YSZ composite cathode leads to a significant drop of cell overpotential [21,22]. Therefore, the manipulation of the electrode/electrolyte interface microstructures actually plays a crucial role in determining the overall cell performance and durability.

The interface charge transfer polarization results from TPBs between anode and electrolyte, and between cathode and electrolyte materials. The diffusion polarization originates from the internal structure including grains connection and porosity of an electrode. The ohmic polarization occurs from electrolyte material and external conducting connector structures. One significant bottleneck in the development of an intermediate temperature solid oxide fuel cell (ITSOFC), which is operated at 500~800 °C, is that the solid electrolyte exhibits low oxygen ionic conductivity at such a temperature, e.g., 600 °C. Apart from lowering the thickness of electrolytes, realizing the capability to acquire a high ionic conductivity composition of electrolytes is a major objective for the ITSOFC. It is obvious that the ionic conductivity can be enhanced via ceria doped with appropriate aliovalent cationic dopants. Co-doping has been certified to successfully increase the electrical characteristics of ceria-based electrolytes [23]. The $(La_{0.75}Sr_{0.2}Ba_{0.05})_{0.175}Ce_{0.825}O_{1.891}$ (LSBC) is a typical electrolyte for ITSOFCs utilized and developed in our research group [24]. When the ceria-based electrolyte material is ready selected for an ITSOFC, the lowering interface charge transfer and diffusion impedances are determined mainly by the electrode materials selection and manipulating the microstructures of electrodes. Thus, how to extend and enlarge TPBs area are significant topics.

Composite electrodes by mixing ionic and electronic conducting materials are used to improve electrodes' performance. Such composite electrodes including anode and cathode help to enhance the properties of mixed electronic–ionic conductors and the inter-component compatibility [7,25–31]. The composite electrodes are good ideas utilized by a variety of mixing and impregnation or infiltration methods to develop efficient anode and cathodes effectively. The mixed electrodes, e.g., Ni/YSZ anode and YSZ/LSM cathode in conventional SOFC extending TPBs, already reduce the interface charge transfer impedance and improve the electrochemical performance, as the schematic electrode microstructures shown in Figure 3.

1.2. Conventional TPBs Extension in Electrodes

In order to improve the stability and activity of the electrode/electrolyte interface, electrode modifications such as impregnation or infiltration can be regarded as an instrumental pathway. By infiltrating a layer of $PrBaMn_2O_{5+\delta}$ (PBM) into $BaZr_{0.1}Ce_{0.7}Y_{0.1}Yb_{0.1}O_{3-\delta}$ (BZCYYb) electrode, a fuel cell substantially enhanced stability and performance at reduced temperatures [32].

The typical electrode TPBs extension microstructure of $La_{0.75}Sr_{0.25}Cr_{0.5}Mn_{0.5}O_{3-\delta}$ (LSCrM)-impregnated anode has been manufactured via infiltrating 70% porous yttria-stabilized zirconia (YSZ) matrixes with an LSCrM solution. The LSCrM is a principal electron conductive phase while the well-sintered YSZ porous anode supplies an ionic conduction route in every part of the electrode. Further, Silver (Ag) and Nickel (Ni) are complemented by nitrate impregnating methods for improving electronic conductivity and electrocatalytic activity. The various impregnated microstructures are shown in Figure 5 [33].
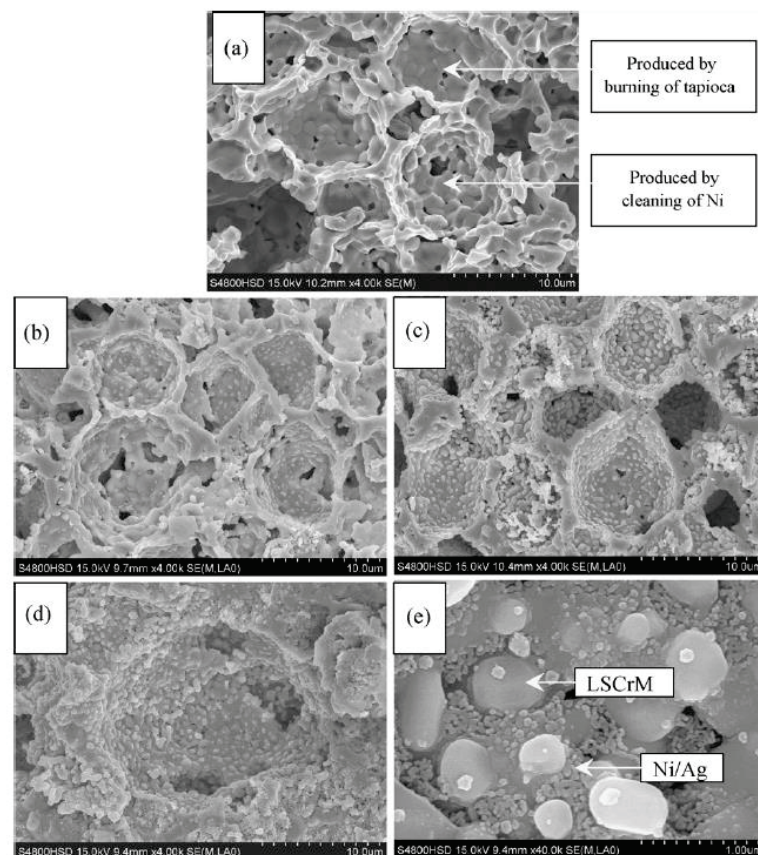
Figure 5. SEM micrographs of the cross-sections of: (**a**) pure YSZ anode backbone; (**b**) ~5 wt.% LSCrM-impregnated YSZ anode; (**c**) ~35 wt.% LSCrM-impregnated YSZ anode; (**d**,**e**) LSCrM/Ni/Ag (~32/6/2 wt.%) impregnated YSZ anode [33].

The interface polarization may be caused by a non-conducting phase at the interface resulting from the solid-state reaction between electrolyte and electrode. Control the interface reaction and extend the TPBs are both considering topics. A typical composite cathode is the adherence of meticulous SDC particles to the surface of crude BSCF cathode particles, which resulted from the mechanical admixture of $Ba_{0.5}Sr_{0.5}Co_{0.8}Fe_{0.2}O_{3-\delta}$ (BSCF) + $Sm_{0.2}Ce_{0.8}O_{1.9}$ (SDC) (70:30 in weight ratio). The phase reaction can contract merely at the interface between BSCF and SDC and insignificantly dominant in particles internal parts, thus, everywhere the whole BSCF cathode particles, individually, with the formation of a thin layer of novel (Ba, Sr, Sm, Ce) (Co, Fe)$O_{3-\delta}$ perovskite phase at a firing temperature as has been shown in Figure 6. The fine SDC particles enclose the BSCF coarse particle and maintain a single phase of SDC and BSCF, individually. The inter-phase intimately adheres BSCF and SDC to reduce the interface polarization. Thus, the sintered BSCF + SDC electrode shows an area specific surface resistance reduction above the BSCF because of the amplified cathode surface area promoted by the meticulous SDC particles. An improved peak power density at 600 °C was achieved for a thin film of the electrolytic cell with the BSCF + SDC cathode fired from 1000 °C [34].
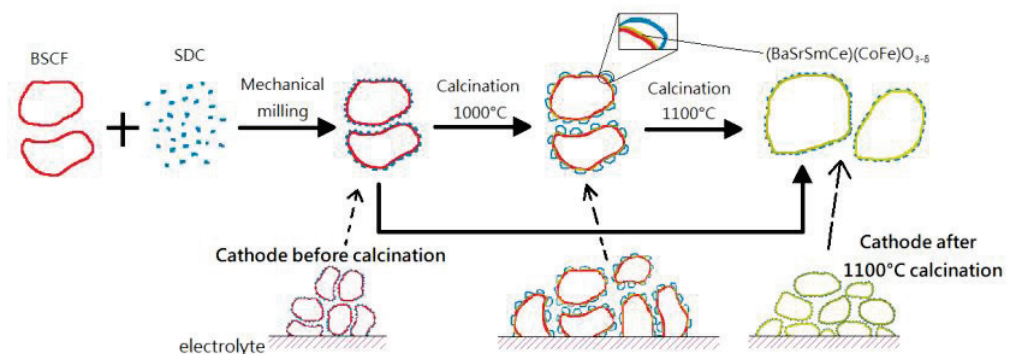
Figure 6. Schematic diagram for the sintering mechanism of BSCF + SDC composite cathode, redrawn from [34].

Other composite electrode examples are also presented as follows. The Ni-BZCY/SDC/BSCF cell with an interfacial reaction that can be manipulated to form a secondary phase at anode Ni-BZCY and SDC with an electronic conductor to benefit cell performance and power output [35]. The secondary phases nickel aluminate spinel ($NiAl_2O_4$) and zirconium titanite ($Zr_5Ti_7O_{24}$) formation by infiltrating a small amount of aluminum titanite (ALT, ~4 wt%) into the Ni-YSZ anode scaffold were found to suppress Ni coarsening and expand the electrode's TPBs [36,37].

Another TPBs extension method is an introduction of the anode functional layer (AFL) with fine microstructure at the anode/electrolyte interface to increase the TPB length and to restrain the activation polarization for hydrogen oxidation [38–40]. This kind of technique meets a trade-off between the enhancement of electrochemical performance due to the increasing TPB and the decrease in performance due to the increased gas diffusion resistance.

1.3. Proposed Core-Shell Electrodes

The SOFC synthesis needs high co-firing temperatures (often above 1000 °C) as to result in chemical reactions between the perovskite-based electrode, such as LSM, and the zirconia-based electrolyte; the formation of a secondary phase at the interface is usually insulating, and thus may impact the stability and performance of a SOFC [16,41–44].

In the conventional impregnated or infiltrated solution into the porous electrode scaffold, the nanoparticles are formed over the electrode scaffold surface at a relatively low temperature, necessarily (<800 °C), as the other way, it is not reactive when sintering under such temperatures. Therefore, the isolated nanoparticles constituted on the scaffold have comparatively disappointing electrical conductivity as a result of the lack of reactive

sintering of a normal infiltration–sintering process. In order to fill nanoparticles to cover the scaffold surface enough, the impregnation or infiltration process is required to repeat several times [45]. Such a repeated process often causes the block of porosity in the electrode and inhibits the thorough impregnation into the electrode/electrolyte interface. If the reactive temperature is so high as to enhance the reaction of impregnated nanoparticles and electrode grains, further coarsening or necking the impregnated nanoparticles or electrode grains significantly [33,46–48]. The particles agglomeration occurs to reduce the electrode porosity. Secondary phases are also generated due to the diffusion of impregnated nanoparticle composition into the electrode lattice seriously. The porosity reduction and too significant secondary phase existence will affect the TPBs function and contribute the polarization increase, also resulting in a coefficient of thermal expansion (CTE) of electrode mismatching with the electrolyte.

A core-shell structure is pre-formed during the preparation of electrode particles. A high enough amount of shell nanoparticles forming a continuous charge transport pathway increases electronic and ionic conductivity of the electrode. The electrode activity is then improved as contrasted with mechanical mixing composite electrodes and traditionally impregnated electrodes. Furthermore, the core-shell electrode configuration can successfully enhance the thermal stability by preventing more sintering and thermomechanical stress because of the CTE matching with the electrolyte. In recent decades, the core-shell electrodes of anode and cathode were developed by our research group to contribute the extending TPBs and solve the mismatching issue of the electrode and electrolyte. Significant improvement in electrocatalytic performance and in impedance have been achieved.

The core-shell is not a new terminology. It has been used for ceramics in several studies [49–51]. However, in our work, the core-shell electrodes pre-formed by chelating solution to extend TPBs were appreciated as a beneficial developing technology in future for SOFC [13]. The main objective of this work was therefore to demonstrate the progress of core-shell electrodes by our efforts to provide a feasible, convenient, cost-effective and time saving TPBs extension technique. The proposed core-shell electrodes, from fabrication by chemical chelating and solution coating processes to electrical and electrocatalytic characterization, are informed in the later parts. Furthermore, the recent developing pseudo-core-shell anode by thin electrolyte impregnation is introduced and compared with other ITSOFC research. The pseudo-core-shell or inverse impregnation is further expected to apply to double ions (H^+ and O^{2-}) conducting low temperature fuel cells.

2. Core-Shell Electrodes Preparation

2.1. Core-Shell Anode Preparation

Anode materials must suffice a number of demands involving enough ionic and electronic conductivities, thermal compatibility, outstanding electrocatalytic (electrochemical oxidation of hydrogen) activity and stable chemistry. An anode utilizes a ceramic composed of a mixing ionic and electronic conductors (MIEC) can enhance the ionic conductivity to the valid range of the TPBs and provides relative electronic conductivity. The perovskite ABO_3 structure is a good candidate of MIEC because it adapts to space and stoichiometric bias owing to doping different ions with distinct valences to either increase the conductive and catalytic activity of tolerant sulfur, or to expand steadiness with productive electrochemical function. The MIEC materials can solve the issues with the commonly used anode material, Ni/YSZ cermet, which exhibits wonderful electrocatalytic characteristics for the gathering of the beating current and fuel oxidation, but it reveals some weaknesses containing the liable sulfur toxin, carbon depositing, growing of Ni-particle and unstable volume in reduction–oxidation (redox) cycling under H_2/H_2O atmospheres [12,52]. The specifically beneficial characteristics of ABO_3 are delivering electrons that jump between mixing valent cations and capturing the conduction band as to raise the conductivity through the donors doped on A-site or the 4d or 5d transition ions doped on the B-site [53,54].

Our work proposed a structure of a core-shell anode that constituted of a core of conducting perovskite and a electrocatalytic shell of CeO_2-based electrolyte. The benefits

of core-shell structure include a simple anode material and structure preparation without the tedious mixing or impregnation of second functional particles to improve conductivity, electrocatalytic activity and thermal matching with the electrolyte. The overall heat treatment cycles may be decreased. The ABO_3 structure of $(Sr_{0.7}La_{0.3})(Ti_{0.9}Nb_{0.1})O_3$ (SLTN) anode reveals relative conductivity in reducing atmospheres. The multiple-elements doped ceria-based electrolyte $(La_{0.75}Sr_{0.2}Ba_{0.05})_{0.175}Ce_{0.825}O_{1.89}$ (LSBC) displays superior ionic and electrocatalytic attributes at intermediate temperatures [24,47,55]. The core-shell particles SLTN-LSBC as anode materials were constructed, and electrical characteristics of anodes were characterized [56].

The anode core was prepared by a ball-milled method using La_2O_3, $SrCO_3$, TiO_2 and Nb_2O_5 as the starting materials. The powders of ball-milled SLTN were calcined at 1100 °C-4 h in air. The raw materials of $La(NO_3)_3 \cdot 6H_2O$, $Sr(NO_3)_2$, $Ba(CH_3COO)_2$ and $Ce(NO_3)_3 \cdot 6H_2O$ were employed in the citric acid-based solution (SV) combustion skill to provide the coating shell. These La, Sr, Ba and Ce salts were dissolved in de-ionized water to constitute an aqueous solution. Before combustion, The SV was composed of a molar ratio of 1:2 for LSBC:citric acid for the mixed aqueous solution. The citric acid ($C_6H_8O_7$) contains three COO^- chelating ligands, which can chelate metallic ions to facilitate the homogeneous formation of shell composition during the combustion process. Hydroxyl groups of polysaccharides can be modified by chemical modification such as the thermal gelation method [57–59]. The expected homogeneous shell coating on our proposed electrode core particles is the same objective as the homogeneous distribution and the absence of agglomeration reported by the chitosan/pectin polymeric matrix to prevent the formation of nanoparticle clusters [60,61].

The calcined core powders of SLTN were put into the citric acid-based LSBC solution, which the molar ratio was SLTN:LSBC = $(100 - x):x$, where x was 0.75, 1.5, 3, 6 or 12. Subsequently, the chemical mixing solution was heated on a hot plate at 90 °C to evaporate the water matter, which transformed into a yellow gel, afterward, which was oven-dried at roughly 100 °C. Accordingly, the dried gel was crushed and calcined at 900 °C for 2 h in the air to fabricate the powders of the core-shell anode. The as-prepared core-shell anode powders were termed as SLTN-x mol% LSBC. A single anode disk was subsequently manufactured by a uniaxial press in a die from all prepared powders of SLTN-x mol% LSBC that was granulated with a binder. The alone anodes were consequently sintered at 1300 °C for 3 h in an activated carbon-reduction atmosphere.

2.2. Core-Shell Cathode Preparation

The mostly studied perovskite cathode materials contained $(La, Sr)MnO_3$ (LSM); $(La, Sr)(Co, Fe)O_3$ (LSCF); and $(Ba, Sr)(Co, Fe)O_3$ (BSCF) series. The LSM material had excellent co-fired matching with a YSZ or ceria-based electrolyte in HTSOFC. Nevertheless, the electron-conductivity of LSM decreased as it was manipulated at an ITSOFC due to lowering temperature. Perovskite LSCF and BSCF with MIEC characteristics have longer-term of TPBs than electron-conductive LSM [62,63]. The electrocatalytic activity of oxygen in LSM is poorer than that in LSCF and BSCF. However, the CTE for both LSCF and BSCF are about $20 \times 10^{-6} K^{-1}$, which are fairly greater than that of the ceria-based electrolyte ($\sim 12.5 \times 10^{-6} K^{-1}$). The present thermal mismatching trouble brings about the questions in the operating temperature of the fuel cell and in co-firing with the electrolyte. Furthermore, there are still having many disadvantages for Co-based cathodes containing the large evaporation owing to the reduction of Co, high cost and the transition of Co^{3+} (with octahedral coordination) from a low- to a high-spin states [64–66]. Ferrate-based materials without cobalt are well candidates for the cathode material since the iron is cheap and reveals nearly zero toxicity. The $Ba_{0.5}Sr_{0.5}FeO_{3-\delta}$ (BSF) has the supreme electrical conductivity among ferrates [67,68] but this perovskite oxide still displays a large CTE [69]. Accordingly, it is difficult to apply for co-firing with ceria-based and zirconia electrolytes directly.

The iron perovskites display prominent conductivities of oxygen ions resulting from the lower B–O bonding energies and the facile transitions of charge carriers between the various coordination polyhedral. They are easily collapsed by the moisture from the air, also unstable at high temperatures and low partial pressures of oxygen [70]. The Ce doping in BSF provides lattice stability, better cathode–electrolyte adhesion and enhanced cell performance by increasing the TPBs in SOFC [71,72].

The as-prepared BSF particles were coated by the Ce component by utilizing an ethanol-water mixed semi-organic solution (SOS). A similar solvent removal and decomposition method was utilized in the production of hydrocolloid film [73]. The Nb was used to modify the B-site of BSF, referred to as BSNF, to enhance it with structural and environmental stability. Subsequently, the La and Ce elements were coated onto the as-prepared BSNF particles also employing an ethanol–water mixed SOS. The stability of the BSF, BSNF structure and the obtained electrical properties were surveyed with respect to the influences of the Ce, La diffusion into the BSF and BSNF [72].

The calcined and pulverized BSF and BSNF powders were dispersed in absolute ethanol, individually. The aqueous solution of 20 mol% $La(NO_3)_3 \cdot 6H_2O$ and 80 mol% $Ce(NO_3)_3 \cdot 6H_2O$ was prepared in DI water, referred to as LC. The $La(NO_3)_3 \cdot 6H_2O$ aqueous solution or $Ce(NO_3)_3 \cdot 6H_2O$ aqueous solution or LC solution was added to the dispersed BSN and BSNF. Hereafter, the volume ratio of water to ethanol in every one reaction mixture was regulated to 1:9. Such SOS containing Ce, La and LC to coat the powders of BSF and BSNF were hence referred to as BS(N)F-y Ce (y = 2.5, 5 and 10 mol%), BSNF-y La and BSNF-y LC (y = 1.25, 3.75, 5, 10, 15, or 25 mol%), respectively, then each was stirred for 6 h and then dried at 80 °C with successive stirring. The powders were later ground and then calcined under 800 °C for 4 h.

The terpineol and ethyl cellulose were further mixed with these calcined powders including the BSF, BS(N)F-y Ce, BSNF-y La and BSNF-y LC. Another powder of the calcined LSBC was mixed with the binder named PB72. The ball-milling machine was employed to homogenize each binder-containing powder. After drying, these powders were granulated utilizing the mortar with a pestle and transited through a screen of 60 mesh. Each of the granulated powders was then pressed in a die employing a uniaxial press to form a disk. The pressed disks were next subjected to traditional sintering in an electric furnace (6 h at 1150 °C for BSF, BS(N)F-y Ce, BSNF-y La and BSNF-y LC electrodes; and 6 h at 1500 °C for LSBC electrolyte).

3. Results and Discussion of Core-Shell Electrodes

3.1. Core-Shell Anode of SLTN-LSBC

If a low ratio of LSBC (e.g., 1.5 mol%) displayed a shell, then the amounts of nanoparticles of LSBC were not clear enough to recognize. Figure 7a shows that the larger particles of the calcined SLTN core were adhered by enough distinguished LSBC nanoparticles (12 mol% LSBC) [56]. The elemental analysis on the core-shell SLTN-12 mol% LSBC powders is easily identified as the inserted EDS spectrum shown in Figure 7a. The primary components of Ti, Ce and Sr were mapped on the morphology of Figure 7a obtained from the EDS elemental analysis. Figure 7c demonstrated the Ce element existed on the nanoparticles of the shell, which further certified the core-shell formation. The Titanium (Ti) and Strontium (Sr) assigned over core-shell major body as shown in Figure 7b,d. The Ti and Sr mapping images demonstrated the core SLTN existed below the LSBC nanoparticles shell.
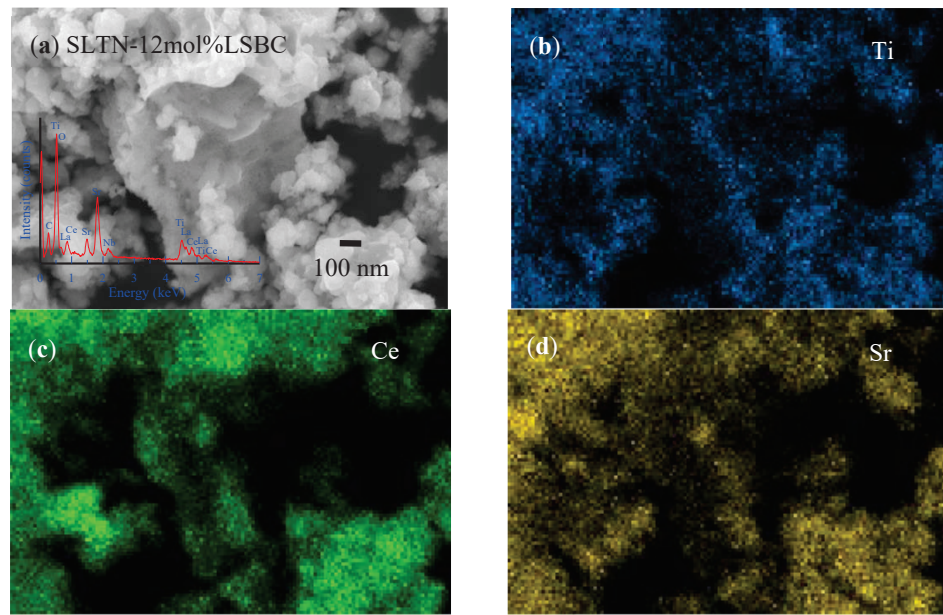
Figure 7. The FESEM images and EDS elemental analyses of the prepared core-shell anode powders, (**a**) FESEM image of SLTN-12 mol% LSBC, the inserted spectrum is its EDS analysis and the EDS elemental mappings on the SLTN-12 mol% LSBC, (**b**) Ti, (**c**) Ce and (**d**) Sr [56].

The conductivity contribution of La and Nb donors-doped perovskite structure was enhanced if the SLTN sintered in the reduction atmosphere. Figure 8 exhibits that the DC conductivity decreased with the increase in the molar ratio of shell LSBC, which demonstrated that the the resistance of shell LSBC affected the electrons hopping as the ratio of shell LSBC increased. The more shell nanoparticles coated on the core, the more favorable its role for ionic conductivity was. A ceria-based shell may increase the electrocatalytic activity but it would lower the electronic conductivity. The lesser shell coating such as 1.5 or 3.0 mol% LSBC shown in Figure 8 maintains appropriate high electronic conductivity and electrocatalytic activity simultaneously. This situation is the electron transfer at the TPB of the electronic core and ionic shell [24,47,55]. Ce^{3+} was possibly formed at the anode in a reduction atmosphere at the higher temperature, 700 °C, in Figure 8 and enhanced the electronic conductivity [74].
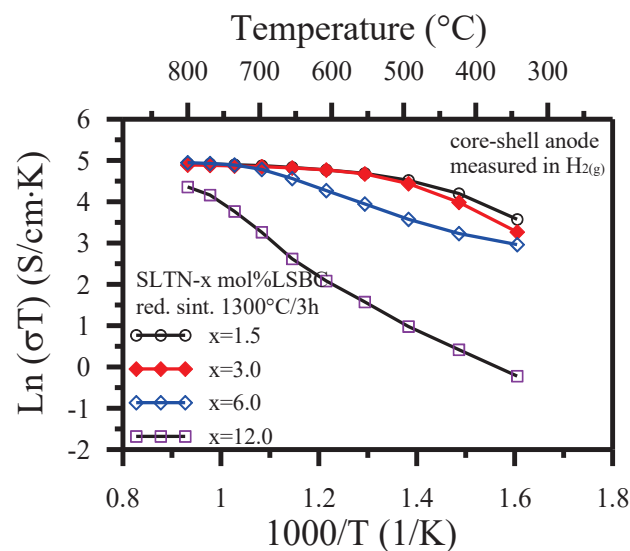
Figure 8. The conductivities of SLTN-x mole% LSBC core-shell anodes after 1300 °C/3 h sintering in activated carbon-reducing atmosphere as a function of measuring temperatures in H_2 atmosphere.

Such few shell coatings less than 3 mol% also altered the peak semiconducting activity to a lower critical temperature (T_c) of 500 °C. Figure 8 exhibits that the conductivity of metallic behavior of the core-shell anode as the measuring temperature is larger than the T_c. The present achievement further proved that the shell of ion may shift the redox reaction to a lower operating temperature than the one without coating ionic shell. Figure 8 reveals that a high covering ratio of shell on core (e.g., 6.0 or 12.0 mol% LSBC) displays a degraded electrical conductivity on the core-shell anode. The lattice oxygen led to the coexistent generation of oxygen vacancies and Ti^{3+} ions at a high temperature and low oxygen partial pressure. More oxygen vacancies produced from a high covering ratio of the ionic shell such as 12 mol% did not distinctly contribute to the overall DC conductivities of the SLTN core [54] as to lower the total conductivities of the core shell anode and owing to the low mobility of oxygen vacancies contrasted with electrons at a temperature of higher than 700 °C.

In addition, measuring the AC impedance of the core-shell anode may provide testimony of the ionic shell of LSBC to enhance the electrocatalytic activity and electron transfer rate. Figure 9 exhibits the AC complex impedance analyses. Those indicate that the LSBC shell (x = 0 to 3.0) profited the impedance decrease of the core-shell anode. However, the larger covering ratio (x = 6.0) of the LSBC shell increased the impedance of the core-shell anode. This result responds to the decrease in DC conductivities for the larger amount of shell coatings. AC impedance data acquired in Figure 9 may be roughly adapted as two depressed impedance semicircles for each anode sample according to RQ equivalent circuits containing parallel resistance/CPE circuits in series [24,56,75–81]. The SOFC is full solid state device, in order to corresponding to the illustrations in Figure 4, the detail electric double layers are not considered and discussed in the work. The depressed arc at a high-frequency range is concerned with the interface charge transfer process, while the arc at a low-frequency range is related to surface diffusion processes and hydrogen dissociation. The three intersections on the ReZ axis from left to right for each x mol% LSBC shell coating express the ohmic resistance (R_e), interface resistance of charge transfer (R_i), and electrocatalytic resistance having no electron transfer (R_c), respectively. The valid resistance dedication is indicated as ReZ(d) = R_c − Ri for diffusion polarization and the interface charge transfer polarization of ReZ(i) = R_i − R_e. In addition to the higher than 6.0 mol% LSBC shell coating, the LSBC shell coating decreased ReZ(d) effectively and increased the ReZ(i) slightly. The present work illustrates the core-shell structure with low LSBC coating increased the electrocatalytic activity of anode due to the extension of TPBs.
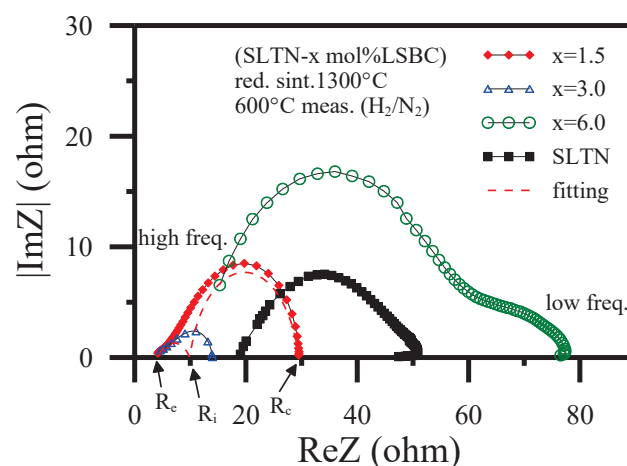
Figure 9. The AC impedance spectra for SLTN-x mol% LSBC core-shell anodes after 1300 °C/3 h sintering in activated carbon-reduction atmosphere then measured at 600 °C in H_2/N_2 atmosphere [56].

3.2. Core-Shell Cathode of BSNF-LC

Although Abd Aziz et al. [7] have reviewed composite cathode materials on the addition of SDC or GDC electrolyte material to traditional cathode materials recently with

relative progress to operate SOFC at intermediate to low temperatures, our core-shell technique is still relevant and exciting to study.

In our study [72], the BSNF coated by LC moderately decreased the core size and enhanced the porosity as shown in Figure 10a–d. Figure 10b exhibits the evident shell particles on the BSNF core resulting from La coating after sintering. Compare Figure 10b with Figure 10c,d, it also shows that the existence of Ce inside the LC coating layer promoted the diffusion of La into BSNF, according to 10LC, overcoming the limited solubility of La. The comparison in Figure 10c,d reveals a tiny morphological change for adding the LC coating between 5 and 10 mol%. The diffusion of La into BSNF constructed an LC layer as to increase the TPBs. Figure 10e, the EBSD micrograph of BSNF-5 LC, obviously illustrates that the LC diffused into the BSNF structure and an LC layer (red dots) developed near the core boundaries of BSNF. Moreover, precipitation was observed as high amounts of LC coating were applied, as shown in Figure 10d. No second phase was discovered in BSNF-3.75 LC or BSF-5 Ce under XRD resolution. It indicated that the Ce could enhance the La solubility into BSNF but a small amount of 3.75 mol% LC cannot change the structure of BSNF or a second phase to be detected. The Ce coating layer decreased the core size and enhanced the porosity of BSF, whereas based on the relative densities and microstructures, the LC coating layer imposed tiny influences on porosity or core size for BSNF.
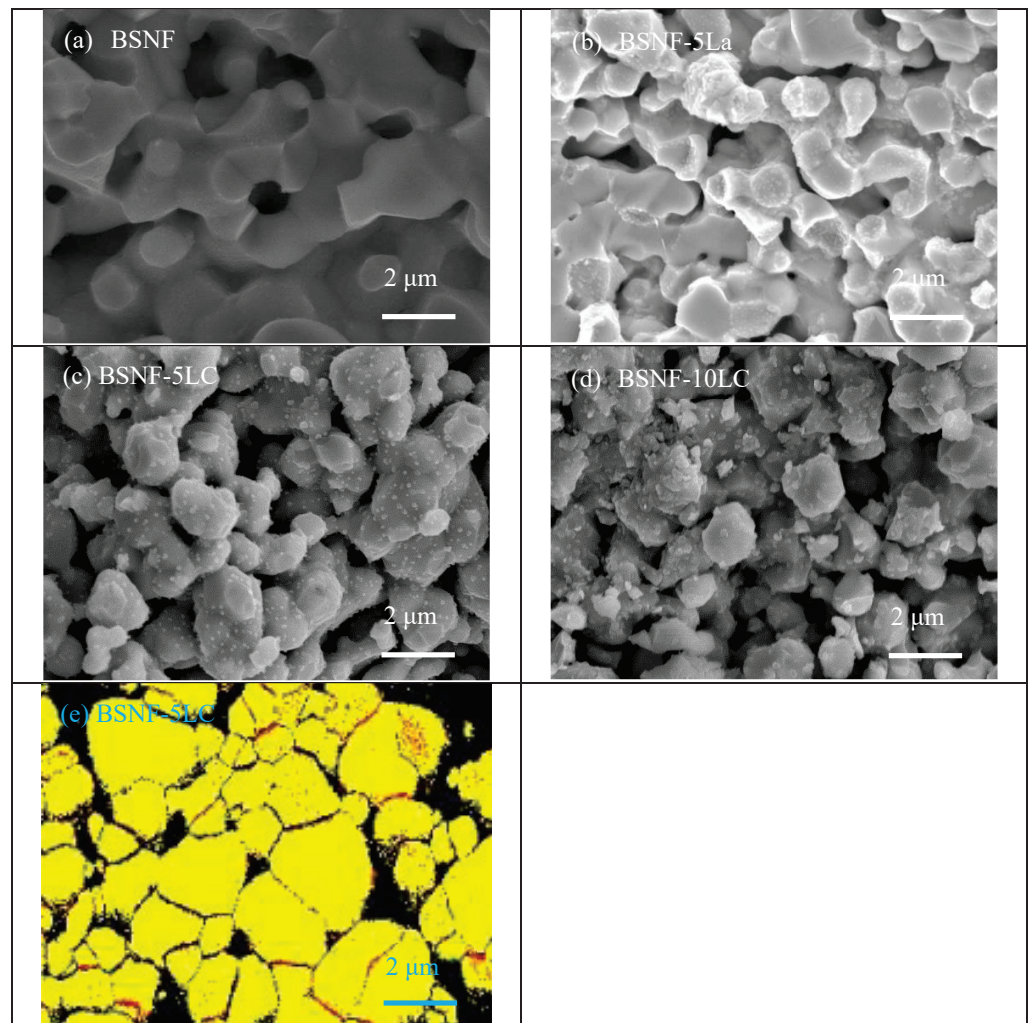
Figure 10. FESEM micrographs of (**a**) BSNF, (**b**) BSNF-5 La, (**c**) BSNF-5 LC and (**d**) BSNF-10 LC sintered at 1150 °C-6 h. EBSD image of (**e**) BSNF-5 LC. Red dots represent LC-species and yellow regions are BSNF grains [72].

Izuki et al. [82] utilized a diffusion couple prepared by depositing LSCF thick film onto the GDC substrate using Pulse Laser Deposition (PLD) technique to study the LSCF/GDC interface reaction. The diffusion couple was then treated at 1000–1200 °C up to 672 h, and a significant diffusion of La into GDC as well as the diffusion of Ce into LSCF were detected. The 3.75 mol% LC shell coated on BSNF under heat-treating at 1150 °C/6 h with little diffusion was then considered reasonably.

Figure 11 demonstrates the conductivities of the BSF (black solid line) with similar values to those of the BSNF (black dashed line). Their peak conductivities were the same, at about 510 °C. Fe cations in ferrate perovskite are in mixed Fe^{3+}/Fe^{4+} valence states [83,84], and the decrease in the electrical conductivity at high temperatures exhibited by ferrate perovskites (such as BSF) is attributable to the release of lattice O and the Fe ions' spin transitions [85]. The DC conductivity of BSF and BSNF reveals that Nb doping did not improve the conductivity of BSF, although it stabilized the perovskite structure. Figure 11 shows that the Ce coating 5 and 10 mol% increased the BSF's conductivity but also increased its transition temperature to above 510 °C. The presence of Ce in the BSF lattice may reduce the Fe ions' spin transitions by compensating for Fe's high valence state. Ce may also suppress the loss of lattice O and modify the electronic conduction [86]. The transition temperature ($T_c \sim 510$ °C) from semiconductor-like to metal-like conductivity for BSNF-3.75 LC (open circle red line) was lower than those of samples exceeding 5 mol% LC-coating. The lower LC-coating concentration on BSNF could enhance its conductivity and reduce the operating temperature. In contrast, using a high LC concentration (e.g., 10 mol%) provided excessive ionic conduction but did not effectively reduce the transition temperature or improve the conductivity.
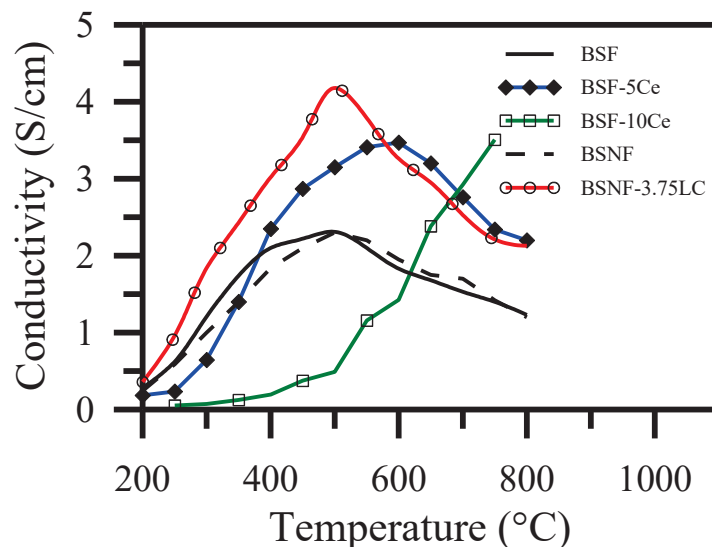
Figure 11. DC conductivity as function of temperature measured in air for BSF, BSF-y Ce (y = 5, 10), BSNF and BSF-3.75 LC [72].

The mixed doping at both the A- and B-sites, such as Ba, Sr for A-site and Nb, Fe for B-site, is important for maintaining the oxides' disordered oxygen vacancy structures [67,87]. The excessive Ce coating on BSF-10 Ce generated a second phase, in which the high porosity and small grain size reduced the Ce-doping effect by increasing the oxygen-vacancy clustering. These effects may delay the metal-like transition and elevate the transition temperature of peak conductivity, as shown in Figure 11. The diffusion of Ce into the BSF lattice induced stress. Extending TPB is believed to enhance the small polaron hopping mechanism and improve the conductivity.

Similar to the core-shell anode impedance analyses in Section 3.2, the AC impedance data of BSNF/LSBC/Pt, (BSNF-5La)/LSBC/Pt and (BSNF-3.75LC)/LSBC/Pt half-cells (Figure 12) also can be approximately fitted to two depressed impedance semicircles ac-

cording to the RQ equivalent circuits [24,72,75–81]. The depressed arc in the intermediate frequency range is still related to the interface charge-transfer process, diferently at low frequencies instead of H_2, the arc is associated with O_2 dissociation and surface diffusion processes on the core-shell cathode grains. Therefore, the effective resistance is ReZ(i) = R_i − R_e for the interface charge transfer and ReZ(d) = R_c − R_i for chemical catalysis reaction. The chemical catalysis enhancement is largely attributable to the decrease of ReZ(d) in the half-cells containing BSNF-x LC core-shell cathode. These half-cells also exhibit significantly decreased interface resistance ReZ(i) and ohmic resistance R_e.
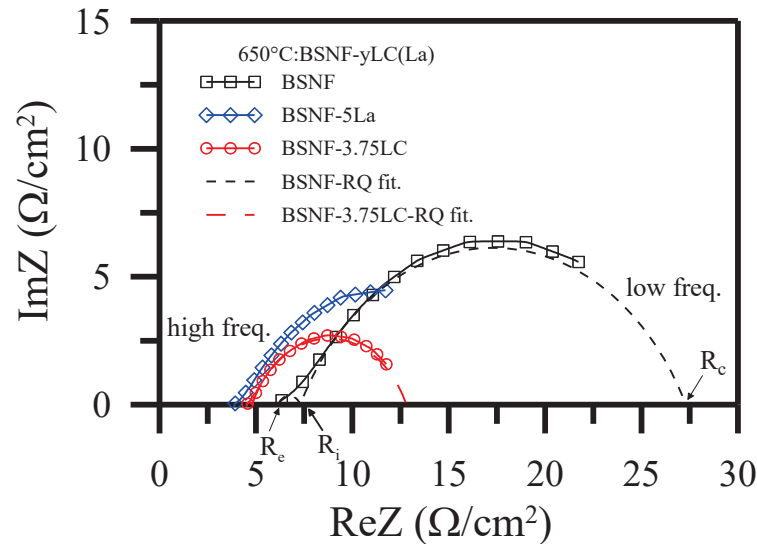
Figure 12. AC impedances of half-cells and RQ fittings for BSNF/LSBC/Pt and (BSNF-3.75 LC)/LSBC/Pt compared with (BSNF-5 La)/LSBC/Pt at 650 °C measurement [72].

The composite cathodes used for IT-SOFCs have been proven as an excellent technique to achieve low polarization and high power. The SDC or GDC electrolyte mixed into LSCF as composite cathodes are well studied [45,88–90]. The benefits are attributed to the enlargement of the TPBs and the excellent adhesion between the electrode and electrolyte by adding electrolyte species to the cathode material. However, the cobalt content is expensive and evaporates during processing and operation. Those are all significant issues when using cobalt-based cathodes. Additionally, the mixing or infiltration amount of electrolyte cannot be controlled precisely in every repeated infiltration process from porous cathode outside surface into cathode inner space sufficiently or in random mixing process that affects the quality of the composite cathode. Generally, a large amount of 50 wt% electrolyte addition [45] was also necessary to obtain the best cathode properties.

The cell reliability depends on the structural stability and optimal CTE matching among the various interfaces. The BSF cathode-LSBC electrolyte interface was observed to exhibit peeling after two cyclic tests. The CTE values of the LSBC electrolyte substrate and various electrode materials, including uncoated BSF and BSNF and shell coated BSF-5 Ce and BSNF-3.75 LC, were measured by a thermal mechanical analyzer (TMA). The linear expansion deviated from referred LSBC (black line in Figure 13) above 450 °C. The linear expansion of BSNF is almost the same as LSBC below temperature 450 °C. Higher than 450 °C, the linear expansion of BSF, BSF-5Ce and BSNF are far larger than LSBC. The BSNF-3.75 LC indicates the smallest deviation from the CTE of electrolyte LSBC.

The CTEs of BSNF-3.75 LC and LSBC below 650 °C with similar relatively could facilitate good interface matching between the cathode and electrolyte while co-firing and operation. The BSNF-3.75 LC half-cell exhibited high power density compared with the uncoated BSNF cathode at 650 °C. This suggests that the LC coating enhanced the power density of the BSNF/LSBC half-cell more significantly than the Ce coating did for the BSF/LSBC half-cell. The core-shell particle-coating by SOS presented in our report could

provide a novel approach for achieving high SOFC performance at a low coating amount and intermediate operation temperature.
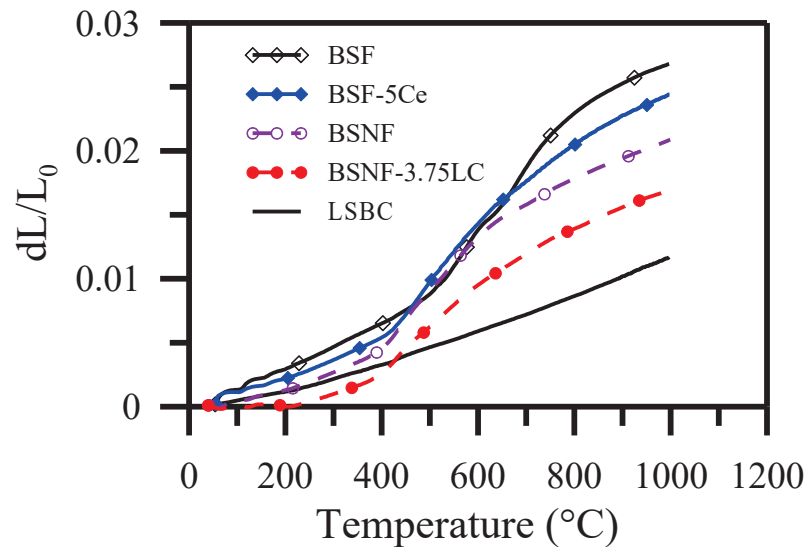
Figure 13. Comparisons of thermal expansion curves vs. temperatures for 1150 °C-6 h sintered BSF, BSF-5Ce, BSNF and BSNF-3.75LC; and 1500 °C-6 h sintered LSBC materials [72].

3.3. Psudo-Core-Shell Anode by Ultrasonic Spray Pyrolyzed Impregnation

An $La_{0.3}Sr_{0.7}TiO_3$ (LST) without Nb addition was prepared like SLTN in Section 2.1 and sintered at 1300 °C/6 h to form an approximately 500 μm thick porous substrate. The LSBC electrolyte with polyethylene glycol (PEG) as a chelating agent was prepared in an aqueous solution with a concentration of 0.01–0.1 M. via an ultrasonic nozzle that atomized nano-sized droplets of the LSBC solution by carrier gas into a hot zone. The precursor droplets were decomposed and deposited on a porous LST anode substrate at a temperature of 250–500 °C in the hot zone. An LSBC thin layer electrolyte was successfully deposited on and impregnated into porous LST anode support to form LST/iLSBC half-cells after co-firing at 1350 °C/6 h. This LSBC impregnation and droplets decomposition in porous LST created core-shell like structure, also termed as pseudo-core-shell or reverse impregnation structure. Continuous ultrasonic spray pyrolysis densified a 2.75 μm thin layer LSBC using 0.1 M precursor concentration, 450 °C substrate temperature, 2 mL/min solution flow rate and 25 mL spray volume [91].

Instead of anode function layer (AFL) [92], our ultrasonic spray pyrolyzed pseudo-core-shell anode substrate improved contact and adhesion between the anode and the electrolyte. The dense electrolyte with a thickness of 2.75 μm, as shown in Figure 14a. The profile of the densified 2.75 μm-thick layer of LSBC (iLSBC) on the porous LST substrate is indicated by the EDS line-scanning analysis also shown in the Figure 14a. The top dense layer showed a clear Ce signal (red color) while a trace Ce signal was detected in the LST substrate region over 30 μm depth. The Ce impregnation into the porous LST anode effectively extended the TPBs from the interface between LSBC and LST into the porous LST inner structure. The LSBC impregnation into porous LST is also further identified by electron backscatter diffraction (EBSD) analyses [91].

Refer to LSTN-LSBC and BSNF-LSBC contained half-shell analyses, LST/iLSBC half-cell has approximately fitting to one ohmic resistance and two depressed impedances according to the RQ equivalent circuits, as shown in Figure 14c. This is equivalent to two parallel resistance (R)/constant phase element (CPE) circuits in series with an ohmic resistance of R_e [75–81,91]. The AC impedances of LST/iLSBC half-cell decreases with the measured temperatures increase and diffusion polarization at low frequency decreases significantly as shown in Figure 14b,c. The ohmic resistance (R_e) and diffusion impedance ReZ(d) significantly decreases and the decrease in ReZ(d) results in an increase in the equiv-

alent capacitance. The impedances ReZ(i) and ReZ(d) of the fuel cell decrease indicated the extension of TPB sites due to electrolyte LSBC impregnation into the porous anode to become a pseudo-core-shell inner coverage. This results in more effective charge transfer and electrocatalytic activity due to longer TPB length and larger area.
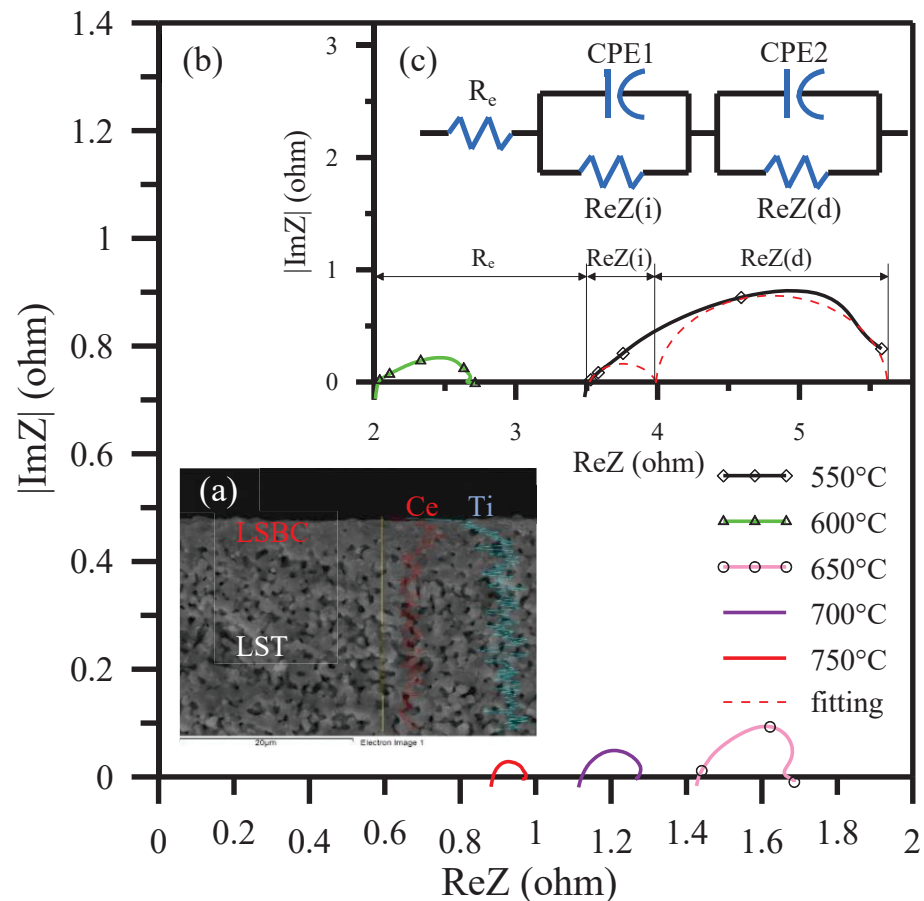
Figure 14. Co-fired iLSBC/LST half-cell prepared by ultrasonic spray pyrolysis and measured at a temperature of 550–750 °C for (**a**) FESEM cross-section of iLSBC/LST with line scanning marking Ce (red color) and Ti (light blue color) elements, AC impedances among (**b**) 650–750 °C and (**c**) 550–600 °C and RQ fitting for 550 °C.

The porous microstructure of SOFC electrodes correlates with the TPBs, gas diffusion and concentration polarization. Adding an interlayer such as an AFL between the electrolyte and anode, and impregnating electrocatalytic particles into the porous anode effectively increased the TPBs and decreased the contact resistance between the electrolyte and the electrode [93–96]. However, the AFL and solution impregnation require additional processing and cost. Repeated impregnation by capillary action may decrease the efficiency of the reforming and electrocatalysis, possibly by hindering and even blocking the fuel gas path through the porous anode structure due to the serious agglomeration of impregnated particles [97]. The ultrasonic spray pyrolyzed thin layer electrolyte could impregnate into the porous anode during deposition to create intimate contact between the anode and electrolyte and act as a dense electrolyte on a highly porous anode support. The sound effects extended TPBs and adhesion of the thin layer electrolyte, enhancing the charge transfer and decreasing the gas diffusion resistances, as the evidence shows in Figure 14.

Our ultrasonic spray pyrolysis pseudo-core-shell deposition technique, using chelating solution precursor, does not require an additional loading press and low pressure or vacuum system. It is operated in an ambient atmosphere with easy adjustment of processing parameters, reduction of synthesis temperature and process cost, as well as

convenient operation. The Table 1 is our fabricated half-cell by ultrasonic spray pyrolysis in comparison with other reference anode supported full cells. In Table 1 [98–105], catalytic metals such as Ni or Ru are required in porous anodes for electrocatalytic activity and electronic conductivity enhancement for cells. The LSBC impregnated into LST from the LSBC electrolyte side and sequent formed dense LSBC thin layer electrolyte satisfying the electrocatalytic activity and conductivity requirements simultaneously. Our ultrasonic spray pyrolysis technique has a lower electrolyte preparation and phase formation temperature of 450 °C. The half-cell consisted of 2.75 μm thickness thin electrolyte with pseudo-core-shell anode could provide a peak power of 325 mW/cm^2 at 700 °C, which is comparable to other reference full cells' performance at 650 °C. The ultrasonic spray pyrolysis for pseudo-core-shell anode also extended TPBs, enhanced the electrolyte adhesion on porous anode, and deposited dense thin layer electrolyte, all in one process for a half-cell.

Table 1. Functional comparisons of anode-supported SOFCs with thin layer of ceria-based electrolyte operated in H$_2$ (or humidified H$_2$) as fuel and air as oxidant atmosphere (cited from the literatures and this work).

Cell Configuration	Electrolyte Prepared Method	Electrolyte Thickness (μm)	Electrolyte Prepared Temperature (°C)	Temperature of Co-Fired with Anode (°C)	Peak Power Density (mW/cm^2)				Ref.
					600 °C	650 °C	700 °C	750 °C	
S.S/Ni + SDC/SCSZ/LSM + SDC/S.S. *	infiltration	7	Tape casting	1350			900		[98]
Ni + GDC/GDC/SSC + GDC	dry pressing	20	600	1350	400				[99]
Ni + SDC/SDC/SSC + SDC	screen printing	30		1350	397				[100]
Ni + GDC/GDC/LSCF + GDC	dip coating	10	commercial	1450	300				[101]
Ni + GDC/GDC/LSCF	spin coating + co-pressing	4	commercial	1300	771				[102]
Ni + GDC/GDC/LSCF	spin coating	19	700	1350	386	492			[103]
Ni + GDC/GDC/LSCF + GDC	spray coating	10	commercial	1450	578				[90]
Ni + Ru + GDC/GDC/SSC	spin coating	40	commercial	1500	250				[104]
Ni + YSZ/GDC/SSC + SDC	repeated spray pyrolysis	2.08	precursor	600	280	350			[105]
LST/LSBC/Pt (half-cell)	ultrasonic spray pyrolysis	2.75	450	1350	142	240	325	377	our work

* S.S.: porous stainless steel; SCSZ: 10ScSZ + 1 mol% CeO$_2$ electrolyte.

In Table 1, Dogdibegovic et al. [98] used higher conductivity SCSZ electrolyte and backbones instead of YSZ, and conventional LSM cathode and SDC-Ni anode were replaced with Pr$_6$O$_{11}$ cathode and higher Ni content in anode. The power density of 1.56 Wcm^{-2} was achieved at 700 °C. Such a result is the highest power density up to date using an H$_2$-air system and almost approaches to the theoretical OCV value. However, the control of optimizing synthesis parameters is critical and must be careful concerning issues. For the comparison of similar electrolyte thickness (2.08 μm) using repeated spray pyrolysis process on Ni + YSZ anode [105] at 600 °C in Table 1, our future work will likely include spray pyrolysis equipment improvement, anode particle modification and full cell preparation for this anode supported half-cell to further enhance the electrochemical performance. In this overview, we demonstrate only half-cell with (pseudo-) core-shell electrode to achieve relative power density due to extending TPB$_S$ with simple, convenient, unexpansive and

environmentally friendly technique. The full cells are under-working to promote the power density and study the core-shell interface electrocatalytic mechanisms. Our studies are further expected to apply to double ions (H^+ and O^{2-}) conducting low temperature fuel cells in the future.

4. Conclusions and Future Respective

The progress of core-shell electrodes in our efforts is demonstrated with an overview. The core-shell electrode particles and pseudo-core-shell structure are prepared by LSBC electrolyte chemical chelating solution coating and reverse impregnation processes in the anode and cathode. The pre-formed core-shell structure in electrodes, including anode and cathode, provide a feasible, convenient, cost-effective and time saving TPBs extension technique.

The prepared anode SLTN and cathode BS(N)F coarse particles were coated with LSBC electrolyte chelating solution to form core-shell structure. For SLTN-LSBC core-shell anode, the sufficient DC conductivity at intermediate temperature only needed a small amount of 1.5 or 3.0 mol% LSBC shell coating on SLTN. Too molar ratio of LSBC shell was not necessary. Similarly, the half-cell of (SLTN-x LSBC) with x < 3.0 mol% exhibited the decrease in interface charge transfer polarization (ReZ(i)) and chemical electrocatalysis polarization (ReZ(d)) effectively.

The La and Ce formed LC shell coating on BSNF electrode particles increased the peak conductivity and achieved the transition temperature of metal-like conductivity to 510 °C. This is beneficial for the function of a BSNF-LC cathode using in ITSOFC. A low amount of 3.75 mol% LC coating on BSNF reduced AC impedance due to the LC electrocatalytic thin shell influence on the core surface of BSNF, which provided ionic conductivity enhancement among TPBs. The LC coating on BSNF particle also enhanced its CTE matching with LSBC electrolyte. The half-cell of (BSNF-3.75 LC)/LSBC/Pt displayed a higher power density than those utilizing the BSNF or BSNF-5 Ce cathodes at 800 °C. The (Ba, La, Ce) and Nb replaced the A- and B-sites of strontium-ferrate could enhance the more stable BSNF perovskite structure.

The ultrasonic spray pyrolyzed LSBC electrolyte droplets impregnated into LST porous anode to form a pseudo-core-shell and continued the deposition as to resulting in a fired thickness of 2.75 μm dense LSBC electrolyte. This pseudo-core-shell anode substrate improved contact between the anode and the electrolyte without anode functional layer. The LST/iLSBC/Pt half-cell achieved a power density of 377 mW/cm^2 at 750 °C. These results proved that the activation, diffusion and ohmic resistances of the cell were effectively decreased using an ultrasonic spray pyrolysis process. The impregnated LSBC extended the TPB area and length, promoting the performance of the half-cell and also providing a beneficial and convenient unique reverse impregnation from electrolyte into porous electrode to fabricate a thin layer of electrolyte. Full cells with core-shell electrodes are prepared and studied in the next stage. The core-shell interface reaction mechanisms are also necessary investigation topics to control the electrochemical performance precisely. Advancing the core-shell technique up to applying double ions (H^+ and O^{2-}) conduction will realize low temperature solid oxide fuel (or electrolyzer) cells in the future.

Author Contributions: Conceptualization, H.-Y.C. and J.-C.W.; data curation, R.-T.W. and H.-Y.C.; investigation, H.-Y.C. and R.-T.W.; methodology, H.-Y.C.; supervision, H.-Y.C. All authors have read and agreed to the published version of the manuscript.

Institutional Review Board Statement: Not applicable.

Informed Consent Statement: Not applicable.

Data Availability Statement: All data are offered by the authors by reasonable request and the novel core-shell electrodes are available from the authors.

Conflicts of Interest: The authors declare no conflict of interest.

References

1. Taner, T. Energy and exergy analyze of PEM fuel cell: A case study of modeling and simulations. *Energy* **2018**, *143*, 284–294.
2. Taner, T. The novel and innovative design with using H$_2$ fuel of PEM fuel cell: Efficiency of thermodynamic analyze. *Fuel* **2021**, *302*, 121109. [CrossRef]
3. Ormerod, M.R. Solid oxide fuel cells. *Chem. Soc. Rev.* **2003**, *32*, 17–28.
4. Hayashi, K.; Yokoo, M.; Yoshida, Y.; Arai, H. Solid oxide fuel cell stack with high electrical efficiency. *NTT Tech. Rev.* **2009**, *7*, 1–5.
5. Antonucci, V.; Branchini, L.; Brunaccini, G.; De Pascale, A.; Ferraro, M.; Melino, F.; Orlandini, V.; Sergi, F. Thermal integration of a SOFC power generator and a Na–NiCl$_2$ battery for CHP domestic application. *Appl. Energy* **2017**, *185*, 1256–1267. [CrossRef]
6. Ng, K.H.; Rahman, H.A.; Somalu, M.R. Review: Enhancement of composite anode materials for low-temperature solid oxide fuels. *Int. J. Hydrog. Energy* **2019**, *44*, 30692–30704. [CrossRef]
7. Abd Aziz, A.J.; Baharuddin, N.A.; Somalu, M.R.; Muchtar, A. Review of composite cathodes for intermediate-temperature solid oxide fuel cell applications. *Ceram. Int.* **2020**, *46*, 23314–23325. [CrossRef]
8. Mahmud, L.S.; Muchtar, A.; Somalu, M.R. Challenges in fabricating planar solid oxide fuel cells: A review. *Renew. Sustain. Energy Rev.* **2017**, *72*, 105–116.
9. Singhal, S.C. Solid oxide fuel cells for power generation. *Wiley Interdiscip. Rev. Energy Environ.* **2013**, *3*, 179–194. [CrossRef]
10. Zhao, F.; Virkar, A.V. Dependence of polarization in anode-supported solid oxide fuel cells on various cell parameters. *J. Power Source* **2005**, *141*, 79–95. [CrossRef]
11. Wang, H.K.; Alfred, J.S.; Venkataraman, T. Trends in electrode development for next generation solid oxide fuel cells. *J. Mater. Chem. A* **2016**, *4*, 17913–17932.
12. Atkinson, A.; Barnett, S.; Gorte, R.J.; Irvine, J.T.S.; McEvoy, A.J.; Mogensen, M.; Singhal, S.C.; Vohs, J.M. Advanced anodes for high-temperature fuel cells. *Nat. Mater.* **2004**, *3*, 17–27. [CrossRef]
13. Zhou, X.W.; Yan, N.; Chuang, K.T.; Luo, J.L. Progress in La-doped SrTiO$_3$ (LST)-based anode materials for solid oxide fuel cells. *RSC Adv.* **2014**, *4*, 118–131. [CrossRef]
14. Brett, D.J.L.; Atkinson, A.; Brandon, N.P.; Skinner, S.J. Intermediate temperature solid oxide fuel cells. *Chem. Soc. Rev.* **2008**, *37*, 1568–1578. [CrossRef]
15. Shen, S.; Yang, Y.; Guo, L.; Liu, H. A polarization model for a solid oxide fuel cell with a mixed ionic and electronic conductor as electrolyte. *J. Power Source* **2014**, *256*, 43–51. [CrossRef]
16. He, S. Electrode/electrolyte interface and interface reactions of solid oxide cells: Recent development and advances. *Prog. Natural Sc. Mater. Int.* **2021**, *31*, 341–372. [CrossRef]
17. Deseure, J.; Bultel, Y.; Dessemond, L.; Siebert, E. Theoretical optimisation of a SOFC composite cathode. *Electrochim. Acta* **2005**, *50*, 2037–2046. [CrossRef]
18. Liu, Y.; Wang, F.; Chi, B.; Pu, J.; Jian, L.; Jiang, S.P. A stability study of impregnated LSCF-GDC composite cathodes of solid oxide fuel cells. *J. Alloys Compd.* **2013**, *578*, 37–43. [CrossRef]
19. Shekhar, R.S.; Bertei, A.; Monder, D.S. Structure-Properties-Performance: Modelling a solid oxide fuel cell with infiltrated electrodes. *J. Electrochem. Soc.* **2020**, *167*, 084523. [CrossRef]
20. Vijay, P.; Tadé, M.O.; Shao, Z.P. Model based evaluation of the electrochemical reaction sites in solid oxide fuel cell electrodes. *Int. J. Hydrogen Energy* **2019**, *44*, 8439–8459. [CrossRef]
21. Fukunaga, H. The relationship between overpotential and the three phase boundary length. *Solid State Ionics* **1996**, *86–88*, 1179–1185. [CrossRef]
22. Mukhopadhyay, M.; Mukhopadhyay, J.; Sharma, A.D.; Basu, R.N. In-situ patterned intra-anode triple phase boundary in SOFC electroless anode: An enhancement of electrochemical performance. *Int. J. Hydrogen Energy* **2011**, *36*, 7677–7682. [CrossRef]
23. Yashima, M.; Takizawa, T. Atomic displacement parameters of ceria doped with rare-earth oxide Ce$_{0.8}$R$_{0.2}$O$_{1.9}$ (R = La, Nd, Sm, Gd, Y, and Yb) and correlation with oxide-ion conductivity. *J. Phys. Chem. C* **2020**, *114*, 2385–2392. [CrossRef]
24. Chang, H.Y.; Wang, Y.M.; Lin, C.H.; Cheng, S.Y. Effects of rapid process on the conductivity of multiple elements doped ceria-based electrolyte. *J. Power Source* **2011**, *196*, 1704–1711. [CrossRef]
25. Takeguchi, T.; Kikuchi, R.; Yano, T.; Eguchi, K.; Murata, K. Effect of precious metal addition to Ni-YSZ cermet on reforming of CH4 and electrochemical activity as SOFC anode. *Catal. Today* **2003**, *84*, 217–222. [CrossRef]
26. Kan, H.; Lee, H. Enhanced stability of Ni-Fe/GDC solid oxide fuel cell anodes for dry methane fuel. *Catal. Commun.* **2010**, *12*, 36–39. [CrossRef]
27. Huang, B.; Wang, S.R.; Liu, R.Z.; Wen, T.L. Preparation and performance characterization of the Fe-Ni/ScSZ cermet anode for oxidation of ethanol fuel in SOFCs. *J. Power Source* **2007**, *167*, 288–294. [CrossRef]

28. Faes, A.; Hessler-Wyser, A.; Presvytes, D.; Vayenas, C.G.; Vanherle, J. Nickel-zirconia anode degradation and triple phase boundary quantification from microstructural analysis. *Fuel Cell* **2009**, *9*, 841–851. [CrossRef]

29. Huang, T.J.; Chou, C.L. Oxygen dissociation and interfacial transfer rate on performance of SOFCs with metal-added (LaSr)(CoFe)O$_3$-(Ce,Gd)O$_{2-\delta}$ cathodes. *Fuel Cell* **2010**, *10*, 718–725. [CrossRef]

30. Li, C.X.; Liu, S.; Zhang, Y.; Li, C.J. Characterization of the microstructure and electrochemical behavior of Sm$_{0.7}$Sr$_{0.3}$Co$_{3-\delta}$ cathode deposited by solution precursor plasma spraying. *Int. J. Hydrogen Energy* **2012**, *37*, 13097–13102. [CrossRef]

31. Küngas, R.; Vohs, J.M.; Gorte, R.J. Effect of the ionic conductivity of the electrolyte in composite SOFC cathodes. *J. Electrochem. Soc.* **2011**, *158*, B743. [CrossRef]

32. Hua, B.; Yan, N.; Li, M.; Sun, Y.F.; Zhang, Y.Q.; Li, J.; Etsell, T.; Sarkar, P.; Luo, J.L. Anode-engineered protonic ceramic fuel cell with excellent performance and fuel compatibility. *Adv. Mater.* **2016**, *28*, 8922–8926. [CrossRef]

33. Zhu, X.; Lü, Z.; Wei, B.; Chen, K.; Liu, M.; Huang, X.; Su, W. Fabrication and performance of membrane solid oxide fuel cells with La$_{0.75}$Sr$_{0.25}$Cr$_{0.5}$Mn$_{0.5}$O$_{3-\delta}$ impregnated anodes. *J. Power Sources* **2010**, *195*, 1793–1798. [CrossRef]

34. Wang, K.; Ran, R.; Zhou, W.; Gu, H.; Zongping Shao, Z.P.; Ahn, J.M. Properties and performance of Ba$_{0.5}$Sr$_{0.5}$Co$_{0.8}$Fe$_{0.2}$O$_{3-\delta}$+Sm$_{0.2}$Ce0$_{.8}$O$_{1.9}$ composite cathode. *J. Power Source* **2008**, *179*, 60–68. [CrossRef]

35. Su, C.; Shao, Z.; Lin, Y.; Wu, Y.; Wang, H. Solid oxide fuel cells with both high voltage and power output by utilizing beneficial interfacial reaction. *Phys. Chem. Chem. Phys.* **2012**, *14*, 12173–12181. [CrossRef] [PubMed]

36. Driscoll, D.R.; McIntyre, M.D.; Welander, M.M.; Sofie, S.W.; Walker, R.A. Enhancement of high temperature metallic catalysts: Aluminum titanate in the nickel-zirconia system. *Appl. Catal. A* **2016**, *527*, 36–44. [CrossRef]

37. Welander, M.M.; Zachariasen, M.S.; Hunt, C.D.; Sofie, S.W.; Walker, R.A. Operando Studies of Redox Resilience in ALT Enhanced NiO-YSZ SOFC Anodes. *J. Electrochem. Soc.* **2018**, *165*, F152–F157. [CrossRef]

38. Wang, Z.; Zhang, N.; Qiao, J.; Sun, K.; Xu, P. Improved SOFC performance with continuously graded anode functional layer. *Electrochem. Commun.* **2009**, *11*, 1120–1123. [CrossRef]

39. Young, D.; Sukeshini, A.M.; Cummins, R.; Xiao, H.; Rottmayer, M.; Reitz, T. Ink-jet printing of electrolyte and anode functional layer for solid oxide fuel cells. *J. Power Source* **2008**, *184*, 191–196. [CrossRef]

40. Lee, K.T.; Vito, N.J.; Wachsman, E.D. Comprehensive quantification of Ni–Gd$_{0.1}$Ce$_{0.9}$O$_{1.95}$ anode functional layer microstructures by three-dimensional reconstruction using a FIB/SEM dual beam system. *J. Power Source* **2013**, *228*, 220–228. [CrossRef]

41. Mitterdorfer, A.; Gauckler, L.J. La$_2$Zr$_2$O$_7$ formation and oxygen reduction kinetics of the La$_{0.85}$Sr$_{0.15}$Mn$_y$O$_3$, O$_2$(g)|YSZ system. *Solid State Ionics* **1998**, *111*, 185–218. [CrossRef]

42. Zhang, J.-P.; Jiang, S.-P.; Jonathan, G.; Love, K.F.; Badwal, S.P.S. Chemical interactions between strontium-doped praseodymium manganite and 3 mol% yttria-zirconia. *J. Mater. Chem.* **1998**, *8*, 2787–2794. [CrossRef]

43. Jiang, S.P.; Zhhang, J.P.; Ramprakash, Y.; Milosevic, D.; Wilshier, K. An investigation of shelf-life of strontium doped LaMnO$_3$ materials. *J. Mater. Sci.* **2000**, *35*, 2735–2741. [CrossRef]

44. Wang, F.; Nishi, M.; Brito, M.E.; Kishimoto, H.; Yamaji, K.; Yokokawa, H.; Horita, T. Sr and Zr diffusion in LSCF/10GDC/8YSZ triplets for solid oxide fuel cells (SOFCs). *J. Power Source* **2014**, *258*, 281–289. [CrossRef]

45. Zhang, L.; Li, X.; Zhang, L.; Cai, H.; Xu, J.; Wang, L.; Long, W. Improved thermal expansion and electrochemical performance of La$_{0.4}$Sr$_{0.6}$Co$_{0.9}$Sb$_{0.1}$O$_{3-\delta}$-Ce$_{0.8}$Sm$_{0.2}$O$_{1.9}$ composite cathode for IT-SOFCs. *Solid State Sci.* **2019**, *91*, 126–132. [CrossRef]

46. Lee, S.; Kim, G.; Vohs, J.M.; Gorte, R.J. SOFC anodes based on infiltration of La$_{0.3}$Sr$_{0.7}$TiO$_3$. *J. Electrochem. Soc.* **2008**, *155*, B1179–B1183. [CrossRef]

47. Kim, G.; Lee, S.; Shin, J.Y.; Corre, G.; Irvine, J.T.S.; Vohs, J.M.; Gorte, R.T. Investigation of the structural and catalytic requirements for high-performance SOFC anodes formed by infiltration of LSCM. *Electrochem. Solid-State Lett.* **2009**, *12*, B48–B52. [CrossRef]

48. Sholklapper, T.Z.; Radmilovic, V.; Jacobson, C.P.; Visco, S.J.; De Jonghe, L.C. Synthesis and stability of a nanoparticle-infiltrated solid oxide fuel cell electrode. Electrochem. *Solid State Lett.* **2007**, *10*, B74–B76. [CrossRef]

49. Chang, H.Y.; Cheng, S.Y.; Sheu, C.I. Controlling Interface Characteristics by Adjusting Core-shell Structure. *Acta Materialia* **2004**, *52*, 5389–5396. [CrossRef]

50. Chang, H.Y.; Cheng, S.Y.; Sheu, C.I.; Wang, Y.H. Core-shell Structure of Strontium Titanate Self-grown by a Hydrothermal Process for Use in Grain Boundary Barrier Layers. *Nanotechnology* **2003**, *14*, 603–608. [CrossRef]

51. Caruso, F. Nanoengineering of particle surfaces. *Adv. Mater.* **2001**, *13*, 11. [CrossRef]

52. Pudmich, G.; Boukamp, B.A.; Gonzalez-Cuenca, M.; Jungen, W.; Zipprich, W.; Tietz, F. Chromite/titanate based perovskites for application as anodes in solid oxide fuel cells. *Solid State Ionics* **2000**, *135*, 433–438. [CrossRef]

53. Gong, M.Y.; Liu, X.B.; Trembly, J.; Johnson, C. Sulfur-tolerant anode materials for solid oxide fuel cell application. *J. Power Source* **2007**, *168*, 289–298. [CrossRef]

54. Li, X.; Zhao, H.L.; Xu, N.S.; Zhou, X.; Zhang, C.J.; Chen, N. Electrical conduction behavior of La, Co co-doped SrTiO$_3$ perovskite as anode material for solid oxide fuel cells. *Int. J. Hydrogen Energ.* **2009**, *34*, 6407–6414. [CrossRef]

55. McIntosh, R.S.; Gorte, R.J. Direct hydrocarbon solid oxide fuel cells. *Chem. Rev.* **2004**, *104*, 4845–4865. [CrossRef] [PubMed]

56. Chang, H.Y.; Wang, S.H.; Wang, Y.M.; Lai, C.W.; Lin, C.H.; Cheng, S.Y. Novel core-shell structure of perovskite anode and characterization. *Int. J. Hydrogen Energy* **2012**, *37*, 7771–7778. [CrossRef]

57. Akalin, G.O.; Taner, O.O.; Taner, T. The preparation, characterization and antibacterial properties of chitosan/pectin silver nanoparticle films. *Polym. Bull.* **2021**, 1–18. [CrossRef]

58. Dhanapal, A.; Sasikala, P.; Rajamani, L.; Kavitha, V.; Yazhini, G.; Banu, M.S. Edible films from polysaccharides. *Food Sci Qual Manag.* **2012**, *3*, 2224–6088.

59. Cazon, P.; Velazquez, G.; Ramirez, J.A.; Vazquez, M. Polysaccharide-based films and coatings for food packaging: A review. *Food Hydrocol.* **2017**, *68*, 136–148. [CrossRef]

60. Altun, T. Preparation and application of glutaraldehyde cross-linked chitosan coated bentonite clay capsules: Chromium (VI) removal from aqueous solution. *J. Chil. Chem. Soc.* **2020**, *65*, 4790–4797. [CrossRef]

61. dos Santos, D.S.; Goulet, P.J.; Pieczonka, N.P.; Oliveira, O.N.; Aroca, R.F. Gold nanoparticle embedded, self-sustained chitosan films as substrates for surface-enhanced Raman scattering. *Langmuir* **2004**, *20*, 10273–10277. [CrossRef] [PubMed]

62. Corbel, G.; Mestiri, S.; Lacorre, P. Physicochemical compatibility of CGO fluorite, LSM and LSCF perovskite electrode materials with $La_2Mo_2O_9$ fast oxide-ion conductor. *Solid State Sci.* **2005**, *7*, 1216–1224. [CrossRef]

63. Nielsen, J.; Hjelm, J. Impedance of SOFC electrodes: A review and a comprehensive case study on the impedance of LSM:YSZ cathodes. *Electrochim. Acta* **2014**, *115*, 31–45. [CrossRef]

64. McIntosh, S.; Vente, J.F.; Haije, W.G.; Blank, D.H.A.; Bouwmeester, H.J.M. Oxygen stoichiometry and chemical expansion of $Ba_{0.5}Sr_{0.5}Co_{0.8}Fe_{0.2}O_{3-\delta}$ measured by in situ neutron diffraction. *Chem. Mater.* **2006**, *18*, 2187–2193. [CrossRef]

65. Wei, B.; Lu, Z.; Huang, X.Q.; Liu, M.L.; Li, N.; Su, W.H. Synthesis, electrical and electrochemical properties of $Ba_{0.5}Sr_{0.5}Zn_{0.2}Fe_{0.8}O_{3-\delta}$ perovskite oxide for IT-SOFC cathode. *J. Power Source* **2008**, *176*, 1–8. [CrossRef]

66. Wang, H.H.; Tablet, C.; Feldhoff, A.; Caro, J. A cobalt-free oxygen-permeable membrane based on the perovskite-type oxide $Ba_{0.5}Sr_{0.5}Zn_{0.2}Fe_{0.8}O_{3-\delta}$. *Adv. Mater.* **2005**, *17*, 1785–1788. [CrossRef]

67. Chen, Z.H.; Ran, R.; Zhou, W.; Shao, Z.P.; Liu, S.M. Assessment of $Ba_{0.5}Sr_{0.5}Co_{1-y}Fe_yO_{3-\delta}$ (y = 0.0–1.0) for prospective application as cathode for IT-SOFCs or oxygen permeating membrane. *Electrochim. Acta* **2007**, *52*, 7343–7351. [CrossRef]

68. Sun, W.; Yan, L.; Zhang, S.; Liu, W. Crystal structure, electrical conductivity and sintering of $Ba_{0.5}Sr_{0.5}Zn_xFe_{1-x}O_{3-\delta}$. *J. Alloy Compd.* **2009**, *485*, 872–875. [CrossRef]

69. Peña-Martínez, J.; Marrero-López, D.; Ruiz-Morales, J.C.; Núñez, P.; Sánchez-Bautista, C.; Dos Santos-García, A.J.; Canales-Vázquez, J. On $Ba_{0.5}Sr_{0.5}Co_{1-y}Fe_yO_{3-\delta}$ (y = 0.1–0.9) oxides as cathode materials for $La_{0.9}Sr_{0.1}Ga_{0.8}Mg_{0.2}O_{2.85}$ based IT-SOFCs. *Int. J. Hydrogen Energ.* **2009**, *34*, 9486–9495. [CrossRef]

70. Manthiram, A.; Kim, J.H.; Kim, Y.N.; Lee, K.T. Crystal chemistry and properties of mixed ionic-electronic conductors. *J. Electroceram.* **2011**, *27*, 93–107. [CrossRef]

71. Deganello, F.; Liotta, L.F.; Longo, A.; Casaletto, M.P.; Scopelliti, M. Cerium effect on the phase structure, phase stability and redox properties of Ce-doped strontium ferrates. *J. Solid State Chem.* **2006**, *179*, 3406–3419. [CrossRef]

72. Wang, Y.M.; Chang, C.M.; Shih, J.S.; Chang, H.Y. Novel lanthanum and cerium coatings on (Ba, Sr)-ferrate cathodes for intermediate-temperature solid oxide fuel cells. *J. Eur. Ceram. Soc.* **2016**, *36*, 3433–3440. [CrossRef]

73. Cagri, A.; Ustunol, Z.; Ryser, E.T. Antimicrobial edible films and coatings. *J. Food Prot.* **2004**, *67*, 833–848. [CrossRef] [PubMed]

74. Huang, J.; Xie, F.; Wang, C.; Mao, Z. Development of solid oxide fuel cell materials for intermediate-to-low temperature operation. *Int. J. Hydrogen Energy* **2012**, *37*, 877–883. [CrossRef]

75. Mizusaki, J.; Okayasu, M.; Yamauchi, S.; Fueki, K. Nonstoichiometry and phase relationship of the $SrFeO_{2.5}$-$SrFeO_3$ system at high temperature. *J. Solid State Chem.* **1992**, *99*, 166–172. [CrossRef]

76. Macdonald, J.R.; Barsoukov, E. *Impedance Spectroscopy Theory, Experiment, and Applications*, 2nd ed.; John Wiley & Sons, Inc.: Hoboken, NJ, USA, 2005.

77. Cesiulis, H.; Tsyntsaru, N.; Ramanavicius, A.; Ragoisha, G. The study of thin films by electrochemical impedance spectroscopy. In *Nanostructures and Thin Films for Multifunctional Applications*; Springer: Cham, Switzerland, 2016; pp. 3–42.

78. Zheng, Y.; Zhang, C.; Ran, R.; Cai, R.; Shao, Z.; Farrusseng, D. A new symmetric solid-oxide fuel cell with $La_{0.8}Sr_{0.2}Sc_{0.2}Mn_{0.8}O_{3-\delta}$ perovskite oxide as both the anode and cathode. *Acta Materialia* **2009**, *57*, 1165–1175. [CrossRef]

79. Jiang, S.P.; Chen, X.J.; Chan, S.H.; Kwok, J.T.; Khor, K.A. $(La_{0.75}Sr_{0.25})(Cr_{0.5}Mn_{0.5})O_3$/YSZ composite anodes for methane oxidation reaction in solid oxide fuel cells. *Solid State Ionics* **2006**, *177*, 149–157. [CrossRef]

80. Fu, C.; Sun, K.; Zhang, N.; Chen, X.; Zhou, D. Electrochemical characteristics of LSCF–SDC composite cathode for intermediate temperature SOFC. *Electrochim. Acta* **2007**, *52*, 4589–4594. [CrossRef]

81. Qiang, F.; Sun, K.; Zhang, N.; Zhu, X.; Le, S.; Zhou, D. Characterization of electrical properties of GDC doped A-site deficient LSCF based composite cathode using impedance spectroscopy. *J. Power Source* **2007**, *168*, 338–345. [CrossRef]

82. Izuki, M.; Brito, M.E.; Yamaji, K.; Kishimoto, H.; Cho, D.-H.; Shimonosono, T.; Horita, T.; Yokokawa, H. Interfacial stability and cation diffusion across the LSCF/GDC interface. *J. Power Source* **2011**, *196*, 7232–7236. [CrossRef]

83. Xiao, G.L.; Liu, Q.; Wang, S.W.; Komvokis, V.G.; Amiridis, M.D.; Heyden, A.; Ma, S.G.; Chen, F.L. Synthesis and characterization of Mo-doped $SrFeO_{3-\delta}$ as cathode materials for solid oxide fuel cells. *J. Power Source* **2012**, *202*, 63–69. [CrossRef]

84. Hodges, J.P.; Short, S.; Jorgensen, J.D.; Xiong, X.; Dabrowski, B.; Mini, S.M.; Kimball, C.W. Evolution of oxygen-vacancy ordered crystal structures in the perovskite series Sr_nFenO_{3n-1} (n = 2, 4, 8, and ∞), and the relationship to electronic and magnetic properties. *J. Solid State Chem.* **2000**, *151*, 190–209. [CrossRef]

85. Liu, X.T.; Zhao, H.L.; Yang, J.Y.; Li, Y.; Chen, T.; Lu, X.G.; Ding, W.Z.; Li, F.S. Lattice characteristics, structure stability and oxygen permeability of $BaFe_{1-x}Y_xO_{3-\delta}$ ceramic membranes. *J. Membrane Sci.* **2011**, *383*, 235–240. [CrossRef]

86. Trofimenko, N.E.; Ullmann, H. Oxygen stoichiometry and mixed ionic-electronic conductivity of $Sr_{1-a}Ce_aFe_{1-b}Co_bO_{3-x}$ perovskite-type oxides. *J. Eur. Ceram. Soc.* **2000**, *20*, 1241–1250. [CrossRef]

87. McIntosh, S.; Vente, J.F.; Haije, W.G.; Blank, D.H.A.; Bouwmeester, H.J.M. Structure and oxygen stoichiometry of $SrCo_{0.8}Fe_{0.2}O_{3-\delta}$ and $Ba_{0.5}Sr_{0.5}Co_{0.8}Fe_{0.2}O_{3-\delta}$. *Solid State Ionics* **2006**, *177*, 1737–1742. [CrossRef]

88. Jiang, S.P. Development of lanthanum strontium cobalt ferrite perovskite electrodes of solid oxide fuel cells—A review. *Int. J. Hydrogen Energy* **2019**, *44*, 7448–7493. [CrossRef]

89. Leng, Y.; Chan, S.H.; Liu, Q. Development of LSCF-GDC composite cathodes for low temperature solid oxide fuel cells with thin film GDC electrolyte. *Int. J. Hydrogen Energy* **2008**, *33*, 3808–3817. [CrossRef]

90. Leng, Y.J.; Chan, S.H.; Jiang, S.P.; Khor, K.A. Low-temperature SOFC with thin film GDC electrolyte prepared in situ by solid-state reaction. *Solid State Ionics* **2004**, *170*, 9–15. [CrossRef]

91. Ko, F.-Y.; Chiu, T.-W.; Wu, R.; Chen, T.-C.; Chang, H.-Y. Thin Layer Electrolyte Impregnation into Porous Anode Supported Fuel Cell by Ultrasonic Spray Pyrolysis. *Int. J. Hydrogen Energy* **2021**, *46*, 16708–16716. [CrossRef]

92. Dai, H.; He, S.; Chen, H.; Guo, L. A novel method of modifying electrolyte surface at mesoscale for intermediate temperature solid oxide fuel cells. *Ceram. Int.* **2016**, *42*, 2045–2050. [CrossRef]

93. Hedayat, N.; Du, Y.; Ilkhani, H. Pyrolyzable pore-formers for the porous-electrode formation in solid oxide fuel cells: A review. *Ceram. Int.* **2018**, *44*, 4561–4576. [CrossRef]

94. Seo, H.; Kishimoto, M.; Ding, C.; Iwai, H.; Saito, M.; Yoshida, H. Improvement in the electrochemical performance of anode supported solid oxide fuel cells by meso- and nanoscale structural modifications. *Fuel Cell* **2020**, *20*, 570–579. [CrossRef]

95. Lu, Y.C.; Gasper, P.; Nikiforov, A.Y.; Pal, U.B.; Gopalan, S.; Basu, S.N. Co-infiltration of nickel and mixed conducting $Gd_{0.1}Ce_{0.9}O_{2-\delta}$ and $La_{0.6}Sr_{0.3}Ni_{0.15}Cr_{0.85}O_{3-\delta}$ phases in Ni-YSZ anodes for improved stability and performance. *JOM* **2019**, *71*, 3835–3847. [CrossRef]

96. Kishimoto, M.; Kawakami, Y.; Otani, Y.; Iwai, H.; Yoshida, H. Improved controllability of wet infiltration technique for fabrication of solid oxide fuel cell anodes. *Scripta Mater.* **2017**, *140*, 5–8. [CrossRef]

97. Tian, Y.T.; Guo, X.; Wu, P.P.; Zhang, X.; Nie, Z.Q. Preparation and evaluation of Ni-based anodes with straight open pores for solid oxide fuel cells. *J. Alloys Compd.* **2020**, *817*, 153244. [CrossRef]

98. Dogdibegovic, E.; Wang, R.; Lau, G.Y.; Tucker, M.C. High performance metal-supported solid oxide fuel cells with infiltrated electrodes. *J. Power Source* **2019**, *410–411*, 91–98. [CrossRef]

99. Xia, C.R.; Liu, M.L. Low-temperature SOFCs based on $Gd_{0.1}Ce_{0.9}O_{1.95}$ fabricated by dry pressing. *Solid State Ionics* **2001**, *144*, 249–255. [CrossRef]

100. Xia, C.R.; Chen, F.L.; Liu, M.L. Reduced-temperature solid oxide fuel cells fabricated by screen printing. *Electrochem. Solid-State Lett.* **2001**, *4*, A52–A54. [CrossRef]

101. Takahashi, S.; Sumi, H.; Fujishiro, Y. Development of cosintering process for anode supported solid oxide fuel cells with gadolinia doped ceria/lanthanum silicate bi-layer electrolyte. *Int. J. Hydrogen Energy* **2019**, *44*, 23377–23383. [CrossRef]

102. Ding, C.; Lin, H.; Sato, K.; Amezawa, K.; Kawada, T.; Mizusaki, J.; Hashida, T. Effect of thickness of $Gd_{0.1}Ce_{0.9}O_{1.95}$ electrolyte films on electrical performance of anode-supported solid oxide fuel cells. *J. Power Source* **2010**, *195*, 5487–5492. [CrossRef]

103. Zhen, Y.D.; Tok, A.I.Y.; Jiang, S.P.; Boey, F.Y.C. Fabrication and performance of gadolinia-doped ceria-based intermediatetemperature solid oxide fuel cells. *J. Power Source* **2008**, *178*, 69–74. [CrossRef]

104. Hibino, T.; Hashimoto, A.; Yano, M.; Suzuki, M.; Sano, M. Rucatalyzed anode materials for direct hydrocarbon SOFCs. *Electrochim. Acta* **2003**, *48*, 2531–2537.

105. Reolon, R.P.; Halmenschlager, C.M.; Neagu, R.; Malfatti, C.F.; Bergmann, C.P. Electrochemical performance of gadoliniadoped ceria (CGO) electrolyte thin films for ITSOFC deposited by spray pyrolysis. *J. Power Source* **2014**, *261*, 348–355. [CrossRef]

A Review on Impedimetric and Voltammetric Analysis Based on Polypyrrole Conducting Polymers for Electrochemical Sensing Applications

Nurul Akmaliah Dzulkurnain [1], Marliyana Mokhtar [2], Jahwarhar Izuan Abdul Rashid [1], Victor Feizal Knight [2], Wan Md Zin Wan Yunus [3], Keat Khim Ong [2], Noor Azilah Mohd Kasim [2] and Siti Aminah Mohd Noor [1,*]

[1] Department of Chemistry and Biology, Centre for Defence Foundation Studies, National Defence University of Malaysia, Sungai Besi Camp, Kuala Lumpur 57000, Malaysia; nurulakmaliah86@gmail.com (N.A.D.); jahwarhar@upnm.edu.my (J.I.A.R.)

[2] Research Centre for Chemical Defence, National Defence University of Malaysia, Sungai Besi Camp, Kuala Lumpur 57000, Malaysia; marliyanamokh@yahoo.com (M.M.); victor.feizal@upnm.edu.my (V.F.K.); ongkhim@upnm.edu.my (K.K.O.); azilah@upnm.edu.my (N.A.M.K.)

[3] Centre for Tropicalisation, National Defence University of Malaysia, Sungai Besi Camp, Kuala Lumpur 57000, Malaysia; wanmdzin@upnm.edu.my

[*] Correspondence: s.aminah@upnm.edu.my

Abstract: Conducting polymers have been widely used in electrochemical sensors as receptors of the sensing signal's analytes and transducers. Polypyrrole (PPy) conducting polymers are highlighted due to their good electrical conductive properties, ease in preparation, and flexibility of surface characteristics. The objective of this review paper is to discuss the theoretical background of the two main types of electrochemical detection: impedimetric and voltammetric analysis. It also reviews the application and results obtained from these two electrochemical detections when utilizing PPy as a based sensing material in electrochemical sensor. Finally, related aspects in electrochemical sensor construction using PPy will also be discussed. It is anticipated that this review will provide researchers, especially those without an electrochemical analysis background, with an easy-to-understand summary of the concepts and technologies used in electrochemical sensor research, particularly those interested in utilizing PPy as a based sensing material.

Keywords: electrochemical sensor; biosensor; impedimetric; voltammetric; polypyrrole; conducting polymer

1. Introduction

Conducting polymers (CPs) play an important role in the design and development of electrochemical sensors. They provide the necessary electrical conductivity to transduce the occurrence of the coupling event into an analytical signal (Figure 1) [1].

CPs are conjugated polymers that possess delocalized π-bonds on the backbone of the polymers. These π-bonds assist in the migration of electrons throughout the polymeric chain. Thus, these polymers can act as conductors, semiconductors, or even superconductors. Besides that, CPs also have high electron affinity and redox activity. The general physical properties of CPs depend on the size and length of the conducting polymer, which can also be described in terms of their molecular weight [2]. There are many types of CPs such as polyaniline (PANI), polypyrrole (PPy), polyacetylene, polyparaphenylene (PPPh), polyparaphenylene vinylene (PPV), polythiophenes (PTh), polydiaminonaphthalene, polyazulene, and poly (3,4-ethylene dioxythiophene) (PEDOT) [3]. Electrically conductive polymers are a class of materials that can be fabricated to generate either transient or static electrical charges because of their physico-chemical properties [4]. Among those polymers, PPy is the most extensively used as a conducting polymer in electrochemical sensing applications because it is a heterocyclic conducting polymer, with good

environmental stability, high electronic conductivity, and biocompatibility compared to other CPs [5–8].
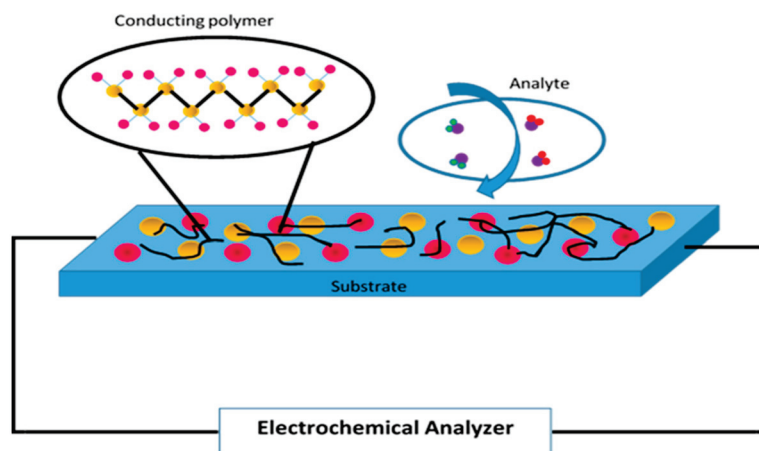
Figure 1. Schematic diagram of a conducting polymer and analyte on an electrochemical sensor.

Furthermore, PPy is easy to synthesize as a black powder chemically and electrochemically as thin films on various electrodes for both aqueous and nonaqueous media [4,9–11]. PPy has also been applied in multidisciplinary applications such as batteries, supercapacitors, coatings, etc. [12–14]. Despite these excellent properties, it also suffers from certain drawbacks, namely, poor thermal solubility and low mechanical stability [15]. These drawbacks can affect the response characteristics and sensitivity to small perturbation of the electrochemical sensor [3]. In the past two decades, scientists have applied different approaches to modifying PPy to improve its properties. These approaches include blending [16], electro-polymerization [17], interpenetrating network formation, and composite synthesis [18,19].

1.1. Synthesis and Preparation of Polypyrrole

PPy is commonly synthesized through chemical or electrochemical oxidation of pyrrole monomer using oxidant agents through a conjugated bond system with the polymer backbone. However, in the presence of only PPy, it may suffer from a certain drawback as mentioned above, and this will restrict the device's application. Therefore, approaches such as blending, electro-polymerization, interpenetrating network formation, and composite synthesis have been done to enhance the PPy properties, thus improving the device's performance.

Hosseini and Entezami, 2003, prepared the polymer by blending PPy with polyvinyl acetate (PVAc), polystyrene (PS), and polyvinyl chloride (PVC) using a chemical method to produce flexible and free-standing blended polymer films. The sensing abilities of these films towards toxic gases and vapors were investigated and it was discovered that the PPy blended film had improved mechanical strength and was also able to exhibit greater environmental stability. Besides that, it was also found the sensoric properties of the PPy blends towards toxic gases and vapors against hydrogen halides, hydrogen cyanide, and halomethyl compounds were better than non-blended PPys. Therefore, it can be surmised from their findings that PPy blends are good candidates for sensing toxic gases and vapors [16].

Meanwhile, Song et al., 2019, prepared three-dimensional graphene oxide with an interconnected porous polypyrrole (pGO/PPy) nanostructure-based actuator through electro-polymerization and sonication. This configuration allowed the actuator to adsorb trace cadmium by the carboxyl functional group in the GO and also was able to widen the electrode detection range of the PPy which was densely covered with gold substrate. From the results obtained, they suggest that the pGO/PPy was a promising material that had an ability to enhance the pre-concentration factors, enrich the potential window and

greatly increase the sensitivity of the cadmium sensor. The cadmium detection in the presence of interference ions showed good selectivity using this pGO/PPy nanostructure based actuator. Besides which, the nanostructure also achieved a wider linear range and a lower limit of detection (LOD). Moreover, this method could be developed into a low cost, portable and reliable sensor that is both sensitive and selective towards cadmium in aqueous systems and could potentially facilitate detection of other heavy metals such as lead, mercury and copper [17].

Hassanein et al., 2017, fabricated biosensors based on chitosan-ZnO/Polypyrrole nanocomposites. The sensor was prepared using the oxidative polymerization of pyrrole monomer with $(NH_4)_2S_2O_8$ as the oxidant and followed by mixing with chitosan–zinc oxide composites. The conductive polymers and oxide nanoparticles (organic–inorganic nanocomposite materials) have been previously widely used because of the novel properties of this nanocomposite which can be attributed to the successful blending of the individual characteristics of the parent constituents into a single material. The advantages of the oxide nanoparticles are in their ability to modify their chemical, mechanical, electrical, structural, morphological, and optical properties under specific circumstances. Moreover, these nanostructure materials have a larger percentage of surface atoms available which possess high reactivity. From the results, it was found that there was a significant improvement in electrical conductivity from the cyclic voltammetry measurements of the $K_3(Fe(CN)_6)$ sample. A large enhancement of the stripping of peak current compared to bare CPE was identified using the square-wave adsorptive anodic stripping voltammetry method. Consequently, the proposed material proved to possess suitable ability as sensing materials in biosensor applications [18].

In other work done by Tlili et al., 2005, they reported the technique of interpenetrating network formation, where they immobilized DNA probes bearing amine groups by covalent grafting on a supporting polypyrrole matrix functionalized with activated ester groups. The immobilization step played an important role in determining the overall performance of the biosensor. In order to achieve high sensitivity and selectivity, it required minimization of non-specific adsorption and stability of the immobilization. Polypyrrole (PPy) conducting polymer was chosen in their study because of its biocompatibility, high hydrophilic character combined with high stability in water and facile incorporation of many counter ions which make it highly suitable as an interface for grafting DNA probes onto a micro-sized surface. From the results, it was discovered that the large surface area obtained by using porous polypyrrole leads to an increase in the density of the immobilized DNA probes, which then helps to monitor more easily the DNA hybridization reaction [19].

In yet another study, Hsu et al., 2014, used the electropolymerization method to incorporate chloro(protoporphyrinato) iron(III) (hemin), polypyrrole (PPy), and silver (Ag) in order to achieve sufficient sensitivity for an environmental dissolved oxygen (DO) sensor. The electropolymerization method provides a strong adhesive bond at the substrate/hemin interface and allows for an increased concentration of hemin. However, due to their poor current collection capacity, electropolymerized films with higher hemin loading do not instead produce proportionally higher current or increased sensitivity. Therefore, co-electropolymerizing hemin and pyrrole to fabricate a sensing electrode for dissolved oxygen sensing applications is one of the better methods for solving this lower sensitivity problem. Thus, this sensor is able to be manufactured at a lower cost and with longer lifespan. In addition, since it is a solid state sensor, it has the potential to be miniaturized and integrated within a micro-fabricated reference electrode to form a complete sensing system at a very low cost [20].

1.2. Electrochemical Sensors

Electrochemical sensors have aroused great interest in providing fast and highly sensitive detection of proteins, which include the antibodies generated during the immune response against infections. Recently, electrochemical sensors have found widespread applications in clinical diagnostics, food safety, food quality, biological analysis, and en-

vironmental monitoring. Electrochemical sensors are sensors that change the effect of an electrochemical reaction of target species on the electrodes into useful signals which demonstrate alterations in potential and conductivity. With the utilization of biofunctionalities in the electrochemical sensor such as recognition and catalysis, these sensors are known as "biosensors" [21]. A typical biosensor is a combination of a transducer and certain biological elements. The biosensor can also be described as an electrochemical, optical, thermal, or piezoelectric biosensor depending on the type of transducer used.

In order to functionalize the biological element during the development of the biosensor, the immobilization step is a crucial step. The most popular biosensor utilizes enzymes as the biological substance with an electrode functioning as a transducer. The enzyme is directly immobilized onto the surface of the electrode, or is immobilized onto the electrode using a suitable matrix. In most cases, there are four strategies for enzyme immobilization that can be considered. These strategies, derived from the chemistry of immobilization, are shown in Figure 2. The first strategy is covalent bonding to the electrode or matrix (Figure 2A). The second is physical adsorption to the electrode or matrix (Figure 2B). The third is entrapment involving the enzyme and the electrode (Figure 2C). The final is affinity, which uses a specific biochemical interaction (Figure 2D). However, these strategies cannot each be considered as the perfect strategy because the optimum biosensor still needs to be selected depending on the specific enzyme and transducer [22].
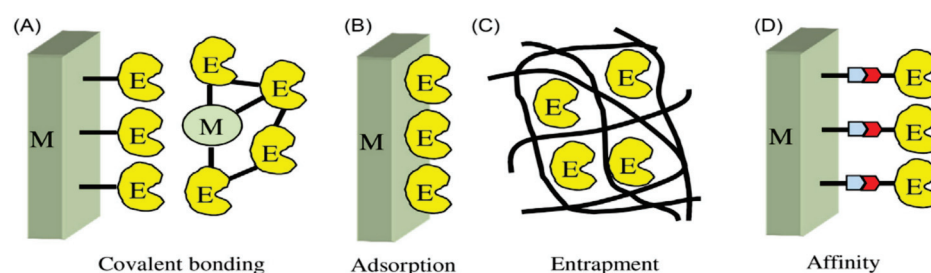
Figure 2. Schematic representation of strategies for enzyme immobilization: Covalent bonding (**A**); Adsorption (**B**); Entrapment (**C**) and Affinity (**D**). E, enzyme; M, matrix [22]. Reproduced with permission from [H. Muguruma], [Biosensors: Enzyme Immobilization Chemistry]; published by [Elsvier], [2018].

The capture of a target analyte onto a bio or non-bioreceptor immobilized on a CP will generate a measurable analytical signal which is then converted into an electrical signal. The electrical signal can be identified using three main types of sensing modes such as potentiometric (membrane potential change); impedimetric (impedance change); and voltametric or amperometric (change of current for an electrochemical reaction with the applied voltage in the former, or with time at a fixed applied potential in the latter) [23]. It is desirable to strategize the development of an electrochemical sensor in order to provide low detection limits, high selectivity, and utilize a limited amount of indicator species. The impedimetric mode measures the targeted analyte through the output of an electrical impedance signal that is proportional to the analyte activity [9,24]; whereas in the voltametric mode, data about an analyte are obtained by measuring the current while applying a working electrode potential. The electrochemical reaction on the electrode surface and the electrode/electrolyte interface layer produces the final current [25]. The voltametric strategies include linear sweep voltammetry (LSV), cyclic voltammetry (CV), differential pulse voltammetry (DPV), and square wave voltammetry (SWV). These strategies provide a detailed measure with a broad range of effectiveness and a low detection limit. Meanwhile, in the amperometric mode, a consistent potential is connected to the working electrode, resulting in a current over time measurement. The difference between the amperometric and voltametric modes is the use of a potential step instead of a potential sweep. Using the amperometric mode will provide more selectivity and sensitivity since the reduction or oxidation potential utilized in the determination is normal for the analyte sample [26].

In this review, the discussion of sensing modes for the electrochemical sensor will be focused on impedimetric and voltametric modes. It will be start with an introduction followed by a description in detail, then the practical impacts of these modes on the electrochemical sensors will be discussed. We aim to present and highlight how these sensing modes can contribute to rationalizing the optimization of PPy based conducting polymers in electrochemical sensor applications.

2. Impedimetric Sensing Mode

In order to describe the response of a PPy based conducting polymer electrochemical sensor towards a low amplitude sinusoidal perturbation as a function of frequency, the impedimetric sensing mode will be used. Impedimetric mode, also known as impedance, is a circuit's ability to measure the resistance towards the flow of an electrical current. To measure the impedance, an electrochemical impedance spectroscope (EIS) is used with the application of a small sinusoidal potential to the working electrode in an electrochemical cell, while measuring the resulting current response. By varying the excitation frequency, *f*, of the applied potential over a range of frequencies, one can calculate the complex impedance, i.e., the sum of the system's real and imaginary impedance components as a function of the frequency (i.e., angular frequency *w*). The results of the impedance measurement can be graphically demonstrated using the Nyquist (Cole–Cole) and Bode plot for all the applied frequencies with the real part of the impedance Z plotted along the *x*-axis and imaginary part plotted along *y*-axis in the latter [27].

2.1. Nyquist Plot

The Nyquist plot is a plot where the imaginary impedance $Z''(\omega)$ is plotted against real impedance $Z'(\omega)$. Generally, the resistance value can directly obtain from Ohm's law as shown in Equation (1), where the resistance is the ratio between voltage, *E*, and current, *I*.

$$R = \frac{E}{I} \tag{1}$$

It assumes an ideal resistor. An ideal resistor occurs when it follows the Ohm's law at all voltage and current levels, where the resistance value is independent of frequency and when AC voltage and current signals are in phase with each other while going through the resistor. However, this does not always happen because in reality, circuit behavior is far more complicated. Therefore, in this concept, the impedance element is much more suitable for use rather than simple resistance to explain the changes measured in the circuit. Impedance is a frequency-dependent measurement of the opposition to current flow in an electric circuit. Impedance measurement is performed by applying an AC excitation voltage to an unknown system while measuring the current. The ratio of the excitation voltage to the current gives the complex impedance of the system.

The first step after impedance measurement is done is the graphical representation from the experimental data. The data from the impedance measurement will consist of three main components which are the real and imaginary impedance, and the frequency. These data will then be represented in Cartesian coordinates as shown in Equation (2):

$$Z(i\omega_i) = Z'_i + iZ''_i \tag{2}$$

Or in polar coordinates as shown in Equation (3):

$$Z(i\omega_i) = |Z_i|e^{i\varphi_i} \tag{3}$$

where $|Z_i| = \left(Z_i'^2 + Z_i''^2\right)^{1/2}$ is the modulus and $\varphi_i = tan^{-1}\left(Z_i''/Z_i'\right)$ is the phase, which corresponds to a given frequency.

The most common plot for impedance representation is based on Equation (2) which is a Nyquist plot with only one semicircle (Figure 3a). It shows the results from an electrical

equivalent circuit that is depicted in Figure 3b, which consists of a resistor and a capacitor in parallel. The direction of the frequency scanning is from high to low frequencies. At higher frequencies, the capacitor's impedance will be very low and a major part of the current will flow through the capacitor. With a decrease in the frequency, the capacitor's impedance increases and a bigger fraction of the current will then flow through the resistor. When most of the current flows through the resistor, the total imaginary resistance Z'' will drop as the real part Z' increases. Sometimes, the plot may consist of several semicircles or only a portion of a semicircle (Figure 3c,e). The different semicircles represent different electrical equivalent circuits and are shown in Figure 3d,f.

(a)

(b)

(c)

(d)

(e)

(f)

Figure 3. *Cont.*

Nyquist Diagram (-Im[Z] vs. Re[Z])

$$Z(f) = R_1 + \frac{\sqrt{2}\,\sigma_1}{\sqrt{j2\pi f}}$$
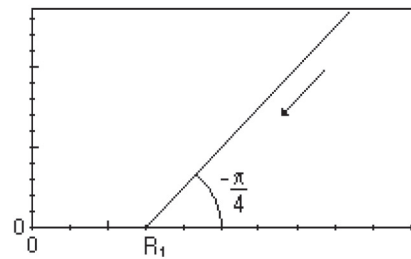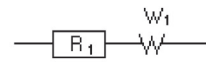
(g)   (h)

Figure 3. Nyquist plot with one semircircle and its equivalent circuit (**a,b**); two semicircles and its equivalent circuit (**c,d**); one semircircle with spike (45°) and its equivalent circuit (**e,f**); only spike (45°) and its electrical equivalent circuit (**g,h**) [28].

The equivalent circuit derived from the plot could then be used to analyze changes or the effects on the electrochemical sensor system that was added or modified. Besides that, the charge transfer resistivity, R_{ct}, also can be obtained from the Nyquist plot. For example, Ramanavicius et al. described an immunosensing system model based on the bovine leukemia virus (BLV) protein (gp51) entrapped within electrochemically synthesized polypyrrole (PPy/gp51). They reported that another element was present in the blood serum sample after it was treated as detected in the fitted equivalent circuit. This was due to the slightly increased measurement of the real part of the impedance spectrum (resistivity increased). It was explained that an additional layer occurred outside the polypyrrole film and proved that the treatment was successful [29]. Devi et al. reported that R_{ct} value was increased with the addition of xanthine oxidase (XOD) in a Zn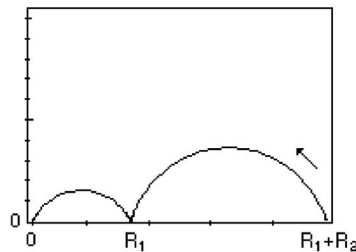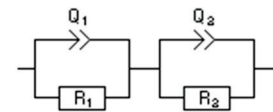O-NPs/PPy/Pt electrode, which is due to the immobilization of XOD onto the ZnO-NPs/PPy/Pt surface. It proved that the use of nanocomposites and PPy electrodeposited on the Pt surface electrode as a support for the immobilization of XOD resulted in an improvement of the xanthine biosensor performance with a detection limit of 0.8 μM [30]. Meanwhile, Chen et al. used impedance analysis to evaluate the charge separation efficiency of a PPy based photoelectrochemical sensor. There were two semicircles obtained from the impedance curve when Cu_2O was added on top of the ITO electrode. The semicircles known as Rct were then reduced to one and became smaller when fabricated with and without Microcystin-LR and $LiClO_4$ as template molecules during the electropolymerization process. As R_{ct} become smaller, the charge transfer efficiency become higher [31]. Furthermore, Bao et al. electrodeposited gold nanoparticles/polypyrrole-reduced graphene oxide nanocomposites (Au/PPy-rGO) on top of a bare glass carbon electrode (GCE) in order to produce excellent sensing performance for mRNA-16. The R_{ct} from a small semicircle (bare GCE) was decreased to almost a straight line (after electrodepositing) in the impedance curve results. When it is being further assembled using catalyzed hairpin assembly (CHA), and hybridization chain reaction (HCR), the R_{ct} semicircle was greatly increased, demonstrating the successful CHA and HCR processes and the fact that more negatively charged DNA polymers were linked on the modified electrode [32]. Akshaya and co-workers researched a Palladium–Gold (PdAu) based electrochemical sensor which was developed by electrodepositing PdAu nanoparticles onto a Polypyrrole (PPy) modified carbon fiber paper (CFP) electrode. They found that with the modification of CFP using the PPy conducting polymer, the R_{ct} decreased, indicating the conducting nature of PPy. Then, with further electrodeposition of PdAu nanoparticles onto the PPy/CFP, the value of R_{ct} become significantly decreased. This confirmed the formation of a highly conducting electronic pathway at the electrode–electrolyte interface where Pd and Au nanoparticles facilitated electron transfer between the analyte and the electrode [33].

2.2. Bode Plot

Even though the Nyquist plot can give significant information on the resistance of the material used, it has one major shortcoming where it is unable to show the frequency used at the focal data point needed. Each point corresponds to a given frequency which is $\omega\ (s^{-1})$ or $f\ (Hz)$, where $\omega = 2\pi f$. Therefore, as an alternative, the data can be represented in a Bode plot by using Equation (3). Generally, the Bode plot provides a more comprehensible description of the electric systems' frequency-dependent behavior than the Nyquist plot, in which frequency values are not clear. In the Bode plot, the data are plotted with log of frequency on the *x*-axis and both the log of absolute value of the impedance ($|Z|$) and phase-shift (θ) on the *y*-axis (Figure 4) [34].
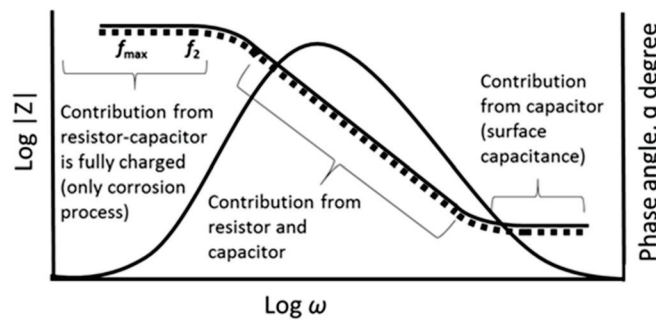
Figure 4. Bode plots of the frequency response (dotted line) and phase angle (solid line) for an electrochemical system.

A typical Bode plot is the same system as shown in Figure 2A. It is simpler to understand as there is only one semicircle that appears on the Nyquist plot. The log $|Z|$ versus log ω curve can be used to determine the values of R_p and R_Ω. At very high and very low frequencies, $|Z|$ becomes independent of frequency. At the highest frequencies, the ohmic resistance controls the impedance and log (R_Ω) can be read from the high frequency horizontal level. On the other hand, at the lowest frequencies, log $(R_p + R_\Omega)$ can be read from the low frequency horizontal portion [35].

Besides that, the Bode plot can also prove the number of semicircles present in the corresponding Nyquist plot. It can be seen from the shapes of the phase angle plots. For example, from the Nyquist plot, a smaller semicircle appears at higher frequencies, followed by second larger semicircle at medium frequencies and a Warburg diffusion effect in low frequencies (Figure 5a). Therefore, to confirm the presence of these two semicircles, the shape from the phase angle graph in the Bode plot will be used (Figure 5b). It can then be seen that the slope is somewhat broadened. Therefore, it proves that there is more than one semicircle present in the Nyquist plot.

(a) (b)
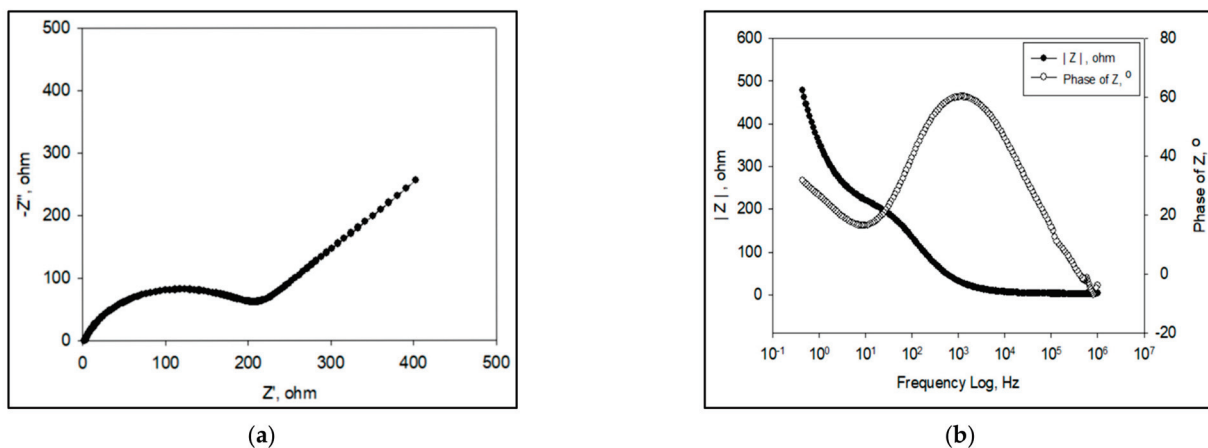
Figure 5. Nyquist plot with two semicircles (**a**) and Bode plot (**b**).

Lee et al. has researched a nicotine electrochemical sensor where a copper hexacyanoferrate-polypyrrole (CuHCF–PPy) nanocomposite was deposited directly onto reduced graphene oxide (rGO) by a direct self-assembly technique. From the impedance results, they obtained two semicircles in their Nyquist plot. This was expected and is due to the presence of two layers' of materials comprising of rGO and the metal layer (CuHCF) or metal-polymer layer (CuHCF-PPy) on the electrodes. Therefore, from the Bode plot, two phase angles were observed. The phase angle in the high (*f*1) frequency regions was attributed to the R_{ct} which happens across the electrode-electrolyte interface (CuHCF or CuHCF-PPy/solution). Meanwhile, the second phase angle (*f*2) was due to the CuHCF or CuHCF-PPy/rGO interface [36]. In research from a different perspective, Ratautaite et al. used Bode plots to evaluate the best frequency for further evaluation of capacity changes as a result of theophylline addition. They found that most sensitive impedance changes were in the frequency range from 10 Hz to 100 Hz. Therefore, in that frequency range, the capacitance changes at certain frequencies were further evaluated [37]. On the other hand, Al-Mokaram et al. used a Bode plot to study the frequency region of R_{ct} of modified electrode nanocomposite films consisting of polypyrrole-chitosan-titanium dioxide (Ppy-CS-TiO$_2$) in the development of a non-enzymatic glucose biosensor. It was found to collect in the frequency range of 0.01–10,000 Hz. The shifting of peaks toward the low frequency region of 1–0.01 Hz for composite and nanocomposite electrodes indicates the fast electron-transfer behavior of the nanocomposites (Figure 6). A perfect linear portion was observed at lower frequencies for the nanocomposite electrode compared to other electrodes. The results indicated that the Ppy-CS-TiO$_2$ nanocomposite was successfully designed and it facilitated a diffusion-limited process at the electrode-solution interface [38].
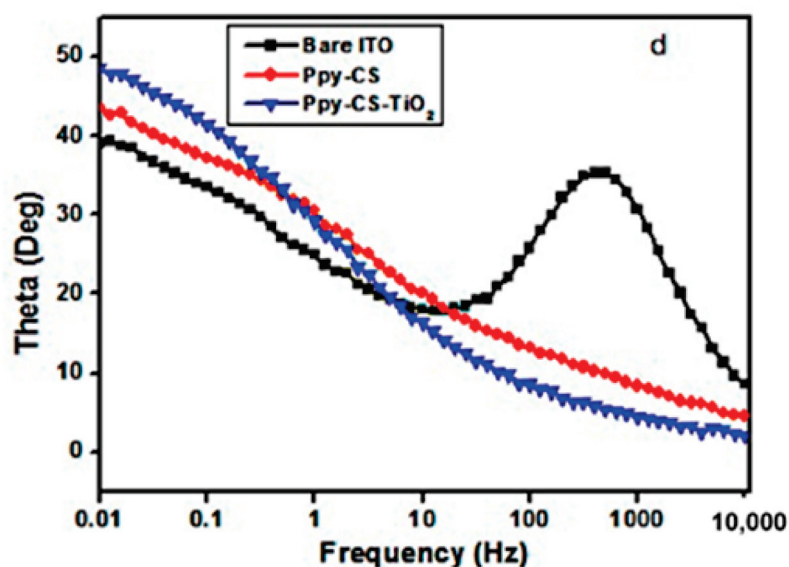
Figure 6. Bode phase plot for 1 mM K$_3$(Fe(CN)$_6$) in 0.1 M KCl at a scan rate of 50 mV s^{-1} vs. (Ag/AgCl) [38].

2.3. Dielectric Constant (ε_r)

Impedance measurements analysis can also provide data on the intrinsic dielectric constant and dielectric loss properties of an electrochemical sensor [39]. Dielectric studies are used to understand the mechanism of conduction and dielectric properties that may be valuable in developing a device's performance and in the design of the electronic devices. According to Ramesan and Santhi, who studied conducting polymer composites of polypyrrole (PPy) with different silver doped nickel oxide (Ag–NiO) nanocomposites, the dielectric constant was found to depend on the polarizability of dipoles in the direction of the applied field. From their results, they found that PPy exhibited a lower dielectric constant compared to all of the nanocomposites they studied [40]. Their argument was

supported by Anilkumar et al., who explained that the lower dielectric constant seen in conducting polymers may be attributed to the interfacial polarization of the composite materials. Interfacial polarization mainly arises from the electrical heterogeneities of the composite materials [41]. Strong interfacial interactions between the polymer and nanoparticles reduce the macromolecular chain's cohesive forces, which increases the dielectric constant of the composite. With further loading of the composites (>10 wt%) in the PPy matrix, it was found to decrease the dielectric constant. This is thought to be due to the formation of aggregates within the PPy matrix. They also found that the dielectric loss of composites is higher than that of PPy. The higher dielectric loss observed might be due to the high surface area, surface domain polarization and the quality of the electrical network formation [42]. With further loading of the composite, the dielectric loss was found to decrease. This may be due to the formation of clusters or discrete aggregates in the PPy matrix, which can prevent the migration of charge carriers through the polymer.

2.4. Dielectric Loss (tan δ)

Dielectric loss is represented by the dissipation factor (tan δ) which is the amount of dissipated energy or electrical loss by insulating material when a voltage is applied to the material [40]. The dielectric loss of a material is directly related to the electrical conductivity of the corresponding matrix. Usually, from the graph of dielectric loss, it always decreases as the frequencies are increased. This is attributed to the time lagging associated with the orientation of dipoles within the polymer matrix. Ramesan and Santhi also studied dielectric loss in their conducting polymer composite of polypyrrole (PPy) with different silver doped nickel oxide (Ag–NiO) content nanocomposite system and found that the tan δ of composites was higher than that of PPy alone. This was similar to their findings in the dielectric constant. Furthermore, when they increased the nanoparticle content, the tan δ value of the composite also increased. This may be due to the high surface area, surface domain polarization, and the quality of the electrical network formation. With further loading of nanocomposites (>10 wt%), the tan δ value was seen to decrease. This might be caused by the formation of clusters or discrete aggregates in the PPy matrix, which then prevented the migration of charge carriers through the polymer [40]. Besides that, Ramesan and co-workers also worked on different types of nanocomposite and polymer matrices. They studied poly (vinyl cinnamate) (PVCin) with different ratios of zinc oxide (ZnO). Their results showed a similar pattern to the other studies [43].

2.5. Impedimetric PPy Based Electrochemical Sensors and Biosensors

In most EIS studies that involve electrochemical sensors, the use of an electroactive probe/indicator has been employed to evaluate an electrode's signal activity. The advantage of using an electroactive probe is that it can serve as a reference point for impedance studies. For example, Arabali et al. fabricated an amplified tramadol electrochemical sensor based on the surface modification of pencil graphite electrode (PGE) by CuO nanoparticle (CuO-NPs) and polypyrrole (PPy). From the impedance results obtained, it confirmed the modification of PGE with PPy and PPy + CuO-NPs was able to improve the electrical conductivity of the sensor and exhibited a highly sensitive electroanalytical sensor for the determination of tramadol [44]. Furthermore, in humidity sensor applications, impedance analysis is commonly used to study the effect on a conducting polymer composite with various different compositions on the percentage of relative humidity measurement, RH%. Su et al. reported that the addition of PPy-Ag into pristine SnO_2 helped to reduce the impedance resistance, thereby increasing its sensitivity especially at low RH%. The study also proved that the impedance decreased as the amount of PPy-Ag increased. The addition of PPy-Ag helped to increase the mobility of solvated ions inside the system [45]. Meanwhile, Jlassi et al. reported that their findings did not follow this trend. They studied the effect of a combination PPy-Ag with modified halloysite nanoclay (HNT) films on RH% sensitivity at three different wt.% (0.25 wt.%, 0.5 wt.%, and 1 wt.%) amounts. The best finding was achieved using PPy-Ag 0.5 wt.% film due to its hydrophilic behavior. They

found that the impedance decreased as the humidity level increased. This is because the higher the humidity level, the higher the amount of moisture absorbed onto the PPy-Ag film, thereby increasing the conductivity of the film [46].

3. Voltametric Sensing Mode

Voltametric sensing mode is a measurement technique where a current is produced by sweeping the potential applied between a reference electrode and a conducting polymer or a conducting polymer modified electrode over a range that is associated with the redox reaction of the analyte [47,48]. It is also known as voltammetry analysis. There are a number of voltammetry techniques used which are described below.

3.1. Cyclic Voltammetry (CV)

One of the most powerful and popular voltammetry techniques used to investigate the reduction and oxidation processes of molecular species is cyclic voltammetry (CV). CV is an analysis to study electron transfer-initiated chemical reactions, which includes catalysis. Generally, a typical graph with a "duck" shaped curve will be obtained from CV analysis which is called a voltammogram or a cyclic voltammogram, as shown in Figure 7.
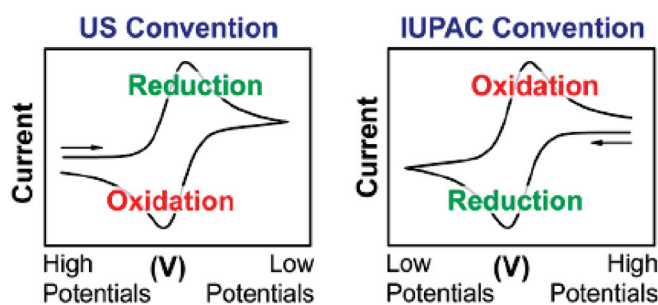
Figure 7. Examples of "duck" shaped cyclic voltammograms [49]. Reproduced with permission from [N. Elgrishi], [A Practical Beginner's Guide to Cyclic Voltammetry]; published by [ACS Publications], [2017].

From the graph, it can be seen that the *x*-axis represents the applied potential (*E*) that is imposed on the system; meanwhile, the *y*-axis is the resulting current (*i*) passed, which is the response during the measurement. Some direct information can be obtained from the CV graph, such as that at the potential axis (*x*-axis), it contains an arrow which indicates the direction of the scanned potential used to record the data. Besides that, it also indicates the beginning and sweep direction of the first segment (or "forward scan"). Sometimes, a crucial parameter also can be found in the graph which is scan rate (*v*). It indicates that the potential was varied linearly at the speed (scan rate) during the experiment: for example, *v* = 100 mV/s [49].

Figure 8 shows the "duck"-shaped voltammogram of a reversible reduction of 1 mM Fc^+ solution to Fc, at a scan rate of 100 mV/s. As the potential is scanned negatively (cathodically) from point A to point D, (Fc^+) is reduced to Fc and it is steadily depleted near the electrode. Simultaneously, a peak cathodic current ($i_{p,c}$) can be observed at point C [50]. It is dictated by the delivery of additional Fc^+ via diffusion from the bulk solution. The volume of solution at the surface of the electrode containing the reduced Fc, called the diffusion layer, continues to grow throughout the scan. This will then slow down the mass transport of Fc^+ to the electrode. Thus, upon scanning of more negative potentials, the diffusion rate of Fc^+ from the bulk solution to the electrode surface becomes slower, resulting in a decrease in the current as the scan continues (C→D). When it reaches the switching potential, D, the scan direction is reversed, and the potential is scanned in the positive (anodic) direction. While the concentration of Fc^+ at the electrode surface is depleted, the concentration of Fc at the electrode surface is increased, satisfying the Nernst equation. The Nernst equation (Equation (4)) can be used in order to predict how

a system will respond to a change of concentration of species in solution or a change in the electrode potential. The Fc presented at the electrode surface is oxidized back to Fc^+ as the applied potential becomes more positive. At points B and E, the concentrations of Fc^+ and Fc at the electrode surface are equal, following the Nernst equation, $E = E_{1/2}$. This corresponds to the halfway potential between the two observed peaks (C and F) and provides a straightforward way to estimate the $E^{0'}$ for a reversible electron transfer, as noted above. The two peaks are separated due to the diffusion of the analyte to and from the electrode.

$$E = E^0 + \frac{RT}{nF}ln\frac{(Ox)}{(Red)} = E^0 + 2.3026\frac{RT}{nF}log_{10}\frac{(Ox)}{(Red)} \tag{4}$$

Figure 8. Concentration profiles (mM) for Fc^+ (blue) and Fc (green) as a function of the distance from the electrode (D, from the electrode surface to the bulk solution, e.g., 0.5 mm) at various points during the voltammogram analysis [49]. (Current flow from A to G.) Reproduced with permission from [N. Elgrishi], [A Practical Beginner's Guide to Cyclic Voltammetry]; published by [ACS Publications], [2017].

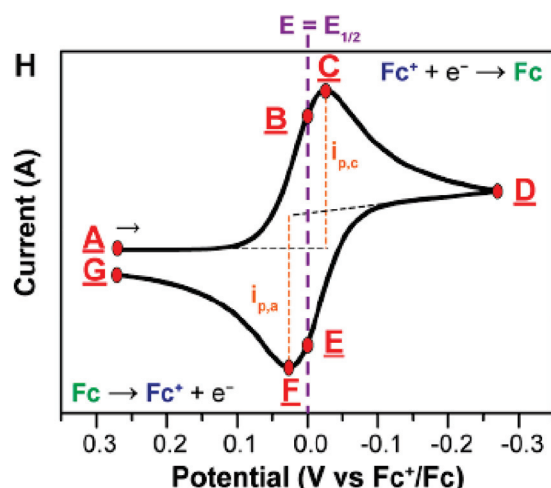Generally, in an electrochemical sensor, cyclic voltammetry is used to study the effect of a conducting polymer's modification towards its current intensity peak. Previously, Kwak et al. reported on the modification of PPy-base with carbon doped polydimethylsiloxane (PPy/ CPDMS). Their results showed current peaks during the reduction and oxidation exhibited at a voltage nearby 1.5 V and −1 V, respectively [51]. As the scan rate increases, the currents peak magnitude tends to increase due to the higher scan rate facilitating a thin diffusion layer between the electrolyte and the PPy surface [49]. However, as the scan rate was increased, the voltage at the corresponding current peaks were not identical during the redox reaction. This implied some degree of chemical irreversibility possibly caused by insufficient electron transfer because of the fast scan rate, or the decomposition of the PPy surface [52,53].

Zaabal et.al modified a glassy carbon electrode with polypyrrole (PPy/GCE) to be used as a promising electrode for electrochemical sensing of adefovir (ADV). They reported a weak anodic peak current obtained at 1.559 V for the unmodified electrode. By modifying the GCE with PPy, the anodic peak was shifted to a more negative potential which was 1.484 V accompanied by an enhancement in the peak height of ADV. The higher anodic response of ADV at the PPy/GCE electrode showed that this modified electrode was more sensitive than GCE alone. The enhanced signals and shift of potential peak towards the negative direction indicated that the modified electrode improves electrochemical reactivity of ADV oxidation as compared to bare GCE. This was probably mainly due to the large effective surface area and subtle electronic conductivity of PPy film, which was beneficial to promoting the electron transfer reaction [54].

Besides having a shift in potential axes, the changes in current peak also give important information; for example, in research done by Chen et al. [55] where they prepared a novel polypyrrole/glassy carbon electrode (PPy/GCE) core-zeolitic imidazolate framework-8 (ZIF-8) shell structure composite for quercetin (QR) determination. They found that the current peak of the QR sensor composed of ZIF-8/PPy/GCE was higher than the bare PPy/GCE electrode. It was due to a larger electrocatalytic surface obtained from ZIF-8 and high charge collectability of the host PPy [54]. A similar trend was observed by Hu at el. [56], where they prepared a novel electrochemical sensor based on ion imprinted polypyrrole and reduced graphene oxide (PPy/rGO) composite for trace level determination of cadmium ion (Cd(II)) in water. They found that with the addition of rGO into PPy/GCE, it increased the rate of electron transfer on the electrode surface and amplified the signal response [56].

Furthermore, Yu et al. developed a new electrochemical sensor based on titanium dioxide (TiO_2) and a PPy molecularly imprinted polymer (MIP) nanocomposite for the highly selective detection of p-nonylphenol in food samples. On just the bare GCE, a well-defined reversible redox peak could be observed. When the GCE was modified with PPy and TiO_2, the current intensity peak was obviously enhanced. It suggested that the modification could result in a larger electrochemical surface area, due to the cavities found in the PPy matrix which could accelerate electron transfer of $(Fe(CN)_6)^{3-/4-}$. After incubation with p-nonylphenol, the MIP absorbed p-nonylphenol molecules and blocked the cavities in the PPy matrix. Thus, the redox peak current intensity decreased as a result of the limitations of electron transfer. In contrast, the electrode modified with PPy and nanoimprinted TiO_2 exhibited a lower current intensity peak compared to PPy with TiO_2 MIP [57].

However, this was found to be different from the findings Ma et al., where they developed an electrochemical biosensor based on sodium alginate-polypyrrole/Au nanoparticles (SA-PPy/AuNPs) nanocomposite for the detection of miRNAs [58]. They reported that the current peak decreased after the modification of bare GCE. The redox peak current of $Fe(CN)_6^{4-/3-}$ slightly decreased due to the poor conductivity of SA and modified hair pin (H1). This could slow down the electron transfer on the surface of the electrode. The GCE/SA-PPy/AuNPs/H1 modified with miRNA-21 and modified hair pin (H2) formed a large number of double helix DNA structures on the surface of the electrode due to the occurrence of the CHA reaction, with a reduction in the redox peak current of $Fe(CN)_6^{4-/3-}$. Finally, a slight decrease in redox peak current was observed after the copper ion (Cu(II)) complex was inserted onto the double helix DNA structure. This could be attributed to the dissolution of the Cu(II) complex in the mixture of dimethyl sulfoxide (DMSO) and water (H_2O) (volume ratio 7:3). However, the observed poor solubility may have triggered a blockage of the electron transfer between the surface of the electrode and the electrolyte [58].

Besides conducting polymer modifications, the current peak of CV can also be affected by the concentration of a sample [30,59–61]. Zhang et al. designed and constructed an electrochemical ammonia sensor based on Ni foam-supported silver/polypyrrole and platinum nanoparticles electrode (Pt-Ag/PPy-NiF). They studied the effect of ammonia concentration on the oxidation current peak of the PPy/Pt/Ag/NiF electrode and found that its current peak increased when the ammonia concentration increases. This happened because of the strength of the synergistic effect between Ni foam and Pt nanoparticles [59]. Suvina et al. developed a polypyrrole-reduced graphene oxide hydrogel composite electrode for the detection of metal ions. They investigated the effect of metal ion concentration on the PPy-rGO hydrogel electrode and observed that the formation of a multilayer metal ion complex accumulated as a pre-deposited monolayer helped increase the peak current [61]. Meanwhile, Devi et al. prepared a mixture of PPy with synthesized zinc oxide nanoparticles (ZnO-NPs) which were then electropolymerized onto a platinum (Pt) electrode to form a ZnO-NPs–polypyrrole (PPy) composite film. Then, xanthine oxidase (XOD) was immobilized onto the nanocomposite film through physiosorption to study the effect

of XOD concentration on the ZnO-NPs/PPy/Pt electrode. They reported that the increases in oxidation current was due to the increased concentration of hydrogen peroxide (H_2O_2) produced during enzymatic reaction [30]. However, it is in contrast to Alagappan et al.'s study, which prepared an electrochemical cholesterol biosensor based on the cholesterol oxidase (ChOx) enzyme immobilized on a gold nanoparticle—functionalized -multiwalled carbon nanotube (MWCNT)—polypyrrole (PPy) nanocomposite modified electrode. They reported that the anodic and cathodic peak currents decreased with an increase in cholesterol concentration. This happened because of an absence of a redox mediator in the system which reduced the electron hopping from the analyte to the enzyme modified electrode [60].

Besides that, the potential difference between the anodic and the cathodic peaks also can be extracted from a cyclic voltammogram. Lo et al. prepared a PPy/CNT/NH_2-ITO composite by electropolymerization onto polypyrrole-aminophenyl-modified flexible indium tin oxide (PPy/NH_2/ITO) electrodes coated with multi-walled carbon nanotubes (CNTs), in the presence of ethylene glycol-bis(2-aminoethylether)-tetraacetic acid (EGTA) as a chelator. They reported that the potential difference of PPy films deposited onto bare ITO was 430 mV [62]. This was high compared to bare ITO which only exhibited 165 mV [63]. This difference can be linked to the absence of any adhesion between the PPy layer and the bare ITO surface. Meanwhile, in the case of PPy/NH_2-ITO, the presence of NH_2 on ITO contributed to an increase in electronic transfers leading to a lower ΔE (181 mV). For PPy/CNT/NH_2-ITO, ΔE = 321 mV. The CVs were consistent with those obtained by impedance measurement.

Pineda et al. [64] investigated the effect of polymerization time on the potential and current peak on polypyrrole (PPy) films with a micro tubular structure decorated with gold nanoparticles. The result showed that the anodic current peak from the voltammogram of the PPy film exhibited a cauliflower-like structure, occurring at 0.05 V, and there was found a small cathodic peak at −0.8 V that was led by a small hump at −0.5 V. Furthermore, these anodic and cathodic current peaks were well-defined at ca. 0.28 V and −0.45 V, respectively, as the electropolymerisation time was increased and the tubular structure was formed. This shows that the tubular structure exhibited a better separation between the faradaic and capacitive contributions in a polymeric deposited film [64].

Another aspect that can be studied through cyclic voltammogram is electrocatalytic behavizr [65,66]. Xing et al. studied the electrocatalytic behavior of polypyrrole/platinum (PPy/Pt) nanocomposites toward hydrogen peroxide (H_2O_2) reduction. They found that in the absence of H_2O_2, no reduction peak was observed with bare glassy carbon electrode (GCE), PPy/GCE, and PPy/Pt/GCE. Upon the addition of H_2O_2, no obvious current from the reduction of H_2O_2 was observed at bare GCE other than a minor increase in the background current. While only a weak reduction peak for H_2O_2 at about −0.28 V was observed on the PPy/GCE electrode, in contrast, on the PPy/Pt/GCE electrode, there was a remarkable reduction peak of H_2O_2 obtained of around −0.2V. This was even higher than the bare Pt electrode in terms of reduction peak current value, indicating that the PPy/Pt/GCE might provide a better electrocatalytic effect than the bare Pt electrode [65].

The electrocatalytic oxidation of an adenine and guanine mixture at bare and modified PPy/graphene/GCE electrodes were studied by Gao et al. [66]. They reported that there was no oxidation signal observed in the CV curves of the PPy/graphene/GCE electrode due to a blocking effect but there was a high current peak observed with the modified PPy/graphene/GCE electrode. The report also concluded that the overoxidized polypyrrole/graphene/glassy carbon electrode (PPyox/graphene/GCE) electrode had the highest current peak of adenine and guanine oxidation which indicated the highest electrocatalytic activity [66].

3.2. Limit of Detection (LOD)

Voltammetry can be used to obtain quantitative information which is deduced from peak current intensity [48]. Usually, it is used to determine the sensitivity value of the sensor.

Sensitivity, analytical sensitivity, functional sensitivity, lower limit of detection (LOD), etc., are terms used to describe the smallest concentration of a measure that can be measured (detected) with statistical significance employing a given analytical procedure [67]. It is also defined as the minimum input quantity that can be distinguished with more than 99% reliability [68]. *LOD* is also a valuable quantitative measurement usually in the healthcare industry where it can be used as a biomarker in the detection of disease, environmental pollutants such as heavy metals, and other chemical contaminants that are part of the environmental liability in contemporary societies [69]. The value of the *LOD* can be determined through calculation using Equation (5).

The equation to calculate the *LOD* is:

$$LOD = \frac{3 \times SD}{m} \tag{5}$$

where *SD* is the magnitude of the error bar at blank while *m* is the slope of the calibration curve of the blank [69]. Before it can be calculated, a graph of current or current density with different concentrations of the sensing material needs to be plotted (Figure 9a).
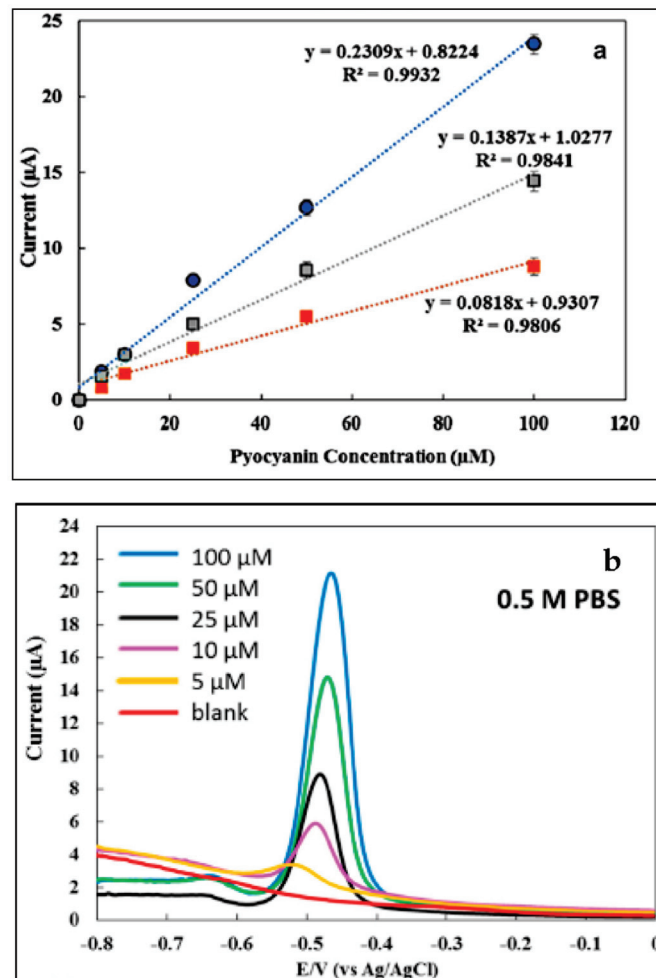
Figure 9. Example graphs of current response with different concentrations of pyocyanin biomarker using a DPV analyzer where the calibration curve for the three different mediums (0.5 M PBS at pH 7.4 (blue), human urine (grey) and human saliva (red)) at the potential range of −0.8 V to 0 V (**a**) and DPV current response of pyocyanin (5–100 μM) in 0.5 M PBS (**b**) [70]. Reproduced with permission from [J.I.A.Rashid], [An electrochemical sensor based on gold nanoparticles-functionalized reduced graphene oxide screen printed electrode for the detection of pyocyanin biomarker in Pseudomonas aeruginosa infection]; published by [Elsevier], [2020].

The current peak (i_p) value can be obtained either from the peak of a cyclic voltammogram (CV), differential pulse voltammogram (DPV), or square wave voltammogram (SWV). Most researchers use DPV and SWV to determine the current peak (Figure 9b). This is because of the high sensitivity of the technique compared to CV. In general, CV can provide essential information, such as the reversibility process and types of redox processes present in an analysis (matrix, analyte, and electrode); however, DPV and SWV are used for quantitative determinations [71].

3.3. Differential Pulse Voltammogram (DPV)

DPV is a technique that involves applying amplitude potential pulses on a linear ramp potential. In DPV, a base potential value is chosen at which there is no faradaic reaction and is then applied to the electrode. The base potential is increased between pulses with equal increments. The current is immediately measured before the pulse application and at the end of the pulse, and the difference between them is recorded (Figure 10). DPV is similar to the first derivative of a linear voltammogram in which the formation of a peak is observed for a given redox process. In the linear sweep technique, it has a shape similar to a wave, and the first derivative originates a peak.
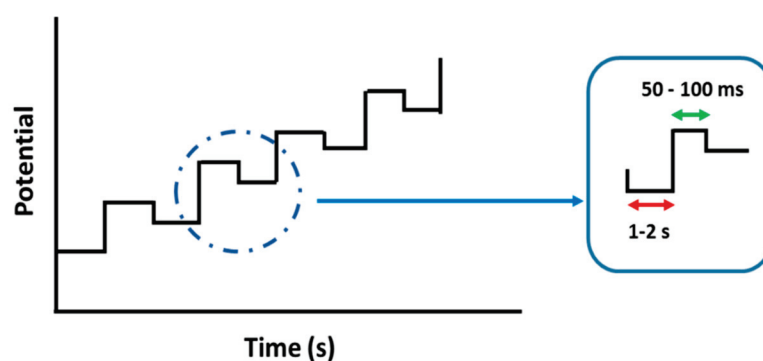
Figure 10. Diagram of the application of pulses in differential pulse voltammetry (DPV).

As in polarography (dropping mercury electrode), the qualitative information of an analyte is given by its half-wave potential ($E_{1/2}$), which corresponds to the potential at half the wave height. Similarly, in DPV, the peak potential, E_p, can be approximately identified through $E_{1/2}$. Increasing the irreversibility, E_p deviates from $E_{1/2}$ as the base of the peak widens and its height decreases. The DPV is therefore a graph of differences between measured currents and applied potentials as shown in Figure 9b [69,72].

3.4. Square Wave Voltammogram (SWV)

Meanwhile, SWV is the fastest and the most sensitive pulse voltammetry technique. The detection limits can be compared with those of chromatographic and spectroscopic techniques. In addition, the analysis of the characteristic parameters of this technique also enables the evaluation of the kinetics and mechanism of the electrode process under study [71,73]. According to Marie et al., the lower limit of detection value means the lowest concentration of glucose (analyte) that can be detected by the device [74].

Zhang et al. constructed an aqueous ammonia sensor using a low cost, high sensitivity, and great stability construct based on Ni foam-supported silver/polypyrrole and platinum nanoparticles electrode (Pt-Ag/PPy-NiF). They found that the ammonia sensor showed a sensitivity of 0.089 mA μM^{-1} with a detection limit of 37 nM and a wide linear range, as well as possessing a good anti-interference capability against many common ions found in water. The Pt-Ag/PPy-NiF electrode possessed a lower detection limit and higher sensitivity compared to most electrochemical aqueous ammonia sensors. Its excellent performance can be mainly attributed to the large specific surface area of the electrode and great electrocatalytic ability of Pt nanoparticles [59].

Salunke et al. prepared a sensor device by electrodepositing gold nanoparticles onto a single PPy nanowire for arsenic detection. They found that the sensitivity of Au-NPs decorated Ppy-NW towards arsenic (for two set of as conc. range) was 0.22 and 4.38 μM^{-1} with a good detection limit of 0.32 μM. Their result was better in respect of sensitivity and LOD, and this could be due to the change in sensor dimensions where they used nanowire as a base material and the gold nanoparticles as the sensing material. This led to the finding of a high surface area as being a dimension factor for the enhancement of sensor sensitivity with rapid detection and accuracy [75].

In other work done by Zaabal et al., they studied a polypyrrole modified glassy carbon electrode (PPy/GCE) for the electrochemical sensing of adefovir (ADV). ADV is a broad-spectrum antiviral agent whose action is as a DNA polymerase inhibitor. The detection limit of ADV obtained was 3.10 nM. Moreover, they also determined ADV in human serum and urine and found that the detection limit was 0.06 μM and 0.04 μM, respectively. Their detection limit value was much lower compared to the findings in other research works [76,77]. This showed that PPy/GCE can be an effective alternative sensor for the electrochemical determination of ADV in commercial pharmaceutical dosage forms and biological fluids.

3.5. PPy Based Voltammetric Sensor

In order to develop sensitive detection instruments, different signal amplification strategies also can be utilized to improve the sensitivity of the sensors used. Ma et al. designed an ultrasensitive and specific electrochemical biosensor for the determination of miRNAs based on SA-PPy/AuNPs. It was analyzed using the SWV technique with a dual signal amplification strategy involving the catalytic hairpin assembly (CHA) reaction and Cu^{2+}/Fe^{3+} catalytic reaction [58]. They found that, with the usage of this dual signal amplification strategy and a sensitive analyzer technique, which was SWV, the LOD value was significantly improved and could be as low as 0.34 fM compared to other research work [78–81]. Table 1 shows the comparison of different methods and signal amplification strategies with miRNA-21 as the target. The CHA reaction was triggered and numerous double helix-DNA were formed in the presence of the target miRNA. Furthermore, the intercalated planar Cu (II) complex could bind with the double-helix DNA, which was employed as a signal amplification molecule in the presence of Fe^{3+}. After the dual signal amplification, the reduction of the Cu (II) complex was recorded to represent miRNA levels.

Table 1. Comparison of different methods and signal amplification strategies with miRNA-21 as the target.

Detection Method	Signal Amplification Strategy	LOD Value	References
Fluorescence	Ligase mediated amplification	314 fM	Chan et al. [80]
DPV	$Fe(CN)_6^{3+}$	10 fM	Low et al. [79]
Chemiluminescence	Cascade enzyme catalytic reaction	1 fM	He et al. [81]
DPV	CHA reaction and RCA	13.5 fM	Wang et al. [78]
SWV	CHA reaction and Cu^{2+}/Fe^{3+} catalytic reaction	0.34 fM	Ma et al. [58]

Table 2 summarizes the electrochemical sensing modes of PPy based electrochemical sensors reviewed in this paper with their possible applications.

Table 2. Summary of electrochemical sensing modes of PPy-based electrochemical sensors with their applications.

Material	Modification/Improvement	Electrochemical Sensing Mode	Application	References
- PPy	SnO_2 Ag-SnO_2	Impedimetric	Humidity sensor	Su et al. 2020 [45]
PPy	Ag (0.5 wt.%)-HNT-DMA	Impedimetric	Humidity sensor	Jlassi et al. 2020 [46]
PPy PPy PPy	ITO NH_2-ITO CNT-NH_2-ITO	Impedimetric Voltammetric	Lead ion detector	Lo et al. 2020 [62]
PPy	MIP(UA)	Impedimetric	Electrochemical quartz crystal microbalance-based sensor	Plausinaitis et al. 2020 [82]
PPy	GCE GCE-SA-AuNPs	Impedimetric Voltammetric	Dectector for miRNA-21	Ma et al. 2020 [58]
PPy PPy	CFP CFP CFP-PdAu	Impedimetric Voltammetric	MMA detector	Akshaya et al. 2020 [31]
PPy	GCE	Voltammetric	Electrochemical sensing of Adefovir	Zaabal et al. 2020 [54]
PPy	Pt-Ag-NiF	Voltammetric	Aqueous ammonia sensor	Zhang et al. 2020 [59]
PPy	Carbon doped polydimethylsiloxane	Impedimetric Voltammetric	Resistive sensor	Kwak et al. 2019 [51]
PPy PPy PPy	GCE TiO_2-MIP-Nafion-GCE TiO_2-MIP-Nafion-GCE in 0.1mM p-nonylphenol NP-TiO_2-MIP-Nafion-GCE TiO_2 NIP/Nafion/GCE	Impedimetric Voltammetric	Food sensor: p-nonylphenol analysis (milk powder)	Yu et al. 2019 [57]
PPy PPy	CuHCF CuHCF rGO rGO-CuHCF rGO-CuHCF	Impedimetric voltammetric	Nicotine detector	Lee et al. 2019 [36]
PPy	SS-Au	Impedimetric voltammetric	Detection of hydroxylamine, nitrite and their mixture	Pineda et al. 2018 [64]
PPy PPy	GCE ZIF-8 nanoparticle ZIF-8 nanoparticle	Impedimetric voltammetric	Quercetin detector	Chen et al. 2019 [55]
PPy	rGO-GCE	Voltammetric	Cadmium detector	Hu et al. 2019 [56]
PPy	GCE Au-rGO-GCE	Impedimetric Voltammetric	Biosensor: microRNA detector	Bao et al. 2019 [32]
PPy	MCM-41	Impedimetric	Humidity sensor	Qi et al. 2018 [83]
PPy PPy PPy	GCE GCE GCE- Au-*f*-MWCNT Au-*f*-MWCNT-ChO*x*-GCE	Impedimetric Voltammetric	Biosensor for cholesterol detection	Alagappan et al. 2018 [60]
PPy PPy PPy	Cu_2O-ITO NIP-Cu_2O-ITO MIP-Cu_2O-ITO	Impedimetric	Imprinted PEC sensor	Chen et al. 2018 [31]
PPy	rGO hydrogel	Voltammetric	Metal ions sensor	Suvina et al. 2018 [61]
Ppy	Au-NPs-NW	Voltammetric	Arsenic detector	Salunke et al. 2017 [75]
PPy PPy	Pt nanocomposite Pt-GCE	Voltammetric	Non-enzymatic electrochemical sensor	Xing et al. 2015 [65]
PPyox	Gr nanocomposite-GCE	Voltammetric	DNA & RNA sensor: detection of adenine and guanine	Gao et al. 2014 [66]
PPy PPy PPy PPy	Pt Pt ZnO-NPs-Pt XOD-ZnO-NPs-Pt	Impedimetric Voltammetric	Xanthine biosensor	Devi et al. 2011 [30]

4. Conclusions

This review presents an overview of the two main electrochemical sensing modes used with electrochemical sensors based on PPy conducting polymers and outlines the significant advances in this field. In this review, the PPy heterocyclic-based conducting polymer was chosen due to its good environmental stability, high electronic conductivity, and biocompatibility. Conducting polymers are considered good sensitive materials for the development of selective, specific, and stable sensing devices. However, having PPy alone as the conducting polymer might not give the best results for an electrochemical sensor or biosensor application. Therefore, modification of the conducting polymer is the way to enhance its properties. To get an in-depth overview of how the modification can improve electrochemical and biosensors, the two main electrochemical techniques, impedimetric and voltametric, should be utilized. From this review, it can be seen that these two techniques play an important role in order to determine the resistivity, reactivity, and sensitivity of the PPy based conducting polymers for use in electrochemical sensors and biosensors. Besides that, they can also help the understanding of the reactivity that occurs when modification of the PPy conducting polymer has been done.

References

1. Tsakova, V.; Seeber, R. Conducting polymers in electrochemical sensing: Factors influencing the electroanalytical signal. *Anal. Bioanal. Chem.* **2016**, *408*, 7231–7241. [CrossRef]
2. Wegner, G. Polymers with Metal-Like Conductivity—A Review of their Synthesis, Structure and Properties. *Angew. Chem. Int. Ed. Engl.* **1981**, *20*, 361–381. [CrossRef]
3. Bashir, S.; Ramesh, S.; Ramesh, K.; Numan, A.; Iqbalc, J. *Conducting Polymer Composites in Electrochemical Sensors*; Central West Publishing: Orange, Australia, 2018.
4. Wang, X.; Gu, X.; Yuan, C.; Chen, S.; Zhang, P.; Zhang, T.; Yao, J.; Chen, F.; Chen, G. Evaluation of biocompatibility of polypyrrole in vitro and in vivo. *J. Biomed. Mater. Res.* **2004**, *68*, 411–422. [CrossRef]
5. Ansari, R. Polypyrrole conducting electroactive polymers: Synthesis and stability studies. *J. Chem.* **2006**, *3*, 186–201. [CrossRef]
6. Gupta, V.K.; Yola, M.L.; Özaltın, N.; Atar, N.; Üstündağ, Z.; Uzun, L. Molecular imprinted polypyrrole modified glassy carbon electrode for the determination of tobramycin. *Electrochim. Acta* **2013**, *112*, 37–43. [CrossRef]
7. Zaabal, M.; Doulache, M.; Bakirhan, N.K.; Kaddour, S.; Saidat, B.; Ozkan, S.A. A facile strategy for construction of sensor for detection of ondansetron and investigation of its redox behavior and thermodynamic parameters. *Electroanalysis* **2019**, *31*, 1279–1290. [CrossRef]
8. Apetrei, C. Novel method based on polypyrrole-modified sensors and emulsions for the evaluation of bitterness in extra virgin olive oils. *Food Res. Int.* **2012**, *48*, 673–680. [CrossRef]
9. Ramanaviciene, A.; Ramanavicius, A. Pulsed amperometric detection of DNA with an ssDNA/polypyrrole-modified electrode. *Anal. Bioanal. Chem.* **2004**, *379*, 287–293. [CrossRef]
10. Viau, L.; Hihn, J.; Lakard, S.; Moutarlier, V.; Flaud, V.; Lakard, B. Full characterization of polypyrrole thin films electrosynthesized in room temperature ionic liquids, water or acetonitrile. *Electrochim. Acta* **2014**, *137*, 298–310. [CrossRef]
11. Li, M.; Zhu, H.; Mao, X.; Xiao, W.; Wang, D. Electropolymerization of polypyrrole at the three-phase interline: Influence of polymerization conditions. *Electrochim. Acta* **2013**, *92*, 108–116. [CrossRef]
12. Nautiyal, A.; Qiao, M.; Cook, J.E.; Zhang, X.; Huang, T.-S. High performance polypyrrole coating for corrosion protection and biocidal applications. *Appl. Surf. Sci.* **2018**, *427*, 922–930. [CrossRef]

13. Wang, J.; Chen, J.; Wang, C.; Zhou, D.; Too, C.O.; Wallace, G.G. Electrochemical synthesis of polypyrrole films using stainless steel mesh as substrate for battery application. *Synth. Met.* **2005**, *153*, 117–120. [CrossRef]
14. Dubal, D.; Patil, S.; Jagadale, A.; Lokhande, C. Two step novel chemical synthesis of polypyrrole nanoplates for supercapacitor application. *J. Alloy. Compd.* **2011**, *509*, 8183–8188. [CrossRef]
15. Yusoff, N. Graphene–Polymer Modified Electrochemical Sensors. In *Graphene-Based Electrochemical Sensors for Biomolecules*; Elsevier B.V.: Amsterdam, The Netherlands, 2019; pp. 155–186.
16. Hosseini, S.H.; Entezami, A.A. Conducting polymer blends of polypyrrole with polyvinyl acetate, polystyrene, and polyvinyl chloride based toxic gas sensors. *J. Appl. Polym. Sci.* **2003**, *90*, 49–62. [CrossRef]
17. Song, Y.; Bian, C.; Hu, J.; Li, Y.; Tong, J.; Sun, J.; Gao, G.; Xia, S. Porous polypyrrole/graphene oxide functionalized with carboxyl composite for electrochemical sensor of trace cadmium (II). *J. Electrochem. Soc.* **2019**, *166*, B95. [CrossRef]
18. Hassanein, A.; Salahuddin, N.; Matsuda, A.; Kawamura, G.; Elfiky, M. Fabrication of biosensor based on Chitosan-ZnO/Polypyrrole nanocomposite modified carbon paste electrode for electroanalytical application. *Mater. Sci. Eng. C* **2017**, *80*, 494–501. [CrossRef]
19. Tlili, C.; Korri-Youssoufi, H.; Ponsonnet, L.; Martelet, C.; Jaffrezic-Renault, N.J. Electrochemical impedance probing of DNA hybridisation on oligonucleotide-functionalised polypyrrole. *Talanta* **2005**, *68*, 131–137. [CrossRef]
20. Hsu, L.; Selvaganapathy, P.R.; Brash, J.; Fang, Q.; Xu, C.-Q.; Deen, M.J.; Chen, H. Development of a low-cost hemin-based dissolved oxygen sensor with anti-biofouling coating for water monitoring. *IEEE Sens. J.* **2014**, *14*, 3400–3407. [CrossRef]
21. Turner, A.; Karube, I.; Wilson, G.S. *Biosensors: Fundamentals and Applications*; Oxford University Press: New York, NY, USA, 1987.
22. Muguruma, H. Biosensors: Enzyme immobilization chemistry. In *Encyclopedia of Interfacial Chemistry: Surface Science and Electrochemistry*; Elsevier: Amsterdam, The Netherlands, 2018; pp. 64–71.
23. Antuña-Jiménez, D.; Díaz-Díaz, G.; Blanco-López, M.C.; Lobo-Castañón, M.J.; Miranda-Ordieres, A.J.; Tuñón-Blanco, P. Chapter 1—Molecularly Imprinted Electrochemical Sensors: Past, Present, and Future. In *Molecularly Imprinted Sensors*; Li, S., Ge, Y., Piletsky, S.A., Lunec, J., Eds.; Elsevier: Amsterdam, The Netherland, 2012; pp. 1–34.
24. Yang, L.; Guiseppi-Elie, A. Impedimetric Biosensors for Nano- and Microfluidics. In *Encyclopedia of Microfluidics and Nanofluidics*; Li, D., Ed.; Springer US: Boston, MA, USA, 2008; pp. 811–823.
25. Wang, B.; Wang, L.; Li, X.; Liu, Y.; Zhang, Z.; Hedrick, E.; Safe, S.; Qiu, J.; Lu, G.; Wang, S. Template-free fabrication of vertically-aligned polymer nanowire array on the flat-end tip for quantifying the single living cancer cells and nanosurface interaction. *Manuf. Lett.* **2018**, *16*, 27–31. [CrossRef]
26. Wang, J.; Musameh, M.; Lin, Y. Solubilization of carbon nanotubes by Nafion toward the preparation of amperometric biosensors. *J. Am. Chem. Soc.* **2003**, *125*, 2408–2409. [CrossRef]
27. Zia, A.I.; Syaifudin, A.M.; Mukhopadhyay, S.; Yu, P.; Al-Bahadly, I.H.; Gooneratne, C.P.; Kosel, J.; Liao, T.-S. Electrochemical Impedance Spectroscopy Based MEMS Sensors for Phthalates Detection in Water and Juices. *J. Phys. Conf. Ser. IOP Publ.* **2013**, *439*, 012026. [CrossRef]
28. Instruments, B.S. *EC-Lab Software V.10.40*; Bio-Logic-Science Instruments: Seyssinet-Pariset, France, 2007.
29. Ramanavicius, A.; Finkelsteinas, A.; Cesiulis, H.; Ramanaviciene, A. Electrochemical impedance spectroscopy of polypyrrole based electrochemical immunosensor. *Bioelectrochemistry* **2010**, *79*, 11–16. [CrossRef] [PubMed]
30. Devi, R.; Thakur, M.; Pundir, C. Construction and application of an amperometric xanthine biosensor based on zinc oxide nanoparticles–polypyrrole composite film. *Biosens. Bioelectron.* **2011**, *26*, 3420–3426. [CrossRef]
31. Chen, J.; Gao, P.; Wang, H.; Han, L.; Zhang, Y.; Wang, P.; Jia, N. A PPy/Cu_2O molecularly imprinted composite film-based visible light-responsive photoelectrochemical sensor for microcystin-LR. *J. Mater. Chem. C* **2018**, *6*, 3937–3944. [CrossRef]
32. Bao, J.; Hou, C.; Zhao, Y.; Geng, X.; Samalo, M.; Yang, H.; Bian, M.; Huo, D. An enzyme-free sensitive electrochemical microRNA-16 biosensor by applying a multiple signal amplification strategy based on Au/PPy–rGO nanocomposite as a substrate. *Talanta* **2019**, *196*, 329–336. [CrossRef]
33. Akshaya, K.; Anitha, V.; Nidhin, M.; Sudhakar, Y.; Louis, G. Electrochemical sensing of vitamin B12 deficiency marker methyl-malonic acid using PdAu-PPy tailored carbon fiber paper electrode. *Talanta* **2020**, *217*, 121028. [CrossRef]
34. Silverman, D.C. *Tutorial on Cyclic Potentiodynamic Polarization Technique*; United States: Washington, DC, USA, 1998.
35. Poursaee, A. Corrosion measurement and evaluation techniques of steel in concrete structures. In *Corrosion of Steel in Concrete Structures*; Woodhead Publishing: Southston, UK, 2016; pp. 169–191.
36. Lee, P.K.; Woi, P.M. Direct self-assembly of CuHCF-PPy nanocomposites on rGO for amperometric nicotine sensing at high concentration range. *J. Electroanal. Chem.* **2019**, *837*, 67–75. [CrossRef]
37. Ratautaite, V.; Janssens, S.D.; Haenen, K.; Nesládek, M.; Ramanaviciene, A.; Baleviciute, I.; Ramanavicius, A. Molecularly imprinted polypyrrole based impedimentric sensor for theophylline determination. *Electrochim. Acta* **2014**, *130*, 361–367. [CrossRef]
38. Al-Mokaram, A.; Amir, M.A.; Yahya, R.; Abdi, M.M.; Mahmud, H.N.M.E. The development of non-enzymatic glucose biosensors based on electrochemically prepared polypyrrole–chitosan–titanium dioxide nanocomposite films. *Nanomaterials* **2017**, *7*, 129. [CrossRef] [PubMed]
39. Sun, T.; Morgan, H. Impedance Measurements of Cells. In *Encyclopedia of Microfluidics and Nanofluidics*; Li, D., Ed.; Springer US: Boston, MA, USA, 2013; pp. 1–4.

40. Ramesan, M.; Santhi, V. Synthesis, characterization, conductivity and sensor application study of polypyrrole/silver doped nickel oxide nanocomposites. *Compos. Interfaces* **2018**, *25*, 725–741. [CrossRef]
41. Anilkumar, T.; Ramesan, M. Synthesis and Electrical Conductivity Studies of Metal Chloro and Nitroxide Group Containing Styrene Butadiene Rubber. *AIP Conf. Proc. Am. Inst. Phys.* **2014**, *1620*, 28–34.
42. Ramesan, M.T.; George, A.; Jayakrishnan, P.; Kalaprasad, G. Role of pumice particles in the thermal, electrical and mechanical properties of poly (vinyl alcohol)/poly (vinyl pyrrolidone) composites. *J. Therm. Anal. Calorim.* **2016**, *126*, 511–519. [CrossRef]
43. Ramesan, M.; Nidhisha, V.; Jayakrishnan, P. Synthesis, characterization and conducting properties of novel poly (vinyl cinnamate)/zinc oxide nanocomposites via in situ polymerization. *Mater. Sci. Semicond. Process.* **2017**, *63*, 253–260. [CrossRef]
44. Arabali, V.; Malekmohammadi, S.; Karimi, F. Surface amplification of pencil graphite electrode using CuO nanoparticle/polypyrrole nanocomposite; A powerful electrochemical strategy for determination of tramadol. *Microchem. J.* **2020**, *158*, 105179. [CrossRef]
45. Su, P.-G.; Lu, P.-H. Electrical and Humidity-Sensing Properties of Impedance-Type Humidity Sensors that Were Made of Ag Microwires/PPy/SnO2 Ternary Composites. *Chemosensors* **2020**, *8*, 92. [CrossRef]
46. Jlassi, K.; Mallick, S.; Mutahir, H.; Ahmad, Z.; Touati, F. Synthesis of In Situ Photoinduced Halloysite-Polypyrrole@ Silver Nanocomposite for the Potential Application in Humidity Sensors. *Nanomaterials* **2020**, *10*, 1426. [CrossRef] [PubMed]
47. Kissinger, P.; Heineman, W.R. *Laboratory Techniques in Electroanalytical Chemistry, Revised and Expanded*; CRC Press: New York, NY, USA, 2018.
48. Lakard, B. Electrochemical Biosensors Based on Conducting Polymers: A Review. *Appl. Sci.* **2020**, *10*, 6614. [CrossRef]
49. Elgrishi, N.; Rountree, K.J.; McCarthy, B.D.; Rountree, E.S.; Eisenhart, T.T.; Dempsey, J.L. A practical beginner's guide to cyclic voltammetry. *J. Chem. Educ.* **2018**, *95*, 197–206. [CrossRef]
50. Compton, R.G.; Banks, C.E. *Understanding Voltammetry*; World Scientific: Hackensack, NJ, USA; London, UK, 2018.
51. Kwak, B.; Bae, J. Integrated Design and Fabrication of a Conductive PDMS Sensor and Polypyrrole Actuator Composite. *IEEE Robot. Autom. Lett.* **2020**, *5*, 3753–3760. [CrossRef]
52. Espinoza, E.M.; Clark, J.A.; Soliman, J.; Derr, J.B.; Morales, M.; Vullev, V.I. Practical aspects of cyclic voltammetry: How to estimate reduction potentials when irreversibility prevails. *J. Electrochem. Soc.* **2019**, *166*, H3175. [CrossRef]
53. Brownson, D.A.; Banks, C.E. *The Handbook of Graphene Electrochemistry*; Springer: London, UK, 2014.
54. Zaabal, M.; Bakirhan, N.K.; Doulache, M.; Kaddour, S.; Saidat, B.; Ozkan, S.A. A New Approach on Sensitive Assay of Adefovir in Pharmaceutical and Biological Fluid Samples Using Polypyrrole Modified Glassy Carbon Electrode. *Sens. Actuators B Chem.* **2020**, *323*, 128657. [CrossRef]
55. Chen, Y.; Huang, W.; Chen, K.; Zhang, T.; Wang, Y.; Wang, J. Facile fabrication of electrochemical sensor based on novel core-shell PPy@ ZIF-8 structures: Enhanced charge collection for quercetin in human plasma samples. *Sens. Actuators B Chem.* **2019**, *290*, 434–442. [CrossRef]
56. Hu, S.; Gao, G.; Liu, Y.; Hu, J.; Song, Y.; Zou, X. An Electrochemical Sensor Based on ion Imprinted PPy/rGO Composite for Cd (II) Determination in Water. *Int. J. Electrochem. Sci.* **2019**, *14*, 11714–11730. [CrossRef]
57. Yu, M.; Wu, L.; Miao, J.; Wei, W.; Liu, A.; Liu, S. Titanium dioxide and polypyrrole molecularly imprinted polymer nanocomposites based electrochemical sensor for highly selective detection of p-nonylphenol. *Anal. Chim. Acta* **2019**, *1080*, 84–94. [CrossRef] [PubMed]
58. Ma, X.; Qian, K.; Ejeromedoghene, O.; Kandawa-Schulz, M.; Wang, Y. Electrochemical detection of microRNA based on SA-PPy/AuNPs nanocomposite with the signal amplification through catalytic hairpin assembly reaction and the spontaneous catalytic reaction of Fe^{3+}/Cu^{2+}. *Electrochim. Acta* **2020**, *362*, 137168. [CrossRef]
59. Zhang, L.; Liu, J.; Peng, X.; Cui, Q.; He, D.; Zhao, C.; Suo, H. Fabrication of a Ni foam-supported platinum nanoparticles-silver/polypyrrole electrode for aqueous ammonia sensing. *Synth. Met.* **2020**, *259*, 116257. [CrossRef]
60. Alagappan, M.; Immanuel, S.; Sivasubramanian, R.; Kandaswamy, A. Development of cholesterol biosensor using Au nanoparticles decorated f-MWCNT covered with polypyrrole network. *Arab. J. Chem.* **2020**, *13*, 2001–2010. [CrossRef]
61. Suvina, V.; Krishna, S.M.; Nagaraju, D.; Melo, J.; Balakrishna, R.G. Polypyrrole-reduced graphene oxide nanocomposite hydrogels: A promising electrode material for the simultaneous detection of multiple heavy metal ions. *Mater. Lett.* **2018**, *232*, 209–212. [CrossRef]
62. Lo, M.; Seydou, M.; Bensghaïer, A.; Pires, R.; Gningue-Sall, D.; Aaron, J.-J.; Mekhalif, Z.; Delhalle, J.; Chehimi, M.M. Polypyrrole-wrapped carbon nanotube composite films coated on diazonium-modified flexible ITO sheets for the electroanalysis of heavy metal ions. *Sensors* **2020**, *20*, 580. [CrossRef]
63. Lo, M.; Diaw, A.K.; Gningue-Sall, D.; Aaron, J.-J.; Oturan, M.A.; Chehimi, M.M. The role of diazonium interface chemistry in the design of high performance polypyrrole-coated flexible ITO sensing electrodes. *Electrochem. Commun.* **2017**, *77*, 14–18. [CrossRef]
64. Pineda, E.G.; Presa, M.R.; Gervasi, C.; Bolzán, A. Tubular-structured polypyrrole electrodes decorated with gold nanoparticles for electrochemical sensing. *J. Electroanal. Chem.* **2018**, *812*, 28–36. [CrossRef]
65. Xing, L.; Rong, Q.; Ma, Z. Non-enzymatic electrochemical sensing of hydrogen peroxide based on polypyrrole/platinum nanocomposites. *Sens. Actuators B Chem.* **2015**, *221*, 242–247. [CrossRef]
66. Gao, Y.-S.; Xu, J.-K.; Lu, L.-M.; Wu, L.-P.; Zhang, K.-X.; Nie, T.; Zhu, X.-F.; Wu, Y. Overoxidized polypyrrole/graphene nanocomposite with good electrochemical performance as novel electrode material for the detection of adenine and guanine. *Biosens. Bioelectron.* **2014**, *62*, 261–267. [CrossRef] [PubMed]

67. Armbruster, D.A.; Pry, T. Limit of blank, limit of detection and limit of quantitation. *Clin. Biochem. Rev.* **2008**, *29*, S49. [PubMed]

68. Guider, R.; Gandolfi, D.; Chalyan, T.; Pasquardini, L.; Samusenko, A.; Pederzolli, C.; Pucker, G.; Pavesi, L. Sensitivity and Limit of Detection of biosensors based on ring resonators. *Sens. Bio-Sens. Res.* **2015**, *6*, 99–102. [CrossRef]

69. Simões, F.R.; Xavier, M.G. Electrochemical Sensors. *Nanosci. Appl.* **2016**, 155–178.

70. Rashid, J.I.A.; Kannan, V.; Ahmad, M.H.; Mon, A.A.; Taufik, S.; Miskon, A.; Khim, O.K.; Yusof, N.A. An electrochemical sensor based on gold nanoparticles-functionalized reduced Graphene oxide screen printed electrode for the detection of Pyocyanin biomarker in Pseudomonas aeruginosa infection. *Mater. Sci. Eng. C* **2020**, *120*, 111625. [CrossRef] [PubMed]

71. Brett, A.M.O. Electrochemistry for probing DNA damage. In *Encyclopeida of Sensors*; Grimes, C.A., Dickey, E.C., Pishko, M.V., Eds.; American Scientific Publishers: Stevenson Ranch, CA, USA, 2006; pp. 1–14.

72. Brett, C.; Oliveira Brett, A.M. *Electrochemistry: Principles, Methods, and Applications*; Oxford University Press: New York, NY, USA, 1993.

73. De Souza, D.; Machado, S.; Avaca, L. Square wave voltammetry. Part 1: Theoretical aspects. *Quim. Nova* **2003**, *26*, 81–89.

74. Marie, M.; Mandal, S.; Manasreh, O. An electrochemical glucose sensor based on zinc oxide nanorods. *Sensors* **2015**, *15*, 18714–18723. [CrossRef]

75. Salunke, R.S.; Kasar, C.K.; Bangar, M.A.; Chavan, P.G.; Shirale, D.J. Electrodeposition of gold nanoparticles decorated single polypyrrole nanowire for arsenic detection in potable water: A chemiresistive sensor device. *J. Mater. Sci. Mater. Electron.* **2017**, *28*, 14672–14677. [CrossRef]

76. Hughes, W.T.; Shenep, J.L.; Rodman, J.H.; Fridland, A.; Willoughby, R.; Blanchard, S.; Purdue, L.; Coakley, D.F.; Cundy, K.C.; Culnane, M. Single-dose pharmacokinetics and safety of the oral antiviral compound adefovir dipivoxil in children infected with human immunodeficiency virus type 1. *Antimicrob. Agents Chemother.* **2000**, *44*, 1041–1046. [CrossRef] [PubMed]

77. Jain, R.; Sharma, R. Voltammetric quantification of anti-hepatitis drug Adefovir in biological matrix and pharmaceutical formulation. *J. Pharm. Anal.* **2012**, *2*, 98–104. [CrossRef] [PubMed]

78. Wang, S.; Lu, S.; Zhao, J.; Ye, J.; Huang, J.; Yang, X. An electric potential modulated cascade of catalyzed hairpin assembly and rolling chain amplification for microRNA detection. *Biosens. Bioelectron.* **2019**, *126*, 565–571. [CrossRef]

79. Low, S.S.; Pan, Y.; Ji, D.; Li, Y.; Lu, Y.; He, Y.; Chen, Q.; Liu, Q. Smartphone-based portable electrochemical biosensing system for detection of circulating microRNA-21 in saliva as a proof-of-concept. *Sens. Actuators B Chem.* **2020**, *308*, 127718.

80. Chan, H.-N.; Ho, S.-L.; He, D.; Li, H.-W. Direct and sensitive detection of circulating miRNA in human serum by ligase-mediated amplification. *Talanta* **2020**, *206*, 120217. [CrossRef]

81. He, C.; Chen, S.; Zhao, J.; Tian, J.; Zhao, S. Ultrasensitive detection of microRNA-21 based on electrophoresis assisted cascade chemiluminescence signal amplification for the identification of cancer cells. *Talanta* **2020**, *209*, 120505. [CrossRef]

82. Plausinaitis, D.; Sinkevicius, L.; Samukaite-Bubniene, U.; Ratautaite, V.; Ramanavicius, A. Evaluation of electrochemical quartz crystal microbalance based sensor modified by uric acid-imprinted polypyrrole. *Talanta* **2020**, *220*, 121414. [CrossRef] [PubMed]

83. Qi, R.; Lin, X.; Dai, J.; Zhao, H.; Liu, S.; Fei, T.; Zhang, T. Humidity sensors based on MCM-41/polypyrrole hybrid film via in-situ polymerization. *Sens. Actuators B Chem.* **2018**, *277*, 584–590. [CrossRef]

Article

Ion Mobility in Thick and Thin Poly-3,4 Ethylenedioxythiophene Films—From EQCM to Actuation

Rudolf Kiefer [1,*], Daniel Georg Weis [2,3], Bharath Kumar Velmurugan [4], Tarmo Tamm [5] and Gerald Urban [3,6]

1. Conducting Polymers in Composites and Applications Research Group, Faculty of Applied Sciences, Ton Duc Thang University, Ho Chi Minh City 700000, Vietnam
2. Institute of Physical Chemistry, Albert-Ludwigs-Universität Freiburg, Albertstraße 21, D-79104 Freiburg im Breisgau, Germany; dgweis@gmx.de
3. FMF—Freiburger Materialforschungszentrum, University of Freiburg, Stefan-Meier-Straße 21, D-79104 Freiburg im Breisgau, Germany; urban@imtek.de
4. Department of Medical Laboratory Science and Biotechnology, Asia University, Taichung 401, Taiwan; bharathvel@gmail.com
5. Intelligent Materials and Systems Lab., Faculty of Science and Technology, University of Tartu, Nooruse 1, 50411 Tartu, Estonia; tarmo.tamm@ut.ee
6. IMTEK—Institute for Microsystem Technology, Laboratory for Sensors, Georges-Koehler-Alle 103, D-79110 Freiburg im Breisgau, Germany
* Correspondence: rudolf.kiefer@tdtu.edu.vn; Tel.: +84-886-905605515

Abstract: Conductive polymer actuators and sensors rely on controlled ion transport coupled to a potential/charge change. In order to understand and control such devices, it is of paramount importance to understand the factors that determine ion flux at various conditions, including the synthesis potential. In this work, the ion transport in thinner poly-3,4-ethylenedioxythiophene (PEDOT) films during charge/discharge driven by cyclic voltammetry is studied by consideration of the electrochemical quartz crystal microbalance (EQCM) and the results are compared to the actuation responses of thicker films that have been synthesized with the same conditions in the bending and linear expansion modes. The effects of polymerization potentials of 1.0 V, 1.2 V, and 1.5 V are studied to elucidate how polymerization potential contributes to actuation, as well the involvement of the EQCM. In this work, it is revealed that there is a shift from anion-dominated to mixed to cation-dominated activity with increased synthesis potential. Scanning electron microscopy shows a decrease in porosity for the PEDOT structure with increasing synthesis potential. EQCM analysis of processes taking place at various potentials allows the determination of appropriate potential windows for increased control over devices.

Keywords: polymerization potentials; EQCM; cyclic voltammetry; ion flux

1. Introduction

For the last decade, a significant amount of research has been dedicated to conductive polymer (CP)-based actuators with bending [1,2] or linear [3,4] actuation modes (including fiber-based materials [5,6]) for applications in micro-actuators [7], biomedical devices [8], smart textiles [6,9], and more. Polypyrrole (PPy) has been a popular choice due to its typically higher strain or displacement output, as well as the possibility for electropolymerization in aqueous solutions, which presents suitability in biomedical [10] and biosensor [11] applications, among others [12]. Poly-3,4-ethylenedioxythiophene polystyrenesulfonate (PEDOT:PSS), also soluble in aqueous solutions has made a comeback with the growing popularity of 3D printing [13] in the field of soft robotics [14]. PEDOT, which is formed by electropolymerization, has not been as intensively studied for actuator materials as PPy, although it is well known for its high electrochemical activity, conductivity, and stability [15].

It may seem strange that while so much work has been dedicated to the development of CP actuators, with a plethora of ideas and prototypes published, real applications are still lacking. The main reason for this appears to be a limited control over materials. With only small changes, such as the solvent [16], electrolyte [17], electrochemical polymerization techniques, or temperature [18], one can obtain CP films with rather different actuation properties, including the given actuation direction. The simplified mechanism of CP response (such as PPy or PEDOT) refers to the Faradaic processes where mobile charges are formed on polymer chains in CP films upon oxidation, which immediately creates a force that causes counterions provided by the electrolyte (with or without a solvent) to approach the chains. The influx of ions and the solvent into the polymer film leads to a change in volume, i.e., undergo expansion. Upon reduction, the charges on the chains are reduced and the counterions (with solvents) leave the polymer film, causing the film to shrink, i.e., undergo contraction. In an ideal case, we have only one mobile ion species that triggers the actuation, which could be either anion-driven or, if immobile anions stayed in the CP, cation-driven. In the latter case, this results in expansion upon reduction (known for PPy/DBS [19], as well as PEDOT/CF_3SO_3 [20] and PEDOT:PSS [21]); however, mixed-species actuation is observed in real materials and over wider potential windows, for instance, in the case of PEDOT/PF_6 films [22,23], which can be observed to experience less intensive expansion upon reduction or oxidation.

In order to move from labs and prototypes to real applications, it is of paramount importance to fundamentally understand the factors governing the mobility of ionic species in CP films and their coupling with a polymer. Since PEDOT has enjoyed significantly less attention, we focus on this material here. The electrochemical quartz crystal microbalance (EQCM) has been shown to be an indispensable property for studying mobile species in CP films [24]; however, due to the entailing viscoelastic effects, an increasing film thickness that is meaningful for use as an actuator in EQCM studies cannot be reliably analyzed [25]. Consequently, only thin films are investigated with EQCM techniques.

Both linear (freestanding) and bending (as bilayers) actuators are considered here with PEDOT deposited under a range of different polymerization potentials. Their behaviors are compared to the EQCM results for thinner films that were prepared under the same conditions. Tetrabutylammonium-hexafluorophosphate (TBAPF$_6$) in propylene carbonate (PC) was chosen as the electrolyte here, which is an electrolyte that usually results in a mixed ion activity. To the best of our knowledge, this is the first time a comparative study of the EQCM and actuation behavior has been presented for PEDOT films.

SEM and EDX spectroscopy are used to provide additional information for the PEDOT-FF (PEDOT free standing films) samples and all electrochemical experiments (including electro-synthesis) are carried out in triplicate.

2. Material and Methods

2.1. Chemicals

Polyethylene terephthalate (PET, thickness of 12 μm) foil was obtained from Ecoplast LLC (Khmelnitskiy, Ukraine) and was used as supplied. AT-cut quartz crystals (5 MHz) of a 15 mm diameter were obtained from KVG Quartz Crystal Technology GmbH (Neckarbischofsheim, Germany). Propylene carbonate (PC, 99%), ethanol (technical grade), 3,4-ethylendioxythiophene (EDOT, 97%), and tetrabutylammonium-hexafluorophosphate (TBAPF$_6$, 99.9%) were purchased from Sigma-Aldrich (Taufkirchen, Germany) and were used as supplied.

2.2. Electropolymerization

The PEDOT films were potentiostatically polymerized (CH Instruments Inc., electrochemical workstation Model 440C, Austin, TX, USA) at polymerization potentials of 1.0 V, 1.2 V, and 1.5 V in a 0.1 M EDOT solution with a 0.1 M TBAPF$_6$-PC electrolyte applied for the actuator devices and EQCM studies. The three-electrode setup consisted of a stainless steel plate (4.5 cm^2 with one side covered with tape to assure PEDOT deposition on only

one side), Ag/AgCl (3 M KCl) as the reference electrode, and a platinum counter electrode (18 cm^2) positioned opposite to the stainless steel plate. The polymerization was carried out under a nitrogen atmosphere at room temperature (25 °C). The PEDOT freestanding films (PEDOT-FF) were removed from the stainless steel electrode and washed several times with PC to remove excess monomers and electrolytes and was then stored for further use with a 0.1 M TBAPF$_6$-PC electrolyte. Different deposition times were applied to compensate for the growth rate of the PEDOT-FF, which depended heavily on the polymerization potential. The polymerization conditions are presented in Table 1.

Table 1. Polymerization parameters of PEDOT-BL and PEDOT-FF with the polymerization time t_P, charge density Q, current density j (by the effect of polymerization potentials), and thickness d.

E_P (V)	t_P (min)		Q (mC cm^{-2})		j (mA cm^{-2})		d (µm)	
	BL	FF	BL	FF	BL	FF	BL	FF
1.0	228 ± 14	327 ±22	333 ± 22	356 ± 21	0.05 ± 0.003	0.06 ± 0.004	4.3 ± 0.4	33 ± 3
1.2	5.2 ± 0.3	8.8 ± 0.4	365 ± 22	378 ± 27	1.46 ± 0.1	1.6 ± 0.1	4.8 ± 0.5	34 ± 2
1.5	0.9 ± 0.1	1.2 ± 0.1	367 ± 30	386 ± 32	6.73 ± 0.4	7.8 ± 0.5	5.2 ± 0.4	38 ± 3

For the bending actuators of the PEDOT-PET bilayers (PEDOT-BL), the PET was sputtered with 100 nm of platinum on one side (resistivity of 400 Ω/sq) and then cut into a strip that was 1.5 cm in length and 0.5 cm in width. The strip was connected as the working electrode and was immersed in the monomer solution with a free length of 1.2 cm. The Pt-PET strip, as a working electrode, was fixed in a polymerization cell (0.1 M EDOT, 0.1 M TBAPF$_6$ in PC at 25 °C under a nitrogen atmosphere) and PEDOT was deposited potentiostatically using a HEKA PG 28 potentiostat/galvanostat (HEKA Electronic GmbH, Reutlingen, Germany). The deposition of PEDOT was monitored and stopped after a charge of 200 mC (~340 mC cm^{-2}) was reached for each polymerization. After polymerization, the PEDOT-BL was discharged in the monomer solution at 0.0 V for 10 min. For each PEDOT-BL or PEDOT-FF sample, at least three independent polymerizations were carried out and the values given in Table 1 are mean values with standard deviations. The PEDOT-BL and PEDOT-FF samples were washed several times in PC to remove the monomer and electrolyte and were then dried in an oven at 60 °C (2 mbar) for 12 h.

2.3. Actuation Measurements

For PEDOT-FF, an in-house linear actuation measurement device was applied and was controlled by in-house software [26] to connect the change of length with the electrochemical signals in real time. The PEDOT-FF samples were cut into lengths of 1.2 cm with a width of 0.4 cm and were fixed between the force sensor and a lower static clamp (free length between clamps of 4 mm at constant force of 9.8 mN) with gold contacts. The PEDOT-FF was set as the working electrode with an Ag/AgCl (3M KCl) reference electrode and a platinum sheet (18 cm^2) as a counter electrode in a three-electrode cell. Electrochemical measurements via cyclic voltammetry (scan rate 5 mV s^{-1} at ±1 V) and square wave potential steps (0.017 Hz, 0.8 V to 0 V, for long term cycling) were taken with the use of a 0.1 M TBAPF$_6$ –PC electrolyte.

PEDOT-BL samples (as working electrode) were fixed in a three-electrode quadratic cell with a 0.1 M TBAPF$_6$-PC with Ag/AgCl (3 M KCl) reference electrode and a platinum sheet as a counter electrode. The electrochemical measurements were controlled by a Jaissle potentiostat (Type 1002 PC.T, IPS Elektroniklabor GmbH & Co. KG, Münster, Germany). The movement of the bilayer over a background of millimeter paper was recorded with a CCD camera (EHD kam06, EHD Imaging GmbH, Damme, Germany) connected to a PC-installed frame grabber card (The Imaging Source DFG/LC1) during the electrochemical measurements (cyclic voltammetry and square potential steps as above). From each recorded movement of the PEDOT-BL, images from the video (captured at

25 frames/s) were extracted and the displacement was read at the tip with a careful selection criterion of measuring samples which did not twist in an out-of-plane direction during the actuation.

2.4. EQCM Measurements

The working principle of the electrochemical quartz crystal microbalance (EQCM) [27] is based on an inverse piezoelectric effect with a quartz crystal working at its resonance frequency. The changes in the mass of the deposited conductive polymer can be determined during reversible redox cycles (ions and solvent exchanged) by the frequency change. The cut AT crystal, with a 15 mm diameter (oscillation area 0.28 cm^2), was coated on both sides with a thin layer (20 nm) of chromium to improve the stability of the following platinum layer that was in the range of 60 nm and was coated via vacuum deposition. The platinum-coated quartz was clamped between two O-rings with one side facing the solution and the other side facing air. An Amel potentiostat (Amel model 533, Milano, Italy) was used to control a three-electrode cell with the platinum-coated quartz as the working electrode, an Ag/AgCl wire reference electrode, and a platinum mesh as a counter electrode. Measurement and data collection was performed with in-house software with a Hameg HM 2122 frequency counter (HAMEG Instruments GmbH, Mainhausen, Germany) connected to an IEEE-488 interface bus (Hewlett-Packard, Palto Alto, CA, USA). The potentiostatic polymerizations (1.0 V, 1.2 V, and 1.5 V) took place in a monomer solution under an argon atmosphere (0.1 M EDOT, 0.1 M TBAPF$_6$ in propylene carbonate), until the resonance frequency decreased by 5 kHz, which corresponds to a mass addition of 14 µg (i.e., a film thickness in range of 400–500 nm). After polymerization, the polymeric layer was discharged at 0.0 V in the monomer solution. Cyclic voltammetry of the PEDOT-deposited quartz at different polymerization potentials (scan rate 10 mV s^{-1}) was performed in an electrolyte solution (0.1 M TBAPF$_6$ in PC) and the changes in frequency (mass) during reversible redox cycles with a potential range of ±1.0 V were recorded. The correlation of frequency change (Δf) to mass change (Δm) in an electrochemical process, with a good linear approximation with a constant C_{QMW} value (gravimetrical proportionality constant), is given in by the Sauerbrey equation (Equation (1)) [28].

$$\Delta m = C_{QMW} \cdot \Delta f \tag{1}$$

The relationship between the changes of mass on the electroactive surface (Δm^{el}, g) to changes of charge (ΔQ, C) is shown in Equation (2) as the modified faradaic law.

$$\Delta Q = n \cdot z \cdot F = z \cdot F \cdot \frac{\Delta m^{el}}{M_R} \tag{2}$$

where F is the Faraday constant (96,492 C mol^{-1}), n is the mole number, z is the number for electrons, and M_R (g mol^{-1}) is the molar mass change in the reaction. It needs to be considered that the active surface (A) between the conductive polymer (PEDOT) A_{el} and the AT quartz crystal (A_{osc} with mass change Δm_{osc}) can be different. As such, Equation (3) denotes the densities of those surfaces ($\rho = \Delta m_{el}/A_{el} = \Delta m_{osc}/A_{osc}$), leading to linear dependence between the change of frequency Δf to the change of charge ΔQ:

$$\Delta f = \frac{M}{z \cdot F \cdot C_{QMW}} \cdot \frac{A_{osc}}{A_{el}} \cdot \Delta Q = \frac{M}{z} \cdot C_{EQMW} \cdot \Delta Q \tag{3}$$

The electrogravimetric proportionality constant C_{EQMW} [29] is a product from the gravimetric proportionality constant C$_{QMW}$, the Faraday constant, and the quotient of surfaces A_{osc}/A_{el}. The equation relates to univalent anions/cations, and, as such, the value for "z" is 1. The term C$_{EQCM}$ is influenced by the experimental setup and must be calibrated (i.e., measured) using metal deposition for a known thickness of Cr and Pt, as well as the area of the electrically oscillated surface (A_{el} = 30.8 mm^2, A_{osc} = 27.38 mm^2), the density of the quartz (ρ_Q = 2.65 10^6 g m^{-3}), the speed of the shear wave (v_Q = 3340 m s^{-1}), and

the resonance frequency (f_Q = 5 MHz), which, in our case, led to a value for C_{EQMW} of -1.98 mol Hz g^{-1}mC^{-1} and -4.85 ng Hz^{-1} for the gravimetric proportionality constant C_{QMW}. The change of frequency Δf against charge ΔQ led to a specific curve where several positions of the slope could be determined, where division by C_{EQMW} yields the molecular weight of the charge compensating species M_{CCS} (Equation (4)).

$$\frac{\Delta f}{\Delta Q} = \frac{slope}{C_{EQMW}} = M_{CCS} \tag{4}$$

2.5. Characterization

Scanning electron microscopy (SEM) and energy dispersive X-ray spectroscopy (EDX) (Philips XL30-FEG, Philips Electron Optics, Hillsboro, OR, USA) of the PEDOT-BL surfaces at 5 kV were used for analysis after polymerization with the samples that were washed and dried. To obtain better images in the SEM measurement, the samples were sputtered with a thin layer of gold in the range of 20 nm. EDX spectroscopy of the PEDOT-BL samples was carried out at the end of the actuation cycles in an oxidized state at 1.0 V for 5 min and in a reduced state at -1.0 V for 5 min. The surface conductivity values of PEDOT-FF and PEDOT-BL were measured using a 4-point probe conductivity meter (Jandle 4-Point Probe Head, Model RM2, Leighton Buzzard, UK).

3. Results and Discussions

The polymerization potential of any conductive polymer is a key factor that influences the properties of the obtained material, including the conductivity, redox activity, ion exchange, and overall actuation. This is illustrated by the linear and bending PEDOT actuators in this work, as the deposition potential is known to influence the PEDOT ion exchange and actuator behavior [23], potentially even playing a role in the actuation direction. In order to make a distinction between the ionic species and the solvent, EQCM measurements were gathered for PEDOT deposited under the same conditions but with a thinner film.

3.1. SEM and EDX Spectroscopy of PEDOT Samples

Figure 1a–c present SEM surface images of the PEDOT-BL samples deposited at different polymerization potentials.

All the films showed surfaces that were rather open and highly porous, while those for the lowest polymerization potential of 1.0 V had the most structured and porous appearances and became somewhat more fused and compacted with a higher polymerization potential; however, there were many more distinct differences for the general smoothness, which was significantly higher for the E_p 1.0 V material, where the surface became rougher with an increasing synthesis potential. This has been demonstrated before in [23,30]. With a higher polymerization potential, the driving force for the reaction is increased, which means the polymerization time is shorter (Table 1). As a result, PEDOT deposition at a higher potential is more greatly controlled by kinetic factors, leading to less ordered polymer films, and the films also become more brittle with a higher polymerization potential. This likely occurs due to increased crosslinking and other bond formation errors. In general, PEDOT is well known for being less sensitive to overoxidation in comparison to polypyrrole due to the substitution of β-carbons. The conductivity results for PEDOT-BL and PEDOT-FF at different polymerization potentials, E_P, are presented in Table 2.
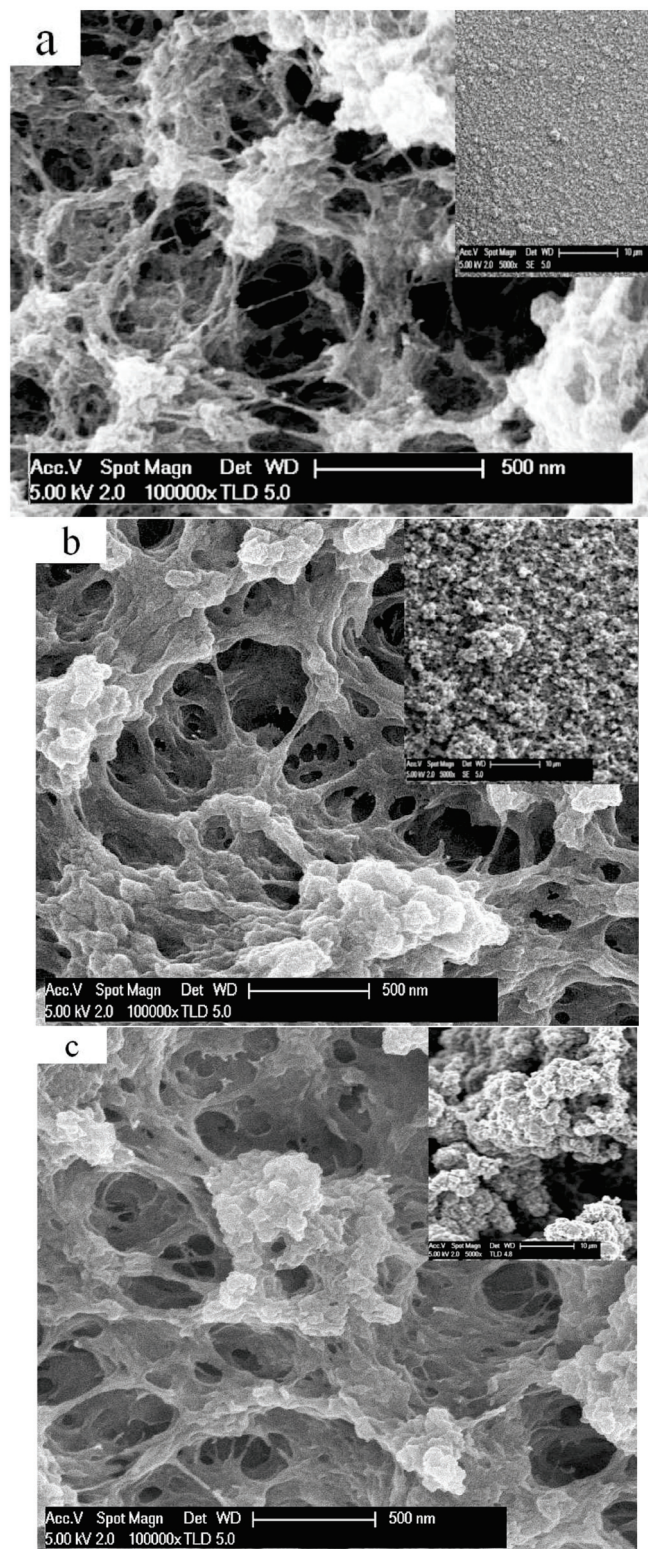
Figure 1. SEM surface images (scale bar denotes 500 nm) with insets (scale bar denotes 10 μm) of PEDOT-BL deposited at different polymerization potentials, E_P, in a TBAPF$_6$-PC electrolyte. (**a**) E_P of 1.0 V; (**b**) E_P of 1.2 V; (**c**) E_P of 1.5 V.

Table 2. Surface conductivities of PEDOT-BL and PEDOT-FF when polymerized at different potentials in an oxidized state.

E_P	PEDOT-FF (S cm^{-1})	PEDOT-BL (S cm^{-1})
1.0 V	6.4 ± 0.6	15.8 ± 1.2
1.2 V	3.5 ± 0.3	8.8 ± 0.7
1.5 V	2.5 ± 0.2	5.9 ± 0.5

While it is difficult to directly compare the conductivities of PEDOT-FF to PEDOT-BL due to the different thicknesses, as well as the presence of the Pt layer on the back side of the bilayer, it can be clearly seen that conductivity decreases with an increased deposition potential for both materials. Moreover, the differences are steeper for 1.0 V to 1.2 V than from 1.2 to 1.5 V. As seen above in the SEM micrographs, a sharper difference in the structure was found as a result, as is also the case for the former potential range. Apparently, the transition from thermodynamic control to kinetic control of the formation process takes place primarily in that potential range, at least under the conditions chosen here.

To determine which ions accompanied the redox switching, EDX spectroscopy was carried out in oxidized and reduced states, and the results are presented in Figure 2a,b, respectively.
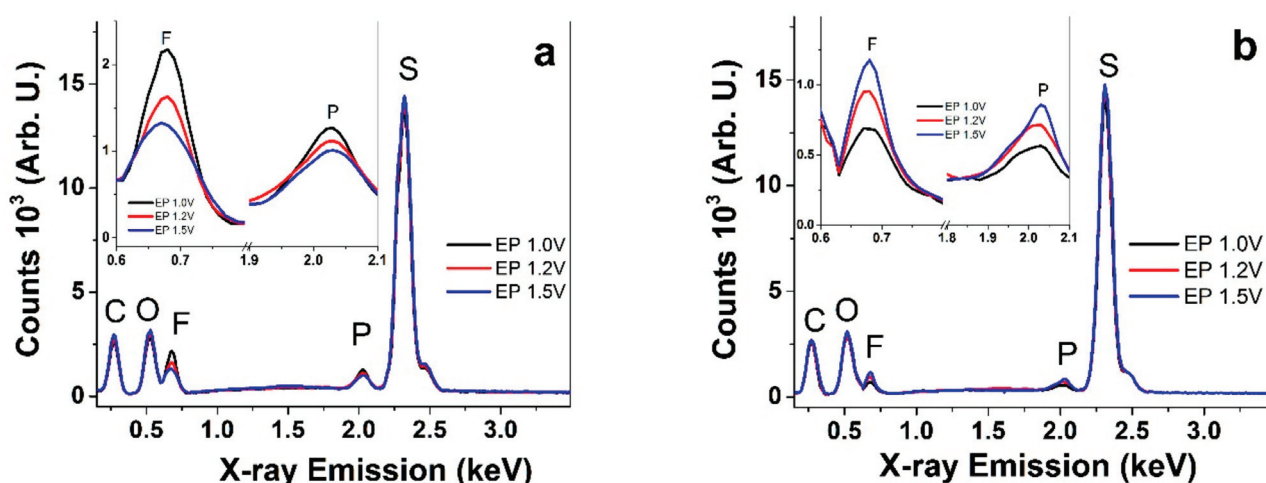
Figure 2. EDX spectra after actuation cycles for PEDOT-BL polymerized at different potentials where E_P = 1.0 V (black), E_P = 1.2 V (red), and E_P = 1.5 V (blue). The insets denote the enhanced peaks of fluorine and phosphorous. (**a**) Oxidized films (polarized 5 min at 1.0 V). (**b**) Reduced films (-1.0 V, 5 min).

The typical peaks for PEDOT films are found at 0.26 keV for carbon (C), 0.52 keV for oxygen (O), 0.67 keV for fluorine (F), 2.04 keV for phosphorous (P), and a strong peak for sulfur (S) at 2.32 keV. The relatively strong peaks of sulfur (PEDOT ring) and oxygen (the dioxy bridge in PEDOT) did not change during oxidation or reduction (Figure 2a,b). The fluorine and phosphorous peaks refer to the anion PF$_6^-$ from TBAPF$_6$. The nitrogen peak from the cation TBA$^+$, found in general at 0.38 keV, was not resolved in the spectra, instead being fused with the strong carbon and oxygen peaks. The insets in Figure 2a,b emphasize the changes in the fluorine and phosphorous peaks, revealing that the fluorine and phosphorous peaks were strong upon oxidation and decreased with an increased polymerization potential. The fluorine peak decreased significantly upon reduction; however, the order was now reversed, with the peak intensity increasing with the synthesis potential. Overall, the spectra indicate that some of the anions are trapped in the films, with

immobilization increasing with an increasing deposition potential. Cations must balance the charge in such cases, thereby resulting in mixed-mode ion transport and actuation.

### 3.2. Cyclic Voltammetry Driven Ion Exchange

Cyclic voltammetric measurements in the voltage range of ± 1.0 V for PEDOT-FF and PEDOT-BL deposited at different polymerization potentials were gathered to investigate the response behaviors with a TBAPF$_6$-PC electrolyte. Cyclic voltammetry is the optimal method to analyze redox cycles, whereas the CV shapes and the concurrent actuation response can help to identify oxidation/reduction processes and ion flux caused by a change in volume. By avoiding overoxidation and overreduction, the charging/discharging coulovoltammetric responses showed closed loops, corresponding to a steady state condition [31] (charging/discharging in balance) (Figure S1a,b).

3.2.1. PEDOT Linear and Bending Actuation

While PEDOT was less sensitive towards the synthesis temperature than, for instance, polypyrrole, the PEDOT-FF polymerized at room temperature was stiff and brittle, which limits linear actuation in comparison to other samples prepared at low temperatures. The curves of the cyclic voltammetry (scan rate of 5 mV s^{-1}) for driven linear actuation, as well the bending displacement of PEDOT-BL, are presented in Figure 3a,b, respectively. The current density curves of the PEDOT-FF films are shown in Figure 3c and those of PEDOT-BL are presented in Figure 3d.

All the strain curves of PEDOT-FF (Figure 3a), as well as the bending displacement curves of PEDOT-BL (Figure 3b), which were deposited at different polymerization potentials, showed mixed actuation modes of expansion upon both oxidation and reduction; however, there was a clear tendency that with an increasing polymerization potential, the expansion upon oxidation decreased and the expansion upon reduction increased, corresponding to a shift from anion-dominated to cation-dominated activity. Taking into consideration that an increasing polymerization potential changes the morphology and compactness of PEDOT, the denser, less porous (Figure 1c), and more cross-linked PEDOT networks created at higher polymerization potentials would partly hinder the flux of the incorporated (solvated) PF$_6^-$ anions, thus limiting the rate and extent of the charge the anions can compensate for. Hence, the expansion upon reduction is a consequence of TBA$^+$ cation ingress to maintain electroneutrality. The trapped PF$_6^-$ anions remaining inside the polymer matrix during reduction can also lead to an increase in the osmotic pressure [32], influencing the solvent content, and thus the swelling during reduction. Another theory by Hillman et al. [33] states that solvent uptake during doping and de-doping depends on the solvent properties. The PC used here might be transported more easily in PEDOT due to its hydrophobic nature. In either case, the differences in the polymerization potentials clearly resulted in structure changes, which is the main factor for increased expansion upon reduction.

The current density of PEDOT-FF (Figure 3c) was much lower than that reached by PEDOT-BL (Figure 3d), which can be primarily explained with the 50% lower conductivity of the freestanding film when compared to the bilayer. In general, the curves share several common features and similar trends can be observed. The main oxidation peak, which is perhaps most clearly seen for the PEDOT-BL (Figure 3d), shifted from 0.21 V to 0.1 V to 0.07 V for films with E$_P$ values of 1.0 V, 1.2 V, and 1.5 V, respectively. This is consistent with the characteristic of increased cation activity. As peaks shifted towards cathodic potentials with an increasing PEDOT deposition potential, this also reduced in intensity, especially on the anodic side of the cycle. A very similar trend can be seen for the PEDOT-FF. The decreasing cycling current density with an increasing formation potential can be attributed to the decrease in conductivity (Table 2), but also to lower counterion mobility.
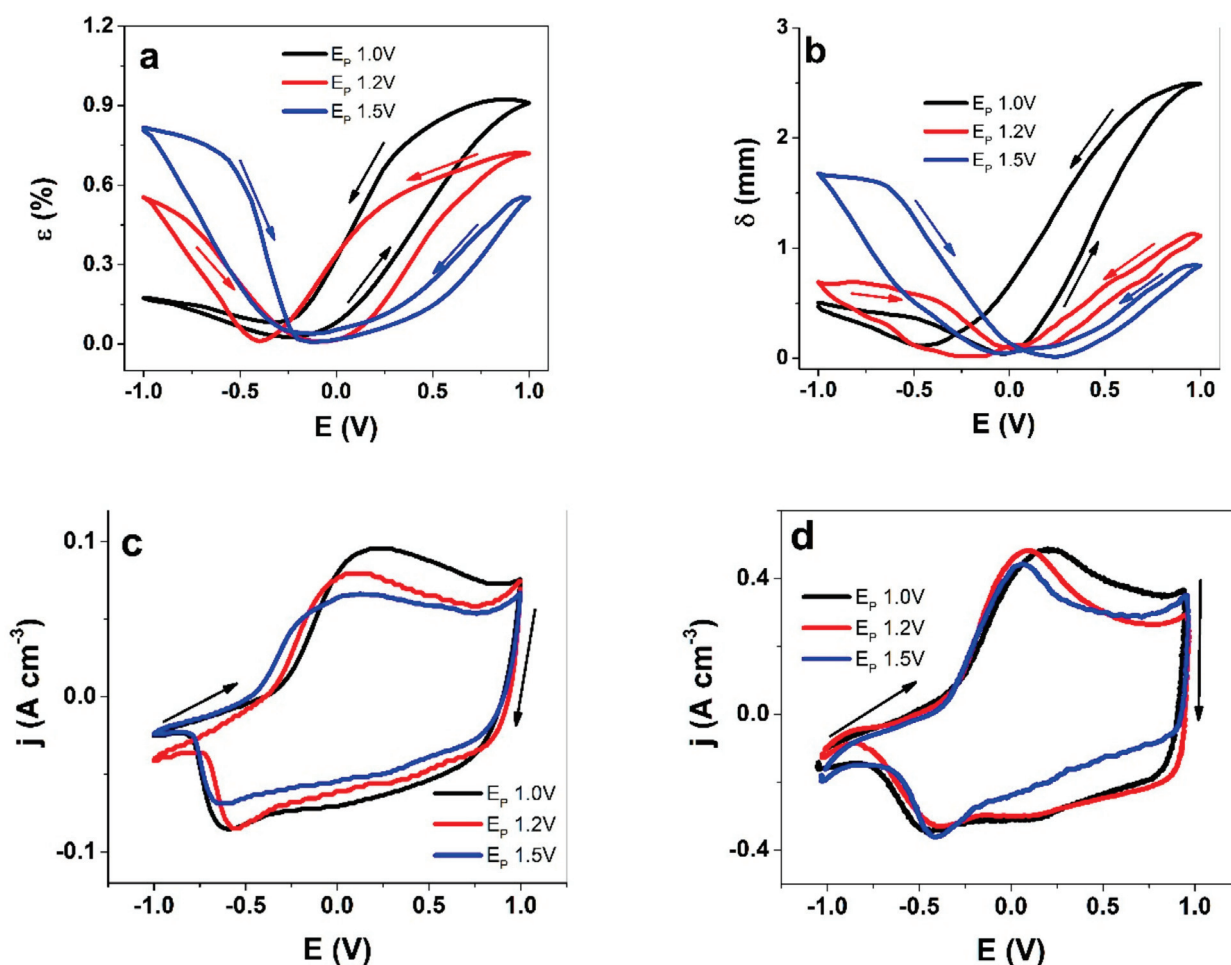
Figure 3. Actuation and current density responses of cyclic voltammetry (scan rate of 5 mV s^{-1}, 3rd cycle) for PEDOT samples polymerized at E$_P$ = 1.0 V (black line), E$_P$ = 1.2 V (red line), and E$_P$ = 1.5 V (blue line). (**a**) Strain (ε) for PEDOT-FF; (**b**) bending displacement (δ) of PEDOT-BL; (**c**) current density (j) of PEDOT-FF; (**d**) current density (j) of PEDOT-BL against the potential (E, ±1.0 V) in the electrolyte TBAPF$_6$-PC. The arrows indicate the scan direction (starting point of −1.0 V).

All of the charge density versus potential curves in Figure S1a,b represent closed cycles, indicating that charging/discharging was in balance for this potential range (±1 V) [31]. Table 3 compares the strain and bending displacement upon oxidation and reduction, as well as the charge densities of PEDOT-FF and PEDOT-BL.

Table 3. Strain ε, bending displacement δ upon oxidation (+1 V)/reduction (−1 V), and charge density Q as per cyclic voltammetry for PEDOT-FF and PEDOT-BL deposited at different polymerization potentials (E$_P$). Values are those extracted from three independent experiments and are shown as mean values with standard deviations.

E$_P$	PEDOT-FF			PEDOT-BL		
	ε (%) +1 V	ε (%) −1 V	Q (C cm^{-3})	δ (mm) +1 V	δ (mm) −1 V	Q (C cm^{-3})
1.0 V	0.92 ± 0.08	0.16 ± 0.01	98 ± 8	2.5 ± 0.2	0.50 ± 0.03	91 ± 8
1.2 V	0.73 ± 0.06	0.56 ± 0.04	87 ± 8	1.1 ± 0.1	0.70 ± 0.05	85 ± 7
1.5 V	0.55 ± 0.05	0.82 ± 0.07	72 ± 7	0.80 ± 0.06	1.7 ± 0.1	74 ± 7

The comparison between the responses of PEDOT-FF and PEDOT-BL shown in Table 3 underline the trends discussed above, i.e., with a higher deposition potential, the strain and bending displacement on the reduction side increases at the expense of the oxidation side. If the net displacement is considered, which is calculated from the differences between the displacements for oxidation and reduction, the mixed ion activity actuators are not ideal options. The typical design goal is to avoid such cases, i.e., trying to obtain approximately pure ion species activity with a single actuation direction for expansion upon either oxidation or reduction. One possible approach to suppress the activity of one ionic species is to embed ion-selective additives, like polymerizable ionic liquids [34] into the CP matrix, which, by maintaining the positive charge independent of the conducting polymer redox state in the blend, leads to selectively anion-active materials, thus primarily resulting in expansion upon oxidation. Without a dedicated selective system, the mobile species can even change over time, as shown recently using electrochemistry and AFM, where, with increased cycling, PEDOT films with a $LiClO_4$ aqueous electrolyte changed their mode from anion-driven to cation-driven [35]. As such, by either selecting different electrolytes or solvents or choosing the right polymerization potential, one can promote the desired control of actuation by avoiding mixed modes. On the other hand, mixed actuation with virtually equal strain upon oxidation and reduction allows mirrored and linear trilayer actuators to be constructed [36]. In either case, it is of paramount importance to understand the factors influencing the actuation mode, which in turn depends on the balance of the mobile species. A relatively small spherical anion like PF_6^- is expected to move in and out of a polymer matrix more easily than bulkier anions, but the actuation results shown here demonstrate otherwise. Consequently, EQCM measurements for thinner films were gathered at the same polymerization potential.

3.2.2. EQCM Measurements

While the EQCM can more reliable distinguish between mass changes from viscoelastic effects at lower film thicknesses, it is also known that very thin films have different ion transport properties. Hence, it is important to find a compromise. PEDOT was deposited potentiostatically here at different polymerization potentials that were equal to those used in the aforementioned actuation studies (E_P values of 1.0 V, 1.2 V, and 1.5 V) for actuator films. The mass changes accompanying the CV-driven processes for the PEDOT films of different formation potentials are presented in Figure 4. Charge–potential curves are presented in Figure S1c, again revealing that the charging/discharging behaviors were in balance.

EQCM analysis allows one to distinguish between mass balance changes in the various regions of a redox cycle. Upon oxidation from −1.0 V to 0.0 V, all the PEDOT films here presented a slightly negative slope, which was virtually invisible for E_p 1.0 V, and the slopes became steeper for higher polymerization potentials. This means that the PEDOT films lost weight in this potential range, as observed before by Kvarnström et al. [37] in a solution of $TBAPF_6$ in acetonitrile. As expected, the bending displacement of PEDOT-BL in the same potential range (Figure 3b) showed contraction. In particular, in the case of the films where the E_P was 1.0 V, the slight mass loss in the beginning of the oxidative scan may (in addition to cation involvement) also be explained by the current still remaining negative at these potentials (Figure 3c), corresponding to ongoing reduction, even as the oxidative scan had started. The next phase started for the potentials corresponding to the oxidation peak in the CV and progressed all the way to 1.0 V, thereby resulting in a significant mass increase for all PEDOT films (Figure 4a). This meant that ions and solvent molecules had moved in, as demonstrated above by the expansion of the PEDOT-BL (Figure 3b). In the reverse scan, from 1.0 V until the reduction peak at −0.4 V, a loss of mass was recorded (negative slope) for all materials, which correlates with the contraction of PEDOT-BL as shown in Figure 3b. In the case of the PEDOT films where E_P = 1.5 V (Figure 4c), a breaking point can clearly be observed at around −0.2 V, which is where the slope changed, indicating a change in the anion-cation participation ratio.
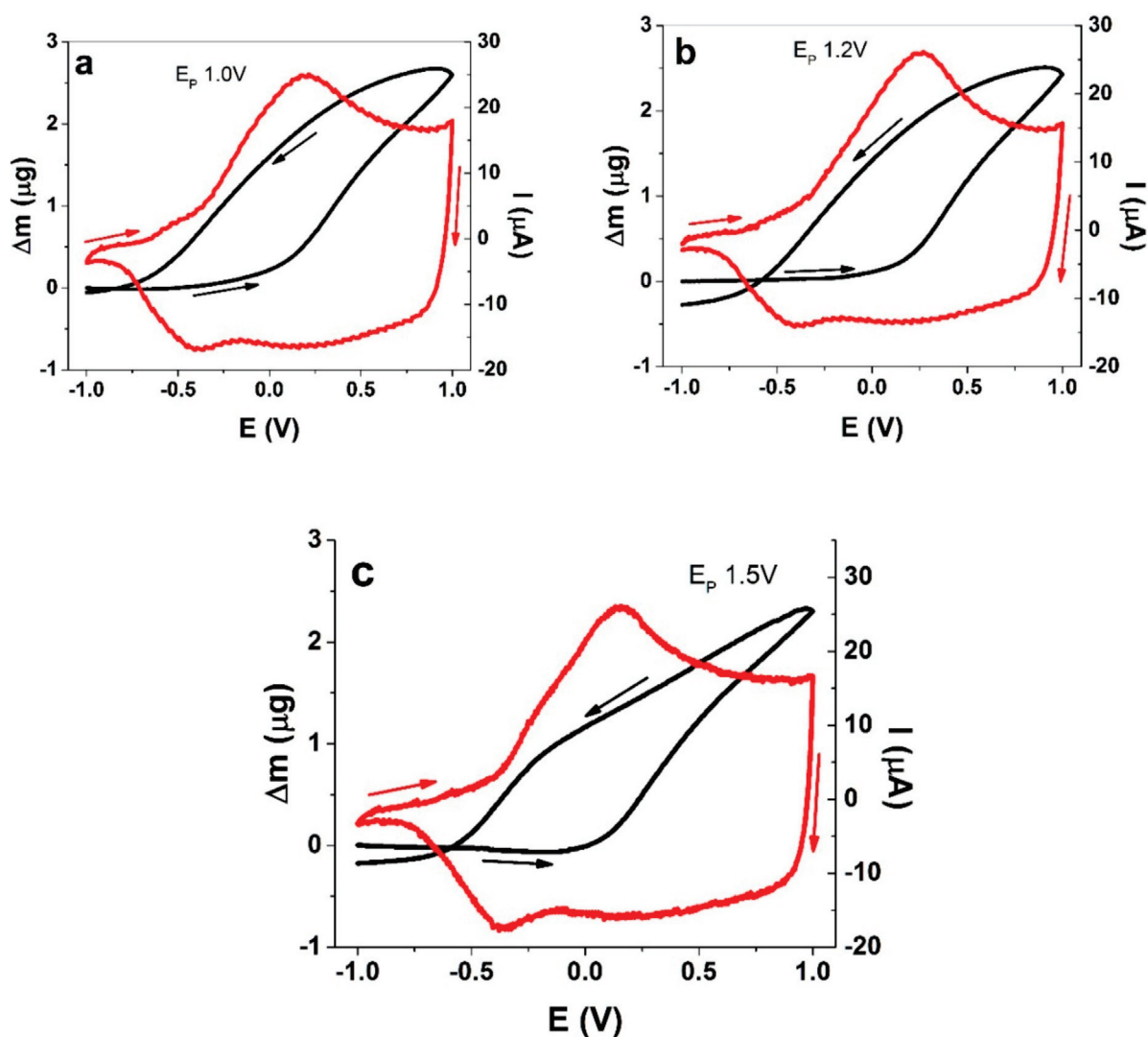
Figure 4. Cyclic voltammetry-driven (± 1.0 V, scan rate of 10 mV s^{-1}, current denoted by the red curve) EQCM measurements (mass change denoted by the black curve) for a TBAPF$_6$-PC electrolyte with PEDOT films polymerized at different polymerization potentials: (**a**) E$_P$ = 1.0 V; (**b**) E$_P$ = 1.2 V; (**c**) E$_P$ = 1.5 V. The arrows indicate the direction of the scan (starting point of -1.0 V).

Plotting the frequency change Δf against the charge ΔQ, as in Equations (2) and (3), the slopes of the curves (Figure S2a–c) of the different regions give the molecular weights of the compensating charge species, i.e., M_{CCS} (Equation (4), dimensionless). The obtained M_{CCS} values indicate the amounts and kinds of ions with or without a solvent (molar mass of PC of 102.09 g·mol^{-1}) that were incorporated or expelled during voltammetric cycling. For TBAPF$_6$, the molecular weight of the anion PF$_6^-$ was 144.96 g·mol^{-1}, and that of the cation TBA$^+$ was 242.47 g·mol^{-1}. In a case where M_{CCS} is greater than the molecular weight of the anion or cation, solvent molecules are likely transported, while negative values smaller than the anion or cation molecular weights hint to mixed processes of simultaneous anion and cation exchange, potentially even in combination with solvent molecules. With the EQCM methodology, the exact determination for which ions move in or out in a mixed activity scenario can only be estimated.

Figure 5a,b show the values of M_{CCS} as a function of the cycle potential for the PEDOT samples polymerized at different potentials, with the values separated for oxidation and reduction. For each polymerization potential, at least three independent measurements

were taken and the results represent mean values with the error bars of the calculated M_{CCS} values.
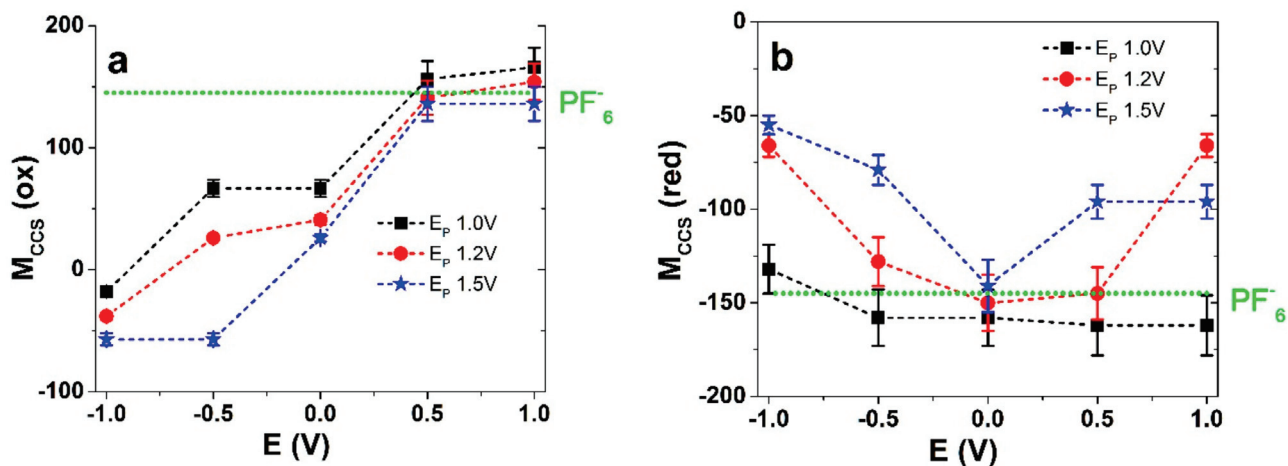
Figure 5. PEDOT deposited at different polymerization potentials where $E_P = 1.0$ V ($\cdot\cdot\blacksquare\cdot\cdot$), $E_P = 1.0$ V ($\cdot\cdot\bullet\cdot\cdot$), and $E_P = 1.5$ V ($\cdot\cdot\bigstar\cdot\cdot$), showing charge compensation for species M_{CCS} in (**a**) oxidation against the potential direction for -1.0 V to $+1.0$ V and (**b**) reduction against the potential direction of 1.0 V to -1.0 V. The included dotted green line represents the molar mass for PF_6^- anions.

It is immediately clear that the trends for the three polymerization potentials were all different. Upon oxidation where $E_P = 1.0$ V, the M_{CCS} values (Figure 5a) for the potentials starting from -1.0 V were negative, i.e., -18 ± 2, followed by -38 ± 4 for $E_P = 1.2$ V, and lower still for $E_P = 1.5$ V with -57 ± 6. The following slopes at a potential of -0.5 V revealed positive values for $E_P = 1.0$ V (67 ± 7) and $E_P = 1.2$ V (26 ± 3), while the values were still negative when $E_P = 1.5$ V. The M_{CCS} values were nowhere near the molecular weights of the ions, where mixed ion actuation takes place from -1.0 V to -0.5 V where cations are expelled and anions are incorporated. This process is likely accompanied by solvent molecules. Vandesteeg et al. [22] likewise proposed cation expulsion instead of anion insertion during oxidation in EDOT-based polymers, but without further investigations. At a potential of 0.0 V the M_{CCS} values were all positive (but still under the molecular weight of PF_6^- anions corresponding to mixed activity). With increasing polymerization potential, the M_{CCS} values decreased (higher cation involvement). This corresponds to the switching region in Figure 3a,b, where contraction changed to expansion. Upon further oxidation, (slopes at 0.5 V and 1.0 V), the films where $E_P = 1.0$ V and $E_P = 1.2$ V had M_{CCS} values in a range above the molecular weight of PF_6^-, corresponding to dominant anion incorporation, along with solvent molecules (as seen in Figure 3a,b with the primary expansion upon oxidation). In the case where $E_P = 1.5$ V, the M_{CCS} value of 136 ± 14 is still slightly lower than the molecular weight of PF_6^-, where the dominant process was still anion incorporation but with some mixed characteristics. It has been proposed that the hysteresis of the cycle might be caused by a variable number of trapped ions in PEDOT network in the considered timeframe [38].

As usual, a reduction scan can be more informative when starting from a fully oxidized and conductive state. For the reverse scan (Figure 5b), in the case where $E_P = 1.0$ V, the M_{CCS} values of -166 and -152 in a potential range from 1.0 V to -0.5 V show a clear indication of (solvated) anion expulsion, thus corresponding to contraction in PEDOT-FF and PEDOT-BL (Figure 2a,b). In the case where $E_P = 1.2$ V, the picture is different. The reduction scan M_{CCS} values do not reflect those for the oxidation scan. While it might be expected that the same solvated PF_6^- anions left the film, the M_{CCS} values of -66 ± 6 do not describe that. Similarly, that discussed above can be explained (in addition to the unlikely cation involvement) by the fact that in the beginning of the reduction scan, the potential

decrease did not immediately stop incomplete oxidation, and some anions still entered the film before beginning to leave. A further reduction from 0.5 V to 0.0 V showed a M_{CCS} result of -150 ± 15, which already corresponds to anions with solvent molecules leaving the PEDOT film. By reaching a potential of -1.0 V, PEDOT-BL and PEDOT-FF (Figure 3a,b) showed small expansion, and the mixed ion involvement was reflected here by a M_{CCS} result of -66 ± 6, as anions were mainly leaving and cations were already moving in (with solvent molecules involved in both processes). The polymerization potential of E_P = 1.5 V differed the most, where, during the whole reduction scan, the M_{CCS} values never reached the anion molecular weight value, corresponding to a mixed ion process throughout, with cation incorporation dominating as the potential dropped, corresponding to a higher strain/displacement for PEDOT-FF and PEDOT-BL upon reduction. The polymerization potentials chosen here have demonstrated significant effects regarding the dominant actuation direction, along with the accompanying ion flux.

To our knowledge, this is the first attempt to analyze the effect of polymerization potential in regard to the anion flux behind the linear and bending actuation modes of PEDOT actuators using EQCM measurements, especially in terms of addressing potential regions individually, thus allowing the tuning of the actuator response by selecting potential windows for desired outcomes. In summary, higher formation potentials of 1.2 V and 1.5 V brought about increased cation involvement in redox processes, while solvent uptake only played a minor role, as discussed before [24]. While some earlier works have shown significant solvent effects [33], their omission of any possible cation involvement does not allow a clear comparison. As seen from the structural description, with an increasing deposition potential, the polymer matrix becomes denser and less permeable for ions. As such, solvation shells are unlikely to remain intact as ions enter the material.

4. Conclusions

Charging/discharging in PEDOT or any other conducting polymer is accompanied by ion flux in order to maintain a neutral net charge. PEDOT polymerized different potentials has been studied here in order to establish the effect of the polymerization potential on the ion mobility and the corresponding expansion. Depending on the given design, such findings are potentially applicable for use in linear (PEDOT-FF) or bending (PEDOT-BL) actuators. The mostly anion-dominated activity seen for PEDOT deposited at 1.0 V gradually shifted to increased cation involvement with increasing deposition potentials of 1.2 V and 1.5 V, which in turn led to the a shift from expansion upon oxidation to mixed and increasing expansion upon reduction. EDX spectroscopy confirmed that, upon reduction, an increasing PF_6^- anion content remained in PEDOT polymerized at higher potentials, calling for cation incorporation in order to maintain a neutral net charge. The SEM micrographs indicated that denser and less porous PEDOT networks were formed at higher polymerization potentials, which might be the main reason for lowered PF_6^- mobility. EQCM measurements confirmed that mixed ion activity (both cation and anions participation) processes accompanied charging/discharging. As mixed activity modes are undesirable in general, the extensive study of PEDOT here enables one to understand the factors behind ion mobility and to either choose polymerization potentials optimal for more controlled actuation or to make maximum use of the mixed activity by choosing conditions for equal expansion upon reduction and oxidation. Future applications of such devices, i.e., where one ion movement process dominates, include soft robotics and smart textiles.

Supplementary Materials: The following are available online at https://www.mdpi.com/article/10.3390/polym13152448/s1: Figure S1. Charge potential curves in cyclic voltammetry ($\pm$ 1.0 V, TBAPF$_6$-PC electrolyte) of PEDOT films made at E_P 1.0 V (black curve), E_P 1.2 V (red curve) and E_P 1.5 V (blue curve) shown in a: for PEDOT-FF, in b: for PEDOT-BL and c: for EQCM measurements. The arrows indicate the start and end points of the 3rd cycle. Figure S2. Cyclic voltammetric (scan rate 10 mV s^{-1}) in TBAPF$_6$-PC electrolyte at ± 1.0 V showing EQCM measurements of frequency f

against charge Q of PEDOT films on quartz crystals polymerized at a: E$_P$ 1.0 V, b: E$_P$ 1.2 V and c: E$_P$ 1.5 V. The arrows indicate the direction of the san (starting point −1.0 V).

Author Contributions: Conceptualization, T.T. and G.U.; Data curation, D.G.W. and B.K.V.; Formal analysis, R.K. and D.G.W.; Funding acquisition, G.U; Investigation, R.K., B.K.V. and T.T.; Methodology, D.G.W. and B.K.V.; Project administration, G.U.; Resources, T.T.; Software, D.G.W.; Supervision, G.U.; Validation, R.K.; Writing–original draft, R.K.; Writing–review & editing, T.T. All authors have read and agreed to the published version of the manuscript.

Institutional Review Board Statement: Not applicable.

Informed Consent Statement: Not applicable.

Data Availability Statement: The data presented in this study are available on request from the Corresponding author.

Conflicts of Interest: The authors declare no conflict of interest.

References

1. Alici, G.; Metz, P.; Spinks, G.M. A methodology towards geometry optimization of high performance polypyrrole (PPy) actuators. *Smart Mater. Struct.* **2006**, *15*, 243–252. [CrossRef]
2. Otero, T.F.; Martinez, J.G. Physical and chemical awareness from sensing polymeric artificial muscles. Experiments and modeling. *Prog. Polym. Sci.* **2015**, *44*, 62–78. [CrossRef]
3. Hara, S.; Zama, T.; Tanaka, N.; Takashima, W.; Kaneto, K. Artificial fibular muscles with 20% strain based on polypyrrole-metal coil composites. *Chem. Lett.* **2005**, *34*, 784–785. [CrossRef]
4. Aydemir, N.; Kilmartin, P.A.; Travas-Sejdic, J.; Kesküla, A.; Peikolainen, A.L.; Parcell, J.; Harjo, M.; Aabloo, A.; Kiefer, R. Electrolyte and solvent effects in PPy/DBS linear actuators. *Sens. Actuators B Chem.* **2015**, *216*, 24–32. [CrossRef]
5. Harjo, M.; Järvekülg, M.; Tamm, T.; Otero, T.F.; Kiefer, R. Concept of an artificial muscle design on polypyrrole nanofiber scaffolds. *PLoS ONE* **2020**, *15*, 1–16. [CrossRef]
6. Maziz, A.; Concas, A.; Khaldi, A.; Stålhand, J.; Persson, N.-K.; Jager, E.W.H. Knitting and weaving artificial muscles. *Sci. Adv.* **2017**, *3*, 1–12. [CrossRef]
7. Jager, E.W.H.; Smela, E.; Ingana, O. Microfabricating Conjugated Polymer Actuators. *Science* **2000**, *290*, 1540–1545. [CrossRef]
8. Smela, E. Conjugated polymer actuators for biomedical applications. *Adv. Mater.* **2003**, *15*, 481–494. [CrossRef]
9. Martinez, J.G.; Richter, K.; Persson, N.K.; Jager, E.W.H. Investigation of electrically conducting yarns for use in textile actuators. *Smart Mater. Struct.* **2018**, *27*. [CrossRef]
10. Yan, B.; Wu, Y.; Guo, L. Recent advances on polypyrrole electroactuators. *Polymers* **2017**, *9*, 446. [CrossRef] [PubMed]
11. Entezami, A.A.; Massoumi, B. Artificial muscles, biosensors and drug delivery systems based on conducting polymers: A review. *Iran. Polym. J.* **2006**, *15*, 13–30.
12. Melling, D.; Martinez, J.G.; Jager, E.W.H. Conjugated Polymer Actuators and Devices: Progress and Opportunities. *Adv. Mater.* **2019**, *31*, 1808210. [CrossRef] [PubMed]
13. Põldsalu, I.; Rohtlaid, K.; Nguyen, T.M.G.; Plesse, C.; Vidal, F.; Khorram, M.S.; Peikolainen, A.L.; Tamm, T.; Kiefer, R. Thin ink-jet printed trilayer actuators composed of PEDOT:PSS on interpenetrating polymer networks. *Sens. Actuators B Chem.* **2018**, *258*, 1072–1079. [CrossRef]
14. Tyagi, M.; Spinks, G.M.; Jager, E.W.H. 3D Printing Microactuators for Soft Microrobots. *Soft Robot.* **2020**, *8*, 1–9. [CrossRef]
15. Pei, Q.; Zuccarello, G.; Ahlskog, M.; Inganäs, O. Electrochromic and highly stable poly(3,4-ethylenedioxythiophene) switches between opaque blue-black and transparent sky blue. *Polymer* **1994**, *35*, 1347–1351. [CrossRef]
16. Ouyang, J.; Li, Y. Effect of electrolyte solvent on the conductivity and structure of as-prepared polypyrrole films. *Polymer* **1997**, *38*, 1971–1976. [CrossRef]
17. Maw, S.; Smela, E.; Yoshida, K.; Stein, R.B. Effects of monomer and electrolyte concentrations on actuation of PPy(DBS) bilayers. *Synth. Met.* **2005**, *155*, 18–26. [CrossRef]
18. Khanh, T.T.; Kesküla, A.; Zondaka, Z.; Harjo, M.; Kivilo, A.; Khorram, M.S.; Tamm, T.; Kiefer, R. Role of polymerization temperature on the performance of polypyrrole/dodecylbenzenesulphonate linear actuators. *Synth. Met.* **2019**, *247*, 53–58. [CrossRef]
19. Smela, E.; Gadegaard, N. Surprising volume change in PPy(DBS): An atomic force microscopy study. *Adv. Mater.* **1999**, *11*, 953–956. [CrossRef]
20. Kiefer, R.; Bowmaker, G.A.; Cooney, R.P.; Kilmartin, P.A.; Travas-Sejdic, J. Cation driven actuation for free standing PEDOT films prepared from propylene carbonate electrolytes containing TBACF3SO3. *Electrochim. Acta* **2008**, *53*, 2593–2599. [CrossRef]

21. Aziz, S.; Martinez, J.G.; Salahuddin, B.; Persson, N.K.; Jager, E.W.H. Fast and High-Strain Electrochemically Driven Yarn Actuators in Twisted and Coiled Configurations. *Adv. Funct. Mater.* **2021**, *31*. [CrossRef]

22. Vandesteeg, N.A.; Madden, P.G.; Madden, J.D.; Anquetil, P.A.; Hunter, I.W. Synthesis and characterization of EDOT-based conducting polymer actuators. *Proc. SPIE* **2003**, *5051*, 349–356. [CrossRef]

23. Weis, D.G.; Kiefer, R.; Zondaka, Z.; Tamm, T.; Urban, G. Polypyrrole and poly (3,4-ethylenedioxythiophene) on silicon cantilever: Role of formation potential in bending displacement. *Synth. Met.* **2021**, *271*, 116653. [CrossRef]

24. Niu, L.; Kvarnström, C.; Ivaska, A. Mixed ion transfer in redox processes of poly(3,4-ethylenedioxythiophene). *J. Electroanal. Chem.* **2004**, *569*, 151–160. [CrossRef]

25. Hillman, A.R.; Daisley, S.J.; Bruckenstein, S. Kinetics and mechanism of the electrochemical p-doping of PEDOT. *Electrochem. Commun.* **2007**, *9*, 1316–1322. [CrossRef]

26. Harjo, M.; Tamm, T.; Anbarjafari, G.; Kiefer, R. Hardware and Software Development for Isotonic Strain and Isometric Stress Measurements of Linear Ionic Actuators. *Polymers* **2019**, *1054*, 1–14. [CrossRef] [PubMed]

27. Buttry, D.A.; Ward, M.D. Measurement of Interfaclal Processes at Electrode Surfaces with the Electrochemical Quartz Crystal Microbalance. *Chem. Rev.* **1992**, *92*, 1355–1379. [CrossRef]

28. Sauerbrey, G. Verwendung von Schwingquarzen zur Wägung dünner Schichten und zur Mikrowägung. *Z. Phys.* **1959**, *155*, 206–222. [CrossRef]

29. Bilger, R.R. *Elektrochemische und Gravimetrische in Situ Untersuchungen an Leitfähigen Polymeron*; Albert-Ludwigs-University: Freiburg i. Brsg., Germany, 1994.

30. Kiefer, R.; Weis, D.G.; Travas-Sejdic, J.; Urban, G.; Heinze, J. Effect of electrochemical synthesis conditions on deflection of PEDOT bilayers. *Sens. Actuators B Chem.* **2007**, *123*, 379–383. [CrossRef]

31. Valero, L.; Otero, T.F.; Martinez, J.G.; Martínez, J.G. Exchanged Cations and Water during Reactions in Polypyrrole Macroions from Artificial Muscles. *ChemPhysChem* **2014**, *15*, 293–301. [CrossRef]

32. Bay, L.; Jacobsen, T.; Skaarup, S.; West, K. Mechanism of actuation in conducting polymers: Osmotic expansion. *J. Phys. Chem. B* **2001**, *105*, 8492–8497. [CrossRef]

33. Robert Hillman, A.; Daisley, S.J.; Bruckenstein, S. Solvent effects on the electrochemical p-doping of PEDOT. *Phys. Chem. Chem. Phys.* **2007**, *9*, 2379–2388. [CrossRef] [PubMed]

34. Kesküla, A.; Peikolainen, A.L.; Kiefer, R.; Tamm, T. Consistent response from conducting polymer actuators: Potential window and embedded charges to avoid mixed ion transport. *Synth. Met.* **2020**, *268*, 116502. [CrossRef]

35. Mocaër, A.; Pillier, F.; Pailleret, A. Switching of the ion exchange behaviour of PEDOT thin films during a potential cycling: An electrochemical atomic force microscopy study. *Electrochim. Acta* **2021**, *138651*. in press. [CrossRef]

36. Kiefer, R.; Nguyen, N.T.; Le, Q.B.; Anbarjafari, G.; Tamm, T. Antagonist concepts of polypyrrole actuators: Bending hybrid actuator and mirrored trilayer linear actuator. *Polymers* **2021**, *13*, 861. [CrossRef]

37. Kvarnström, C.; Neugebauer, H.; Blomquist, S.; Ahonen, H.J.; Kankare, J.; Ivaska, A. In situ spectroelectrochemical characterization of poly (3, 4-ethylenedioxythiophene). *Electrochim. Acta* **1999**, *44*, 2739–2750. [CrossRef]

38. Hillman, A.R.; Daisley, S.J.; Bruckenstein, S. Ion and solvent transfers and trapping phenomena during n-doping of PEDOT films. *Electrochim. Acta* **2008**, *53*, 3763–3771. [CrossRef]

Article

Natural Rubber-TiO$_2$ Nanocomposite Film for Triboelectric Nanogenerator Application

Weeraya Bunriw [1], **Viyada Harnchana** [2,3,*], **Chalathorn Chanthad** [4] **and Van Ngoc Huynh** [5]

[1] Materials Science and Nanotechnology Program, Faculty of Science, Khon Kaen University, Khon Kaen 40002, Thailand; weeraya_b@kkumail.com
[2] Department of Physics, Khon Kaen University, Khon Kaen 40002, Thailand
[3] Institute of Nanomaterials Research and Innovation for Energy (IN-RIE), NANOTEC-KKU RNN on Nanomaterials Research and Innovation for Energy, Khon Kaen University, Khon Kaen 40002, Thailand
[4] National Nanotechnology Center (NANOTEC), NSTDA, 111 Thailand Science Park, Paholyothin Road, Klong Luang, Pathum Thani 12120, Thailand; chalathorn@nanotec.or.th
[5] DTU Bioengineering, Department of Biotechnology and Biomedicine, Technical University of Denmark, 2800 Kongens Lyngby, Denmark; vannh@dtu.dk
* Correspondence: viyada@kku.ac.th

Abstract: In this research, natural rubber (NR)-TiO$_2$ nanocomposites were developed for triboelectric nanogenerator (TENG) application to harvest mechanical energy into electrical energy. Rutile TiO$_2$ nanoparticles were used as fillers in NR material to improve dielectric properties so as to enhance the energy conversion performance of the NR composite TENG. The effect of filler concentration on TENG performance of the NR-TiO$_2$ composites was investigated. In addition, ball-milling method was employed to reduce the agglomeration of TiO$_2$ nanoparticles in order to improve their dispersion in the NR film. It was found that the TENG performance was significantly enhanced due to the increased dielectric constant of the NR-TiO$_2$ composite films fabricated from the ball-milled TiO$_2$. The TENG, fabricated from the NR-TiO$_2$ composite using 24 h ball-milled TiO$_2$ at 0.5%wt, delivered the highest power density of 237 mW/m^2, which was almost four times higher than that of pristine NR TENG. Furthermore, the applications of the fabricated NR-TiO$_2$ TENG as a power source to operate portable electronics devices were also demonstrated.

Keywords: natural rubber; triboelectric nanogenerator; TiO$_2$ nanoparticles; dielectric constant

1. Introduction

Energy harvesting technologies have attracted great attention because of the significance in producing sustainable energy sources to overcome energy crisis and climate change. In addition, the rapidly increasing number of personal electronic devices and other components for the Internet of Things (IoT) platform leads to the increasing demand for energy. Triboelectric nanogenerator (TENG) is a mechanical energy harvesting device based on the combination of contact electrification and electrostatic induction effects [1]. TENG has gained much interest due to its high energy conversion efficiency with high power output, straightforward fabrication process, and low cost [2]. Apart from energy harvesting applications, TENGs also have the potential to be used for many self-powered sensor applications, including physical, chemical, gas, and liquid sensors [3–6].

A wide range of materials can be used to fabricate TENG; most of them are polymeric materials [7]. The common known materials are polytetrafluoroethylene (PTFE) [8,9], polydimethylsiloxane (PDMS) [10,11], polyvinylidenefluoride (PVDF) [12,13], and polymethyl methacrylate (PMMA) [14,15]. Natural rubber (NR) or polyisoprene is one of the natural polymers with good flexibility and strength employed in a wide range of applications [16]. Most of NR products, such as car tires, gloves, shoe insoles, and mattresses, involve the applications in direct contact with mechanical energy sources. NR is one of the triboelectric materials located in the triboelectric series possessing slightly negative polarity [7]. In this

regard, the fabrication of NR-based TENGs would be beneficial for boosting power output to realize practical applications of the TENG.

Generally, the output performance of TENG is a function of triboelectric charges on triboelectric materials which depend on electrification between two triboelectric materials, surface area, and ability of surface to hold charges [17,18]. In order to improve triboelectric charge density on the surface, many approaches have been proposed, including surface patterning with nanostructures [19,20] and improving dielectric properties of triboelectric materials [21–24]. For the latter case, filling nanomaterials, such as SiO_2, TiO_2, $BaTiO_3$, and $SrTiO_3$ in polymer triboelectric materials, were reported to improve dielectric constant and TENG performance [23]. Among these filler materials, TiO_2 is an extensively used material for a wide range of applications due to many excellent physical and chemical properties, including optical-electronics [25], photocatalytic properties[26], chemically stability, nontoxicity, as well as low cost. TiO_2 exists in three main polymorph phases including anatase, brookite, and rutile [27]. Among them, rutile-TiO_2 exists as the most thermodynamically stable phase and exhibits a high dielectric constant [28,29].

In this work, rutile-TiO_2 nanoparticles were incorporated into NR material forming NR-TiO_2 composite film which was then used as a triboelectric material to convert mechanical energy into electricity. However, the NR-TiO_2 composite fabricated by mixing the TiO_2 nanoparticles directly with NR latex did not greatly improve the TENG output, possibly due to the agglomeration of as-received TiO_2 nanoparticles. In the present work, the ball-milling method is proposed as an effective and straightforward method to alleviate the agglomeration of TiO_2 nanoparticles prior to mixing with NR latex, thereby improving the dispersion of nanoparticles in the NR matrix. The effects of milling times and the concentration of TiO_2 nanoparticles in the NR film on dielectric properties and TENG output performance were investigated. The performance of the NR-TiO_2 TENG was probed under a vertical contact-separation mode. The morphologies and dielectric properties of the composite films were examined using a scanning electron microscope (SEM) and an impedance analyzer, respectively.

2. Materials and Methods

2.1. Preparation of NR-TiO2 Composite Films

The commercial NR latex (purchased from the Thai Rubber Latex Group Public Co., Ltd., Samut Prakan, Thailand) with a dry rubber content of 61% and rutile TiO_2 nanoparticles (Briture Co., Ltd., Hefei, China) were used in this work. NR latex and the as-received TiO_2 nanoparticles at 0.1, 0.2, 0.3, 0.4, and 0.5%wt were mixed by magnetic stirring for 5 min to ensure a homogeneous mixing. Then, 2 mL of the mixture was cast on an FTO substrate (Bangkok Solar Power Co., Ltd., Chachoengsao, Thailand) with an area of 4 cm × 4 cm so as to control the film thicknesses of approximately 0.5 mm. Three samples were prepared for each of the experimental conditions. The cast samples were then left to dry at room temperature for 4 days and cured at 80 °C for 2 h. In the present work, low curing temperature with long curing durations were employed in order to control the uniformity of the film top surface. Then, the samples were tested for the TENG performance, as described in Section 2.3.

In addition, the TiO_2 nanoparticles were dry ball-milled prior to mixing with NR latex. Yttria-stabilized zirconia balls and TiO_2 nanoparticles were put in a polyethylene (PE) plastic vial at the ball to a powder weight ratio (BPR) of 4:1. The ball-milling process was performed at a milling speed of 250 rpm for 6, 12, and 24 h. The ball-milled TiO_2 nanoparticles were then incorporated to NR latex following the same procedure, as described above. The composite films with ball-milled TiO_2 for 6, 12, and 24 h were labeled as "NR-TiO_2-B6h, NR-TiO_2-B12h, and NR-TiO_2-B24h", respectively.

2.2. Material Characterizations

The morphologies and crystal structure of the composite films were investigated using a SEM (FEI, Helios Nanolab, Waltham, MA, USA) and an X-ray diffraction technique (XRD)

(PANalytical EMPYREAN, Malvern, UK), respectively. Dielectric constants were measured using an impedance analyzer (Keysight, E4990A, Colorado Springs, CO, USA) at room temperature. Chemical functional group analysis was performed using a fourier transform infrared spectroscopy (FTIR) (TENSOR27).

2.3. TENG Output Measurement

The output performances of the NR-based TENGs were tested by measuring electrical output voltage and current using a vertical contact-separation mode with a single electrode configuration. A PTFE sheet was used as a contact triboelectric material. The voltage and current output signals were acquired under the mechanical impact force of 10 N with impact frequency of 5 Hz using an oscilloscope (Tektronix DPO2002B, Tektronix China Ltd, Shang Hai, China) and a digital ammeter (Kiethley DMM6500, Tektronix China Ltd, Shang Hai, China), respectively.

3. Results

The electrical output of the NR-TiO$_2$ at 0.1–0.5%wt were measured under a vertical contact-separation mode with a single electrode configuration, as presented in Figure 1. PTFE was used as a contact material with negative triboelectric polarity. The electrical voltage and current were generated by the physical contact-separation of the NR-TiO$_2$ film and PTFE surfaces. When the surfaces are in contact, the electrification effect causes electrons to be transferred between the two materials, resulting in the formation of positive and negative charges on surfaces of NR-TiO$_2$ film and PTFE, respectively. When the two surfaces were separated, electrostatic induction of triboelectric charges allowed free electrons in the electrical contact to flow, neutralizing triboelectric charges on the surface. Under the repeated contact-separation, the alternative current was generated.
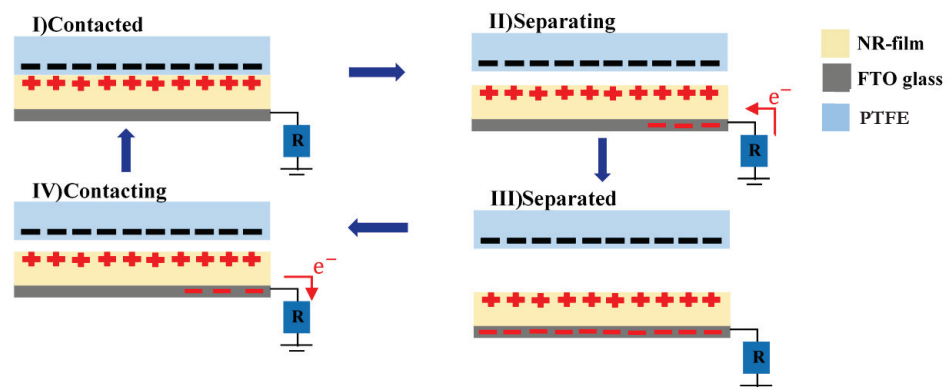
Figure 1. Schematic diagram of the device configuration for measuring energy conversion performance with working mechanism of the fabricated TENG under a vertical-contact separation mode with single electrode configuration.

The generated voltage and current of the fabricated NR-TiO$_2$ TENGs using as-received TiO$_2$ powders are presented in Figure 2a,b, respectively. The electrical outputs of the NR-TiO$_2$ TENGs with as-received TiO$_2$ increased with increasing TiO$_2$ content and were at the highest in the NR-TiO$_2$ 0.5%wt TENG, which were 78.4 V and 7.0 µA, respectively. However, the improvement of electrical output was not significant. It was suspected that the as-received TiO$_2$ nanoparticles were agglomerated, giving rise to the poor dispersion in the NR matrix.
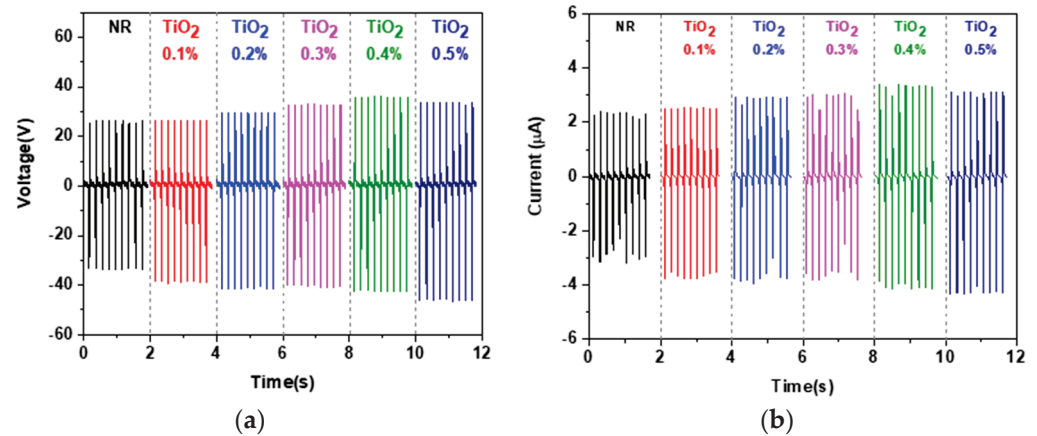
Figure 2. (**a**) Electrical output voltage and (**b**) current of the NR-TiO$_2$ 0.1–0.5%wt.

In order to improve the dispersion in the NR matrix, TiO$_2$ nanoparticles were ball-milled for 6, 12, and 24 h periods, prior to mixing with the NR latex to form composite materials. The ball-milled TiO$_2$ at 0.1–0.5%wt (same as above experiment) were added to NR latex. Electrical output voltage and current of all the ball-milled NR-TiO$_2$ TENG are displayed in Figure 3 and are summarized in Figure 4. It was found that ball-milled TiO$_2$ helped to improve the electrical outputs of NR-TiO$_2$ TENG, which increased with ball-milling time. The dependence of electrical output on TiO$_2$ concentration of the ball-milled TiO$_2$ TENG exhibited the same trend, as electrical output increased with increasing TiO$_2$ concentration. The addition of the 24-h-ball-milled TiO$_2$ nanoparticles into NR significantly improved TENG performance, and the highest output voltage of 113 V and current of 9.8 µA was achieved from the NR-TiO$_2$-B24h-0.5%wt TENG. The enhancement of TENG performance was attributed to the disintegration of TiO$_2$ nanoparticles at long ball-milling times, producing the well-dispersion in the NR polymer matrix. The role of TiO$_2$ nanoparticles on TENG performance will be further discussed in the dielectric properties in the following section.
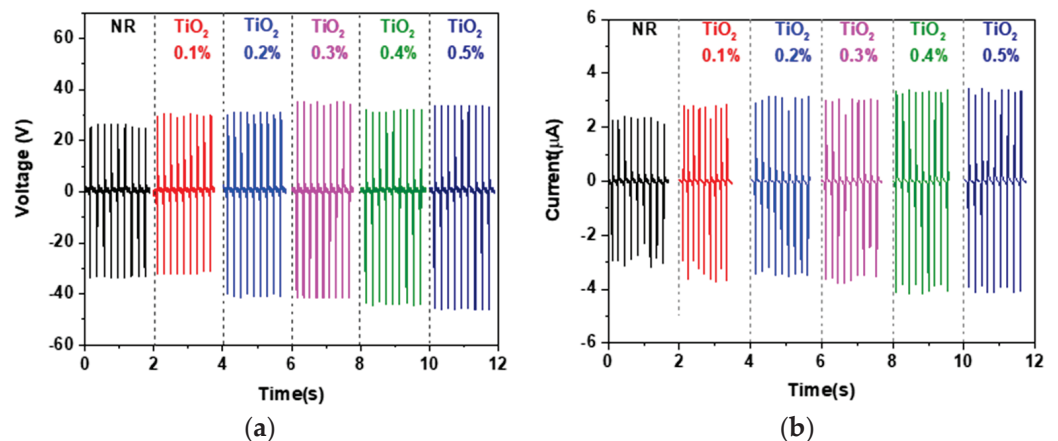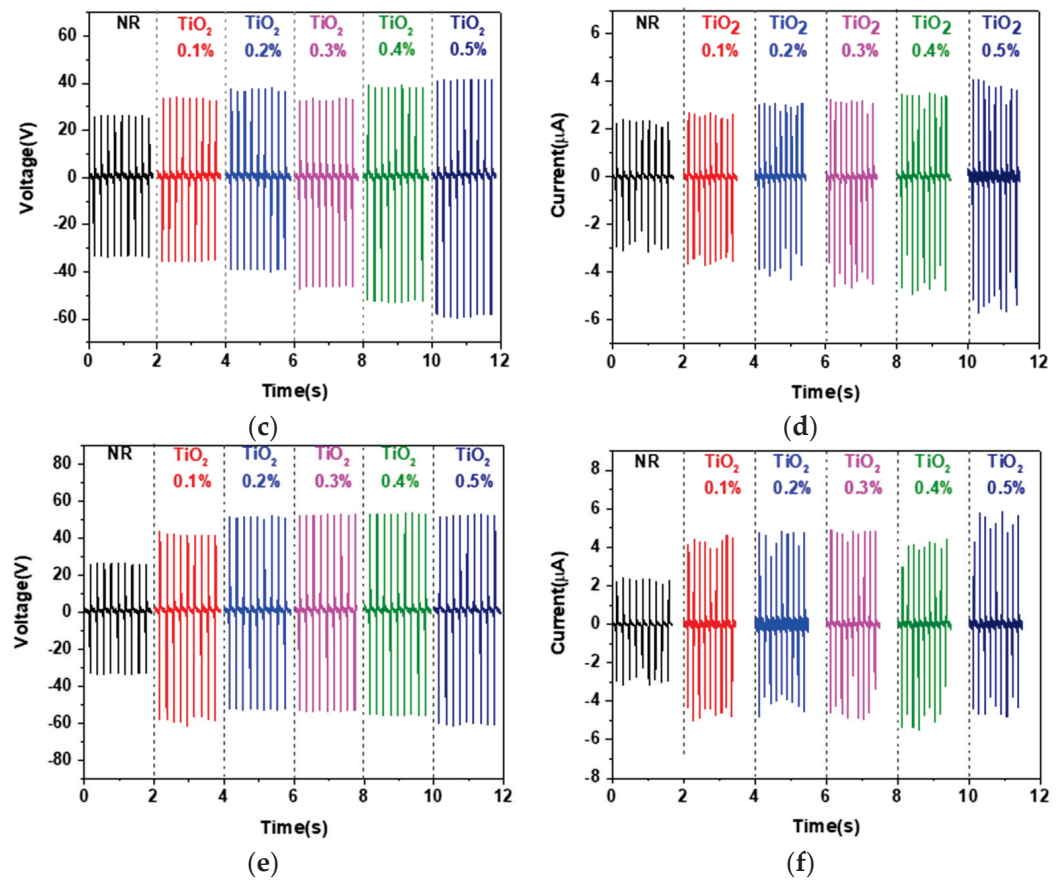

Figure 3. *Cont.*

Figure 3. Electrical voltage and current of (**a**,**b**) NR-TiO$_2$-B6h TENG, (**c**,**d**) NR-TiO$_2$-B12h, (**e**,**f**) NR-TiO$_2$-B24h 0.1–0.5%.
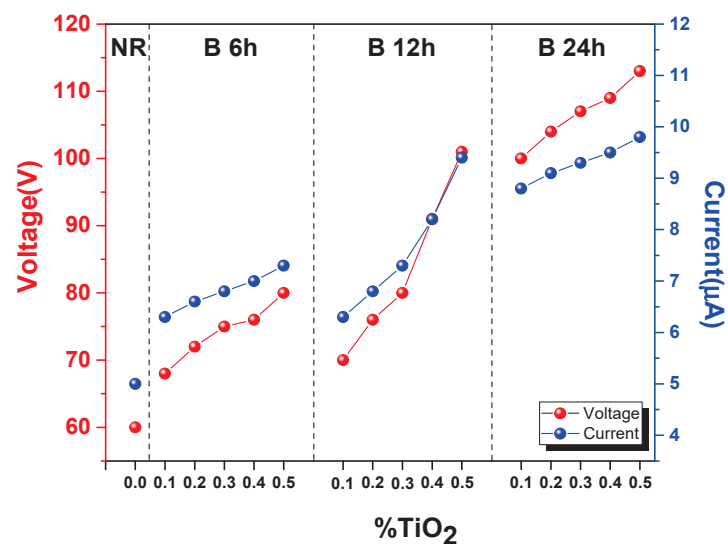

Figure 4. Electrical voltage and current of NR TENG and the NR-TiO$_2$-composite TENGs fabricated from ball-milled TiO$_2$ at 6, 12, and 24 h at 0.1–0.5%wt concentration.

The SEM images of the plain NR film, NR-TiO$_2$, NR-TiO$_2$-B6h, NR-TiO$_2$-B12h, and NR-TiO$_2$-B24h composite films at TiO$_2$ 0.5%wt are displayed with the insets of their TiO$_2$ nanoparticle fillers in Figure 5. Clearly, the dispersion of TiO$_2$ without the ball-milling treatment was poor, as evidenced by the large agglomeration size of particles observed in SEM images of TiO$_2$ powders and NR composite film. The agglomeration of TiO$_2$

nanoparticles was less observed in the ball-milled TiO_2 powders, which was reduced with increasing ball-milling times, contributing to the better dispersion in the NR composite films accordingly. The physical appearances of the NR and NR-TiO_2-B24h 0.1–0.5%wt composite films are presented in Figure 6. The transparency of the pure NR film decreased as the TiO_2 content increased.
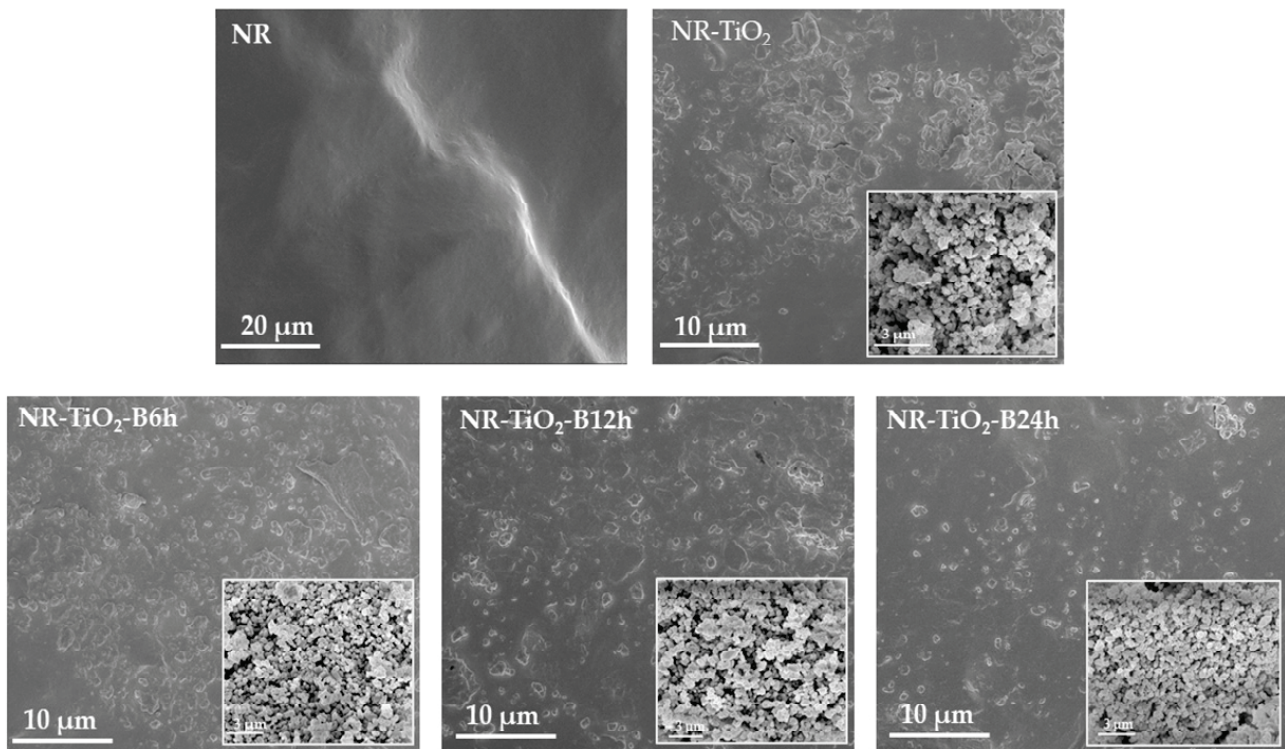

Figure 5. SEM images of the pristine NR film, NR-TiO_2, NR-TiO_2-B6h, NR-TiO_2-B12h and NR-TiO_2-B24h composite films at 0.5%wt with the insets of their TiO_2 particles fillers.
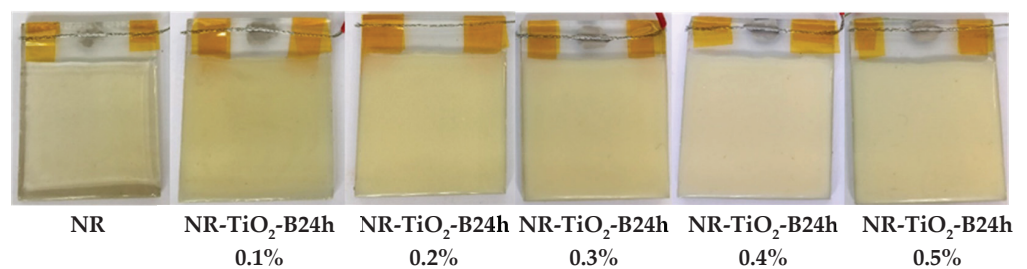
Figure 6. Digital photograph of the NR and NR-TiO_2-B24h 0.1–0.5%wt.

The rutile phase of as-received and ball-milled TiO_2 at 6, 12, and 24 h samples were confirmed by the XRD patterns as shown in Figure 7a (JCPDS No. 21–1276). This suggested that the ball-milling process did not change the crystal structure of the TiO_2 nanoparticles. In this study, ball-milling was employed to break up the agglomerated particles and rutile phase is the most stable structure of TiO_2; therefore, it should not cause the microstructural change of the particles. FTIR analysis of the NR and NR-TiO_2-B24h 0.5%wt was performed and presented in Figure 7b. FTIR spectra of the NR and NR-TiO_2-B24h 0.5%wt film are relatively similar, consisting of C-H stretching at 2850–2960 cm^{-1} and 1300–1400 cm^{-1} and C=C stretching at 839 cm^{-1} of polyisoprene molecules [30], and some C-O hydroxyl groups from non-rubber components in latex such as inorganic substances, proteins, phospholipids, carbohydrates, and fatty acids [16,31]. This suggested that no chemical bond was formed between TiO_2 and NR polymer.
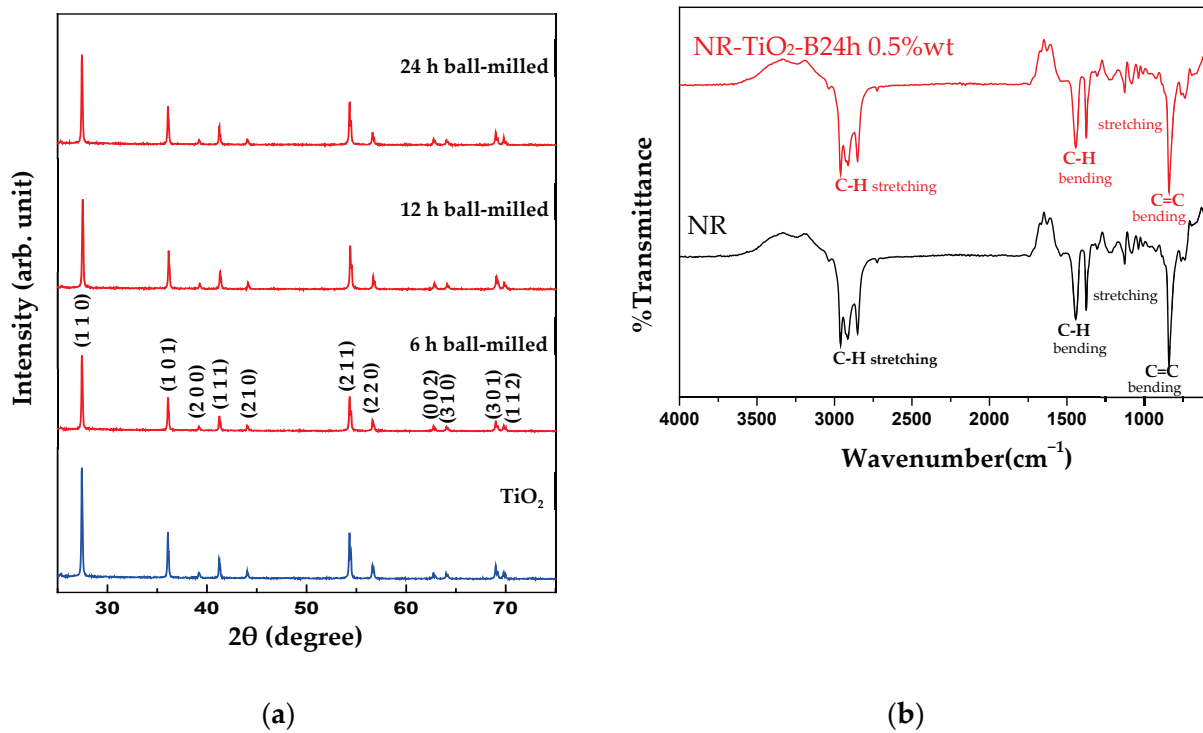
Figure 7. (**a**) XRD spectra of as-received TiO$_2$ and ball-milled TiO$_2$ at 6, 12, and 24 h. (**b**) FTIR spectra of the NR film and NR-TiO$_2$-B24h 0.5%wt composite film.

TENG electrical output is essentially a function of triboelectric charge density (σ) that forms upon contact electrification. For the contact mode TENG under open-circuit (OC) condition, the open-circuit voltage (V_{oc}) is expressed by [32]

$$V_{oc} = \frac{\sigma x(t)}{\varepsilon_0} \qquad (1)$$

and short circuit current (I_{sc}) is given by

$$I_{sc} = \frac{S\sigma d_0 v(t)}{(d_0 + x(t))^2} \qquad (2)$$

where ε_0, S, d_0, $x(t)$, and $v(t)$ are electrical permittivity of free space, contact area size, effective thickness constant, separation distance, and contact electrode velocity, respectively.

Triboelectric charge density depends on the material contact couple, contact area, as well as the charge storing ability of the surface. In the latter case, it refers to the dielectric constant of the material. For a contact-separation mode TENG which can be considered by a capacitive model, triboelectric charge is proportional to the capacitance of the device, which is given by [18]

$$C = \frac{\varepsilon_0 \varepsilon_r S}{d} \qquad (3)$$

where ε_r is dielectric constant and d is thickness of triboelectric material.

Dielectric constants of the NR-TiO$_2$-B24h 0.1–0.5%wt films measured at the frequencies ranging from 10^2–10^8 Hz is presented in Figure 8. The dielectric constant at 1 kHz of the NR-TiO$_2$-B24h was found to increase with TiO$_2$ concentration. The improvement of dielectric constant in the NR-TiO$_2$-B24h films with increasing TiO$_2$ concentration was ascribed to the fact that TiO$_2$ has a greater dielectric constant than NR. The addition of increasing TiO$_2$ filler concentration to NR polymer matrix gave rise to the increasing dielectric constant of the composites. The dielectric constant contributed to the charge capacitance at the

surfaces of triboelectric materials, which intensified triboelectric charges that attributed to the increased electrical output of the TENG.
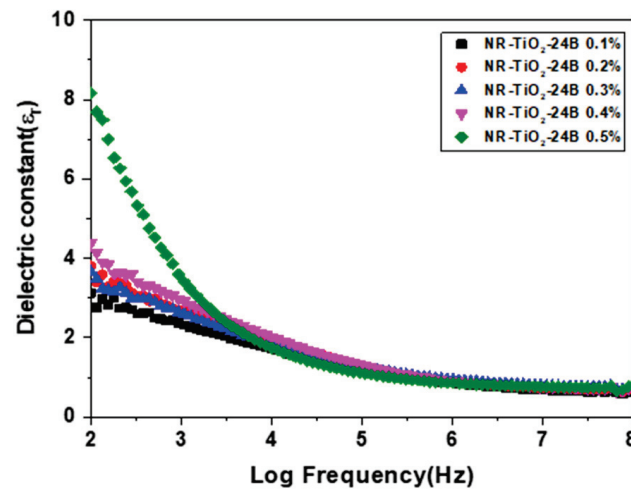

Figure 8. Dielectric constant of the NR-TiO$_2$-B24h 0.1–0.5%wt.

The dependence of the output performance on the contact-separation frequency were also studied. The voltage and current outputs of the NR-TiO$_2$-B24h 0.5%wt TENG were measured at operation frequencies ranging from 2–10 Hz, as presented in Figure 9a,b, respectively. It was found that electrical outputs depended on working frequency, and that the highest peak-to-peak voltage and current were 204 V and 13 µA, respectively, at a working frequency of 10 Hz. The increased electrical output was caused by charge retention on the surface due to a short contact-separation cycle at high frequencies.
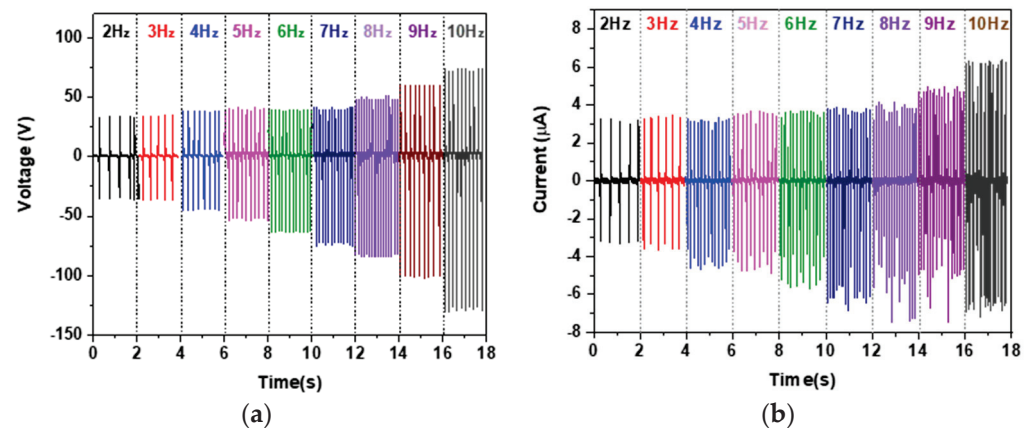

Figure 9. The frequency dependence of (**a**) electrical voltage and (**b**) current of the NR-TiO$_2$-B24h 0.5%wt TENG.

The delivered power density of the NR-TiO$_2$ TENG was also studied by measuring voltage and current at different load resistances ranging from 1–100 MΩ. The plot of voltage and current versus load resistances is shown in Figure 10a. The working power density of 200–237 mW/m^2 was achieved at load resistances ranging from 3–20 MΩ and the maximum power density of 237 mW/m^2 was achieved at a matched load resistance of 7 MΩ (Figure 10b), which was 3.6 times larger than that of pristine NR TENG (66 mW/m^2). This electrical output was enough to charge up a 10, 22, and 47 µF capacitors, as presented in a voltage profile in Figure 10c, and was able to charge a 99 µF to operate a portable calculator and light up 60 green LEDs, as demonstrated in Figure 10d and Video S1 in the Supplementary Materials. In addition, a TENG device was fabricated which was able to

light up 21 green LEDs by hand pressing, as demonstrated with the inset showing the schematic diagram of device components in Figure 10e.

(a)

(b)

(c)

(d)

(e)
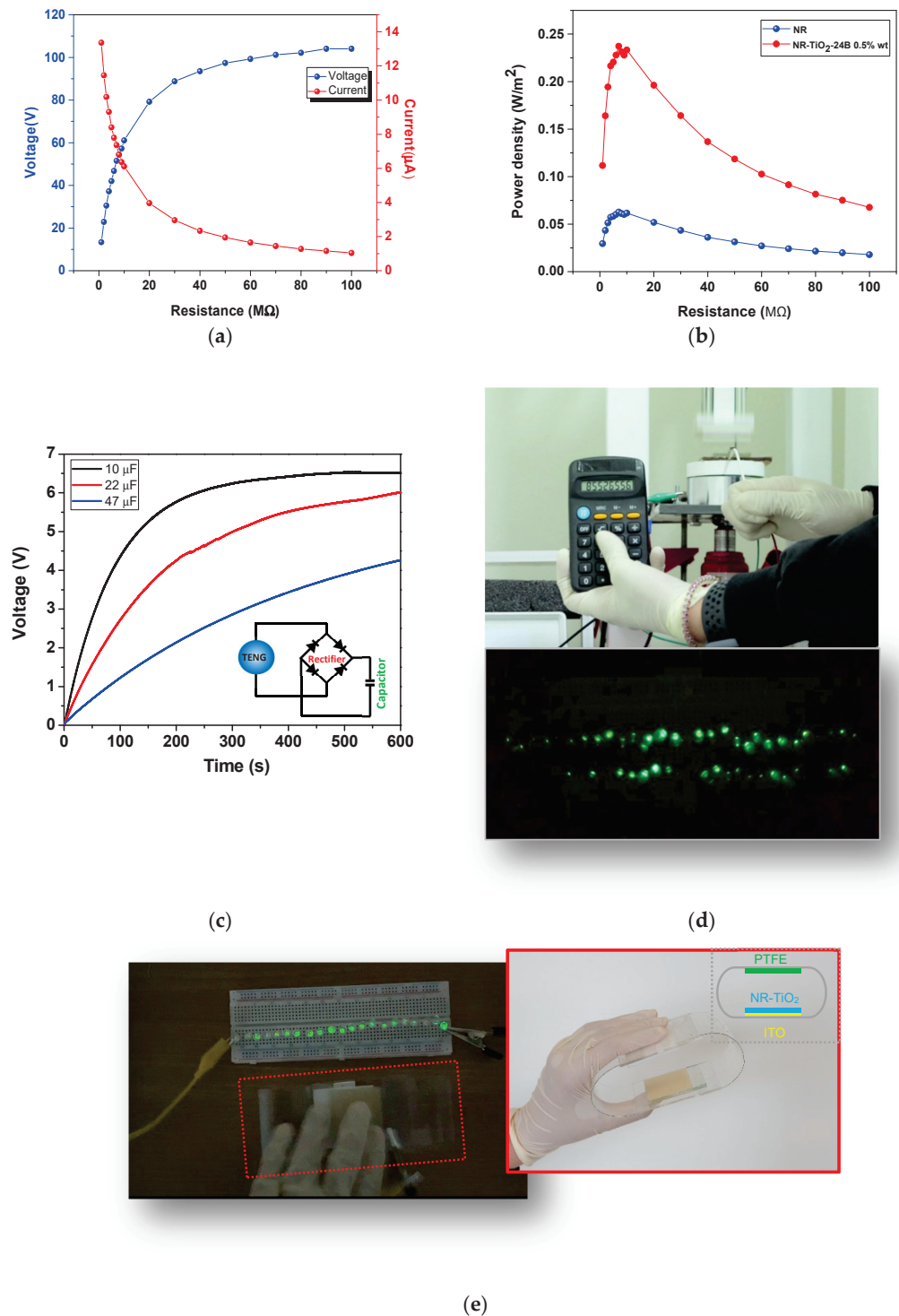
Figure 10. (**a**) The plot of voltage and current output versus load resistance and (**b**) Power density of the NR-TiO$_2$-B24h 0.5%wt TENG compared to NR TENG. (**c**) Voltage profile of TENG to charge up the 10, 22, and 47 µF capacitors. (**d**) The demonstrations of TENG to operate a portable calculator (top) and to light up 60 green LEDs (bottom). (**e**) The fabricated TENG device able to light up 21 green LEDs by hand pressing with the inset showing a schematic diagram of device components.

4. Discussion

In the present work, the development of NR TENG with enhanced performance was demonstrated by the incorporation of TiO_2 nanoparticles. The improved TENG performance was attributed to the enhanced triboelectric charge density by enhancing the dielectric constant of materials, as discussed in the previous section. TiO_2 nanoparticles were employed as an effective filler for improving dielectric constant of NR composite film due to the high dielectric constant of TiO_2. However, the agglomeration of nanoparticles suppressed the dispersion of nanoparticles in the NR matrix leading to an insignificant improvement of TENG performance, as presented in Figure 2. In this work, the simple and efficient approach to reduce the agglomeration of TiO_2 nanoparticles using ball-milling was proposed. TiO_2 nanoparticles were ball-milled prior to mixing with NR latex, which was found to effectively reduce the agglomeration of nanoparticles, as evidenced by SEM images (Figure 5), which then consequently produced the well-dispersion of TiO_2 in NR-TiO_2 composite films. In this work, the milling time of 24 h was found to efficiently reduce the agglomeration and produce the uniformly dispersed TiO_2 in the NR films. The power output enhancement of the NR-TiO_2-B24h was attributed to the improved dielectric constant due to the good dispersion of TiO_2 nanoparticles. This suggested that ball-milling was an effective treatment to alleviate the agglomeration of TiO_2 nanoparticles, which magnified the TENG electrical output to about 1.5 times higher than the untreated TiO_2 composite TENG.

Comparing to other previous reports, the fabricated TENG showed a superior performance than the PDMS-Kapton-implanted TENG with a power density of 8.44 mW/m^2 [33], the 2D woven wearable TENG fabricated from nylon and polyester threads with a power density of 2.33 mW/m^2 [34], and approaching a propeller TENG made of PTFE and Al triboelectric materials with a power density of 283.95 mW/m^2 [35]. In addition, comparing to the NR-based TENG, the NR-TiO_2 TENG exhibited the comparable output power to the NR-Ag TENG in our previous report which was 262.4 mW/m^2 [36]. The slightly lower TENG electrical output of the NR-TiO_2 composite than that of the NR-Ag one was attributed to the lower dielectric constant of the NR-TiO_2. The conductive Ag filler produced stronger interfacial polarization than the TiO_2 semiconductor filler in the NR insulating matrix [37]. Therefore, the main contribution for the improved dielectric constant of NR-TiO_2 was from the intrinsic dielectric property of TiO_2, as described earlier.

One of the most attractive aspects for employing NR as triboelectric material is the ability to scale up the production for large-area energy harvesting, owing to its low fabrication cost and feasibility to form composite with other materials. Comparing to other triboelectric polymers mentioned above, the costs of NR and TiO_2 are much lower. In addition, the fabrication process of NR-TiO_2 composite in the present work is straightforward, low cost and effective, which is promising for the development of large-scale energy harvesting device.

5. Conclusions

The NR-TiO_2 TENG for harvesting mechanical energy into electricity was successfully fabricated. The addition of rutile TiO_2 nanoparticles at 0.5%wt of NR latex to form NR-TiO_2 composite was found to enhance energy conversion efficiency of the TENG. The modification of TiO_2 by the ball-milling technique for 24 h prior to mix with NR materials was found to effectively disintegrate TiO_2 nanoparticles which consequently helped the dispersion of the nanoparticle fillers in the polymer matrix. Owing to the high dielectric constant of TiO_2 fillers, the dielectric constant of the NR-TiO_2-B24h film increased with increasing TiO_2 concentration. The NR-TiO_2-B24h film with improved dielectric constant attributed to the enhancement of TENG electrical output with the highest power density of 237 mW/m^2. This work showed the potential applications of NR-TiO_2 TENG as an environmentally friendly power source for portable electronic devices.

References

1. Fan, F.-R.; Tian, Z.-Q.; Lin Wang, Z. Flexible triboelectric generator. *Nano Energy* **2012**, *1*, 328–334. [CrossRef]
2. Wu, C.; Wang, A.C.; Ding, W.; Guo, H.; Wang, Z.L. Triboelectric nanogenerator: A foundation of the energy for the new era. *Adv. Energy Mater.* **2019**, *9*, 1802906. [CrossRef]
3. Ding, W.; Wu, C.; Zi, Y.; Zou, H.; Wang, J.; Cheng, J.; Wang, A.C.; Wang, Z.L. Self-powered wireless optical transmission of mechanical agitation signals. *Nano Energy* **2018**, *47*, 566–572. [CrossRef]
4. Yao, G.; Xu, L.; Cheng, X.; Li, Y.; Huang, X.; Guo, W.; Liu, S.; Wang, Z.L.; Wu, H. Bioinspired triboelectric nanogenerators as self-powered electronic skin for robotic tactile sensing. *Adv. Funct. Mater.* **2020**, *30*, 1907312. [CrossRef]
5. Yang, Y.; Zhang, H.; Lin, Z.-H.; Liu, Y.; Chen, J.; Lin, Z.; Zhou, Y.S.; Wong, C.P.; Wang, Z.L. A hybrid energy cell for self-powered water splitting. *Energy Environ. Sci.* **2013**, *6*, 2429–2434. [CrossRef]
6. Zhu, J.; Zhu, M.; Shi, Q.; Wen, F.; Liu, L.; Dong, B.; Haroun, A.; Yang, Y.; Vachon, P.; Guo, X.; et al. Progress in teng technology—A journey from energy harvesting to nanoenergy and nanosystem. *EcoMat* **2020**, *2*, e12058. [CrossRef]
7. Wang, Z.L. Triboelectric nanogenerators as new energy technology for self-powered systems and as active mechanical and chemical sensors. *ACS Nano* **2013**, *7*, 9533–9557. [CrossRef]
8. Wang, M.; Zhang, N.; Tang, Y.; Zhang, H.; Ning, C.; Tian, L.; Li, W.; Zhang, J.; Mao, Y.; Liang, E. Single-electrode triboelectric nanogenerators based on sponge-like porous ptfe thin films for mechanical energy harvesting and self-powered electronics. *J. Mater. Chem. A* **2017**, *5*, 12252–12257. [CrossRef]
9. Liu, D.; Yin, X.; Guo, H.; Zhou, L.; Li, X.; Zhang, C.; Wang, J.; Wang, Z.L. A constant current triboelectric nanogenerator arising from electrostatic breakdown. *Sci. Adv.* **2019**, *5*, eaav6437. [CrossRef] [PubMed]
10. Ko, Y.H.; Nagaraju, G.; Lee, S.H.; Yu, J.S. Pdms-based triboelectric and transparent nanogenerators with zno nanorod arrays. *ACS Appl. Mater. Interfaces* **2014**, *6*, 6631–6637. [CrossRef]
11. Harnchana, V.; Ngoc, H.V.; He, W.; Rasheed, A.; Park, H.; Amornkitbamrung, V.; Kang, D.J. Enhanced power output of a triboelectric nanogenerator using poly(dimethylsiloxane) modified with graphene oxide and sodium dodecyl sulfate. *ACS Appl. Mater. Interfaces* **2018**, *10*, 25263–25272. [CrossRef]
12. Lee, J.P.; Lee, J.W.; Baik, J.M. The progress of pvdf as a functional material for triboelectric nanogenerators and self-powered sensors. *Micromachines* **2018**, *9*, 532. [CrossRef] [PubMed]
13. Shaikh, M.O.; Huang, Y.-B.; Wang, C.-C.; Chuang, C.-H. Wearable woven triboelectric nanogenerator utilizing electrospun pvdf nanofibers for mechanical energy harvesting. *Micromachines* **2019**, *10*, 672. [CrossRef]
14. Jian, G.; Meng, Q.; Jiao, Y.; Meng, F.; Cao, Y.; Wu, M. Enhanced performances of triboelectric nanogenerators by filling hierarchical flower-like TiO_2 particles into polymethyl methacrylate film. *Nanoscale* **2020**, *12*, 14160–14170. [CrossRef] [PubMed]
15. Busolo, T.; Ura, D.P.; Kim, S.K.; Marzec, M.M.; Bernasik, A.; Stachewicz, U.; Kar-Narayan, S. Surface potential tailoring of pmma fibers by electrospinning for enhanced triboelectric performance. *Nano Energy* **2019**, *57*, 500–506. [CrossRef]

16. Candau, N.; Chazeau, L.; Chenal, J.-M.; Gauthier, C.; Munch, E. A comparison of the abilities of natural rubber (nr) and synthetic polyisoprene cis-1,4 rubber (ir) to crystallize under strain at high strain rates. *Phys. Chem. Chem. Phys.* **2016**, *18*, 3472–3481. [CrossRef] [PubMed]

17. Niu, S.; Wang, Z.L. Theoretical systems of triboelectric nanogenerators. *Nano Energy* **2015**, *14*, 161–192. [CrossRef]

18. He, X.; Guo, H.; Yue, X.; Gao, J.; Xi, Y.; Hu, C. Improving energy conversion efficiency for triboelectric nanogenerator with capacitor structure by maximizing surface charge density. *Nanoscale* **2015**, *7*, 1896–1903. [CrossRef]

19. Kim, D.; Jeon, S.-B.; Kim, J.Y.; Seol, M.-L.; Kim, S.O.; Choi, Y.-K. High-performance nanopattern triboelectric generator by block copolymer lithography. *Nano Energy* **2015**, *12*, 331–338. [CrossRef]

20. Zou, Y.; Xu, J.; Chen, K.; Chen, J. Advances in nanostructures for high-performance triboelectric nanogenerators. *Adv. Mater. Technol.* **2021**, *6*, 2000916. [CrossRef]

21. Fang, Z.; Chan, K.H.; Lu, X.; Tan, C.F.; Ho, G.W. Surface texturing and dielectric property tuning toward boosting of triboelectric nanogenerator performance. *J. Mater. Chem. A* **2018**, *6*, 52–57. [CrossRef]

22. Kim, Y.J.; Lee, J.; Park, S.; Park, C.; Park, C.; Choi, H.-J. Effect of the relative permittivity of oxides on the performance of triboelectric nanogenerators. *RSC Adv.* **2017**, *7*, 49368–49373. [CrossRef]

23. Chen, J.; Guo, H.; He, X.; Liu, G.; Xi, Y.; Shi, H.; Hu, C. Enhancing performance of triboelectric nanogenerator by filling high dielectric nanoparticles into sponge pdms film. *ACS Appl. Mater. Interfaces* **2016**, *8*, 736–744. [CrossRef] [PubMed]

24. Shi, K.; Zou, H.; Sun, B.; Jiang, P.; He, J.; Huang, X. Dielectric modulated cellulose paper/pdms-based triboelectric nanogenerators for wireless transmission and electropolymerization applications. *Adv. Funct. Mater.* **2020**, *30*, 1904536. [CrossRef]

25. Zhu, T.; Gao, S.-P. The stability, electronic structure, and optical property of tio2 polymorphs. *J. Phys. Chem. C* **2014**, *118*, 11385–11396. [CrossRef]

26. Schneider, J.; Matsuoka, M.; Takeuchi, M.; Zhang, J.; Horiuchi, Y.; Anpo, M.; Bahnemann, D.W. Understanding TiO₂ photocatalysis: Mechanisms and materials. *Chem. Rev.* **2014**, *114*, 9919–9986. [CrossRef]

27. Hanaor, D.A.H.; Sorrell, C.C. Review of the anatase to rutile phase transformation. *J. Mater. Sci.* **2011**, *46*, 855–874. [CrossRef]

28. Wypych, A.; Bobowska, I.; Tracz, M.; Opasinska, A.; Kadlubowski, S.; Krzywania-Kaliszewska, A.; Grobelny, J.; Wojciechowski, P. Dielectric properties and characterisation of titanium dioxide obtained by different chemistry methods. *J. Nanomater.* **2014**, *2014*, 124814. [CrossRef]

29. Ali, I.; Suhail, M.; Alothman, Z.A.; Alwarthan, A. Recent advances in syntheses, properties and applications of TiO₂ nanostructures. *RSC Adv.* **2018**, *8*, 30125–30147. [CrossRef]

30. Longseng, R.; Khaokong, C. Hexamethylene diamine-modified epoxidized natural rubber and its effect on cure characteristics and properties of natural rubber blends. *Iran. Polym. J.* **2020**, *29*, 1113–1121. [CrossRef]

31. Tanaka, Y. Structural characterization of natural polyisoprenes: Solve the mystery of natural rubber based on structural study. *Rubber Chem. Technol.* **2001**, *74*, 355–375. [CrossRef]

32. Niu, S.; Wang, S.; Lin, L.; Liu, Y.; Zhou, Y.S.; Hu, Y.; Wang, Z.L. Theoretical study of contact-mode triboelectric nanogenerators as an effective power source. *Energy Environ. Sci.* **2013**, *6*, 3576–3583. [CrossRef]

33. Zheng, Q.; Shi, B.; Fan, F.; Wang, X.; Yan, L.; Yuan, W.; Wang, S.; Liu, H.; Li, Z.; Wang, Z.L. In vivo powering of pacemaker by breathing-driven implanted triboelectric nanogenerator. *Adv. Mater.* **2014**, *26*, 5851–5856. [CrossRef]

34. Liu, J.; Gu, L.; Cui, N.; Bai, S.; Liu, S.; Xu, Q.; Qin, Y.; Yang, R.; Zhou, F. Core-shell fiber-based 2D woven triboelectric nanogenerator for effective motion energy harvesting. *Nanoscale Res. Lett.* **2019**, *14*, 311. [CrossRef] [PubMed]

35. Roh, H.; Yu, J.; Kim, I.; Chae, Y.; Kim, D. Dynamic analysis to enhance the performance of a rotating-disk-based triboelectric nanogenerator by injected gas. *ACS Appl. Mater. Interfaces* **2019**, *11*, 25170–25178. [CrossRef] [PubMed]

36. Suphasorn, P.; Appamato, I.; Harnchana, V.; Thongbai, P.; Chanthad, C.; Siriwong, C.; Amornkitbamrung, V. Ag nanoparticle-incorporated natural rubber for mechanical energy harvesting application. *Molecules* **2021**, *26*, 388. [CrossRef] [PubMed]

37. Kao, K.C. 2. Electric polarization and relaxation. In *Dielectric Phenomena in Solids*; Kao, K.C., Ed.; Academic Press: San Diego, CA, USA, 2004; pp. 41–114.

Article

PMMA Application in Piezo Actuation Jet for Dissipating Heat of Electronic Devices

Yu-Teng Chang [1,*]**, Rong-Tsu Wang** [2,*] **and Jung-Chang Wang** [3,*]

1 Department of Information Management, Yu Da University of Science and Technology, Miaoli County 36143, Taiwan
2 Department of Marketing and Logistics Management, Yu Da University of Science and Technology, Miaoli County 36143, Taiwan
3 Department of Marine Engineering (DME), National Taiwan Ocean University (NTOU), Keelung 202301, Taiwan
* Correspondence: cyt@ydu.edu.tw (Y.-T.C.); rtwang@ydu.edu.tw (R.-T.W.); jcwang@ntou.edu.tw (J.-C.W.); Tel.: +886-2-24622192 (ext. 7109/7139) (J.-C.W.)

Abstract: The present study utilizes an acrylic (PMMA) plate with circular piezoelectric ceramics (PC) as an actuator to design and investigate five different types of piezo actuation jets (PAJs) with operating conditions. The results show that the heat transfer coefficient of a device of PAJ is 200% greater than that of a traditional rotary fan when PAJ is placed at the proper distance of 10 to 20 mm from the heat source, avoiding the suck back of surrounding fluids. The cooling effect of these five PAJs was calculated by employing the thermal analysis method and the convection thermal resistance of the optimal PAJ can be reduced by about 36%, while the voltage frequency, wind speed, and noise were all positively correlated. When the supplied piezoelectric frequency is 300 Hz, the decibel level of the noise is similar to that of a commercial rotary fan. The piezoelectric sheets had one of two diameters of 31 mm or 41 mm depending on the size of the tested PAJs. The power consumption of a single PAJ was less than 10% of that of a rotary fan. Among the five types of PAJ, the optimal one has the characteristics that the diameter of the piezoelectric sheet is 41 mm, the piezoelectric spacing is 2 mm, and the length of the opening is 4 mm. Furthermore, the optimal operating conditions are a voltage frequency of 300 Hz and a placement distance of 20 mm in the present study.

Keywords: PMMA; acrylic; actuation jets; PAJ; piezoelectric ceramic; thermal analysis

1. Introduction

With the advances in integrated circuit packaging technology and the miniaturization process, the density of the circuit packages embedded in electronic components and the speed of such circuits have improved. In addition, the frequency of operation and heat generation have been relatively increased. If electronic components operate under high temperatures over a long period of time, their lifetimes may be shortened and their efficiency may be reduced. The use of piezoelectric sheets with polymeric materials for the purpose of heat dissipation was first proposed by Toda [1,2] in 1978. He presented a piezoelectric fan which was produced by using polyvinylidene fluoride resin 2 (PVF2) to make the fan blades, which were combined with the piezoelectric ceramics to generate a swayable cantilever beam structure. The result was a piezoelectric fan that could be compared with other small fans in terms of their effectiveness when used for heat dissipation in electronic products. In recent years, there has been significant interest conveyed in the polymer of PVDF (PVF2 or polyvinylidene difluoride) due to it revealing the strongest piezoelectric properties among these merchant polymers. PVDF (homo- and co-polymers) is generally synthesized and polymerized under the emulsion or suspension between 5 and 160 °C and between 5 and 350 atm. This contains generating the biaxially aligned film of PVF2 via admixing in changing capacities of polymethyl methacrylate

(PMMA), which is miscible with PVDF. PVDF has extreme pureness and a semi-crystal thermoplastic fluoropolymer, which can be used in chemical manufacturing facilities and has high mechanical strength, electronics and electricals, wonderful chemical resistance, specialized fields, good processability, energy-related applications, and piezoelectric and thermoelectric properties [3–8]. Chen et al. [9] demonstrated the wonderful performance for practical electrowetting and energy storage applications of the P(VDF-TrFE)/PMMA (PVT/PMMA)-blended films synthesized by a facile solution-blending method. Moreover, the PVT/PMMA blend containing 20 wt% PMMA with significantly enhanced energy storage capability and reduced remnant polarization even turned out to be a superior material for capacitor applications. Mahapatra et al. [10] investigated the latest development in piezoelectric (smart) materials for various applications in energy harvesting and self-powered sensors including vibrations, human motion, and mechanical loads, etc., in detail. They indicated that the enhancing efficiency of light and temperature-based piezoelectric energy harvesting provides endless future possibilities to fulfill growing energy requirements. Furthermore, the technical advancements in materials, device integration, and fabrication procedures in the piezoelectric energy sector will play a major role in dealing with the global energy crisis by exploiting sensors and self-sufficient batteries. Yoo et al. [11,12] employed dual-piezoelectric sheets to improve the vibration behaviors of piezoelectric and polymeric materials. Several types of dual-piezoelectric sheets were designed and then tested with different voltage levels in order to examine the effects of heat exchange by measuring the amplitude of the materials and the wind speed. The findings showed that when the length of a dual-piezoelectric sheet is increased, the harmonic vibration frequency will be reduced. Moreover, when the mezzanine is made from aluminum materials, it can reduce the amount of energy wasted and the cost.

Kalel and Wang [13] studied the integration of a PVDF-based un-bimorph actuator with a layer of one-way shape memory polymers (1W-SMPs) to achieve maximum bending of the piezoelectric cantilever actuator. The results exhibit a maximum bending angle of 40° at a DC field of 20 V/μm after 60 s between the SMP layer mounted at the center of the actuator and a length half of the PVDF layer, in which structure could be utilized for high unidirectional bending piezoelectric microactuators. Wu et al. [14] discussed using the jet airstream of a piezoelectric synthetic jet generator to enforce heat convection effects. A synthetic jet enhances the cooling effect of its components. When the surface temperature reaches 100 °C, the natural power of the convection dissipation is 2 W, whereas when synthetic jet actuators are employed, the maximum dissipation effect can reach 17 W. When the same power is supplied to the actuator, its dissipation power can be three times bigger than that of the common means of dissipating heat. Ko et al. [15] investigated a piezoelectric fan in motionless air utilizing the CFD and observations with an IR camera. The results showed that the temperature of the heat source is regionally lowered by 28 °C and it is very valid to cool it regionally. Ebrahimi et al. [16,17] studied the vortex advancement on all sides of the tips of vibrational cantilever plates with different structures and oscillating behavior. The vortex regimes depended on the length of the cantilever and Reynold number (Re). The results showed that conquering damping can occupy over 50% of the total power input to a piezoelectric fan and exploit it for heat transfer purposes. Smith et al. [18,19] investigated the influence of the Re and the height of the cavity on the synthetic jet flow field. For the same Reynolds number of 2000, as a near flow field of a synthetic jet can generate vortex pairs, it can create a greater jet stream than a continuous jet flow. A distant flow field was similar to a continuous jet flow. Influences of freestream on the piezoelectric fans were carried out to analyze the inlet velocities (from 0 to 7 m/s) at the side of the fan [20]. The influence of the freestream on the tip vortex is major in that the freestream reduces the vortex intensity just after separation from the fan tip. The side vortex is also affected slightly by the freestream. Both vortices are yet deducted by the freestream and drift away from the fan after separation from the fan edge. Wu et al. [21] used piezoelectric sheets in the heat dissipation of electronic components and used the ANSYS software package for experiments and comparison. The simulation results and comparison found

few differences. They also discussed the factors that influence the harmonic frequency and harmonic amplitude, including the length of the piezoelectric materials, placement and distribution, and fixed boundary conditions. The analysis was conducted by changing previous parameters to design four different patterns as alternatives in order to determine the optimal construction. Kercher et al. [22] used synthetic jet technology to manage the heat dissipation of electronic components. Their experimental findings indicated that a piezoelectric synthetic jet had two times better cooling efficiency than the fans presently used as cooling technology.

Many research studies have focused on the aerodynamic performance of oscillating piezoelectric fans with flexible beams composed of polymeric materials because of their potential as active cooling mechanisms for thermal management applications. Conway et al. [23] investigated the influence of crossbeam thickness (1 and 3.7 mm) on the flow field generated by an oscillating crossbeam composed of polymeric materials using a custom-designed particle-image velocity (PIV) facility and numerical analysis. The results inform the design for use in thermal management applications and beneficial for thermal applications where there are constricted environments of oscillating cooling solutions. Liu et al. [24] studied the vibration and cooling performances of the piezoelectric cooling fan using finite element and experimental methods. The numerical results have good agreements with the experimental measurements. Additionally, for the cooling purpose, the piezoelectric cooling fan needs to work under the natural frequency. The aspect ratio of the optimal geometry of the fan blade is 2:3. Jalilvand et al. [25] evaluated the cooling performance of various configurations of synthetic jet-based thermal solution modules based on thermal resistance analysis. The results display that more than 12 W of heat can be dissipated by a DCJ (Dual Cooling Jet). Zhou et al. [26] explored and examined an active enhanced impingement cooling of a circular jet using a piezoelectric fan with low power consumption. The results show that the impingement cooling of the jet enhances as the Re increased. Usually, the new jet can supply superior performance of heat transfer at a small gap and a high Re. A circular enclosure divided by a movable barrier has been numerically investigated inside a separated circular attachment in the presence of a flexible wall [27]. The results verify that the degree of distortion of the plate is straightly dependent on the number of forces. A broad scope of PMMA (PolyMethyl MethAcrylate) polymers is regularly employed for various applications in engineering. The distinct properties of PMMA including the low density, cheap, esthetics, suitable physical and mechanical properties, ease of manufacture, and readily melt-processible technique can be fabricated into parts by injection and compression molding. Accordingly, PMMA is frequently applied in chemical processing equipment (e.g., tubes, valves, pumps, pipes, and fittings), sensors, and actuators, etc. Some chemical modifications and mechanical reinforcement techniques involving adding various types of nanofibers, nanoparticles, nanofillers, nanotubes, and hybrid materials (nanoparticles) are made known to enhance the functions of thermal and dielectric properties and tensile strength of PMMA-based materials in recent decades [28–33]. The present study utilizes the piezo actuation jet (PAJ) with the PMMA plate for dissipating heat of electronic devices. The polymeric material of PMMA in the present paper is manufactured through a thermoplastic injection molding and rapid-uniform heating and cooling cycle system associated with a vapor chamber technology, which can improve the tensile strength and decrease the deficiency of the welding lines of a plastic product [34,35]. Tsai et al. [36] exhibited that the plastic products with two opposite gates were found to enhance by 6.8 °C and 10 °C of tensile strength compared with the traditional one, and the other plastic product with eight holes plate is reduced from 12 μm to 0.5 μm of the depth of the welding line.

2. Research Methods

A device of piezo actuation jet (PAJ) consists of a circular piezoelectric sheet and acrylic (PMMA) plate, which was a completely new method of heat dispersion in the present paper. The powders of PMMA named ACRYREX $^{®®}$ CM-207 with high smoothness,

clear transparency, and high gloss were supplied by CHI MEI CORPORATION (Taiwan) in this study. This study investigated different design patterns, including layouts with differences in the piezoelectric sheet size, spacing, and area, with the different types of devices ultimately being used with a high-power LED (HI-LED) [37–42] to determine the best PAJ used when combining several PAJs in series. Connecting the PAJs in series increases the overall amount of wind and allows for the addition or subtraction of devices according to the area of the heat source to effectively control the volume of the device of the PAJ and achieve the optimal dissipation effect. The research procedure is shown in Figure 1a. The PAJ (piezo actuation jet) device, respectively, includes two strategies containing performance measurement and structural design.
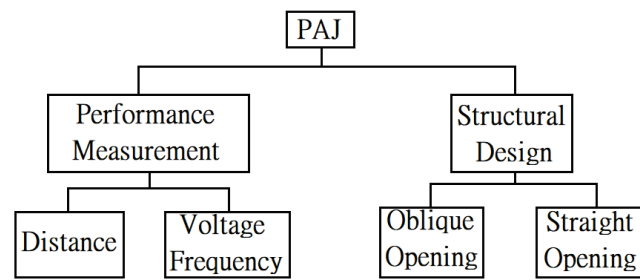
(**a**) Research procedure
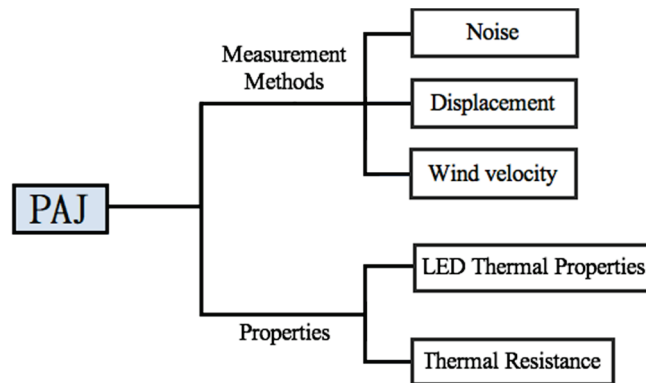
(**b**) Performance measurement

Figure 1. Experimental procedure. (**a**) Research procedure; (**b**) Performance measurement.

2.1. Performance Measurement

Figure 1b consists of a flow chart detailing the performance measurement of PAJ, which contained measurement methods and properties. The individual performance measurement included noise, displacement, and wind speed. These three parameters were employed in a HI-LED module to conduct thermal performance experiments in order to determine the properties of each device through thermal analysis. The properties are the LED thermal properties and thermal resistance.

2.1.1. Noise

A handmade soundproof box was used in the noise experiment as shown in Figure 2, and the rotary fan adopted in the subsequent experiments was used in the sound proof test. The material of the soundproof box sheet is acrylic having a thickness is 5 mm and the size is $350 \times 250 \times 250$ mm^3, which is covered with wave-shaped soundproof cotton with a thickness of 50 mm. The decibel meter named by DSL-333 (Tecpel Co., Ltd., Taipei, Taiwan) as a measurement range between 30 and 130 dB with a resolution of 0.1 dB and an error of ± 1.5 dB and the frequency response is between 30 Hz and 8 kHz. Outside the box, the rotary fan produced a noise with a value of 62.4 dB, while when placed inside the soundproof box, it produced a noise measured at 50.7 dB. The background

volume of the testing room was measured to be 41.6 dB, yet after correction according to the standard noise control Equation (1), that value was corrected to 50.1 dB. This proves that the soundproof box has good soundproofing ability. The volume correction of the background was displayed in Equation (1).

$$L_0 = 10 log \left(10^{0.1L_1} - 10^{0.1L_2} \right) \tag{1}$$

L_0: Measured value of the intended sound source
L_1: Measured value of the total volume
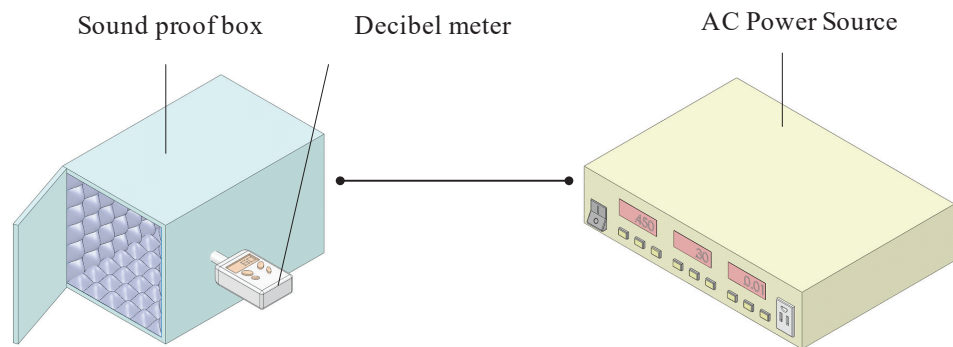L_2: Measured value of background volume

Figure 2. Noise experiment.

2.1.2. Displacement

Piezoelectric ceramics (PC) can be used to convert electrical energy into mechanical energy and to transfer energy to the metal foil. The experiment of displacement used a clamp to secure the device of PAJ and sensor head. The high-frequency current flowing through the sensor head coil generates a high-frequency magnetic field, which interferes with the degree of the impedance of the sensor head and is converted into a voltage output. While the voltage signal is being transferred to the digital oscilloscope to generate waveforms, it can be calculated into the displacement or amplitude of the metal sheet as shown in Figure 3. The sensing head named EX-305 (KEYENCE, Co., Ltd., Taipei, Taiwan) has a frequency response of 18 kHz and resolution of 0.4 μm. The distance between the sensing head and piezoelectric patches is 1 mm and the operating temperature is between −10 °C and 60 °C.
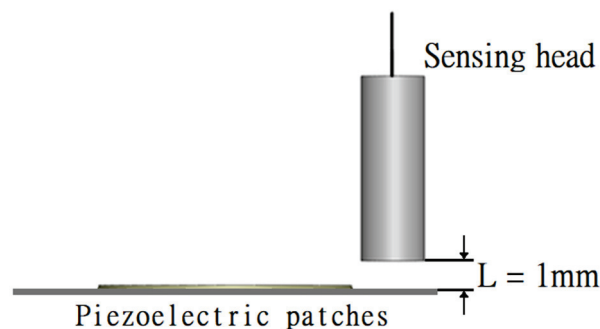
Figure 3. Schematic diagram of jet path.

2.1.3. Wind Speed

The purpose of this experiment was to determine the optimal placement of the PAJ device and the heat source in order to enhance the heat dissipation effect. In general, the volume of air displaced by a rotary fan is inversely proportional to its placement and the wind speed of the fan will decrease with increasing distance. Moreover, when the fan is too close to the heat source, the jet resistance increases, and the heat dissipation effect may

be poorer than natural convection. Thus, the placement distance is an important parameter. A clamp was used to fix the device of PAJ and the distance between it and the hot wire anemometer was changed in increments of 5 mm. Wind speeds were measured at distances of 5, 10, 15, 20, and 25 mm, respectively. Figure 4 exhibits the hot wire anemometer named TES-1341(TES Co., Ltd., Taipei, Taiwan), which can measure wind velocity between 0 and 30 m/s with a resolution of 0.01 m/s and an error of ±3%.

Figure 4. Hot wire anemometer.

2.1.4. Thermal Resistance Network Analysis

The HI-LED as shown in Figure 5a with dimensions of $36 \times 34 \times 2.6$ mm^3 and power of 10 W dissipation design used in this study primarily utilizes thermal resistance to evaluate the characteristics of the LED package. Additionally, it can be used to judge the dissipation capacity of a heat sink by observing the level of thermal resistance. That is, a greater thermal resistance indicates a weaker heat dissipation effect. Equation (2) reveals the definition of thermal resistance.
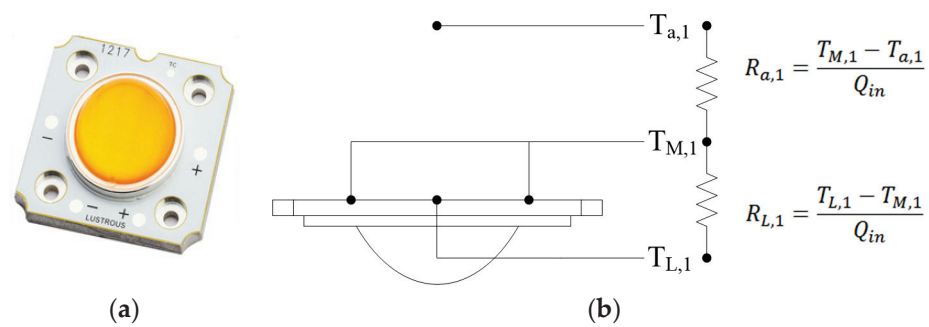

| (**a**) | (**b**) |

Figure 5. LED Module network. (**a**) HI-LED, (**b**) Thermal resistance network.

$$R_T = \frac{T_j - T_a}{Q} \tag{2}$$

R_T: Total thermal resistance, T_j: Temperature of the interface, T_a: Temperature of the environment, Q: Power consumption

Five devices of PAJ were fabricated using a variety of parameters, such as the piezo-electric sheet spacing, size, and the opening area, to establish performance test methods and to conduct cooling experiments in hopes that the PAJs can be applied to the heat dissipation of HI-LEDs. According to LED cooling modules, the thermal resistance of an LED can be analyzed in two parts. The first part is the thermal resistance of the heat

diffusion ($R_{L,1}$). The second part is the thermal resistance of the natural convection ($R_{a,1}$), as shown in Figure 5b. The thermal resistance of the heat diffusion ($R_{L,1}$): heat is transferred to the substrate by heat. Since the surface area of the heat radiation substrate is greater than that of the heat source, the rate of heat diffusion is affected by the thermal conductivity of the material, such that the diffusion resistance that is generated, which can be calculated according to Equation (3), is defined as the temperature difference between the center of the LED substrate temperature ($T_{L,1}$) and the average temperature of the substrate interface ($T_{M,1}$) divided by the total power (Q_{in}).

$$R_{L,1} = \frac{T_{L,1} - T_{M,1}}{Q_{in}} \tag{3}$$

The thermal resistance of heat convection ($R_{a,1}$): the energy transmission created by the density difference between the substrate temperature and the air is called natural convection. A fan can also be installed to enhance the convection effect, resulting in a phenomenon called forced convection. Heat is dispersed into the air via convection and this transfer process is called the thermal resistance of heat convection. Equation (4) defines the temperature difference between the average temperature of the substrate interface ($T_{M,1}$) and the ambient temperature ($T_{a,1}$) divided by the power (Q_{in}).

$$R_{a,1} = \frac{T_{M,1} - T_{a,1}}{Q_{in}} \tag{4}$$

To simplify, in the diagram of the network analysis $R_{L,1} + R_{a,1} = R_{T,1}$ of the thermal resistance; $R_{T,1}$ is the total thermal resistance as shown in Equation (5).

$$R_{T,1} = \frac{(T_{L,1} - T_{a,1})}{Q_{in}} \tag{5}$$

2.2. Structural Design-Two Patterns

The device of PAJ composes of circular piezoelectric sheets and a PMMA plate. The material of the circular piezoelectric sheets is Lead Zirconated Titanite (PZT), which XRD (X-ray Diffraction) patterns reveal the chemical formula of $Pb(Zr_{0.44}Ti_{0.56})O_3$ as shown in Figure 6. The present study investigated different design patterns, including designs with differences in the piezoelectric sheet size, as well as differences in the spacing and the opening area of the piezoelectric sheet. The tested PAJs were divided into two types according to the design of the jet channels. The first type utilized a linear jet path, as shown in Figure 7a, in which the jet channel outlet has smooth, straight lines and a larger opening area. The second type utilized a flared jet channel, as shown in Figure 7b, the area of the outlet was reduced and the flaring was increased, directing the airflow around the shunt, and increasing the heat dissipation area. The materials of the two jet channels are the PMMA manufactured by the technology of the insert injection molding process with the local heating mechanism of the vapor chamber [34–36], which improves the final strength of the product. The product of PMMA strength can be enhanced outstandingly and reduce the defect of the welding lines with a yield rate of up to 100% through this fabricating procedure. The PMMA has a density of 1.16 g/cm^3, a melting point of 135 °C, a glass temperature of 102 °C, the thermal conductivity of 0.23 W/mk, and tensile strength of 78 MPa in the present paper. Figure 7c exhibited the real PAJ of the second type. These three sets of parameters were used to create five devices with different specifications for comparison. The detailed specifications are shown in Table 1. In addition, the previous literature has indicated that increasing the height of the cavity will directly affect the performance of the jet strength and performance. Therefore, the case5 device served as the control for the case1 device because the two devices are made using piezoelectric sheets with the same diameter and the same opening length, but the spacing between the piezoelectric sheets increased from 2 mm to 3 mm.
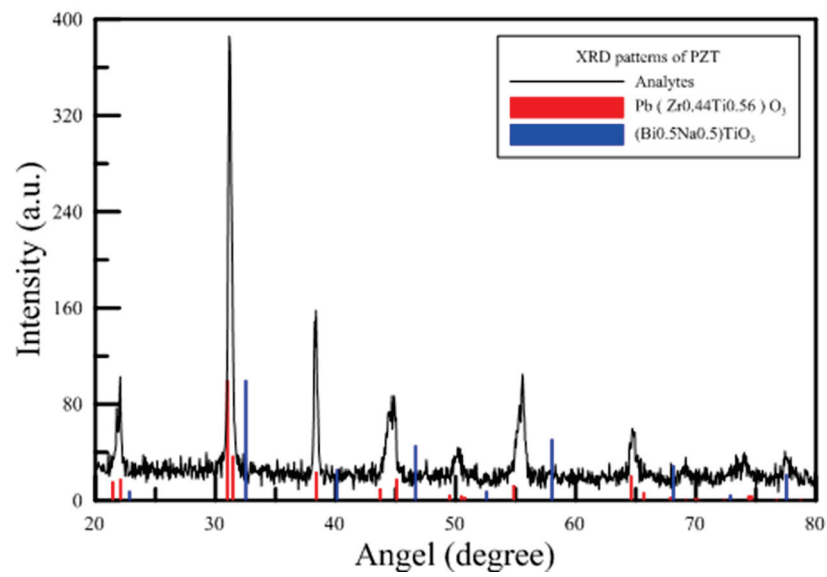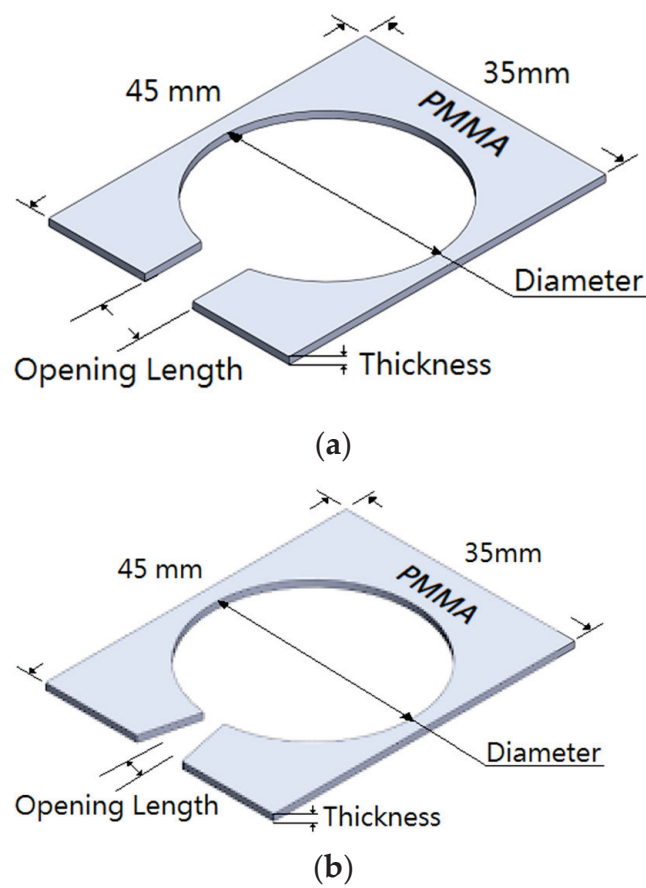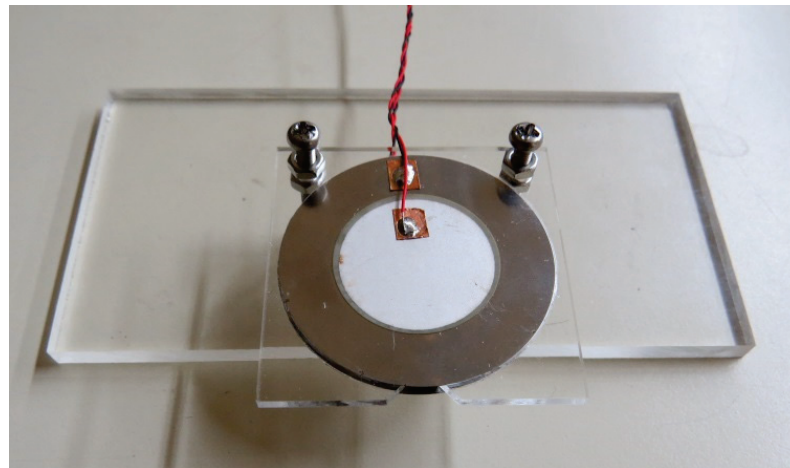
Figure 6. XRD patterns of the present PZT.

(**a**)

(**b**)

Figure 7. *Cont.*

(**c**)

Figure 7. Schematic diagram of jet path. (**a**) Linear type (**b**) Flared type (**c**) Real PAJ.

Table 1. Specifications of devices of piezo actuation jet.

Case No.	Diameter (mm)	Cavity Volume (mm^3)	Opening Length (mm)	Opening Area (mm^2)	Spacing (mm)
Case1	41	2513.3	10	20	2
Case2	41	2513.3	4	8	2
Case3	31	1413.7	10	20	2
Case4	31	1413.7	4	8	2
Case5	41	3769.9	10	30	3

3. Results and Discussion

This study focused on the characteristics of the device of PAJs with respect to their capacity for heat dissipation when used with a HI-LED. The linear jet path may provide a greater amount of wind, but the wind speed was low. While the linear jet path can effectively reduce the thermal resistance of thermal diffusion, for LED lights more than 3 W, the cooling effect is poor. When the device of the piezo actuation jet is too close to the heat source, the high temperature surrounding the heat source will be returned, causing the chamber temperature to rise and reducing the cooling effect. The flared jet path has a narrower outlet area to enhance the wind speed of the jet stream and can significantly reduce the thermal resistance of thermal convection. Moreover, the flared design on both sides of the jet path can increase the cooling area and slightly reduce the diffusion resistance. We altered the structural designs of the devices, as well as their operating conditions and placement in order to investigate the impacts of such changes on the cooling effect. We chose the optimal design and input conditions and then determined how to improve the performance of a device of piezo actuation jet. The size of the piezoelectric sheet will directly influence the performance of the device of the piezo actuation jet. In the present study, we used 41 mm and 31 mm piezoelectric sheets to conduct experiments under the same conditions. The area of the device of the piezo actuation jet was only 4% of the current commercial rotary fan.

3.1. Experiment of Performance Measurement

A piezoelectric sheet is a material that converts electricity into sound. The tone and intensity of the sounds produced depend on the voltage and the frequency of the electricity supplied to the sheet. In this study, the voltage was fixed at the maximum value of 30 V. The measurement range of the frequency was between 50 and 450 Hz. At the same time, we investigated the relationship between voltage frequency and metal sheet displacements.

3.1.1. Noise

This experiment made use of a handmade soundproof box. The background noise of the testing room was 41.6 dB, while inside the soundproof box it was 31.4 dB. The results were plotted according to the size of the piezoelectric sheet used in the given device. Figure 8a shows the results for three test devices named by case1, case2, and case5, in which the diameter of the piezoelectric sheet was 41 mm. As can be seen in Figure 8, the devices with piezoelectric sheets of the same size had a similar trend in terms of the growth of the noise produced. There was a significant increase in the volume at 150 Hz. With increasing frequency, the results of the noise intensity formed a parabola. The red line indicates the decibel level tested, 50.7 dB when the rotary fan was placed in the soundproof box. This was 1 dB lower compared to the device of piezo actuation jet at 300 Hz. Since the opening length was longer for the case1 and case5 devices, those devices had fewer places on which to fix the piezoelectric sheets than the case2 device, such that they caused more noise due to the free vibrations of the metal foil. The spacing of the piezoelectric sheet was larger in the case5 device. Therefore, the vibration noise produced by the device was about 1–2 dB louder than that produced by the case1 device, which is not very different. Figure 8b shows the results for the device of PAJs in which the diameter of the piezoelectric sheet was 31 mm (e.g., the case3 and case4 devices). As shown in the figure, the noise produced by the case3 device exhibited linear growth, while the slope of the parabola for the case4 device was roughly similar to a straight line. When the frequency was set at 125 to 225 Hz, the volume and the tone for both devices remained similar. Meanwhile, the case3 device produced a higher volume than the case4 device since it had a longer length of opening. The experimental results showed that the three devices of piezo actuation jets produced noise similar to that of the rotary fan at 300 Hz. At frequencies from 60 Hz–150 Hz, however, the noises caused by the three devices of PAJs were lower than that of the rotary fan. In addition, a device of piezo actuation jet has no wind shear effect; therefore, it can reduce its noise effectively by adopting a low operating frequency.

(a)

Figure 8. *Cont.*

(b)
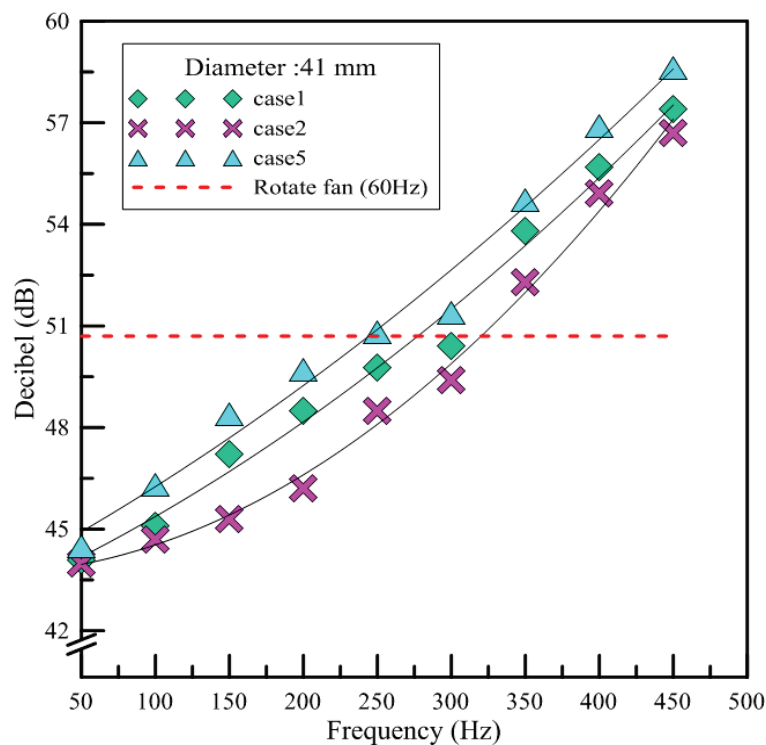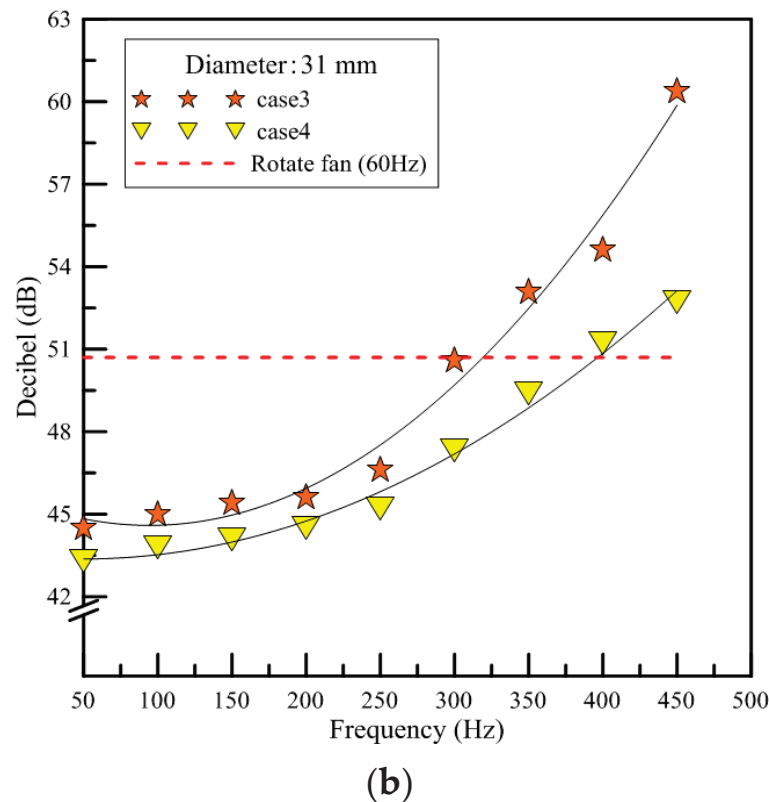
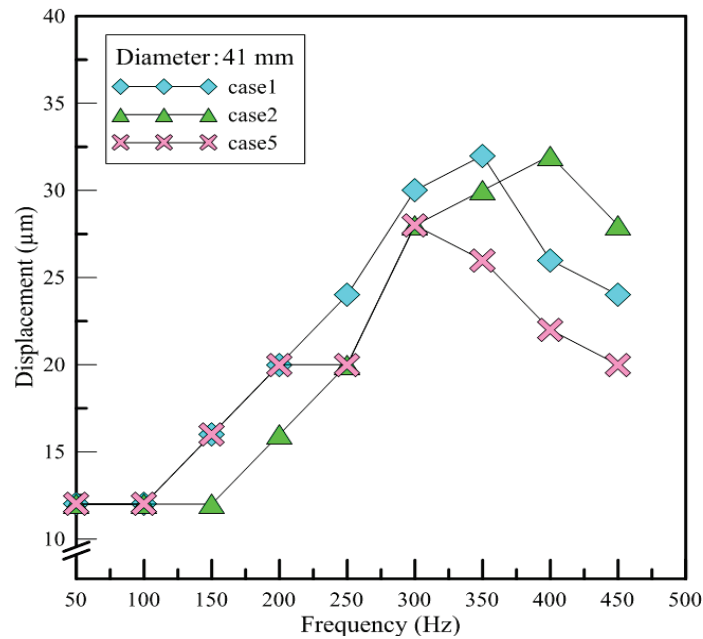**Figure 8.** The results of noise measurement. (**a**) Case1, case2, case5 (**b**) Case3, case4.

3.1.2. Displacement

When constructing a device of PAJ, the number of adhesives used and the fixed probes will be slightly different due to human error. However, it can be speculated from the findings that the same types of piezoelectric sheets have similar vibration behaviors. Figure 9a shows the displacement results for the test PAJs in which the diameter of the piezoelectric sheet was 41 mm. As shown in Figure 8, the amount of displacement exhibited a stair-step pattern, increasing every 50 to 100 Hz. The displacement divided by the frequency was between about 0.1 to 0.2 μm. Figure 9b shows the displacement results for the test PAJs in which the diameter of the piezoelectric sheet was 31 mm. When the frequency was below 280 Hz, there were no significant changes in the amount of displacement. The amount of displacement increased dramatically, however, when the frequency range was 290 to 300 Hz; the ratio of the displacement and the frequency was between 0.1 and 0.2 μm. The two different types of piezoelectric sheets exhibited completely different vibration behaviors in the same measurement range, yet for both types, the ratio of the displacement and the frequency was between 0.1 and 0.2 μm. The amount of displacement can be estimated using the input voltage frequency and the vibration is related to the type of piezoelectric sheet.
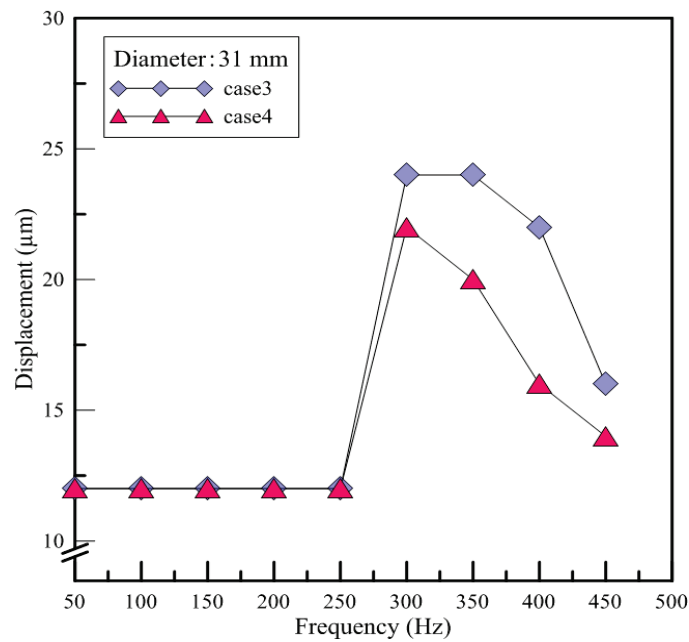
3.1.3. Wind Speed

Since the wind speeds of the rotary fan and the piezoelectric fan are not high, if the distance from the heat source is too great, the air jet cannot exchange heat with the heat source and the effect of forced convection cannot function properly. In this section, the wind speed is used to determine the cooling effect and the size of the wind velocity perturbation can be regarded as the indicator for the strength of the turbulence. Figure 10 shows the wind speed of devices at different distances from the hot-wire anemometer. The results show that the wind speed and placement of the rotary fan and devices are inversely proportioned. In case3, the wind speeds measured at 15 mm and 20 mm are larger than at 10 mm. This is because the wind speed is weak in case3 and generates a pair of vortexes at

15 to 20 mm to disturb the ambient air. Therefore, the wind speed is higher. When placed at 25 mm, it will not be affected. In case4, a larger wind speed is generated at 20 mm, while at 25 mm it is not affected. The devices of PAJ are unstable at low frequencies. The interval time between expansion and compression is longer so that it should be no outward expansion flow field, but only the inward airflow into the cavity. When a higher wind speed is generated during the compression, it causes unstable wind speeds. Therefore, accuracy is lower. When frequencies are above 150 Hz, the time interval is shortened and it can be regarded as a continuous outward airflow and the wind speeds will stabilize.
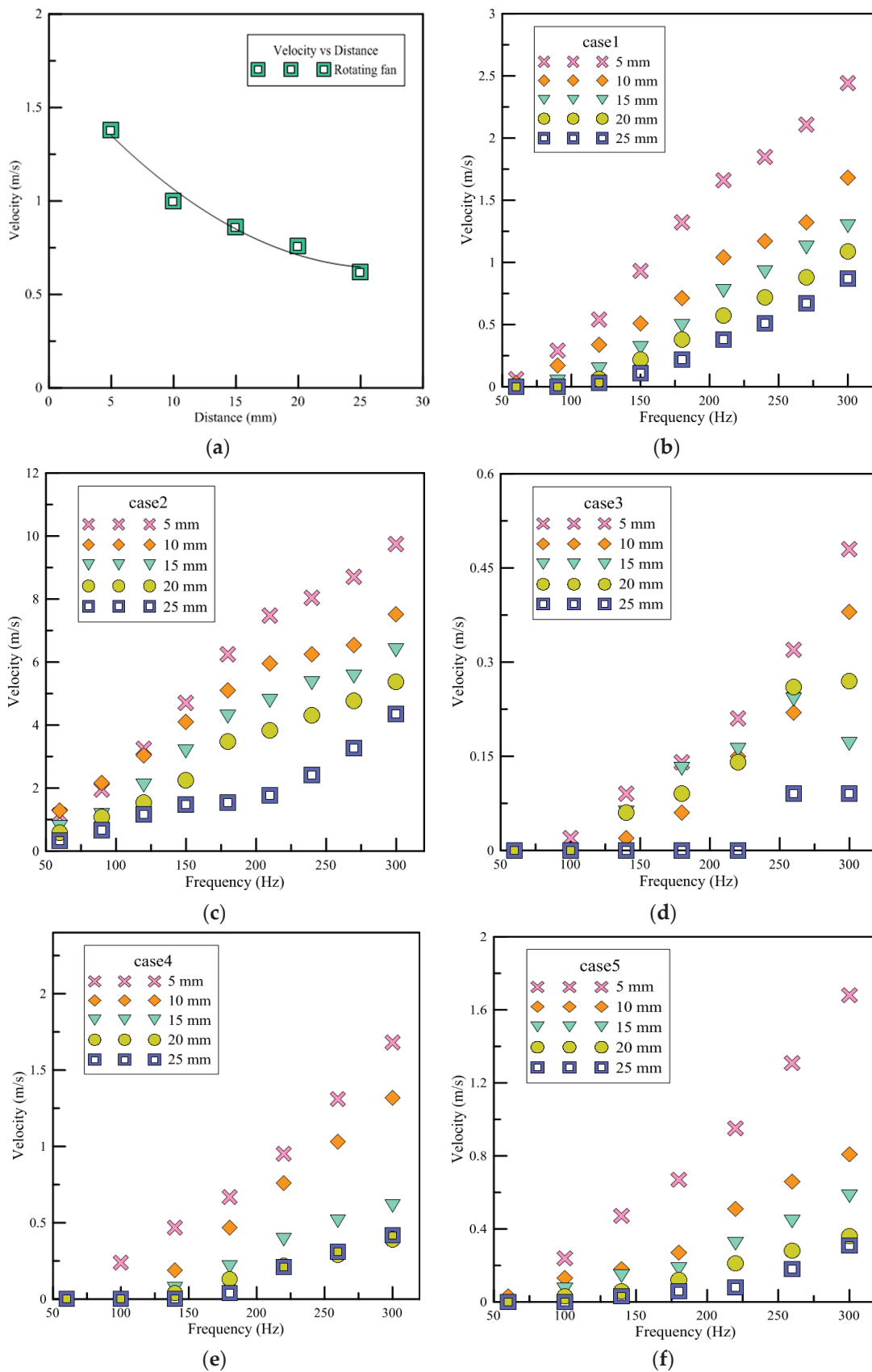

Figure 9. The results of displacement measurement. (**a**) Case1, case2, case5 (**b**) Case3, case4.

Figure 10. Each device when the wind speed and placement diagrams under different frequencies. (**a**) Rotary fan (**b**) Case1 (**c**) Case2 (**d**) Case3 (**e**) Case4 (**f**) Case5.

3.2. LED Thermal Performance Experiment

For a single LED, the operating temperature is approximately −40 °C to 80 °C, yet the temperature of the light-emitting crystal can reach about 120 °C which has a tremendous impact on the luminous efficiency and the lifespan, so the temperature must be kept under 80 °C. The temperature of the LED module will be stable after 30 min; therefore, it was recorded every 40 min in this experiment. The original design of LED was for 3 W in the present study. However, the natural temperature of the jet exceeds 80 °C at 4 W, so the wattage supply was no longer increased. Since the power supply can not directly set the wattage and only the voltage and current can be altered, these were adjusted to a similar wattage. The energy supplied to the LED will not be completely converted to light; currently, the light efficiency of white LEDs is about 30%, while the other 70% is converted to heat. The devices of PAJ used in the experiment were tested under the same operating conditions; the ambient temperature was 25.3 °C, the input voltage was 30 V, the voltage frequency was 300 Hz, and they were, respectively, placed at distances of 5 mm, 10 mm, 15 mm, 20 mm and 25 mm to analyze the different cooling effects by observing the changes in thermal resistances. Figure 11a compares the position and the total thermal resistance. Among the five designs, case2 has the best cooling effect when placed at 20 mm, reducing the LED module temperature to 36.4 °C, which is lower than the natural convection when supplied 1 W. Therefore, it can continuously increase the wattage of LED lights to provide better illumination capability. The worst cooling effects were achieved when placing the device at 5 mm in case4 and at 25 mm in case3. It can be seen that even though the device of PAJ consisted of small pieces of piezoelectric sheets with a diameter of 31 mm and had a flared jet path and smaller spacing, its cooling effect is not ideal from the present findings. This is mainly because the measured amplitude of displacement in the vibration experiment based on a diameter of 31 mm is small. The volume flow rate of the air that can be forced into the cavity is low and the jet strength is weak so that there was no significant improvement in convection. When the device of PAJ was placed at 5 mm in case5, it lowered the temperature of the LED module to 26.3 °C, whereas case1 reduced the temperature to 27.1 °C. The results show that when increasing the distance between the piezoelectric sheets, the cooling capability of the device of PAJ deteriorates.
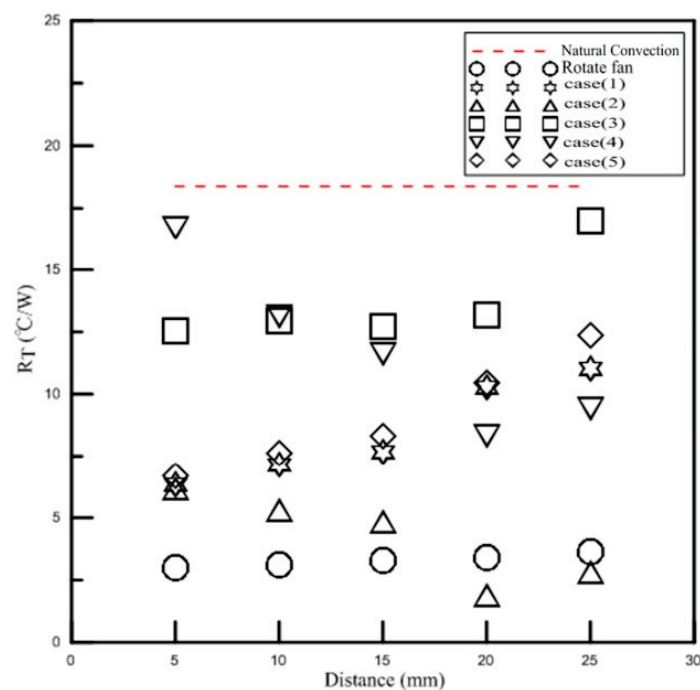
(**a**)

Figure 11. *Cont.*
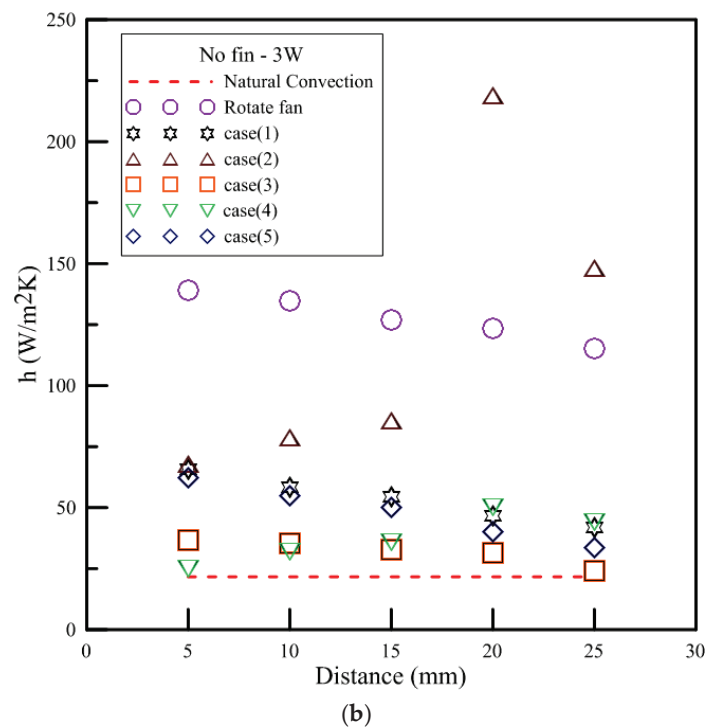
Figure 11. 3W LED experimental data. (**a**) Position vs. total thermal resistance (**b**) Position vs. heat convection coefficient.

Figure 11b compares the position and heat convection coefficient. The heat convection coefficient for case1 is 129 W/m^{2}K placed at 5 mm. When the placing distance increased to 25 mm, the heat convection coefficient reduced to 81.7 W/m^{2}K. The efficiency of the heat convection decreased as distance increased. The heat convection coefficient of the case2 is 132.9 W/m^{2}K placed at 5 mm. In addition, it can upgrade to three times if placed at 20 mm. The heat convection coefficients of case3 and case4 are about 48 to 98 W/m^{2}K, respectively. The enhanced heat convection efficiency is not large compared to other devices of piezo actuation jet, yet it still can be applied to the heat source with low wattage. Case5 can enhance its convection efficiency to between 157% and 288% compared to natural convection. The case1, case3, and case5 can be applied to the heat source at a short distance due to the experimental results and previous analysis. Since they have larger opening lengths and areas, they can inhale a wider range of the air jet around with large air volume but low wind speed. If placed too far away from the heat source, then it can not achieve its cooling effect. The PAJ device placed with 5 mm had the best cooling performance among these five locations. Besides, case2 and case4 had the best heat dissipation effect at 20 mm. case2 and case4 have higher wind speeds, increasing distance is conducive to sucking in the surrounding fluid and to avoid hot air is sucked back again. However, the strength of the airflow is limited. When the distance increases to 25 mm, the strength of the airflow will decrease and is not conducive to heat dissipation.

4. Conclusions

The present study designed a novel type of piezoelectric fan and investigated operating input conditions such as voltage frequency, placement distance, spacing between piezoelectric sheets, piezoelectric sheet size, and noise produced. The experimental results show that when a device of piezo actuation jet is placed too close to the heat source, the high temperature will suck back the surrounding fluids, causing the fluid chamber temperature to rise and the cooling effect to be reduced. However, the preferred design and operating conditions can fully make use of the device with a better cooling effect than traditional rotary fans. Additionally, the device should be placed 10 to 20 mm from the heat source to ensure that the temperature of the air returned to the chamber will be able to achieve an

optimal cooling effect. However, if the device of the PAJ is placed too far away, it will not be able to send wind to the heat source and will not be able to effectively dissipate heat. The device of 41 mm increases the opening area and the spacing of the piezoelectric sheet, the performance is still better than the device consisting of 31 mm piezoelectric sheets. Moreover, the power consumption comparison results show that the power needed for the device of piezo actuation jet to reduce temperature 1 °C is only 10% to 25% of the power needed of a rotary fan and the device of piezo actuation jet has lower costs. Finally, about 25 devices of PAJ can be connected in series while taking up no more space, which can offer above twenty-five times the number of heat convection effects.

References

1. Toda, M. Theory of air flow generation by a resonant type PVF2 bimorph cantilever vibrator. *Ferroelectrics* **1978**, *22*, 911–918. [CrossRef]
2. Toda, M. Voltage-Induced large amplitude bending device-PVF 2 Bimorph-its properties and applications. *Ferroelectrics* **1981**, *32*, 127–133. [CrossRef]
3. Kumar, V.; Babu, T.; Tiwari, B. A literature review of the research on ferroelectric polymers. *J. Phys. Conf. Ser.* **2021**, *1913*, 012064. [CrossRef]
4. Elnabawy, E.; Hassanain, A.H.; Shehata, N.; Popelka, A.; Nair, R.; Yousef, S.; Kandas, I. Piezoelastic PVDF/TPU Nanofibrous Composite Membrane: Fabrication and Characterization. *Polymers* **2019**, *11*, 1634. [CrossRef]
5. Oh, W.J.; Lim, H.S.; Won, J.S.; Lee, S.G. Preparation of PVDF/PAR Composites with Piezoelectric Properties by Post-Treatment. *Polymers* **2018**, *10*, 1333. [CrossRef]
6. Dzedzickis, A.; Sutinys, E.; Bucinskas, V.; Samukaite-Bubniene, U.; Jakstys, B.; Ramanavicius, A.; Morkvenaite-Vilkonciene, I. Polyethylene-Carbon Composite (Velostat®) Based Tactile Sensor. *Polymers* **2020**, *12*, 2905. [CrossRef]
7. He, Z.; Rault, F.; Lewandowski, M.; Mohsenzadeh, E.; Salaün, F. Electrospun PVDF Nanofibers for Piezoelectric Applications: A Review of the Influence of Electrospinning Parameters on the β Phase and Crystallinity Enhancement. *Polymers* **2021**, *13*, 174. [CrossRef] [PubMed]
8. Kaspar, P.; Sobola, D.; Částková, K.; Knápek, A.; Burda, D.; Orudzhev, F.; Dallaev, R.; Tofel, P.; Trčka, T.; Grmela, L.; et al. Characterization of Polyvinylidene Fluoride (PVDF) Electrospun Fibers Doped by Carbon Flakes. *Polymers* **2020**, *12*, 2766. [CrossRef]
9. Chen, J.; Xiong, X.; Zhang, Q.; Shui, L.; Shen, S.; Yang, H.; Zhu, Z.; Zhang, F. P (VDF-TrFE)/PMMA blended films with enhanced electrowetting responses and superior energy storage performance. *Polymers* **2019**, *11*, 526. [CrossRef]
10. Mahapatra, S.D.; Mohapatra, P.C.; Aria, A.I.; Christie, G.; Mishra, Y.K.; Hofmann, S.; Thakur, V.K. Piezoelectric Materials for Energy Harvesting and Sensing Applications: Roadmap for Future Smart Materials. *Adv. Sci.* **2021**, 2100864. [CrossRef] [PubMed]
11. Yoo, J.H.; Hong, J.I.; Cao, W. Piezoelectric ceramic bimorph coupled to thin metal plate as cooling fan for electronic devices. *Sens. Actuators A Phys.* **2000**, *79*, 8–12. [CrossRef]
12. Yoo, J.H.; Hong, J.I.; Park, C.Y. Characteristics of piezoelectric fans using PZT ceramics. In Proceedings of the IEEE 5th International Conference on Properties and Applications of Dielectric Materials, Seoul, Korea, 25–30 May 1997; Volume 2, pp. 1075–1081.
13. Kalel, S.; Wang, W.-C. Integration of SMP with PVDF Unimorph for Bending Enhancement. *Polymers* **2021**, *13*, 415. [CrossRef]
14. Wu, S.; Mai, J.; Tai, Y.C.; Ho, C.M. Micro heat exchanger by using MEMS impinging jets. In Technical Digest. IEEE International MEMS 99 Conference. In Proceedings of the 12th IEEE International Conference on Micro Electro Mechanical Systems (Cat. No. 99CH36291), Orlando, FL, USA, 21 January 1999; pp. 171–176.
15. Ko, J.; Oh, M.H.; Choi, M. Effects of piezoelectric fan on cooling flat plate in quiescent air. *Eur. J. Mech. B/Fluids* **2021**, *88*, 199–207. [CrossRef]
16. Ebrahimi, N.D.; Wang, Y.; Ju, Y.S. Sensors and actuators A: Physical mechanisms of power dissipation in piezoelectric fans and their correlation with convective heat transfer performance. *Sens. Actuators A Phys.* **2018**, *272*, 242–252. [CrossRef]

17. Ebrahimi, N.D.; Eldredge, J.D.; Ju, Y.S. Wake vortex regimes of a pitching cantilever plate in quiescent air and their correlation with mean flow generation. *J. Fluids Struct.* **2019**, *84*, 408–420. [CrossRef]

18. Smith, B.L.; Swift, G.W. A comparison between synthetic jets and continuous jets. *Exp. Fluids* **2003**, *34*, 467–472. [CrossRef]

19. Smith, B.L.; Swift, G.W. Power dissipation and time-averaged pressure in oscillating flow through a sudden area change. *J. Acoust. Soc. Am.* **2003**, *113*, 2455–2463. [CrossRef]

20. Park, S.H.; Oh, M.H.; Kim, Y.-H.; Choi, M. Effects of freestream on piezoelectric fan performance. *J. Fluids Struct.* **2019**, *87*, 302–318. [CrossRef]

21. Wu, T.; I Ro, P.; Kingon, A.I.; Mulling, J.F. Piezoelectric resonating structures for microelectronic cooling. *Smart Mater. Struct.* **2003**, *12*, 181–187. [CrossRef]

22. Kercher, D.; Lee, J.-B.; Brand, O.; Allen, M.; Glezer, A. Microjet cooling devices for thermal management of electronics. *IEEE Trans. Components Packag. Technol.* **2003**, *26*, 359–366. [CrossRef]

23. Conway, C.; Jeffers, N.; Agarwal, A.; Punch, J. Influence of thickness on the flow field generated by an oscillating cantilever beam. *Exp. Fluids* **2020**, *61*, 1–19. [CrossRef]

24. Liu, T.J.-C.; Chen, Y.-S.; Ho, H.-Y.; Liu, J.-T. Vibration and cooling performances of piezoelectric cooling fan: Numerical and experimental investigations. *MATEC Web Conf.* **2020**, *306*, 04002. [CrossRef]

25. Jalilvand, A.; Mochizuki, M.; Saito, Y.; Kawahara, Y.; Singh, R.; Wuttijumnong, V. Cooling Performance Evaluation of Synthetic Jet Based Thermal Solution Module. *J. Therm. Sci. Eng. Appl.* **2015**, *7*, 031010. [CrossRef]

26. Zhou, W.; Yuan, L.; Wen, X.; Liu, Y.; Peng, D. Enhanced impingement cooling of a circular jet using a piezoelectric fan. *Appl. Therm. Eng.* **2019**, *160*, 114067. [CrossRef]

27. Shahrestani, A.B.; Alshuraiaan, B.; Izadi, M. Combined natural convection-FSI inside a circular enclosure divided by a movable barrier. *Int. Commun. Heat Mass Transf.* **2021**, *126*, 105426. [CrossRef]

28. Matamoros-Ambrocio, M.; Sánchez-Mora, E.; Gómez-Barojas, E.; Luna-López, J. Synthesis and Study of the Optical Properties of PMMA Microspheres and Opals. *Polymers* **2021**, *13*, 2171. [CrossRef]

29. Lin, G.; Li, D.; Liu, M.; Zhang, X.; Zheng, Y. Rheology, non-isothermal crystallization behavior, mechanical and thermal properties of PMMA-modified carbon fiber-reinforced poly (ethylene terephthalate) composites. *Polymers* **2018**, *10*, 594. [CrossRef]

30. Thakur, V.K.; Thunga, M.; Madbouly, S.A.; Kessler, M. PMMA-g-SOY as a sustainable novel dielectric material. *RSC Adv.* **2014**, *4*, 18240–18249. [CrossRef]

31. Yuan, M.; Xu, L.; Cui, X.; Lv, J.; Zhang, P.; Tang, H. Facile Synthesis of Ultrahigh Molecular Weight Poly(Methyl Methacrylate) by Organic Halides in the Presence of Palladium Nanoparticles. *Polymers* **2020**, *12*, 2747. [CrossRef]

32. El-Bashir, S.; Althumairi, N.; Alzayed, N. Durability and Mechanical Performance of PMMA/Stone Sludge Nanocomposites for Acrylic Solid Surface Applications. *Polymers* **2017**, *9*, 604. [CrossRef]

33. Zafar, M.S. Prosthodontic Applications of Polymethyl Methacrylate (PMMA): An Update. *Polymers* **2020**, *12*, 2299. [CrossRef]

34. Wang, J.-C.; Li, A.-T.; Tsai, Y.-P.; Hsu, R.-Q. Analysis for diving regulator applying local heating mechanism of vapor chamber in insert molding process. *Int. Commun. Heat Mass Transf.* **2011**, *38*, 179–183. [CrossRef]

35. Wang, J.-C.; Chang, T.-L.; Lee, Y.-W. *Insert Molding Process Employing Vapour Chamber*; IntechOpen: London, UK, 2012.

36. Tsai, Y.-P.; Wang, J.-C.; Hsu, R.-Q. The effect of vapor chamber in an injection molding process on part tensile strength. *Exp. Tech.* **2009**, *35*, 60–64. [CrossRef]

37. Wang, R.-T.; Wang, J.-C. Optimization of heat flow analysis for exceeding hundred watts in HI-LEDs projectors. *Int. Commun. Heat Mass Transf.* **2015**, *67*, 153–162. [CrossRef]

38. Wang, J.-C.; Wang, R.-T.; Chang, T.-L.; Hwang, D.-S. Development of 30Watt high-power LEDs vapor chamber-based plate. *Int. J. Heat Mass Transf.* **2010**, *53*, 3990–4001. [CrossRef]

39. Wang, J.-C. Thermoelectric transformation and illuminative performance analysis of a novel LED-MGVC device. *Int. Commun. Heat Mass Transf.* **2013**, *48*, 80–85. [CrossRef]

40. Tucker, R.; Khatamifar, M.; Lin, W.; McDonald, K. Experimental investigation of orientation and geometry effect on additive manufactured aluminium LED heat sinks under natural convection. *Therm. Sci. Eng. Prog.* **2021**, *23*, 100918. [CrossRef]

41. Wang, J.-C. Thermal investigations on LED vapor chamber-based plates. *Int. Commun. Heat Mass Transf.* **2011**, *38*, 1206–1212. [CrossRef]

42. Wang, R.T.; Wang, J.C. Analysis of thermal conductivity in HI-LEDs lighting materials. *J. Mech. Sci. Technol.* **2017**, *31*, 2911–2921. [CrossRef]

Article

Design of Dopant and Lead-Free Novel Perovskite Solar Cell for 16.85% Efficiency

Syed Abdul Moiz * and **Ahmed N. M. Alahmadi**

Department of Electrical Engineering, Umm Al Qura University, Makkah 21955, Saudi Arabia; anmahmadi@uqu.edu.sa
* Correspondence: sasyed@uqu.edu.sa

Abstract: Halide based perovskite offers numerous advantages such as high-efficiency, low-cost, and simple fabrication for flexible solar cells. However, long-term stability as well as environmentally green lead-free applications are the real challenges for their commercialization. Generally, the best reported perovskite solar cells are composed of toxic lead (Pb) and unstable polymer as the absorber and electron/hole-transport layer, respectively. Therefore, in this study, we proposed and simulated the photovoltaic responses of lead-free absorber such as cesium titanium (IV) bromide, Cs_2TiBr_6 with dopant free electron phenyl-C_{61}-butyric acid methyl ester (PCBM), and dopant free hole transport layer N,N′-Di(1-naphthyl)-N,N′-diphenyl-(1,1′-biphenyl)-4,4′-diamine (NPB) for the Ag/BCP/PCBM/Cs_2TiBr_6/NPB/ITO based perovskite solar cell. After comprehensive optimization of each layer through vigorous simulations with the help of software SCAPS 1D, it is observed that the proposed solar cell can yield maximum power-conversion efficiency up to 16.85%. This efficiency is slightly better than the previously reported power-conversion efficiency of a similar type of perovskite solar cell. We believe that the outcome of this study will not only improve our knowledge, but also triggers further investigation for the dopant and lead-free perovskite solar cell.

Keywords: solar cell; photovoltaic response; perovskite; lead-free; dopant-free; Cs_2TiBr_6; NPB; PCBM

1. Introduction

From the last few years, the power-conversion efficiency of perovskite solar cell has jumped from 3.8 to 25.5%, showing a remarkable progress in the history of photovoltaic industry [1]. Among these perovskite materials, methylammonium lead iodide ($MAPbI_3$) has shown an excellent performance for photovoltaic applications. Unfortunately, lead is a highly toxic material and its presence in the environment can seriously destroy our soil, water, and other natural resources [2]. Hence, it is highly recommended to replace lead with other lead-free perovskite materials for future photovoltaic applications.

Recently, a novel lead-free perovskite compound such as cesium titanium (IV) bromide (Cs_2TiBr_6) is being very popular and many researchers believe that this perovskite material has the full potential to replace $MAPbI_3$ for photovoltaic applications [3–5]. The Cs_2TiBr_6 perovskite offers excellent electrical, optical, and photovoltaic responses and similarly the incorporation of stable titanium (Ti) formulate Cs_2TiBr_6 a robust perovskite to tolerate higher thermal, electrical, environmental, and irradiation stresses [6].

For an efficient perovskite solar cell, the proper selection of both electron and hole-transport material is also very crucial. In this study, PCBM is used as a dopant free electron-transport layer with absorber Cs_2TiBr_6 for the novel perovskite solar cell. Generally, PCBM based fullerenes and their derivatives demonstrate excellent electron transport parameters which cause the reduction of the hysteresis of the photovoltaic responses [7,8]. For most cases, dopant-free bathocuproine (BCP) as a buffer layer between the cathode and PCBM is highly recommended to further improve the hysteresis, power-conversion efficiency, and stability of the perovskite solar cell [9]. Therefore, both BCP/PCBM combinations were used as an electron-transport layer for the proposed perovskite solar cell.

For the hole-transport layer, NPB (NPB or NPD both these abbreviations are frequently used for the same material) is a highly stable and commonly reported material for the perovskite solar cell [10,11]. The improved stability response of NPB compared to the other organic/polymer hole transport layer is mainly due to the hydrophobic nature of the NPB layer [12,13]. However, the doping of NPB may initiate many complex chemical processes leading to long-term stability issues for photovoltaic applications especially at a higher temperature [14–17]. Therefore, the dopant free NPB as a hole-transport layer was used for the current proposed perovskite solar cell.

Figure 1a,b depicts the schematic structure and the energy-band alignment diagram for the proposed p-i-n type perovskite solar cell, where ohmic Ag and ITO contacts are used as front-end cathode and back-end anode, respectively. The band alignment, as shown in Figure 1b, is nearly consistent with the natural flow of photocarrier transport in both the conduction as well as the valence band, which is the first step towards the design of an efficient solar cell for maximum photovoltaic response.
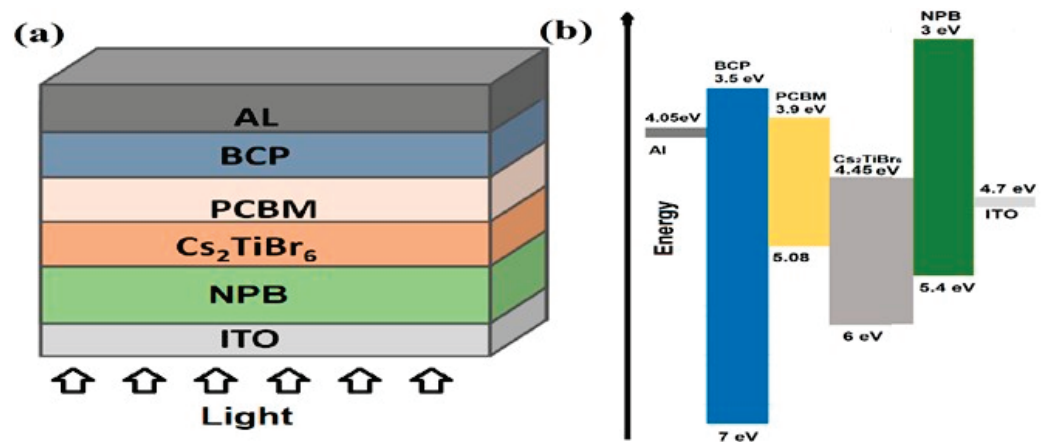
Figure 1. (**a**) The schematic structure, and (**b**) the energy-band alignment diagram of the proposed Ag/BCP/PCBM/Cs$_2$TiBr$_6$/NPB/ITO solar cell.

Simulation and modelling are one of the simplest, low-cost, and highly regarded methods for the comprehensive investigation and optimization for photovoltaic response [18]. In the literature, various simulation and modelling tools are available and here the solar cell capacitance simulator-1 dimension (SCAPS 1D) is selected for this study. The SCAPS 1D is a general-purpose tool and highly recommended by various research groups for the simulation and modelling of perovskite solar cell [19,20]. Therefore, in this study, we proposed, designed, simulated, and optimized the novel lead-free and dopant-free perovskite solar cell as Ag/BCP/PCBM/Cs$_2$TiBr$_6$/NPB/ITO for maximum power-conversion efficiency with the help of the SCAPS 1D software.

2. Simulation Method and Device Parameters

The comprehensive simulation of the proposed lead and dopant free solar cell is performed using SCAPS 1D (version 3.3.07), as discussed above. SCAPS 1D is an excellent simulation platform, which is used to simulate the various types of one-dimension photovoltaic response. Broadly speaking, SCAPS 1D implements a set of photovoltaic models to simulate any type of photovoltaic response [19–21].

SCAPS 1D offers an interface to couple the fundamental photovoltaic equations governed by the user-defined geometry and material parameters for each layer. The fundamental equations used in these simulations are Poisson equations, device continuity equations, drift-diffusion charge transport model, recombination losses with defects model, optical absorption models, etc. These fundamental models can be further explored as:

1. Poisson model states that the one-dimension (x) Laplacian of the electrostatic potential field (φ) is equal to the ratio of total volume charge density and the permittivity

$$\frac{d^2\varnothing(x)}{dx^2} = \frac{q}{\in_o \in_r} \left(p(x) - n(x) + N_D - N_A + \rho_p - \rho_n \right) \tag{1}$$

where q is the electronic charge (1.602×10^{-19} C), ε_0 is the permittivity of vacuumed, ε_r is the relative semiconductor permittivity, N_D/N_A are the shallow donor/acceptor impurity density, $n(x)/p(x)$ are the electron/hole density at a position x, and ρ_n/ρ_p are the electron/hole density distribution.

2. The device continuity model states that change in the electron/hole current density (J_n/J_p) over a specific time as a function of position is equal to the result of generation (G) and the recombination (R) of electron/hole, respectively.

$$\frac{dJ_n}{dx} = G - R \tag{2}$$

$$\frac{dJ_p}{dx} = G - R \tag{3}$$

3. The semiconductor charge transport model describes that the total electron/hole current density (J) is the sum of electron/hole drift and diffusion current density

$$J = J_n + J_p \tag{4}$$

$$J_n = D_n \frac{dn}{dx} + \mu_n \, n \frac{d\varnothing}{dx} \tag{5}$$

$$J_p = D_p \frac{dp}{dx} + \mu_p \, p \frac{d\varnothing}{dx} \tag{6}$$

where D_n/D_p are the electron/hole diffusion coefficient and μ_n/μ_p are the electron/hole mobility, respectively.

4. For the optical absorption coefficient, SCAPS offers different options for the calculation of the absorption coefficient $\alpha(\lambda)$, but in this study, we use the following equation depending on the relation of photons (h is the plank constant and ν is the photon frequency) and perovskite (as a absorber layer) energy bandgap (E_g)

$$\alpha(\lambda) = \left(A + \frac{B}{h\nu} \right) \sqrt{h\nu - E_g} \tag{7}$$

Further detailed information about the simulation methodology can be found in our previous published paper [22]. All the materials parameters are extracted from the reported literature for BCP, PCBM, Cs_2TiBr_6, and NPB, which are listed in Table 1 [22–28]. Similarly, for photovoltaic characterization, the proposed device was simulated under solar illumination of air mass AM 1.5 G at 1 sun photons intensity (1000 W/m^2), where ambient temperature of 300 K was used for photovoltaic simulation.

Table 1. Materials parameters of BCP, PCBM, Cs_2TiBr_6, and NPB incorporated for these simulations are listed, where each layer thickness is just reported for the first estimation, which will further improve in later stages of the simulation.

Photovoltaic Parameters	Symbol	Unit	BCP	PCBM	Cs_2TiBr_6	NPB
Thickness	Th	nm	10	300	150	100
Energy Band Gap	Eg	eV	3.5	1.9	1.6	3
Electron Affinity	χ	eV	3.7	3.9	4.47	2.4
Dielectric Permittivity (Relative)	ε	-	10	4	10	3
Effective Density of States at Valence Band	N_V	cm^{-3}	2.2×10^{18}	2.2×10^{21}	1×10^{19}	1×10^{21}

<div align="center">**Table 1.** *Cont.*</div>

| Photovoltaic Parameters	Symbol	Unit	BCP	PCBM	Cs$_2$TiBr$_6$	NPB
Effective Density of States at Conduction Band	N$_C$	cm^{-3}	1.8×10^{18}	1.8×10^{20}	1×10^{19}	1×10^{21}
Hole Thermal Velocity	Ve	cm/s	1×10^7	1×10^7	1×10^7	1×10^7
Electron Thermal Velocity	Vh	cm/s	1×10^7	1×10^7	1×10^7	1×10^7
Electron Mobility	μe	cm^2/V·s	2×10^{-2}	1×10^{-1}	44	6.1×10^{-5}
Hole Mobility	μ$_h$	cm^2/V·s	2×10^{-3}	1.5×10^{-2}	2.5	6.1×10^{-4}
Uniform Shallow Donor Doping	Nd	cm^{-3}	1×10^{21}	1×10^{20}	1×10^{13}	1×10^{13}
Uniform Shallow Acceptor Doping	Na	cm^{-3}	1×10^{10}	1×10^{13}	0	1×10^{16}
Defect Density	N$_t$	cm^{-3}	1×10^{14}	1×10^{14}	1×10^{17}	1×10^{15}

3. Results and Discussion

As we have selected undoped materials, therefore the thickness of each layer was only optimized for the current proposed perovskite solar cell. The film thickness of hole-transport layer, perovskite absorber, and electron-transport layer play a very crucial role to optimize the overall photovoltaic response of perovskite solar cell. Both the electron-transport layer and hole-transport layer interact not only with the perovskite layer but also with their respective electrode materials. The interaction between PCBM and cathode interface is improved by incorporating a very thin layer of BCP with already reported optimized parameters as shown in Table 1, therefore the BCP layer is not further optimized in this study.

3.1. Thickness Optimization of Electron Transport Layer

For the non-inverted perovskite solar cell, the PCBM film-thickness depends on many factors such as charge collection from the perovskite layer, perovskite surface traps density, electron/hole recombination, carrier transport process, and electrode surface roughness. Therefore, in the first stage, the thickness of PCBM (as an electron-transport layer) was optimized for the proposed solar cell. In order to determine the optimize PCBM thickness for the proposed solar cell, we performed a series of photo current-voltage simulations and calculated the photovoltaic parameters such as open-circuit voltage, short-circuit current, fill-factor, and power-conversion efficiency by varying the PCBM thickness from 10 to 1000 nm, as shown in Figure 2. From the figure, it is observed that the open-circuit voltage sharply decreases from 2.5 volts and then saturates at close to 1.5 volts. While the short-circuit current, fill-factor, and most importantly power-conversion efficiency follow different trends with respect to the open-circuit voltage, where these responses sharply rise and then saturate at nearly 400 nm of PCBM thickness, as shown in Figure 2. Thus, it can be inferred from the above trends that the 400 nm is the optimum thickness of PCBM as an electron-transport layer for the proposed solar cell.

Generally, it is believed that the thinner PCBM layer may lead towards an improved charge transport process for the solar cell [29]. On the other hand, the solar cell is inherently a diode in nature and its photovoltaic response also depends on diode parameters such as the diode ideality factor, barrier-height, threshold-voltage, series resistance, shunt resistance, reverse saturation current, etc. and these parameters become further complex for the space-charge limited behavior of polymer diode [30–34]. Our simulation result shows that the thicker PCBM improves the device performance, which can be justified due to the better diode properties as it is also reported by many other researchers for the PCBM layer [35,36].
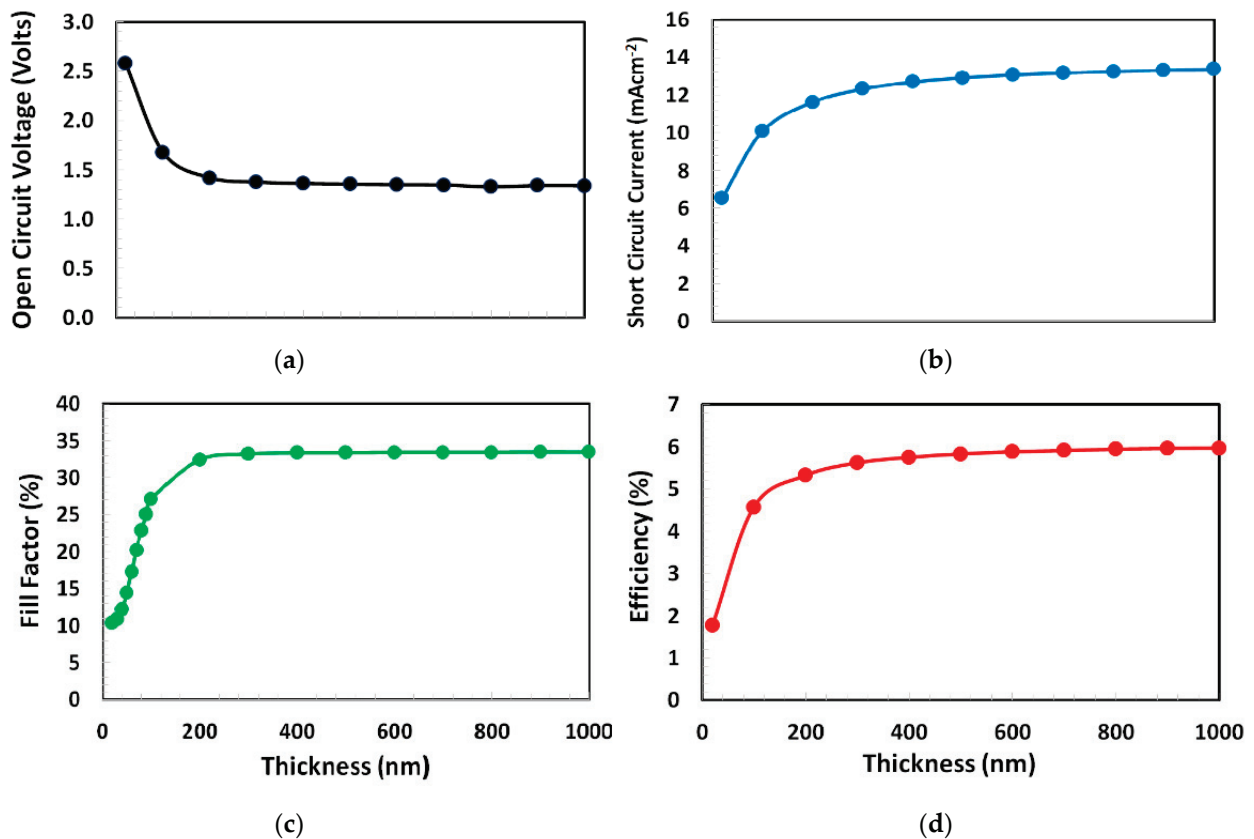
Figure 2. (**a**) Open-circuit voltage, (**b**) short-circuit current, (**c**) fill-factor, and (**d**) power-conversion efficiency of proposed solar cell Ag/BCP/PCBM/Cs$_2$TiBr$_6$/NPB/ITO as a function of PCBM layer thickness from 10 to 1000 nm.

### 3.2. Thickness Optimization of Hole Transport Layer

By incorporating the optimized thickness of PCBM (400 nm), the thickness of NPB was optimized using the same material parameters, as shown in Table 1. Similar to other conducting polymers, the variable-range hopping charge-transport process in NPB is also complicated in nature and depends on the film thickness of the polymer [37]. Similarly, the nature and density of traps states that perovskite-polymer interfaces are very crucial to define the transport through the polymer. Therefore, the interface trap states between the polymer and perovskite absorber layer are introduced in the simulation, where detailed information about the interface trap states are listed in Table 2.

Table 2. Interface traps parameters between the Cs$_2$TiBr$_6$ and NPB layer.

Parameters	Unit	Cs$_2$TiBr$_6$/NPB
Defect Type	-	Neutral
Capture cross section for electron	cm^{-3}	1×10^{14}
Capture cross section for electron	cm^{-3}	1×10^{14}
Enerfetic Distribution	-	Single
Energy level with respect to Ev	eV	6.0×10^{-1}
Characteristic Energy	eV	~0.1
Defect Density	cm^{-3}	4.5×10^{18}

In order to optimize the thickness of NPB as the hole-transport layer a series of simulations were performed and the photovoltaic responses were determined by varying the thickness of NPB from 10 to 1000 nm and the obtained photovoltaic parameters such as open-circuit voltage, short-circuit current, fill-factor, and power-conversion efficiency are shown in Figure 3. The figures clearly demonstrate that the open-circuit voltage behavior

is different from the other parameter's response. The open circuit voltage monotonously decreases as the thickness of NPB increases. Nevertheless, the short-circuit current, fill-factor, and power-conversion efficiency demonstrate a very similar response, where all these photovoltaic parameters and most importantly the power-conversion efficiency are slightly improved from 10 to 100 nm approximately and continuously degraded when the thickness of NPB increases from 100 to 1000 nm. Therefore, from the above results, it can be justified that the 100 nm is the most optimum thickness of NPB (gives maximum power-conversion efficiency ~16.5%) as the hole-transport layer for the current proposed Ag/BCP/PCBM/Cs_2TiBr_6/NPB/ITO perovskite solar cell.
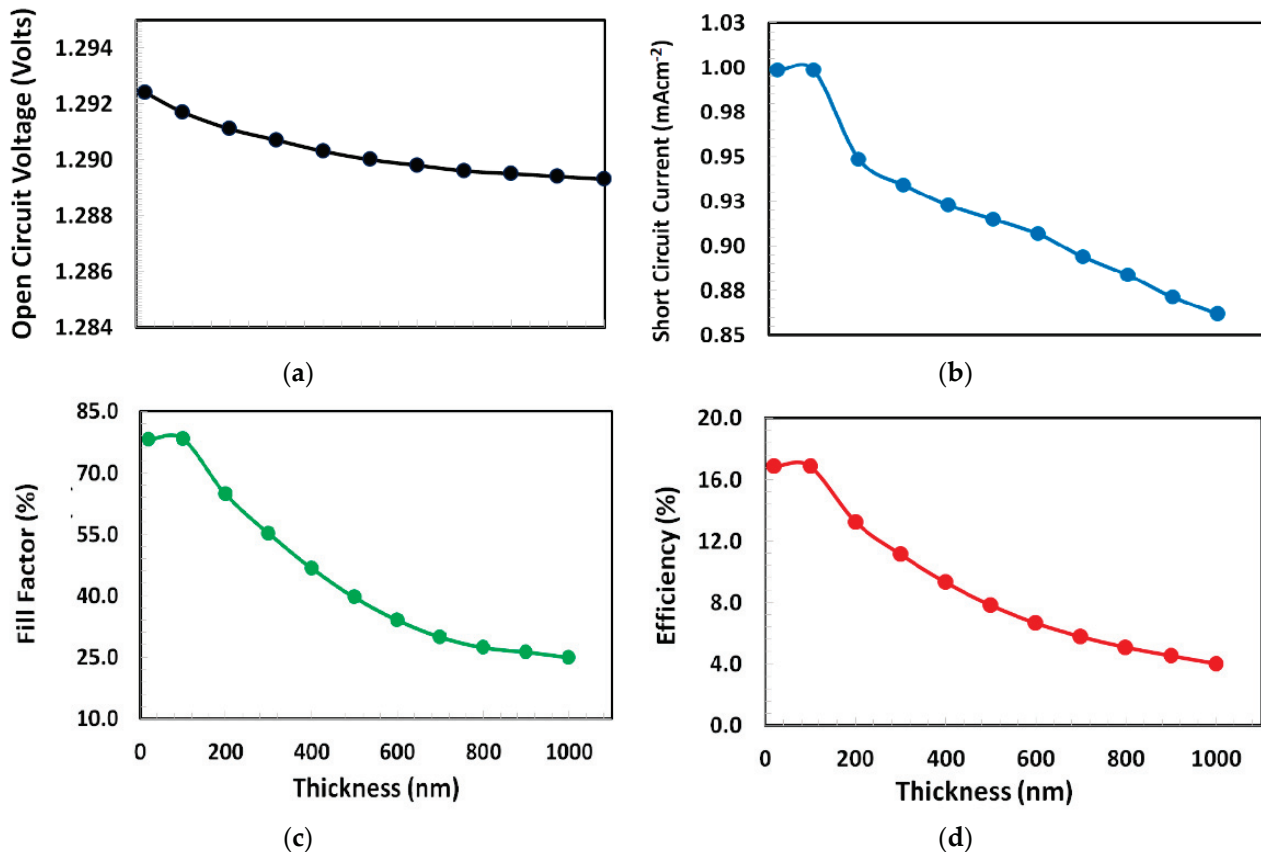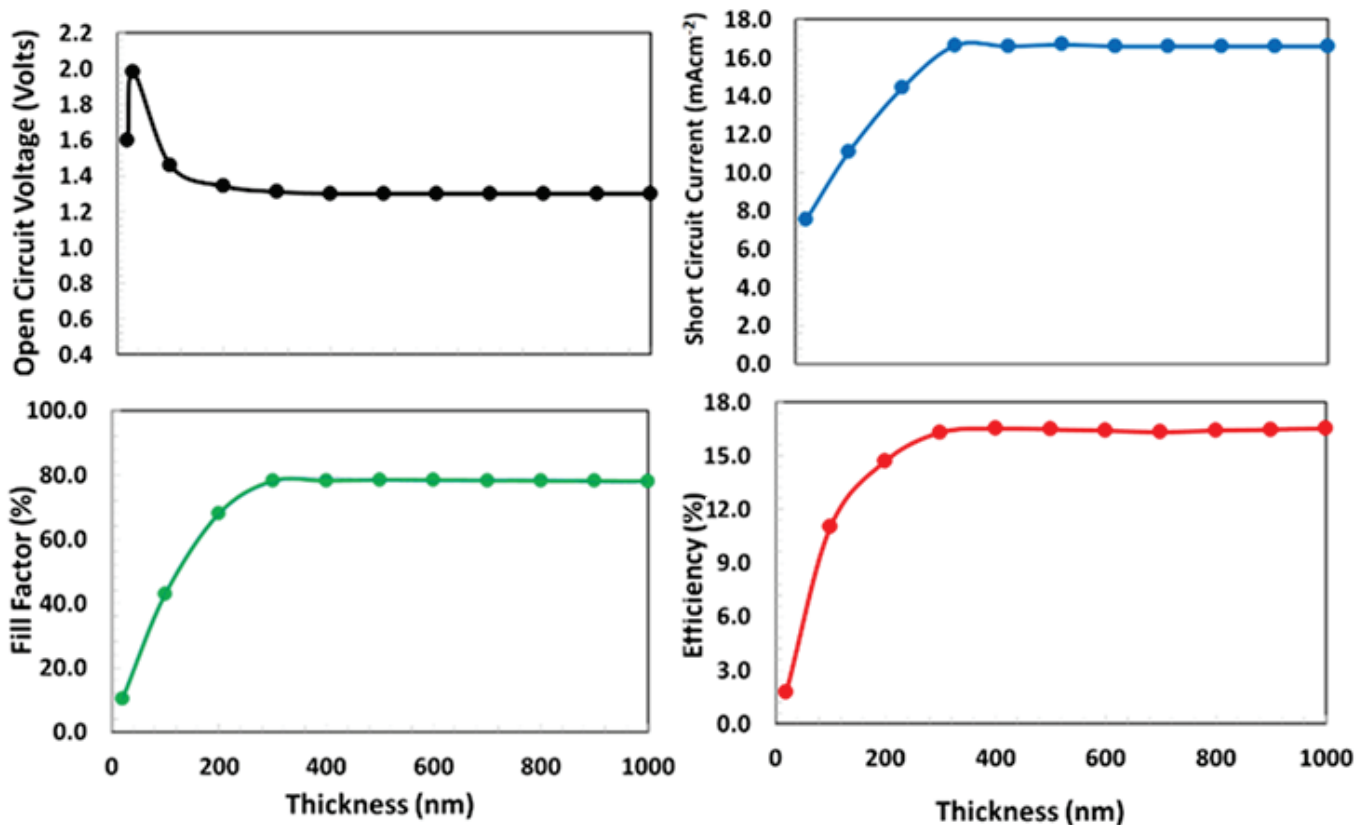

Figure 3. (**a**) Open-circuit voltage, (**b**) short-circuit current, (**c**) fill-factor, and (**d**) power-conversion efficiency of proposed solar cell Ag/BCP/PCBM/Cs_2TiBr_6/NPB/ITO as a function of NPB layer thickness varied from 10 to 1000 nm.

3.3. Optimization of Cs_2TiBr_6 as the Absorber Layer

The thickness optimization of the perovskite absorber layer is considered as one of the most crucial parts for the overall design of the proposed device for efficient performance. Either a very thin or very thick perovskite layer, is problematic in nature for the photovoltaic application. The thin perovskite layer offers poor photon absorption, while the thick perovskite layer compromises higher electron-holes recombination and hence degrades the photovoltaic response. Therefore, the optimum absorber layer thickness is the balance trade-off between these two factors. For the determination of design thickness of absorber layer, the optimized thickness of both PCBM (400 nm) and NPB (100 nm) layers and interface defect states were used in the proposed device and then a series of photo current-voltage simulations were carried-out. The photovoltaic parameters such as open-circuit voltage, short-circuit current, fill-factor, and power-conversion efficiency were calculated by varying the Cs_2TiBr_6 perovskite layer thickness from 10 to 1000 nm, as shown in Figure 4. From the figure, it is observed that photovoltaic parameters such as the fill-factor, short-circuit current, and power-conversion efficiency follow one trend, while the open-circuit

voltage follows different trends from the others. The fill-factor, short-circuit current, and power-conversion efficiency sharply rise and then saturate at nearly 350 nm of the absorber layer thickness, as shown in Figure 4. However, the open-circuit voltage shows a little different behavior, it sharply increases at 50 nm and then gradually decreases and becomes stable at nearly 200 nm of the absorber layer thickness. As the proposed device reaches the maximum power-conversion efficiency at 350 nm of the absorber layer thickness, therefore, it can be inferred from the above discussion that the 350 nm can be estimated as the optimized thickness (gives maximum power-conversion efficiency ~16.5%) for the perovskite absorber layer for the proposed solar cell.

Figure 4. (**a**) Open-circuit voltage, (**b**) short-circuit current, (**c**) fill-factor, and (**d**) power-conversion efficiency of proposed solar cell Ag/BCP/PCBM/Cs_2TiBr_6/NPB/ITO as a function of Cs_2TiBr_6 thickness from 10 to 1000 nm.

3.4. Photovoltaic Response of Proposed Solar Cell

Figure 5 shows the simulated current-voltage responses of the proposed solar cell both in the dark and in the presence of illumination, where the optimized thickness of PCBM (400 nm), NPB (100 nm), and Cs_2TiBr_6 (350 nm) as the electron-transport layer, hole-transport layer, and absorber layer were already incorporated in the simulation with interface defects states as discussed above. Both curves demonstrate the characteristics behavior of a photovoltaic diode response. In the dark current-voltage response, the proposed solar-cell shows a very low current passing-through the device especially at an earlier stage of the applied voltages. After the threshold voltage (approximately at 1.1 volts) both electrodes Ag and ITO started to inject relatively a large number of electrons and holes as the forward bias current [38,39]. Using the standard technique reported in the literature, the diode ideality factor was estimated as 1.3, which reflects the quality of the proposed diode as a solar cell [40,41].

Similarly, the proposed solar cell is also simulated for the photovoltaic response in the fourth quadrant operating between the open circuit and short circuit current, where a large amount of current flows when the solar-cell is illuminated, but this illuminated current is in the opposite direction compared to the dark current-voltage response, as shown in Figure 5. From the figure, it is clearly observed that the optimized device shows a reasonable photovoltaic response under the AM 1.5 illumination. As a result of this characterization, the photovoltaic parameters such as open-circuit voltage, short-circuit current. and fill-factor are extracted from the figure as 1.29 volts, 16.66 mA·cm^{-2}, and 78.11%, respectively. All these photovoltaic parameters lead to the maximum power-conversion efficiency for the optimized proposed solar cell up to 16.85%. This efficiency is better than the previously reported power-conversion efficiency of a doped-free, lead-free perovskite solar cell [42].
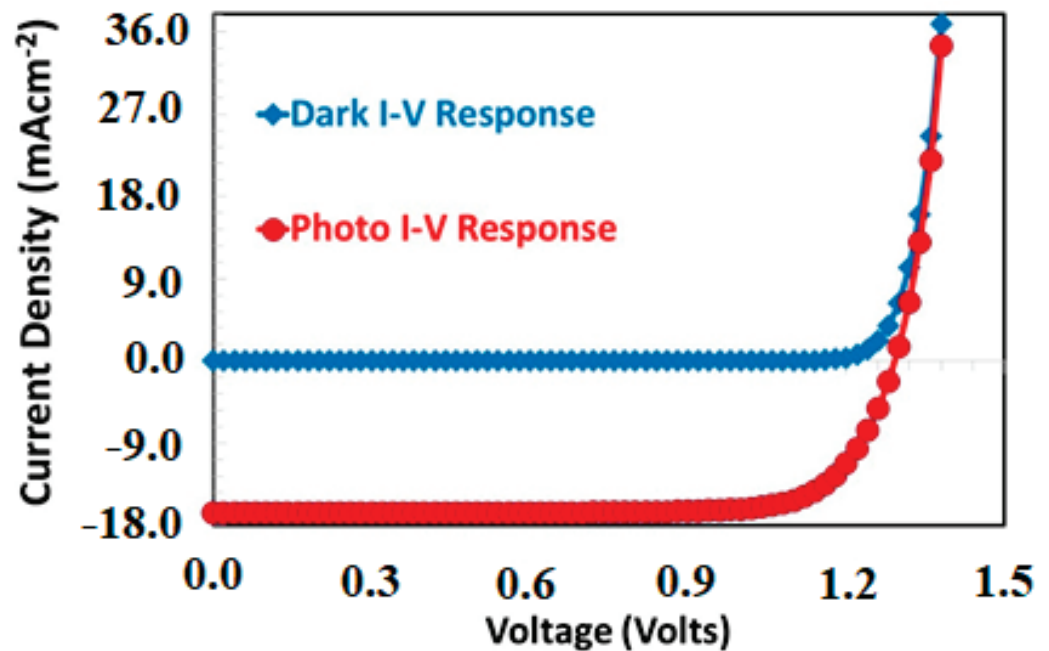

Figure 5. The simulated dark and AM 1.5 photovoltaic current responses of the proposed Ag/BCP/PCBM/Cs$_2$TiBr$_6$/NPB/ITO solar cell as a function of applied voltage.
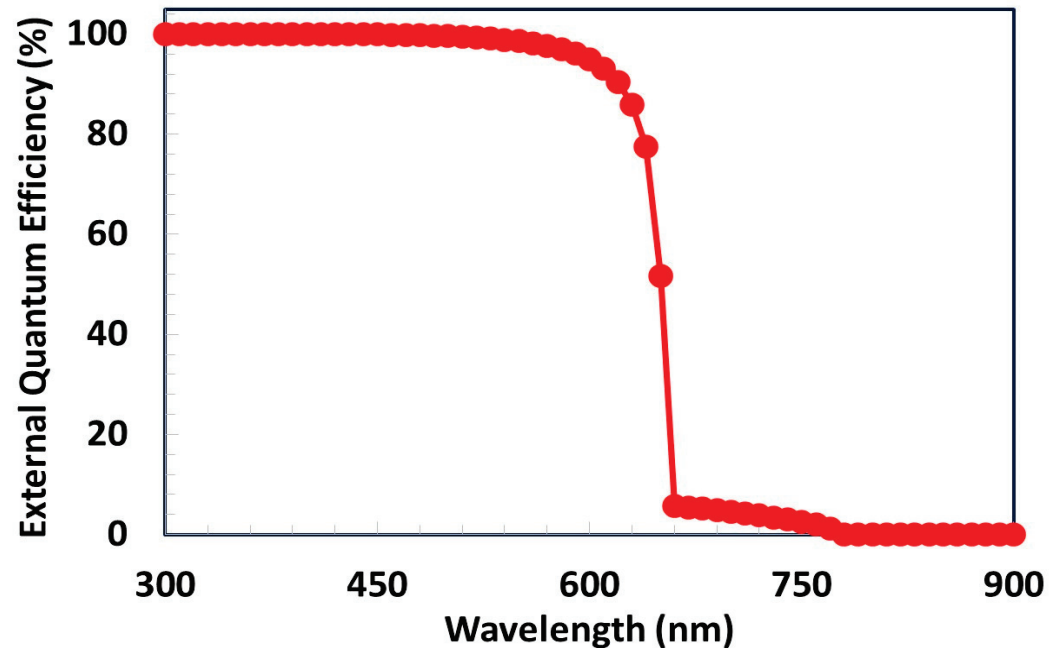
3.5. External Quantum Efficiency of Proposed Solar Cell

The external quantum efficiency response of the proposed Ag/BCP/PCBM/Cs$_2$TiBr$_6$/PTAA/ITO solar cell was simulated as a function of photons wavelength and the result is shown in Figure 6. The quantum efficiency for a photovoltaic device can be defined as the fraction of the free carriers collected from the respective electrodes to the total number of incident photons of a given wavelength (or energy) onto the top surface of the solar cell. Mathematically, the quantum efficiency and short-circuit current (J_{sc}) are directly related to each other as a function of photon wavelength ($\varphi(\lambda)$) and can be expressed as [43,44]

$$J_{SC} = q \int \varphi(\lambda)\, QE(\lambda) d\lambda \qquad (8)$$

Here, we theoretically analyzed the external quantum efficiency of the proposed solar cell as a function of wavelength from 300 to 1000 nm, as shown in Figure 6. For simplicity, the observed external quantum efficiency response can be classified into two well-define regions. (i) Region I: Between 300 to 700 nm, (ii) Region II: Above 700 nm. In region I, the reduction of quantum efficiency is generally observed due to the reflection of photons as well as the low carrier diffusion length. As Cs$_2$TiBr$_6$ has a very high career diffusion length, therefore the excellent quantum efficiency response (>95%) is observed compared to the ideal quantum efficiency (100%) for region I [4]. It can be clearly demonstrated that the

front-end (ITO) of proposed solar cell offers low optical reflections of photons. Hence, the proposed device shows the maximum external quantum efficiency for region I, which is a reasonably well-accepted value, as shown in Figure 6. In addition, as the energy band gap of Cs_2TiBr_6 is 1.55 eV, consequently, no photons are absorbed inside the proposed device for the higher photon's wavelength for region II, as shown in Figure 6.

Figure 6. External quantum efficiency response as a function of incident photon wavelength for the proposed solar cell.

3.6. Thermal Stability of the Proposed Solar Cell

The perovskite based solar cell has many types of defects, which in turn leads to some issues such as high carrier recombinational losses, degradation of interfacial contacts, and hence poor photovoltaic stability. The photovoltaic degradation becomes further aggravated when the perovskite solar cell is exposed to the higher ambient temperature. Therefore, the proposed solar cell is further characterized for the stability analysis by calculating the variation of photovoltaic parameters as a function of ambient temperature varied from 300 to 450 °K, as shown in Figure 7. From the figure, it is clearly observed that all the photovoltaic parameters are gradually degraded at higher temperature, but the rate of thermal degradation is different for each photovoltaic parameter. For a given temperature range if a linear model is applied for the relation between the normalized photovoltaic parameter and ambient temperature then their slope can be used as the rate of degradation (per °K) for a given photovoltaic parameter. From the figure, it is realized that both the short-circuit current and fill-factor shows very slow thermal degradation (rates of degradation are 2×10^{-4} and 3×10^{-4} per °K, respectively), while the open-circuit voltage and power-conversion efficiency also show very slow thermal degradation but higher than those in the short-circuit current and fill-factor for the proposed solar cell (rates of degradation are 1×10^{-3} and 1.5×10^{-3} per °K, respectively). Therefore, it can be stated from the above discussion that the proposed solar cell shows a relatively stable behavior within the given temperature range.
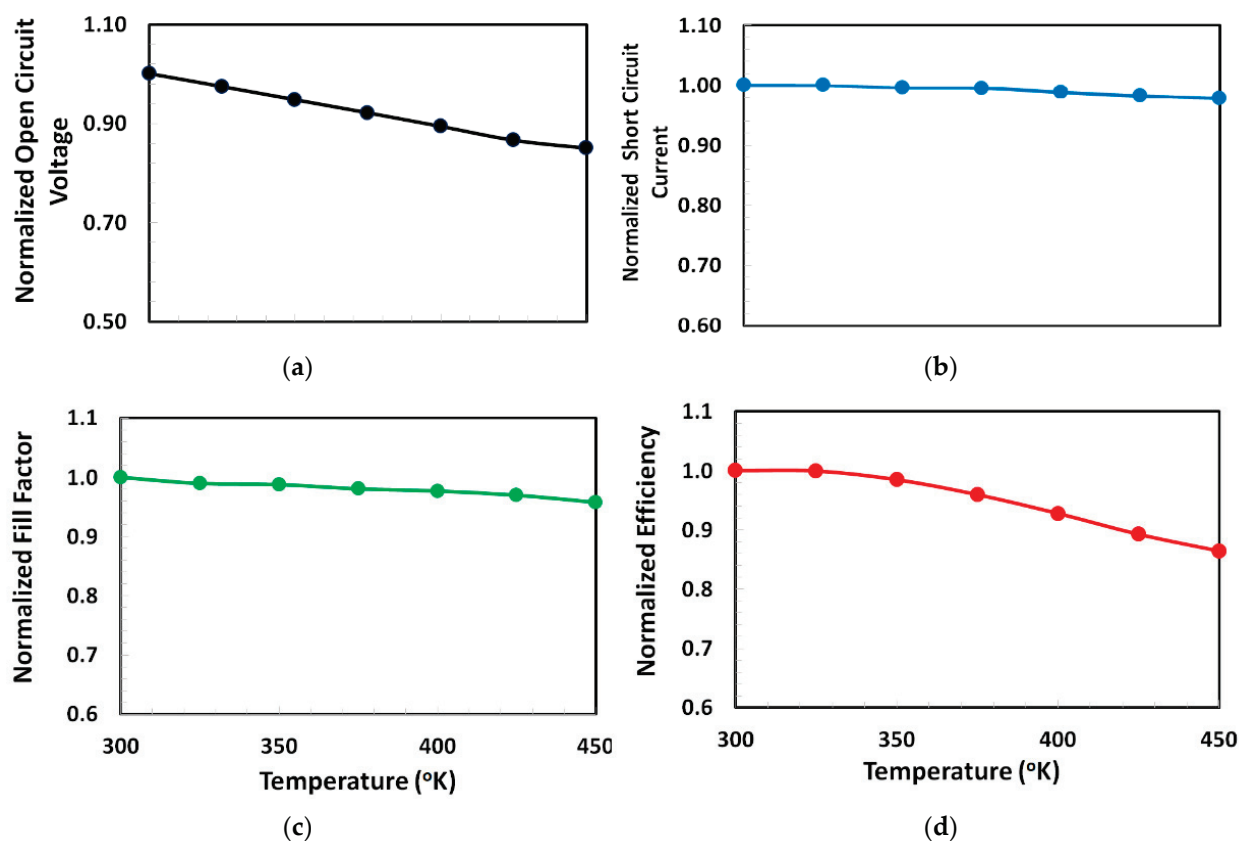
Figure 7. Degradation response of (**a**) normalized open-circuit voltage, (**b**) normalized short-circuit current, (**c**) normalized fill-factor, and (**d**) normalized power-conversion efficiency of the proposed solar cell Ag/BCP/PCBM/Cs$_2$TiBr$_6$/NPB/ITO as a function of ambient temperature varied from 300 to 450 °K.

4. Conclusions

Toxicity and stability are the main hurdles for the commercialization of the perovskite solar cell. For this purpose, a planar p-i-n type perovskite solar cell is proposed, and the stability is improved by the proper selection of doping-free hole-transport (NPB) and electron-transport layer (PCBM). On the other hand, to avoid toxicity a novel lead-free perovskite compound cesium titanium (IV) bromide (Cs$_2$TiBr$_6$) is incorporated as the absorber layer and finally the Ag/BCP/PCBM/Cs$_2$TiBr$_6$/NPB/ITO solar cell was proposed as the lead and dopant free perovskite solar cell. For photovoltaic characterization, we theoretically analyzed, and optimized the proposed solar cell with the help of SCAPS 1D. After a comprehensive optimization of each layer, it is observed that the proposed perovskite solar cell can yield with maximum power-conversion efficiency up to 16.85%. We believe that the outcome of this study will help in the fabrication of lead and dopant free highly efficient and stable perovskite solar cell for future applications.

Author Contributions: S.A.M. and A.N.M.A. contributed equally for the conceptualization, methodology, validation, formal analysis, and writing of the manuscript. All authors have read and agreed to the published version of the manuscript.

Conflicts of Interest: The authors declare no conflict of interest.

References

1. Kim, G.-H.; Kim, D.S. Development of Perovskite Solar Cells with >25% Conversion Efficiency. *Joule* **2021**, *5*, 1033–1035. [CrossRef]
2. Giustino, F.; Snaith, H.J. Toward Lead-Free Perovskite Solar Cells. *ACS Energy Lett.* **2016**, *1*, 1233–1240. [CrossRef]
3. Ju, M.-G.; Chen, M.; Zhou, Y.; Garces, H.F.; Dai, J.; Ma, L.; Padture, N.P.; Zeng, X.C. Earth-Abundant Nontoxic Titanium(IV)-Based Vacancy-Ordered Double Perovskite Halides with Tunable 1.0 to 1.8 EV Bandgaps for Photovoltaic Applications. *ACS Energy Lett.* **2018**, *3*, 297–304. [CrossRef]
4. Chen, M.; Ju, M.-G.; Carl, A.D.; Zong, Y.; Grimm, R.L.; Gu, J.; Zeng, X.C.; Zhou, Y.; Padture, N.P. Cesium Titanium(IV) Bromide Thin Films Based Stable Lead-Free Perovskite Solar Cells. *Joule* **2018**, *2*, 558–570. [CrossRef]
5. Pecunia, V.; Occhipinti, L.G.; Chakraborty, A.; Pan, Y.; Peng, Y. Lead-Free Halide Perovskite Photovoltaics: Challenges, Open Questions, and Opportunities. *APL Mater.* **2020**, *8*, 100901. [CrossRef]
6. Euvrard, J.; Wang, X.; Li, T.; Yan, Y.; Mitzi, D.B. Is Cs2TiBr6 a Promising Pb-Free Perovskite for Solar Energy Applications? *J. Mater. Chem. A* **2020**, *8*, 4049–4054. [CrossRef]
7. Chiang, C.-H.; Wu, C.-G. Bulk Heterojunction Perovskite–PCBM Solar Cells with High Fill Factor. *Nat. Photonics* **2016**, *10*, 196–200. [CrossRef]
8. Said, A.A.; Xie, J.; Zhang, Q. Recent Progress in Organic Electron Transport Materials in Inverted Perovskite Solar Cells. *Small* **2019**, *15*, 1900854. [CrossRef]
9. Asgary, S.; Moghaddam, H.M.; Bahari, A.; Mohammadpour, R. Role of BCP Layer on Nonlinear Properties of Perovskite Solar Cell. *Sol. Energy* **2021**, *213*, 383–391. [CrossRef]
10. Jeon, N.J.; Lee, H.G.; Kim, Y.C.; Seo, J.; Noh, J.H.; Lee, J.; Seok, S.I. O-Methoxy Substituents in Spiro-OMeTAD for Efficient Inorganic–Organic Hybrid Perovskite Solar Cells. *J. Am. Chem. Soc.* **2014**, *136*, 7837–7840. [CrossRef]
11. Tran, C.D.T.; Liu, Y.; Thibau, E.S.; Llanos, A.; Lu, Z.-H. Stability of Organometal Perovskites with Organic Overlayers. *AIP Adv.* **2015**, *5*, 087185. [CrossRef]
12. Jiang, X.; Wang, D.; Yu, Z.; Ma, W.; Li, H.-B.; Yang, X.; Liu, F.; Hagfeldt, A.; Sun, L. Molecular Engineering of Copper Phthalcyanines: A Strategy in Developing Dopant-Free Hole-Transporting Materials for Efficient and Ambient-Stable Perovskite Solar Cells. *Adv. Energy Mater.* **2019**, *9*, 1803287. [CrossRef]
13. Li, Y.; Cole, M.D.; Gao, Y.; Emrick, T.; Xu, Z.; Liu, Y.; Russell, T.P. High-Performance Perovskite Solar Cells with a Non-Doped Small Molecule Hole Transporting Layer. *ACS Appl. Energy Mater.* **2019**, *2*, 1634–1641. [CrossRef]
14. Tumen-Ulzii, G.; Qin, C.; Matsushima, T.; Leyden, M.R.; Balijipalli, U.; Klotz, D.; Adachi, C. Understanding the Degradation of Spiro-OMeTAD-Based Perovskite Solar Cells at High Temperature. *Sol. RRL* **2020**, *4*, 2000305. [CrossRef]
15. Zhang, F.; Yao, Z.; Guo, Y.; Li, Y.; Bergstrand, J.; Brett, C.J.; Cai, B.; Hajian, A.; Guo, Y.; Yang, X.; et al. Polymeric, Cost-Effective, Dopant-Free Hole Transport Materials for Efficient and Stable Perovskite Solar Cells. *J. Am. Chem. Soc.* **2019**, *141*, 19700–19707. [CrossRef] [PubMed]
16. Lee, I.; Rolston, N.; Brunner, P.-L.; Dauskardt, R.H. Hole-Transport Layer Molecular Weight and Doping Effects on Perovskite Solar Cell Efficiency and Mechanical Behavior. *ACS Appl. Mater. Interfaces* **2019**, *11*, 23757–23764. [CrossRef]
17. Pham, H.D.; Yang, T.C.-J.; Jain, S.M.; Wilson, G.J.; Sonar, P. Development of Dopant-Free Organic Hole Transporting Materials for Perovskite Solar Cells. *Adv. Energy Mater.* **2020**, *10*, 1903326. [CrossRef]
18. Verschraegen, J.; Burgelman, M. Numerical Modeling of Intra-Band Tunneling for Heterojunction Solar Cells in Scaps. *Thin Solid Films* **2007**, *515*, 6276–6279. [CrossRef]
19. Burgelman, M.; Nollet, P.; Degrave, S. Modelling Polycrystalline Semiconductor Solar Cells. *Thin Solid Films* **2000**, *361–362*, 527–532. [CrossRef]
20. Burgelman, M.; Decock, K.; Khelifi, S.; Abass, A. Advanced Electrical Simulation of Thin Film Solar Cells. *Thin Solid Films* **2013**, *535*, 296–301. [CrossRef]
21. Simya, O.K.; Mahaboobbatcha, A.; Balachander, K. A Comparative Study on the Performance of Kesterite Based Thin Film Solar Cells Using SCAPS Simulation Program. *Superlattices Microstruct.* **2015**, *82*, 248–261. [CrossRef]
22. Moiz, S.A.; Alahmadi, A.N.M.; Aljohani, A.J. Design of a Novel Lead-Free Perovskite Solar Cell for 17.83% Efficiency. *IEEE Access* **2021**, *9*, 54254–54263. [CrossRef]
23. Zhao, Z.; Gu, F.; Li, Y.; Sun, W.; Ye, S.; Rao, H.; Liu, Z.; Bian, Z.; Huang, C. Mixed-Organic-Cation Tin Iodide for Lead-Free Perovskite Solar Cells with an Efficiency of 8.12%. *Adv. Sci.* **2017**, *4*, 1700204. [CrossRef] [PubMed]
24. Chen, L.-C.; Tseng, Z.-L.; Huang, J.-K. A Study of Inverted-Type Perovskite Solar Cells with Various Composition Ratios of $(FAPbI_3)_{1-x}(MAPbBr_3)_x$. *Nanomaterials* **2016**, *6*, 183. [CrossRef]
25. Madan, J.; Shivani; Pandey, R.; Sharma, R. Device Simulation of 17.3% Efficient Lead-Free All-Perovskite Tandem Solar Cell. *Sol. Energy* **2020**, *197*, 212–221. [CrossRef]
26. Jayan, K.D.; Sebastian, V. Comprehensive Device Modelling and Performance Analysis of MASnI3 Based Perovskite Solar Cells with Diverse ETM, HTM and Back Metal Contacts. *Sol. Energy* **2021**, *217*, 40–48. [CrossRef]
27. Karimi, E.; Ghorashi, S.M.B. Investigation of the Influence of Different Hole-Transporting Materials on the Performance of Perovskite Solar Cells. *Optik* **2017**, *130*, 650–658. [CrossRef]
28. Franckevičius, M.; Mishra, A.; Kreuzer, F.; Luo, J.; Zakeeruddin, S.M.; Grätzel, M. A Dopant-Free Spirobi[Cyclopenta[2,1-b:3,4-B']Dithiophene] Based Hole-Transport Material for Efficient Perovskite Solar Cells. *Mater. Horiz.* **2015**, *2*, 613–618. [CrossRef]

29. Wang, Y.; Zhang, T.; Zhang, P.; Liu, D.; Ji, L.; Chen, H.; Chen, Z.D.; Wu, J.; Li, S. Solution processed PCBM-CH$_3$NH$_3$PbI$_3$ heterojunction photodetectors with enhanced performance and stability. *Org. Electron.* **2018**, *5*, 263–268. [CrossRef]

30. Karimov, K.S.; Ahmed, M.M.; Moiz, S.A.; Babadzhanov, P.; Marupov, R.; Turaeva, M.A. Electrical Properties of Organic Semiconductor Orange Nitrogen Dye Thin Films Deposited from Solution at High Gravity. *Eurasian Chem. Technol. J.* **2003**, *5*. [CrossRef]

31. Moiz, S.A.; Alahmadi, A.N.M.; Karimov, K.S. Improved Organic Solar Cell by Incorporating Silver Nanoparticles Embedded Polyaniline as Buffer Layer. *Solid State Electron.* **2020**, *163*, 107658. [CrossRef]

32. Moiz, S.A.; Alahmadi, A.N.M.; Aljohani, A.J. Design of Silicon Nanowire Array for PEDOT:PSS-Silicon Nanowire-Based Hybrid Solar Cell. *Energies* **2020**, *13*, 3797. [CrossRef]

33. Moiz, S.A.; Khan, I.A.; Younis, W.A.; Masud, M.I.; Ismail, Y.; Khawaja, Y.M. Solvent Induced Charge Transport Mechanism for Conducting Polymer at Higher Temperature. *Mater. Res. Express* **2020**, *7*, 095304. [CrossRef]

34. Moiz, S.A.; Nahhas, A.M.; Um, H.-D.; Jee, S.-W.; Cho, H.K.; Kim, S.-W.; Lee, J.-H. A Stamped PEDOT:PSS–Silicon Nanowire Hybrid Solar Cell. *Nanotechnology* **2012**, *23*, 145401. [CrossRef] [PubMed]

35. Wang, D.; Elumalai, N.K.; Mahmud, M.A.; Upama, M.B.; Wright, M.; Chan, K.H.; Xu, C.; Uddin, A. Effect of PCBM Film Thickness on the Performance of Inverted Perovskite Solar Cells. In Proceedings of the 2016 IEEE 43rd Photovoltaic Specialists Conference (PVSC), Portland, OR, USA, 5–10 June 2016; pp. 1670–1672. [CrossRef]

36. Kam, Z.; Yang, Q.; Wang, X.; Wu, B.; Zhu, F.; Zhang, J.; Wu, J. Enhanced Absorbance and Electron Collection in Inverted Organic Solar Cells: Optical Admittance and Transient Photocurrent Analyses. *Org. Electron.* **2014**, *15*, 1306–1311. [CrossRef]

37. Chu, T.-Y.; Song, O.-K. Thickness Dependence of the Trap States in Organic Thin Film of N,N′-Bis(Naphthalen-1-Yl)-N,N′-Bis(Phenyl) Benzidine. *Appl. Phys. Lett.* **2007**, *91*, 073508. [CrossRef]

38. Um, H.-D.; Moiz, S.A.; Park, K.-T.; Jung, J.-Y.; Jee, S.-W.; Ahn, C.H.; Kim, D.C.; Cho, H.K.; Kim, D.-W.; Lee, J.-H. Highly Selective Spectral Response with Enhanced Responsivity of N-ZnO/p-Si Radial Heterojunction Nanowire Photodiodes. *Appl. Phys. Lett.* **2011**, *98*, 033102. [CrossRef]

39. Miyano, K.; Tripathi, N.; Yanagida, M.; Shirai, Y. Lead Halide Perovskite Photovoltaic as a Model p–i–n Diode. *Acc. Chem. Res.* **2016**, *49*, 303–310. [CrossRef] [PubMed]

40. Moiz, S.A.; Ahmed, M.M.; Karimov, K.S. Estimation of Electrical Parameters of OD Organic Semiconductor Diode from Measured I-V Characteristics. *ETRI J.* **2005**, *27*, 319–325. [CrossRef]

41. Bohlin, K.E. Generalized Norde Plot Including Determination of the Ideality Factor. *J. Appl. Phys.* **1986**, *60*, 1223–1224. [CrossRef]

42. Sha, Y.; Bi, E.; Zhang, Y.; Ru, P.; Kong, W.; Zhang, P.; Yang, X.; Chen, H.; Han, L. A Scalable Integrated Dopant-Free Heterostructure to Stabilize Perovskite Solar Cell Modules. *Adv. Energy Mater.* **2021**, *11*, 2003301. [CrossRef]

43. McIntosh, K.R.; Lau, G.; Cotsell, J.N.; Hanton, K.; Bätzner, D.L.; Bettiol, F.; Richards, B.S. Increase in External Quantum Efficiency of Encapsulated Silicon Solar Cells from a Luminescent Down-Shifting Layer. *Prog. Photovolt. Res. Appl.* **2009**, *17*, 191–197. [CrossRef]

44. Stranks, S.D.; Eperon, G.E.; Grancini, G.; Menelaou, C.; Alcocer, M.J.P.; Leijtens, T.; Herz, L.M.; Petrozza, A.; Snaith, H.J. Electron-Hole Diffusion Lengths Exceeding 1 Micrometer in an Organometal Trihalide Perovskite Absorber. *Science* **2013**, *342*, 341. [CrossRef] [PubMed]

Gold-Nanoparticle-Deposited TiO$_2$ Nanorod/Poly(Vinylidene Fluoride) Composites with Enhanced Dielectric Performance

Pornsawan Kum-onsa [1], Narong Chanlek [2], Jedsada Manyam [3], Prasit Thongbai [4,5,*], Viyada Harnchana [4,5], Nutthakritta Phromviyo [6] and Prinya Chindaprasirt [6]

[1] Materials Science and Nanotechnology Program, Faculty of Science, Khon Kaen University, Khon Kaen 40002, Thailand; pornsawan.kumonsa@gmail.com
[2] Synchrotron Light Research Institute (Public Organization), 111 University Avenue, Muang District, Nakhon Ratchasima 30000, Thailand; Narong@slri.or.th
[3] Nanotechnology Center (NANOTEC), National Science and Technology Development Agency (NSTDA), Pathum Thani 12120, Thailand; jedsada@nanotec.or.th
[4] Department of Physics, Faculty of Science, Khon Kaen University, Khon Kaen 40002, Thailand; viyada@kku.ac.th
[5] Institute of Nanomaterials Research and Innovation for Energy (IN-RIE), NANOTEC-KKU RNN on Nanomaterials Research and Innovation for Energy, Khon Kaen University, Khon Kaen 40002, Thailand
[6] Sustainable Infrastructure Research and Development Center, Department of Civil Engineering, Faculty of Engineering, Khon Kaen University, Khon Kaen 40002, Thailand; nutthaphrom@gmail.com (N.P.); prinya@kku.ac.th (P.C.)
* Correspondence: pthongbai@kku.ac.th

Abstract: Flexible dielectric polymer composites have been of great interest as embedded capacitor materials in the electronic industry. However, a polymer composite has a low relative dielectric permittivity ($\varepsilon' < 100$), while its dielectric loss tangent is generally large ($\tan\delta > 0.1$). In this study, we fabricate a novel, high-permittivity polymer nanocomposite system with a low $\tan\delta$. The nanocomposite system comprises poly(vinylidene fluoride) (PVDF) co-filled with Au nanoparticles and semiconducting TiO$_2$ nanorods (TNRs) that contain Ti^{3+} ions. To homogeneously disperse the conductive Au phase, the TNR surface was decorated with Au-NPs ~10–20 nm in size (Au-TNRs) using a modified Turkevich method. The polar β-PVDF phase was enhanced by the incorporation of the Au nanoparticles, partially contributing to the enhanced ε' value. The introduction of the Au-TNRs in the PVDF matrix provided three-phase Au-TNR/PVDF nanocomposites with excellent dielectric properties (i.e., high $\varepsilon' \approx 157$ and low $\tan\delta \approx 0.05$ at 1.8 vol% of Au and 47.4 vol% of TNRs). The ε' of the three-phase Au-TNR/PVDF composite is ~2.4-times higher than that of the two-phase TNR/PVDF composite, clearly highlighting the primary contribution of the Au nanoparticles at similar filler loadings. The volume fraction dependence of ε' is in close agreement with the effective medium percolation theory model. The significant enhancement in ε' was primarily caused by interfacial polarization at the PVDF–conducting Au nanoparticle and PVDF–semiconducting TNR interfaces, as well as by the induced β-PVDF phase. A low $\tan\delta$ was achieved due to the inhibited conducting pathway formed by direct Au nanoparticle contact.

Keywords: gold nanoparticle; titanium dioxide nanorod; poly(vinylidene fluoride); heat treatment; hybrid nanoparticle; modified Turkevich method

1. Introduction

With recent developments in the electronic industry, dielectric polymer composite materials have attracted increasing interest for a wide range of applications, such as energy storage devices, dielectric capacitors, and electromechanical actuators [1,2]. Poly(vinylidene fluoride) (PVDF) has been used as a dielectric polymer material due to its high energy density, high electric break down field, and flexibility [3,4]. However, the relative dielectric permittivity (ε') of PVDF is too low (≈ 10 [3]) for electronic applications.

Many studies have attempted to fabricate polymer composites with high ε' values by incorporating fillers into the PVDF matrix. Two-phase ceramic/polymer and metal/polymer composites have been synthesized and widely studied for improving the dielectric performance of polymer composite materials [5–11]. Several ceramic/polymer composites, such as $CaCu_3Ti_4O_{12}$/PVDF [5,12], $CaCu_3Ti_4O_{12}$/polystyrene [13], $BaTiO_3$/PVDF [6], $Ba_{0.5}Sr_{0.5}TiO_3$/P(VDF-CTFE) [14], and $Ba_{0.6}Sr_{0.4}TiO_3$/PVDF [15], have high ε' values (~50–80 at 1 kHz). The ε' of a ceramic/polymer composite is generally below 100 even at a high ceramic loading (50 vol%), while its dielectric loss tangent ($\tan\delta$) is also elevated (>0.1 at 1 kHz and ~25 °C) [5,16]. However, metal/polymer composites, such as Ni/PVDF, Ni/P(VDF-CTFE) [17,18], MWCNT/PVDF [8,19], and Ag/PVDF [7,20], can exhibit significantly higher ε' at low concentrations of conducting fillers than ceramic/PVDF composites. It is difficult to maintain the filler loading at the percolation threshold (f_c) to achieve a high relative permittivity. Metal/polymer composites generally exhibit significantly large $\tan\delta$ and electrical conductivity (σ) values at f_c. It should be noted that the metal/polymer composites with extreme ε' values also have high $\tan\delta$ and σ, which limits the practical applications of these metal/polymer composites.

Owing to such challenges, developing polymer composites with high ε' and low $\tan\delta$ values is desirable. Several researchers have studied and reported three-component composites comprising metal, ceramic, and polymer matrices, such as $Ba(Fe_{0.5}Nb_{0.5})O_3$/Ni/PVDF, $Ni/CaCu_3Ti_4O_{12}$/PVDF, $Ni/BaTiO_3$/PVDF, $Na_{0.5}Bi_{0.5}Cu_3Ti_4O_{12}$/MWCNTs/PVDF, and $Ag/Na_{0.5}Bi_{0.5}Cu_3Ti_4O_{12}$ [21–25]. In particular, a novel composite with structured hybrid fillers has been of great interest. Recently, many studies on PVDF-based composites filled with hybrid nanoparticles have been reported. Luo et al. [26] reported a novel polymer composite filled with Ag-$BaTiO_3$ hybrid nanoparticles. This Ag-$BaTiO_3$/PVDF composite exhibited a high ε' (160) with $\tan\delta \approx 0.11$ at a filler volume fraction ($f_{Ag\text{-}BT}$) of 0.568. This $\tan\delta$ value is much lower than those reported in many conventional three-phase polymer composites; unfortunately, it is still much larger than 0.05, which is an acceptable value for capacitor applications. Although incorporating Ag-$BaTiO_3$ hybrid nanoparticles can increase the ε' of a composite, the ε' of ferroelectric $BaTiO_3$ is generally strongly dependent on its Curie temperature. Furthermore, most ferroelectric oxides are piezoelectric, which results in mechanical resonance in the device during charging and discharging, thereby limiting its reliability [27].

Rutile-TiO_2 is one of the most widely used oxides in electronic materials, sensors, and semiconductors [28,29]. Furthermore, rutile-TiO_2 can exhibit colossal dielectric properties when a minor portion of Ti^{4+} is reduced to Ti^{3+} due to the existence of oxygen vacancies and/or substitution by pentavalent ions (e.g., Nb^{5+} or Ta^{5+}). Polaron-like electron hopping between Ti^{3+} and Ti^{4+} ions can cause a significant increase (by a factor of ~10^4) in dielectric permittivity [30]. Since TiO_2 is not a ferroelectric ceramic, TiO_2 nanoparticles were used as a filler in various polymer composites [31–33]. Unfortunately, the ε' values of the TiO_2/polymer composites are still significantly low owing to the low ε' of the TiO_2 nanoparticles. Polymer composites filled with modified TiO_2 nanoparticles such as Ag-TiO_2 hybrid particles and $Ag@TiO_2$ core–shell structures were developed to enhance ε' [34–37]. Although these composites can exhibit high ε' values of ~60–150, large $\tan\delta$ values are generally obtained (~0.1–1) at high filler concentrations (70 vol%) [34,35]. Among various metal nanoparticles, gold nanoparticles are widely used as fillers to improve the insulation properties of polymer materials because they are nontoxic and less likely to be oxidized [38]. A significantly enhanced ε' (~54-118) and low $\tan\delta$ (<0.06) were achieved in Au-$BaTiO_3$/PVDF [39] and Au-$BiFeO_3$/PVDF, with only a small amount of Au in the third phase of each polymer composite ($f_{Au} < 0.02$) [40]. According to previous works [39,40], the Au-$BaTiO_3$/PVDF and Au-$BiFeO_3$/PVDF composites not only exhibited high ε' values, but their $\tan\delta$ and σ were also suppressed due to the incorporation of the Au nanoparticles. Therefore, the conductive Au phase nanoparticle is one of the most interesting conductive phases for use as a filler in three-phase polymer composites.

To the best of our knowledge, there is a lack of substantial information on polymer composites incorporated with Au-TiO$_2$ hybrid nanoparticles. Therefore, in this study we aimed to fabricate a novel nanocomposite comprising a PVDF polymer matrix, Au nanoparticles, and TiO$_2$ nanorods (TNRs). TNRs have higher surface areas than spherical TiO$_2$; therefore, they lead to stronger interfacial polarization and a significantly enhanced ε'. Herein, Au-TNR/PVDF nanocomposites with enhanced ε' and low tanδ were fabricated. A modified Turkevich method was used to attach Au onto the surfaces of the TNRs. The Au-TNR/PVDF nanocomposites were prepared through liquid-phase-assisted dispersion and hot-pressing methods. Several properties of these nanocomposites such as their morphologies, microstructures, phase structures, chemical stages, and dielectric properties were investigated, and the significantly improved dielectric properties of the nanocomposites are discussed.

2. Experimental Section

2.1. Preparation of Heat-Treated TNRs

TNRs (99.5% purity) with particle size <100 nm were purchased from Sigma-Aldrich. Heat treatment at 500 °C for 3 h in air was performed on the TNRs to evaporate the moisture.

2.2. Preparation of Au-TNR Hybrid Nanoparticles

Au-TNR hybrid nanoparticles were prepared through a modified Turkevich method. The corresponding procedure is described as follows: heat treatment of TNR powder was carried out by ultrasonically dispersing the powder in deionized water for 30 min. Then, the white TNR suspension was stirred using a magnetic stirrer at ~25 °C for 30 min, after which 1 mM HAuCl$_4$·3H$_2$O was dissolved in the TNR solution under constant stirring. After the solution was heated to 300 °C, 38.8 mM of sodium citrate (>99.0%, Sigma-Aldrich) solution was dissolved in the TNR solution. To ensure a complete reaction, the suspension was stirred until its color changed from white to purple. The purple suspension was sequentially cooled to room temperature, centrifuged at 8500 rpm, and washed several times with deionized water. Finally, Au-TNR hybrid nanoparticles were obtained without agglomeration by freeze-drying.

2.3. Preparation of Au-TNR/PVDF Nanocomposites

Au-TNR/PVDF nanocomposites containing Au-TNR fillers with different f_{Au} and f_{TNRs} values were prepared through liquid-phase-assisted dispersion and hot-pressing methods. First, Au-TNR hybrid nanoparticles and the PVDF powder (M$_w$ ~ 534,000, Sigma-Aldrich) were mixed by ball-milling with ZrO$_2$ in ethanol for 3 h. Second, the mixture was dried at 80 °C to evaporate ethanol, after which the mixed powder was pressed at 200 °C for 30 min at 10 MPa. Finally, the Au-TNR/PVDF nanocomposite sample, with a diameter and thickness of ~12 mm and ~0.5–1 mm, respectively, was obtained at room temperature. Au-TNR/PVDF nanocomposite samples with $f_{Au\text{-}TNRs}$ = 0.094, 0.216, 0.294, 0.383, 0.492, and 0.624 are referred to as Au-TNRs/PVDF-1, Au-TNRs/PVDF-2, Au-TNRs/PVDF-3, Au-TNRs/PVDF-4, Au-TNRs/PVDF-5, and Au-TNRs/PVDF-6, respectively. The separated volume fractions of Au and TNRs for each composite sample are listed in Table 1.

Table 1. Volume fraction of Au (f_{Au}), TNRs (f_{TNRs}), Au-TNRs ($f_{Au-TNRs}$), ε', $\tan\delta$, and σ_{ac} at 1 kHz and room temperature for nanocomposites with varying filler amounts.

Sample	f_{Au}	f_{TNRs}	$f_{Au-TNRs}$	ε'	$\tan\delta$	σ_{ac} (10^{-11} S·cm^{-1})
PVDF	0	0	0	10.8	0.020	4.1
Au-TNR/PVDF-1	0.005	0.089	0.094	29.1	0.012	20.3
Au-TNR/PVDF-2	0.010	0.206	0.216	37.1	0.028	59.1
Au-TNR/PVDF-3	0.013	0.281	0.294	53.8	0.062	188.6
Au-TNR/PVDF-4	0.016	0.367	0.383	57.7	0.075	242.8
Au-TNR/PVDF-5	0.018	0.474	0.492	156.7	0.048	427.7
Au-TNR/PVDF-6	0.021	0.603	0.624	226.3	0.052	657.6
TNR/PVDF	0	0.5	0	65.9	0.028	103.5

2.4. Characterization

The phase structures of the PVDF filler and Au-TNR/PVDF nanocomposites were characterized by X-ray diffractometry (XRD, PANalytical, EMPYREAN). The surface morphologies of Au, TNRs, and the Au-TNR nanoparticles were revealed using transmission electron microscopy (TEM, FEI Tecnai G2 20). The chemical composition of each element in the Au-TNR hybrid nanoparticles was analyzed by X-ray photoelectron spectroscopy (XPS, PHI5000 VersaProbe II, ULVAC-PHI, Japan) at the SUT-NANOTEC-SLRI Joint Research Facility, Synchrotron Light Research Institute (SLRI), Thailand. The fracture microstructures, distributions, and percentages of each element in the Au-TNR/PVDF nanocomposites were investigated by focused ion beam–field emission scanning electron microscopy (FIB–FESEM, FEI Helios Nanolab G3 CX). The samples were fractured using liquid N_2 and their surfaces were sputtered with Au before SEM characterization. The crystalline phases of the nanocomposites were determined using Fourier-transform infrared spectroscopy (FTIR, Bruker, TENSOR27) in the 700–1800 cm^{-1} wavelength range. The dielectric properties of the samples were analyzed using an impedance analyzer (KEYSIGHT E4990A) in the 10^2–10^6 Hz and −60–150 °C frequency and temperature ranges, respectively, with an oscillation voltage of 0.5 V. Before any dielectric measurement, both sides of each circular sample were coated with Ag to form electrodes.

3. Results and Discussion

Figure 1 displays TEM images showing the morphologies of the Au, TNRs, and Au-TNR hybrid nanoparticles. The Au nanoparticles are spherical with diameters of 10–20 nm. Meanwhile, the heat-treated TNRs are rod-shaped with slightly different aspect ratios, while some Au clusters are dotted on the TNR surfaces of the Au-TNR hybrid nanoparticles, revealing that the Au nanoparticles successfully formed on the TNR surfaces.
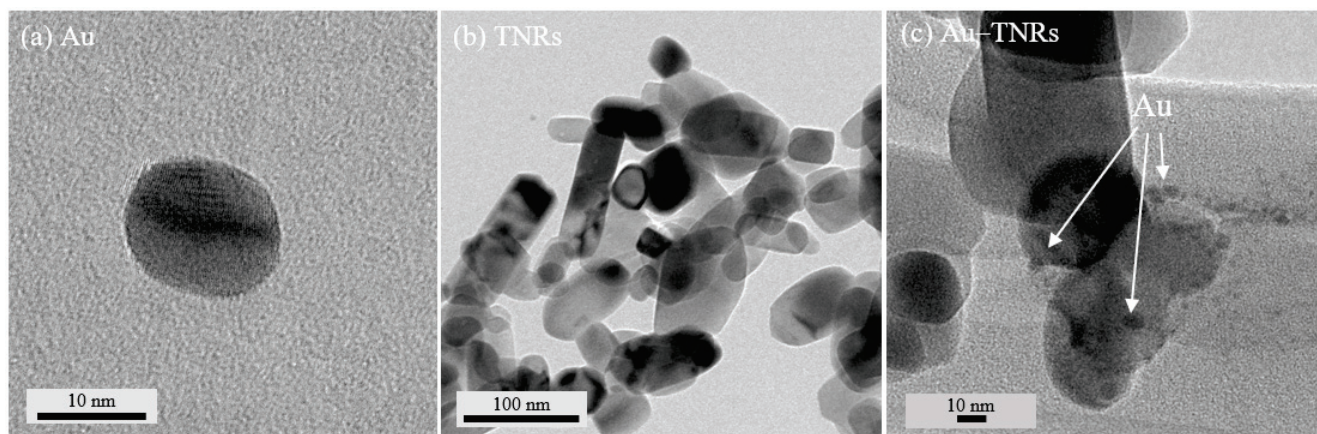

Figure 1. TEM images of (**a**) Au, (**b**) TNRs, and (**c**) Au-TNR hybrid nanoparticles.

Figure 2 shows XPS spectra of the Au-TNR powder. As shown in Figure 2a, Au 4*f* peaks were observed at 83.33 and 86.98 eV, which are assigned to Au $4f_{7/2}$ and Au $4f_{5/2}$, respectively [41,42]. This confirmed the existence of Au in the prepared Au-TNR powder. As shown in Figure 2b, small Ti 2*p* peaks were observed at binding energies of 457.69 and 461.34 eV, respectively, corresponding to the presence of Ti^{3+}. Ti 2*p* signals was observed at binding energies of 458.75 and 464.41 eV, indicating the presence of Ti^{4+} [43]. The Ti^{3+}/Ti^{4+} ratio was found to be 7.52%. Figure 2c shows three of O 1*s* XPS peaks; the peak at 529.99 eV can be attributed to the oxygen lattice (Ti–O) [28,43]. Additional peaks were observed at 531.29 and 532.32 eV, which can be attributed to the oxygen vacancy in the rutile structure [28] and hydroxyl groups [43], respectively. The detected Ti^{3+} in the Au-TNR powder is likely to have originated from oxygen vacancies, which can be explained by Equations (1) and (2).

$$O_O^x \rightarrow \frac{1}{2}O_2 + V_O^{\bullet\bullet} + 2e^- \tag{1}$$

$$Ti^{4+} + e^- \rightarrow Ti^{3+} \tag{2}$$

The presence of the Ti^{3+} ions can cause a significant increase in conductivity, thereby leading to electron hopping between the Ti^{3+} and Ti^{4+} ions under an applied electric field. The XPS results confirmed the existence of Au, Ti^{3+}, and oxygen vacancies, which affected ε' enhancement in the Au-TNR/PVDF nanocomposites.
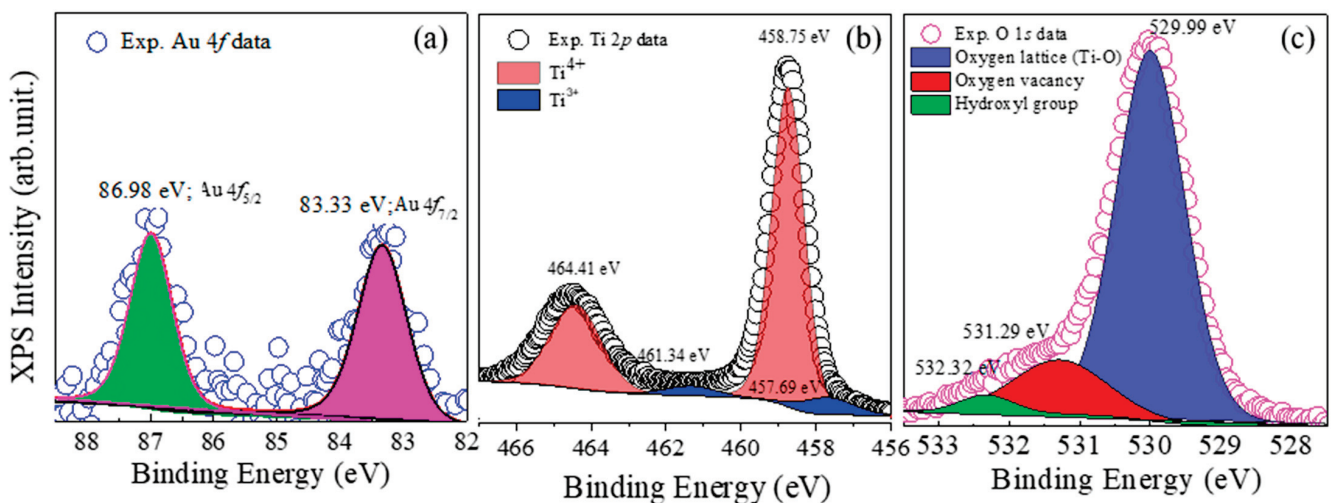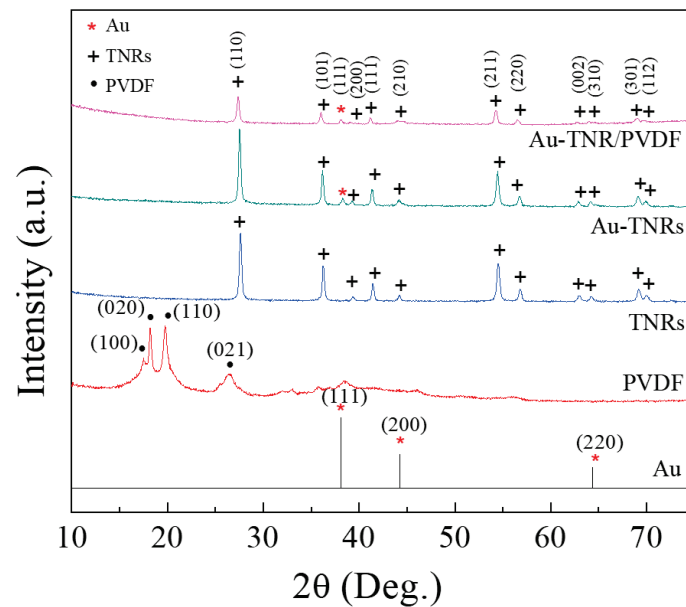

Figure 2. XPS spectra of Au-TNR hybrid nanoparticles; (**a**) Au 4*f*, (**b**) Ti 2*p*, and (**c**) O 1*s*.

The XRD patterns of Au, PVDF, TNRs, Au-TNR nanoparticles, and Au-TNR/PVDF nanocomposites were obtained in the 10–80° 2θ range, as shown in Figure 3. The XRD pattern of the PVDF polymer corresponds to the (100), (020), (110), and (021) planes of the α-phase [4]. The XRD pattern of the TNRs showed peaks similar to those of the tetragonal structure of the rutile phase according to the standard reported in JCPDS 21-1276; no impurity phase was detected. In the case of the Au-TNR hybrid nanoparticles and Au-TNR/PVDF nanocomposites, the XRD peak for Au can be observed at 2θ ≈ 38.11 and assigned as a (111) plane (JCPDS 00-00-1172), confirming the existence of Au in the hybrid particles and Au-TNR/PVDF nanocomposites. Therefore, the Au nanoparticles were confirmed to exist in the Au-TNR nanoparticles and Au-TNR/PVDF nanocomposites. Meanwhile, no PVDF diffraction peaks were observed in the Au-TNR/PVDF nanocomposite sample, which can be attributed to the semicrystalline nature of PVDF, which is shielded by the stronger crystalline diffraction intensity of the TNRs compared to PVDF.

Figure 3. XRD patterns of the Au standard data Au standard (JCPDS 00-00-1172), TNRs, fabricated Au-TNR hybrid nanoparticles, and Au-TNR/PVDF-4 nanocomposite.

The FTIR spectra of the PVDF polymer nanocomposites filled with the TNRs and Au-TNRs are shown in Figure 4. Both nanocomposite systems consisted of α-, β-, and γ-PVDF phases. Weak transmittance bands observed at 766 and 976 cm^{-1} are attributed to the nonpolar α-phase [4], consistent with the XRD result (Figure 3). As the characteristic bands of the β- and γ-phase overlapped at 840 cm^{-1}, they were difficult to distinguish. However, the characteristic band at 1279 cm^{-1} only corresponds to the β-phase [4]. As shown in Figure 4, the transmittance intensity of the β-phase for the three-phase Au-TNR/PVDF-5 composite is stronger than that of the two-phase TNR/PVDF composite, particularly at 1279 cm^{-1}. To estimate the %β-phases in the nanocomposites, the absorption ratios of the β- and α-phase were compared. Equation (3) was used to quantify the relative fraction of the β-phase (F(β)) [4], assuming that only the β- and α-phase exist:

$$F(\beta) = \frac{A_\beta}{(K_\beta/K_\alpha)A_\alpha + A_\beta} \tag{3}$$

where A_α and A_β are the absorption bands at 766 and 840 cm^{-1}, respectively, and K_α and K_β are the absorption coefficients of the respective bands ($K_\alpha = 6.1 \times 10^4$ and $K_\beta = 7.7 \times 10^4$ cm$^2 \cdot$mol^{-1}). The calculated F(β) of the two-phase and three-phase nanocomposites were 0.220 and 0.331, respectively. The negative charge of the Au nanoparticles causes an increase in amount of the polar β-phase of the PVDF nanocomposites [44], leading to a Au-TNR/PVDF nanocomposite with a significantly enhanced ε′ [45].

The fracture cross-sectional images of the nanocomposites containing various Au-TNR hybrid particles are shown in Figure 5. The microstructure of the PVDF polymer is shown in Figure 5a and reveals that the PVDF molecules form a continuous phase. Figure 5b,c show the microstructures of the Au-TNRs/PVDF-2 and Au-TNRs/PVDF-4 nanocomposites. The Au-TNR hybrid nanoparticles are dispersed homogeneously in the PVDF matrix without aggregation. Some air voids and Au-TNR nanoparticle aggregation were observed with increasing Au-TNR hybrid particle content, as exemplified by Au-TNR/PVDF-6, as shown in Figure 5d.
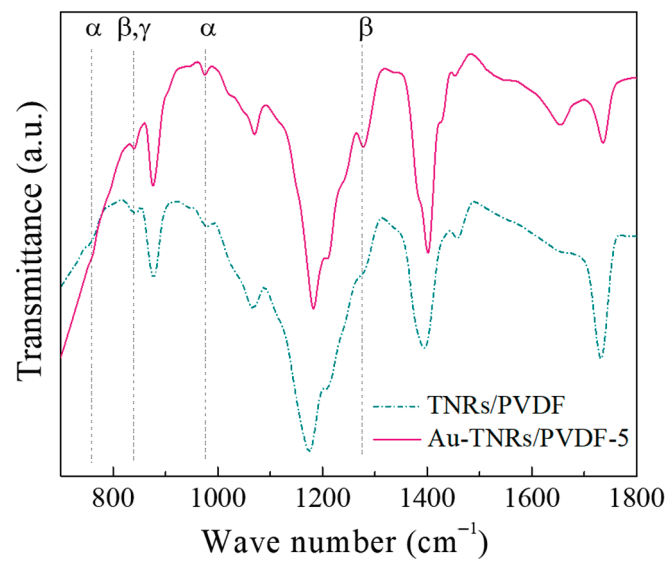
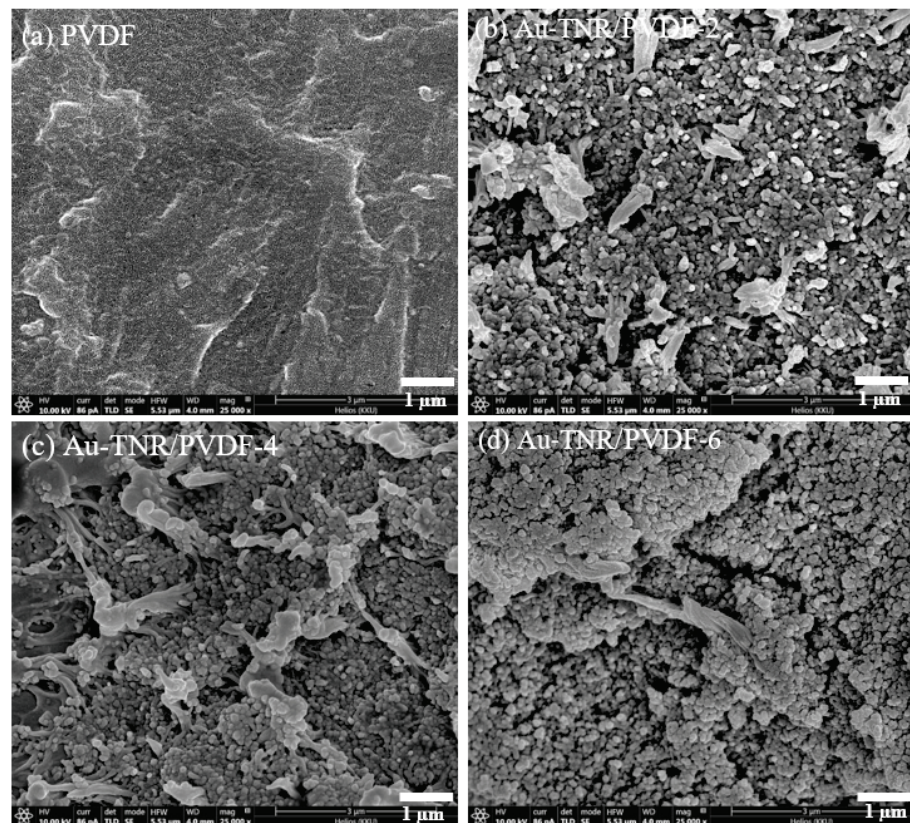**Figure 4.** FTIR spectra of the TNR/PVDF and Au-TNR/PVDF-5 nanocomposites.

Figure 5. SEM cross-section images of (**a**) PVDF, (**b**) Au-TNR/PVDF-2, (**c**) Au-TNR/PVDF-4, and (**d**) Au-TNR/PVDF-6.

SEM element maps and EDS were employed to further confirm the existence of Au in the three-phase nanocomposites. As shown in Figure 6, the microstructure of Au-TNR/PVDF-4 exhibited Au clusters dispersed on the TNR surfaces that are surrounded by the PVDF matrix. EDS was used to determine that Au, Ti, O, C, and F are present in the nanocomposite at levels of 1.3, 57, 24.5, 14.3, and 2.9 wt%, respectively.
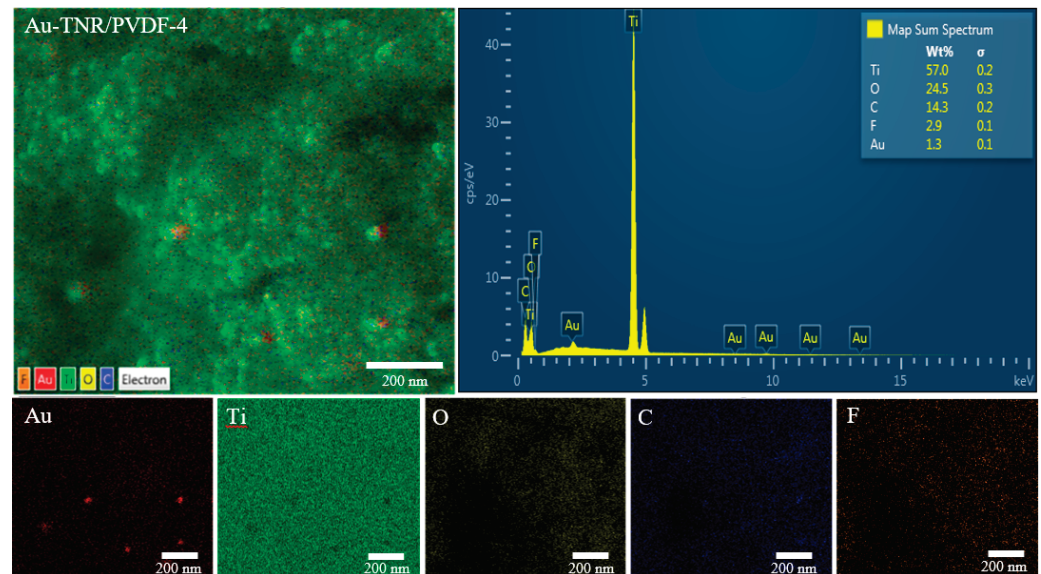
Figure 6. Element mapping and EDS-FESEM characterization of Au-TNR/PVDF-4.

The frequency dependences of ε', tanδ, and σ_{ac} of nanocomposites with different volume fractions of Au-TNRs ($f_{Au\text{-}TNRs}$) at room temperature are shown in Figure 7. As shown in Figure 7a, the ε' increased with increasing $f_{Au\text{-}TNRs}$. A significant enhancement in ε' was achieved by incorporating small amounts of Au and TNR nanoparticles in the nanocomposite. The enhanced ε' value of the Au-TNR/PVDF-6 composite was ~226 at 1 kHz, which is ~20 times larger than that of a pure PVDF polymer ($\varepsilon' \approx 10.78$). The increase in ε' for the three-phase Au-TNR/PVDF nanocomposites can be ascribed to the formation of Au-TNR hybrid nanoparticles. A large amount of blocked charges at the interface between TNR-PVDF and Au-PVDF can enhance interfacial polarization, which is known as Maxwell–Wagner–Sillars (MWS) polarization [6,46]. Therefore, in an electric field, the enhanced interfacial polarization enhances the ε' of the Au-TNR/PVDF nanocomposites. Another factor is the semiconductor nature of the TNR nanoparticles, which can produce interfacial polarization over a wide range of frequencies. Moreover, the ε' behavior of each sample exhibits a similar trend in the 10^2–10^6 Hz range. Meanwhile, the tanδ values of the Au-TNR/PVDF nanocomposites decreased as the frequency was increased to approximately 10^4 kHz and gradually increased at higher frequencies, as shown in Figure 7b. This increase in tanδ is generally consistent with the dielectric relaxation of the pure PVDF polymer [6]. Considering a low-frequency range, tanδ of the Au-TNR/PVDF nanocomposites increased with increasing $f_{Au\text{-}TNRs}$. The increased tanδ value as a result of increased filler loading is attributed to the conduction of free charge carriers [6,47], which corresponds to the increase in $f_{Au\text{-}TNRs}$. Furthermore, for the composites with high filler loading, it is observed that tanδ continuously increases with decreasing frequency from 10^3 to 10^2 Hz. This observation was resulted from the conduction of free charge carriers, which is more prominent in a low-frequency range. The increase in tanδ in the high-frequency range is attributed to the α_a relaxation from the glass transition in the PVDF polymer [6,48]. Th tanδ of the nanocomposite increases slowly with increasing Au-TNR content. Interestingly, tanδ is exceptionally low for all nanocomposites at 1 kHz. The maximum value of tanδ is less than 0.08 at a frequency of 1 kHz. The tanδ value of Au-TNR/PVDF-6 is 0.05, which is much lower than values obtained in other work (tanδ > 0.1) that used Ag@TiO$_2$ as fillers [34,35,37,49]. As shown in Figure 7c, the σ_{ac} value of the Au-TNR/PVDF nanocomposite increased slightly with increasing Au-TNR content. At $f_{Au\text{-}TNRs}$ = 0.624, the σ_{ac} value of the nanocomposite was only 6.58×10^{-9} S·cm^{-1} at 1 kHz, which is lower than that of the other three-phase composite systems (>10^{-7} S·cm^{-1}) [34,35]. These results confirm that no conducting network is formed, indicating that the Au-TNR-PVDF nanocomposites exhibit good insulation properties.
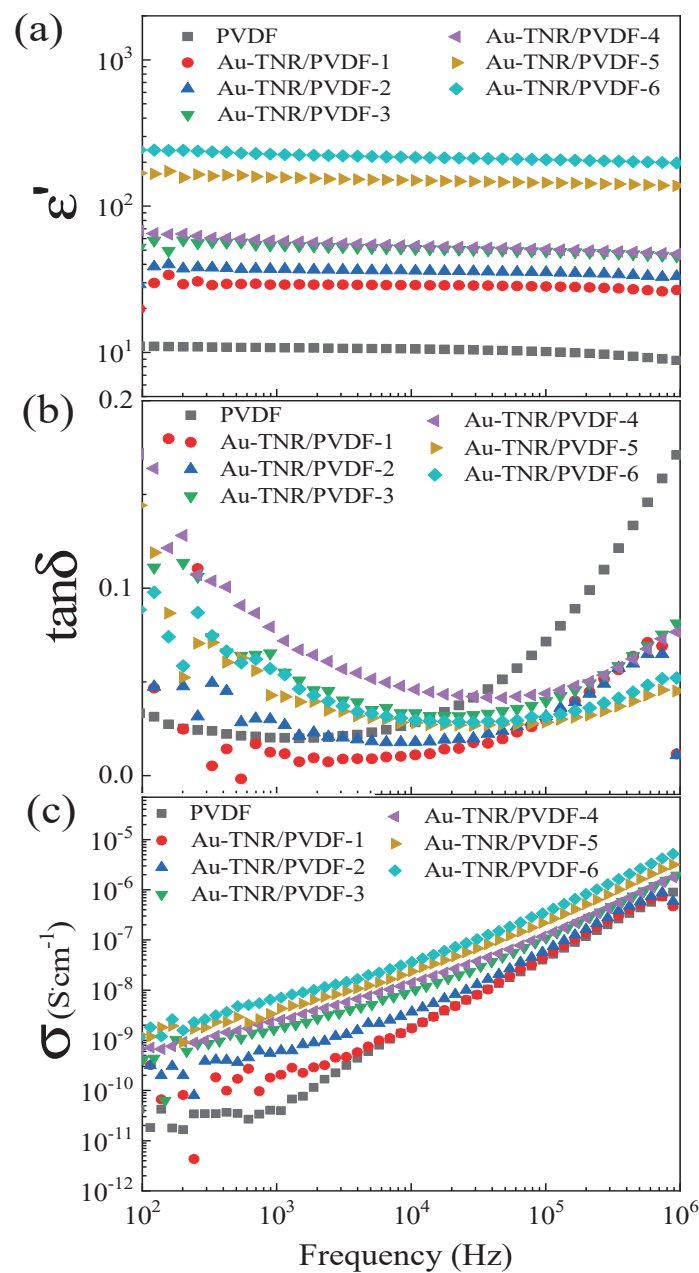
Figure 7. Frequency dependence of (**a**) ε', (**b**) tanδ, and (**c**) σ for nanocomposites with varying amounts of Au-TNRs.

Figure 8 shows the ε' and tanδ of Au-TNR/PVDF at 1 kHz as functions of temperature. As shown in Figure 8a, steady values of ε' were observed for almost all nanocomposites with increasing temperature. Only Au-TNR/PVDF-5 and Au-TNR/PVDF-6 exhibited ε' values that were slightly temperature dependent. Figure 8b shows the tanδ relaxation peaks in the pure PVDF polymer. The first relaxation was observed between −40 and 0 °C, which can be attributed to the β-relaxation of PVDF. The second relaxation was observed at a temperature above 40 °C, which can be attributed to the α-relaxation [50].
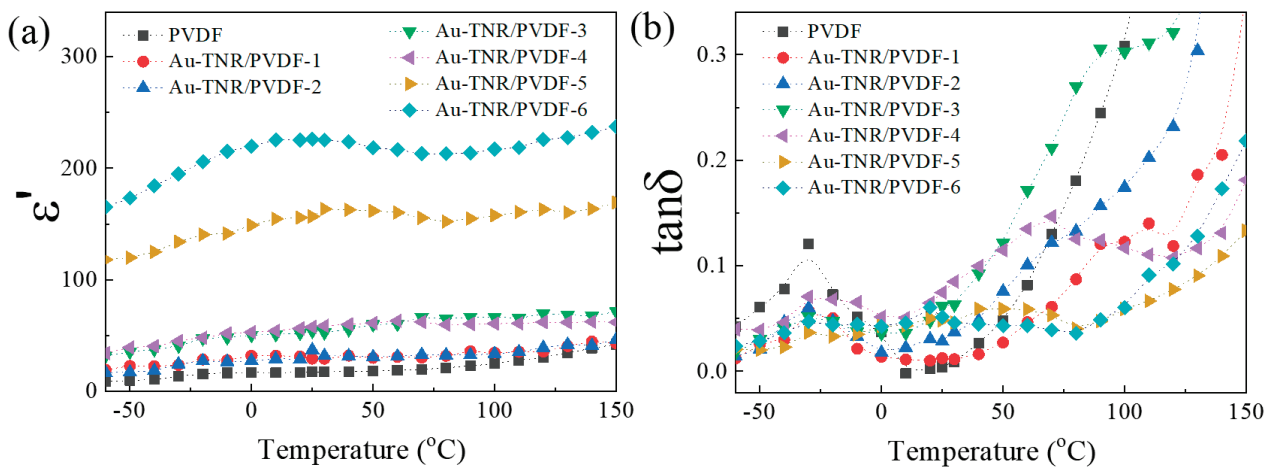
Figure 8. Temperature dependence of (**a**) ε' and (**b**) tanδ for nanocomposites with varying amounts of Au-TNRs.

Figure 9a shows the ε' values of TNR/PVDF and Au-TNR/PVDF-5 as a function of frequency. The ε' value of the three-phase nanocomposite (Au-TNR/PVDF-5) was found to be much higher than that of the two-phase nanocomposite (TNR/PVDF) (with nearly the same total volume fraction of filler) in the 10^2–10^6 Hz frequency range, which indicates that the addition of a small amount of Au nanoparticles can result in a significant enhancement in the ε' of a polymer composite. Interestingly, the tanδ value of the Au-TNR/PVDF-5 nanocomposite at 1 kHz was 0.048. These excellent dielectric properties of Au-TNR/PVDF are not only due to the introduction of the Au-TNR hybrid nanoparticles, but also due to the increasing polar β-phase in the PVDF matrix, which was confirmed by FTIR spectroscopy (Figure 4). The large interfacial area of the semiconducting TNRs is one of the most important factors that significantly increases the dielectric response in the nanocomposite. As shown in Figure 9b, although tanδ of the Au-TNR/PVDF-5 nanocomposite was increased over the measured frequency range compared to that of the two-phase TNR/PVDF nanocomposite, the obtained tanδ value was lower than 0.08 in the frequency range of 10^2–10^6 Hz.
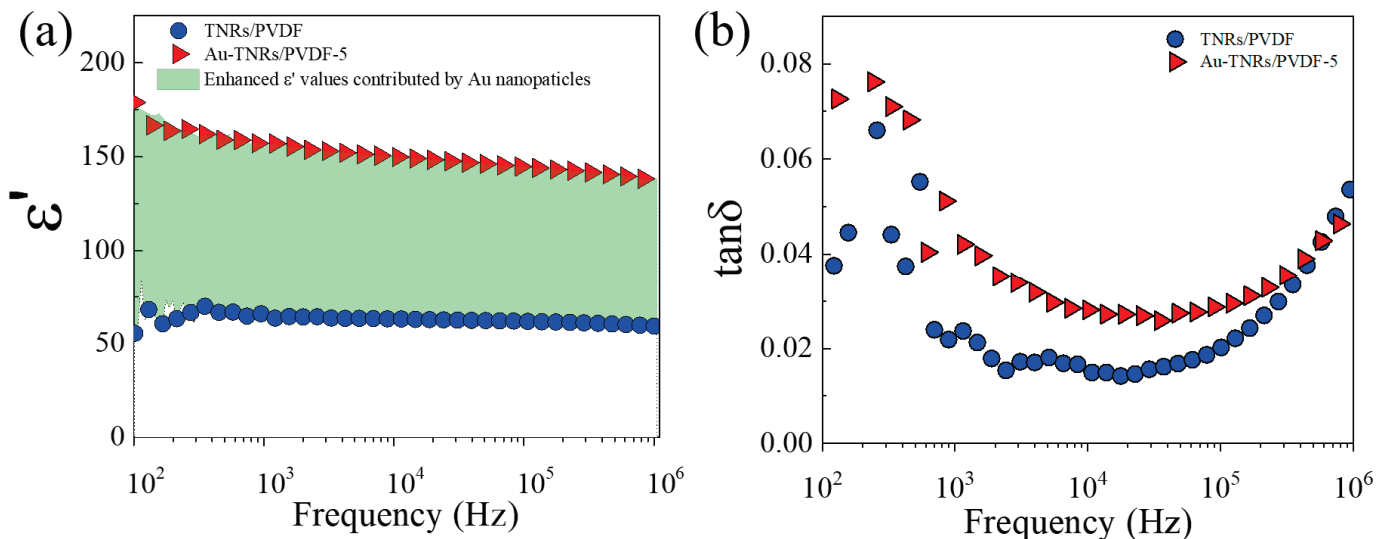

Figure 9. Frequency dependence of (**a**) ε' and (**b**) tanδ for TNR/PVDF and Au-TNR/PVDF-5 at 20 °C; the different ε' values (green area) resulted from the Au nanoparticles.

The ε' values of the Au-TNR/PVDF nanocomposites could not be fitted to two-phase composite models consisting of a ceramic and a polymer (e.g., effective medium theory (EMT), Maxwell–Garnett, Yamada, logarithmic [5,51]) with high Au-TNR contents, as

demonstrated in the inset of Figure 10. This is due to interfacial polarization at the interface between fillers and PVDF polymer matrix. Moreover, the ε' values of the Au-TNR/PVDF nanocomposites could not be fitted to the percolation model, which is employed for metal/polymer dual phases. As shown in Figure 10, the dielectric behavior of the Au-TNR/PVDF nanocomposites is in good agreement with the EMPT model [35,52], which combines the EMT model with percolation theory, as shown in Equation (4):

$$\varepsilon_{\text{eff}} = \varepsilon_{\text{PVDF}}\left[1 + \frac{f_{\text{TNRs}}(\varepsilon_{\text{TNRs}} - \varepsilon_{\text{PVDF}})}{\varepsilon_{\text{PVDF}} + \text{n}(1 - f_{\text{TNRs}})(\varepsilon_{\text{TNRs}} - \varepsilon_{\text{PVDF}})}\right]\left|\frac{f_{\text{c}} - f}{f}\right|^{-q} \tag{4}$$

where ε_{eff} is the effective ε' of the Au-TNR/PVDF composite, f_{TNRs} is the volume fraction of the TNRs, f_{c} is the percolation threshold, $\varepsilon_{\text{PVDF}}$ is the ε' of PVDF ($\varepsilon_{\text{PVDF}} = 10.78$), $\varepsilon_{\text{TNRs}}$ is the ε' of TNRs ($\varepsilon_{\text{TNRs}} = 150$), n is the morphology fitting factor, and q is the critical exponent. Due to the semiconducting nature of TNRs and conducting nature of Au nanoparticles, f is assigned as the volume fraction of Au-TNR hybrid particles, which can influence the percolation behavior of the composites. For the curve fitted using the EMPT model, the optimum fitting parameters were determined to be: n = 0.11, q = 1.0, and f_{c} = 0.8. It is worth noting that n and q are very close to those reported for the Ag-BaTiO$_3$/PVDF (n = 0.11) [52] and the Ni-BaTiO$_3$/PVDF (q = 1.0) [23], respectively. The percolation threshold is expected to occur at a high filler loading (f_{c} = 0.8), which is much higher than the maximum filler loading used in this current study, and is due to the small amount of conductive Au nanoparticles used and the hybrid structure of the Au-TNR particles. Therefore, the percolation network (or conduction pathway) would not be formed in the Au-TNR/PVDF composite because the hybrid structures of the Au-TNRs prevent the formation of conducting pathways because the randomly grown Au nanoparticles do not continuously coat the TNR surface. The large increase in the ε' value is primarily attributed to interfacial polarization between the Au–PVDF, Au–TNR, and TNR–PVDF interfaces.
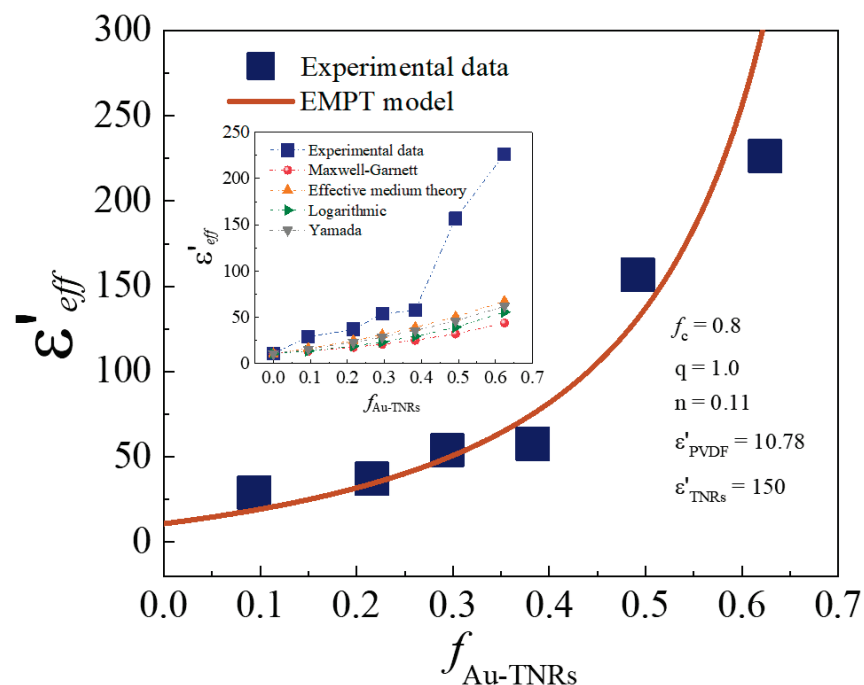
Figure 10. Experimental data of ε' for the Au-TNR/PVDF nanocomposites at 1 kHz and 20 °C fitted by the effective medium theory (EMPT) model; inset is the experimental data of ε' for the Au-TNR/PVDF nanocomposites fitted by two-phase various theoretical models.

4. Conclusions

This study presented a novel method for successfully achieving high ε' and low tanδ in three-phase PVDF polymer-matrix nanocomposites. The dielectric properties of a PVDF polymer improved significantly by incorporating conductive Au nanoparticles and semi-conductive TNRs with enlarged interfacial areas. The Au nanoparticles were discretely attached to the TNR surfaces to enhance interfacial polarization and simultaneously prevent the formation of conducting pathways in the insulative PVDF matrix. As a result, a high ε' (~157) and low tanδ (~0.05) were obtained in the three-phase nanocomposite filled with 1.8 vol% Au and 47.4 vol% TNRs. The dielectric response in the two-phase TNR/PVDF composite increased by more than a factor of two after introducing small amounts of Au nanoparticles. This dielectric behavior is described using the EMPT model. The results indicate that Au nanoparticles significantly contribute to enhancing interfacial polarization and creating a more polar β-PVDF phase, which increases ε'. In contrast, due to the small amount of Au nanoparticles used and their discrete growth on the TNRs, the value of tanδ remained low. To further investigate the possible use of the Au-TNR/PVDF nanocomposites in capacitor applications, fabrication conditions that produce nanocomposite thin films need be studied.

References

1. Zhang, S.; Zhang, N.; Huang, C.; Ren, K.; Zhang, Q.M. Microstructure and electromechanical properties of carbon nanotube/poly(vinylidene fluoride—trifluoroethylene—chlorofluoroethylene) composites. *Adv. Mater.* **2005**, *17*, 1897–1901. [CrossRef]
2. Beier, C.W.; Sanders, J.M.; Brutchey, R.L. Improved breakdown strength and energy density in thin-film polyimide nanocomposites with small barium strontium titanate nanocrystal fillers. *J. Phys. Chem. C* **2013**, *117*, 6958–6965. [CrossRef]
3. Thakur, V.K.; Gupta, R.K. Recent progress on ferroelectric polymer-based nanocomposites for high energy density capacitors: Synthesis, dielectric properties, and future aspects. *Chem. Rev.* **2016**, *116*, 4260–4317.
4. Martins, P.; Lopes, A.C.; Lanceros-Mendez, S. Electroactive phases of poly(vinylidene fluoride): Determination, processing and applications. *Prog. Polym. Sci.* **2014**, *39*, 683–706. [CrossRef]
5. Thomas, P.; Varughese, K.T.; Dwarakanath, K.; Varma, K.B.R. Dielectric properties of poly(vinylidene fluoride)/cacu3ti4o12 composites. *Compos. Sci. Technol.* **2010**, *70*, 539–545. [CrossRef]

6. Yu, K.; Niu, Y.; Zhou, Y.; Bai, Y.; Wang, H.; Randall, C. Nanocomposites of surface-modified batio3nanoparticles filled ferroelectric polymer with enhanced energy density. *J. Am. Ceram. Soc.* **2013**, *96*, 2519–2524. [CrossRef]

7. Huang, X.; Jiang, P.; Xie, L. Ferroelectric polymer/silver nanocomposites with high dielectric constant and high thermal conductivity. *Appl. Phys. Lett.* **2009**, *95*, 242901. [CrossRef]

8. Wang, L.; Dang, Z.-M. Carbon nanotube composites with high dielectric constant at low percolation threshold. *Appl. Phys. Lett.* **2005**, *87*, 042903. [CrossRef]

9. Moharana, S.; Mahaling, R.N. Preparation and properties of benzoxazine (ba) based bifeo3-poly(vinylidene fluoride) (pvdf) composites: Enhanced dielectric constant and suppressed loss. *Polym. Plast. Technol. Mater.* **2021**, *60*, 1122–1134.

10. Kishor Kumar, M.J.; Kalathi, J.T. Investigation on the dielectric performance of pvdf-hfp/lzo composites. *J. Alloy. Compd.* **2020**, *843*, 155889.

11. Zhang, Y.; Wang, W.; Zhang, J.; Ni, Y. Dielectric relaxation processes in pvdf composite. *Polym. Test.* **2020**, *91*, 106801. [CrossRef]

12. Thomas, P.; Satapathy, S.; Dwarakanath, K.; Varma, K.B.R. Dielectric properties of poly(vinylidene fluoride)/cacu3ti4o12 nanocrystal composite thick films. *Express Polym. Lett.* **2010**, *4*, 632–643. [CrossRef]

13. Amaral, F.; Rubinger, C.P.L.; Henry, F.; Costa, L.C.; Valente, M.A.; Barros-Timmons, A. Dielectric properties of polystyrene–ccto composite. *J. Non Cryst. Solids* **2008**, *354*, 5321–5322. [CrossRef]

14. Zhang, L.; Wu, P.; Li, Y.; Cheng, Z.Y.; Brewer, J.C. Preparation process and dielectric properties of ba0.5sr0.5tio3–p(vdf–ctfe) nanocomposites. *Compos. Part B Eng.* **2014**, *56*, 284–289. [CrossRef]

15. Li, K.; Wang, H.; Xiang, F.; Liu, W.; Yang, H. Surface functionalized ba0.6sr0.4tio3 /poly(vinylidene fluoride) nanocomposites with significantly enhanced dielectric properties. *Appl. Phys. Lett.* **2009**, *95*, 202904. [CrossRef]

16. Su, Y.-L.; Sun, C.; Zhang, W.-Q.; Huang, H. Fabrication and dielectric properties of na0.5bi0.5cu3ti4o12/poly(vinylidene fluoride) composites. *J. Mater. Sci.* **2013**, *48*, 8147–8152. [CrossRef]

17. Dang, Z.M.; Lin, Y.H.; Nan, C.W. Novel ferroelectric polymer composites with high dielectric constants. *Adv. Mater.* **2003**, *15*, 1625–1629. [CrossRef]

18. Zhang, L.; Bass, P.; Cheng, Z.Y. Revisiting the percolation phenomena in dielectric composites with conducting fillers. *Appl. Phys. Lett.* **2014**, *105*, 042905. [CrossRef]

19. Begum, S.; Ullah, H.; Kausar, A.; Siddiq, M.; Aleem, M.A. Fabrication of epoxy functionalized mwcnts reinforced pvdf nanocomposites with high dielectric permittivity, low dielectric loss and high electrical conductivity. *Compos. Sci. Technol.* **2018**, *167*, 497–506. [CrossRef]

20. Audoit, J.; Laffont, L.; Lonjon, A.; Dantras, E.; Lacabanne, C. Percolative silver nanoplates/pvdf nanocomposites: Bulk and surface electrical conduction. *Polymer* **2015**, *78*, 104–110. [CrossRef]

21. Wang, Z.; Wang, T.; Fang, M.; Wang, C.; Xiao, Y.; Pu, Y. Enhancement of dielectric and electrical properties in bfn/ni/pvdf three-phase composites. *Compos. Sci. Technol.* **2017**, *146*, 139–146. [CrossRef]

22. Yang, W.; Yu, S.; Sun, R.; Ke, S.; Huang, H.; Du, R. Electrical modulus analysis on the ni/ccto/pvdf system near the percolation threshold. *J. Phys. D Appl. Phys.* **2011**, *44*, 475305. [CrossRef]

23. Dang, Z.M.; Shen, Y.; Nan, C.W. Dielectric behavior of three-phase percolative ni–batio3/polyvinylidene fluoride composites. *Appl. Phys. Lett.* **2002**, *81*, 4814–4816. [CrossRef]

24. Su, Y.; Gu, Y.; Feng, S. Composites of nbcto/mwcnts/pvdf with high dielectric permittivity and low dielectric loss. *J. Mater. Sci. Mater. Electron.* **2017**, *29*, 2416–2420. [CrossRef]

25. Su, Y.; Gu, Y.; Li, H.; Geng, F. Ag-nbcto-pvdf composites with enhanced dielectric properties. *Mater. Lett.* **2016**, *185*, 208–210. [CrossRef]

26. Luo, S.; Yu, S.; Sun, R.; Wong, C.P. Nano ag-deposited batio3 hybrid particles as fillers for polymeric dielectric composites: Toward high dielectric constant and suppressed loss. *ACS Appl. Mater. Interfaces* **2014**, *6*, 176–182. [CrossRef]

27. Arbatti, M.; Shan, X.; Cheng, Z.Y. Ceramic–polymer composites with high dielectric constant. *Adv. Mater.* **2007**, *19*, 1369–1372. [CrossRef]

28. Hu, W.; Liu, Y.; Withers, R.L.; Frankcombe, T.J.; Noren, L.; Snashall, A.; Kitchin, M.; Smith, P.; Gong, B.; Chen, H.; et al. Electron-pinned defect-dipoles for high-performance colossal permittivity materials. *Nat. Mater.* **2013**, *12*, 821–826. [CrossRef] [PubMed]

29. Homes, C.C.; Vogt, T. Colossal permittivity materials: Doping for superior dielectrics. *Nat. Mater.* **2013**, *12*, 782–783. [CrossRef]

30. Tuichai, W.; Danwittayakul, S.; Chanlek, N.; Thongbai, P. Nonlinear current-voltage and giant dielectric properties of al^{3+} and ta^{5+} co-doped tio$_2$ ceramics. *Mater. Res. Bull.* **2019**, *116*, 137–142. [CrossRef]

31. Tse, M.-Y.; Wei, X.; Wong, C.-M.; Huang, L.-B.; Lam, K.-H.; Dai, J.; Hao, J. Enhanced dielectric properties of colossal permittivity co-doped tio2/polymer composite films. *RSC Adv.* **2018**, *8*, 32972–32978. [CrossRef]

32. Kim, K. Characterization of poly(vinylidenefluoride-co-hexafluoropropylene)-based polymer electrolyte filled with rutile tio2 nanoparticles. *Solid State Ion.* **2003**, *161*, 121–131. [CrossRef]

33. An, N.; Liu, H.; Ding, Y.; Zhang, M.; Tang, Y. Preparation and electroactive properties of a pvdf/nano-tio2 composite film. *Appl. Surf. Sci.* **2011**, *257*, 3831–3835. [CrossRef]

34. Chen, X.; Liang, F.; Lu, W.; Zhao, Y.; Fan, G.; Wang, X. Improved dielectric properties of ag@tio2/pvdf nanocomposites induced by interfacial polarization and modifiers with different carbon chain lengths. *Appl. Phys. Lett.* **2018**, *112*, 162902. [CrossRef]

35. Liang, F.; Zhang, L.; Lu, W.-Z.; Wan, Q.-X.; Fan, G.-F. Dielectric performance of polymer-based composites containing core-shell ag@tio2 nanoparticle fillers. *Appl. Phys. Lett.* **2016**, *108*, 072902. [CrossRef]

36. Yang, D.; Huang, S.; Ruan, M.; Wu, Y.; Li, S.; Wang, H.; Zhang, J.; Ma, H.; Guo, W.; Zhang, L. Controllable dielectric performance of polymer composites via the coulomb-blockade effect with core–shell structured nano-particles. *J. Mater. Chem. C* **2017**, *5*, 7759–7767. [CrossRef]

37. Xu, N.; Xiao, X.; Yang, H.; Yu, E.; Zhang, Q. Enhanced dielectric constant and suppressed dielectric loss of ternary composites based on ag-p(vdf-hfp) matrix and tio2 nanowires. *Ceram. Int.* **2016**, *42*, 12475–12481. [CrossRef]

38. Daniel, M.C.; Astruc, D. Gold nanoparticles: Assembly, supramolecular chemistry, quantum-size-related properties, and applications toward biology, catalysis, and nanotechnology. *Chem. Rev.* **2004**, *104*, 293–346. [CrossRef]

39. Phromviyo, N.; Thongbai, P.; Maensiri, S. High dielectric permittivity and suppressed loss tangent in pvdf polymer nanocomposites using gold nanoparticle–deposited batio$_3$ hybrid particles as fillers. *Appl. Surf. Sci.* **2018**, *446*, 236–242. [CrossRef]

40. Kum-onsa, P.; Chanlek, N.; Putasaeng, B.; Thongbai, P. Improvement in dielectric properties of poly(vinylidene fluoride) by incorporation of au–bifeo3 hybrid nanoparticles. *Ceram. Int.* **2020**, *46*, 17272–17279. [CrossRef]

41. Pramanik, G.; Humpolickova, J.; Valenta, J.; Kundu, P.; Bals, S.; Bour, P.; Dracinsky, M.; Cigler, P. Gold nanoclusters with bright near-infrared photoluminescence. *Nanoscale* **2018**, *10*, 3792–3798. [CrossRef] [PubMed]

42. Zhou, C.; Sun, C.; Yu, M.; Qin, Y.; Wang, J.; Kim, M.; Zheng, J. Luminescent gold nanoparticles with mixed valence states generated from dissociation of polymeric au (i) thiolates. *J. Phys. Chem. C Nanomater. Interfaces* **2010**, *114*, 7727–7732. [CrossRef]

43. Liu, G.; Fan, H.; Xu, J.; Liu, Z.; Zhao, Y. Colossal permittivity and impedance analysis of niobium and aluminum co-doped tio2 ceramics. *RSC Adv.* **2016**, *6*, 48708–48714. [CrossRef]

44. Ribeiro, C.; Costa, C.M.; Correia, D.M.; Nunes-Pereira, J.; Oliveira, J.; Martins, P.; Gonçalves, R.; Cardoso, V.F.; Lanceros-Méndez, S. Electroactive poly(vinylidene fluoride)-based structures for advanced applications. *Nat. Protoc.* **2018**, *13*, 681–704. [CrossRef]

45. Kumar, S.; Supriya, S.; Kar, M. Enhancement of dielectric constant in polymer-ceramic nanocomposite for flexible electronics and energy storage applications. *Compos. Sci. Technol.* **2018**, *157*, 48–56. [CrossRef]

46. Ren, L.; Meng, X.; Zha, J.-W.; Dang, Z.-M. Coulomb block effect inducing distinctive dielectric properties in electroless plated barium titanate@silver/poly(vinylidene fluoride) nanocomposites. *RSC Adv.* **2015**, *5*, 65167–65174. [CrossRef]

47. Chen, G.; Wang, X.; Lin, J.; Yang, W.; Li, H.; Wen, Y. Interfacial polarity modulation of kta0.5nb0.5o3 nanoparticles and its effect on dielectric loss and breakdown strength of poly(vinylidene fluoride) nanocomposites with high permittivity. *J. Phys. Chem. C* **2016**, *120*, 28423–28431. [CrossRef]

48. Song, Y.; Shen, Y.; Hu, P.; Lin, Y.; Li, M.; Nan, C.W. Significant enhancement in energy density of polymer composites induced by dopamine-modified ba0.6sr0.4tio3 nanofibers. *Appl. Phys. Lett.* **2012**, *101*, 152904. [CrossRef]

49. Dang, Z.-M.; You, S.-S.; Zha, J.-W.; Song, H.-T.; Li, S.-T. Effect of shell-layer thickness on dielectric properties in ag@tio2core@shell nanoparticles filled ferroelectric poly(vinylidene fluoride) composites. *Phys. Status Solidi A* **2010**, *207*, 739–742. [CrossRef]

50. Lopes, A.C.; Costa, C.M.; Serra, R.S.i.; Neves, I.C.; Ribelles, J.L.G.; Lanceros-Méndez, S. Dielectric relaxation, ac conductivity and electric modulus in poly(vinylidene fluoride)/nay zeolite composites. *Solid State Ion.* **2013**, *235*, 42–50. [CrossRef]

51. Chen, G.; Yang, W.; Lin, J.; Wang, X.; Li, D.; Wang, Y.; Liang, M.; Ding, W.; Li, H.; Lei, Q. Geometrical shape adjustment of kta0.5nb0.5o3 nanofillers for tailored dielectric properties of kta0.5nb0.5o3/pvdf composite. *J. Mater. Chem. C* **2017**, *5*, 8135–8143. [CrossRef]

52. Fang, F.; Yang, W.; Yu, S.; Luo, S.; Sun, R. Mechanism of high dielectric performance of polymer composites induced by batio3-supporting ag hybrid fillers. *Appl. Phys. Lett.* **2014**, *104*, 132909. [CrossRef]

Article

Estimations on Properties of Redox Reactions to Electrical Energy and Storage Device of Thermoelectric Pipe (TEP) Using Polymeric Nanofluids

Qin Gang [1], Rong-Tsu Wang [2],* and Jung-Chang Wang [3],*

[1] College of Chemistry and Chemical Engineering, Shanghai University of Engineering Science, Shanghai 201620, China; qin1862199@163.com

[2] Department of Leisure Management, Yu Da University of Science and Technology, Miaoli County 36143, Taiwan

[3] Department of Marine Engineering (DME), National Taiwan Ocean University (NTOU), Keelung 202301, Taiwan

* Correspondence: rtwang@ydu.edu.tw (R.-T.W.); jcwang@ntou.edu.tw (J.-C.W.); Tel.: +886-2-2462-2192 (ext. 7109 or 7139) (J.-C.W.)

Abstract: A thermoelectric pipe (TEP) is constructed by tubular graphite electrodes, Teflon material, and stainless-steel tube containing polymeric nanofluids as electrolytes in this study. Heat dissipation and power generation (generating capacity) are both fulfilled with temperature difference via the thermal-electrochemistry and redox reaction effects of polymeric nanofluids. The notion of TEP is to recover the dissipative heat from the heat capacity generated by the relevant machine systems. The thermal conductivity and power density empirical formulas of the novel TEP were derived through the intelligent dimensional analysis with thermoelectric experiments and evaluated at temperatures between 25 and 100 °C and vacuum pressures between 400 and 760 torr. The results revealed that the polymeric nanofluids composed of titanium dioxide (TiO_2) nanoparticles with 0.2 wt.% sodium hydroxide (NaOH) of the novel TEP have the best thermoelectric performance among these electrolytes, including TiO_2 nanofluid, TiO_2 nanofluid with 0.2 wt.% NaOH, deionized water, and seawater. Furthermore, the thermal conductivity and power density of the novel TEP are 203.1 W/(m·K) and 21.16 W/m^3, respectively.

Keywords: polymeric nanofluid; two-step synthesis; electrochemistry; redox reaction; thermal performance; thermoelectric pipe

1. Introduction

High heat flux generated by many electronic products has recently been comprehensively causing hotspot problems that need to be improved immediately with novel technologies with excellent performances. At present, many 3-C (Computers, Consumers, and Communications) electronic products employ heat pipe [1–5] and vapor chamber [6–11] thermal modules to become the standard equipment, so as to increase the heat dissipation efficiency of the goods and reduce the temperature of the heat sources [12–14]. These two-phase flow heat transfer facilities have high thermal conductivities compared to those of the large-footprint metal material heat sinks [15]. Wang et al. [16,17] showed that the maximum three-dimensional and effective thermal conductivity of the vapor chamber is up to 910 W/mK, many times that of the pure copper base plate at heat flux of over 100 W/cm^2. If it can lower the temperature of the heat source simultaneously and then recycle the heat dissipated, it will be a great contribution to the green energy industry on the basis of conserving energy. Nowadays, as shown in the present paper, it is possible to utilize the temperature effects on electrochemical and thermal activities [18] to accomplish this intention, which can supply a cooling function for the electronic devices and simultaneously exploit the wasted heat energy to generate direct current electric power. Tan et al. [19]

found reasonable charging rates for lithium-ion battery management systems' design at different initial temperatures employing the thermal-electrochemistry coupled model, which investigates the temperature effects on electrochemical and thermal characteristics.

The first voltaic cell/pile of the world was developed by Alessandro Volta, an Italian physicist, between the end of the 18th century and the beginning of the 19th century. It can gather and provide a stable current via the electrochemistry reduction-oxidation (redox) reaction. Hereafter, in 1832, Michael Faraday, an English scientist, depicted in detail the electrochemistry phenomena about the electrolysis process between electric energy and chemical decomposition through solution containing ions. Wang et al. [20–22] utilized the metal oxide nanofluids as an electrolyte (thermoelectric nanofluids) compared with various aqueous solutions according to pH value, Zeta potential, viscosity, and IEP to display the best particle fraction, stability, and settled current output. These results indicated that the thermoelectric nanofluids (Al_2O_3 nanofluid) with temperature variation make use of the temperature effects on electrochemical and thermal activities, which depict the thermoelectric conversion function of temperature gradient into electric power generation in order to improve the application rate of the wasted thermal energy. Nanofluids are widely considered as the innovative nanotechnology-based heat transfer fluids, which have been certified for reforming the energy conversion procedure efficiency [23,24]. The creative notion of thermoelectric nanofluids is energetic and extremely dependable energy transformation that generates electricity in applications in which the heat will be dissipated. For the recent developments in thermal and electrical conductivities of this novel thermal fluid, various factors affect it, including the cluster of nanoparticle type, temperature, preparation methods, surfactant, and volume concentration. It was found that the rise in temperature and volume concentration of nanofluids generally led to linearly incrementing their thermal and electrical conductivities [25–27]. Heyhat and Irannezhad [28] created the thermoelectrical conductivity (TEC) ratio according to the acquired experimental data and thoroughly checked it. Results displayed that both the temperature and concentration have affirmative effects on the thermal and electrical conductivities of nanofluids. Geng et al. [29] discussed the effects of base fluid, temperature, solid volume concentration, and nanoparticle type on electrical conductivity of nanofluid and found that the electrical conductivity generally increases as temperature and solid volume fraction increase. Kim and Park [30] investigated the influence of the multi-walled carbon nanotubes (MWCNTs) nanofluid as an electrolyte on the energy storage capacity in vanadium redox flow battery, which was inspected and contrasted with the primitive electrolyte.

This study develops a thermoelectric pipe (TEP) device for the first time depending on the temperature effects on electrochemical and thermal activities having heat conduction performance and suitability, which adopted the polymeric nanofluid as an electrolyte. According to [21], the 2.0 wt.% titanium dioxide (TiO_2) nanofluid had the best suspension stability and overall thermoelectric properties among the three nanofluids, including the Al_2O_3, ZnO, and TiO_2, in the thermoelectric generation experiments. Pinchuk and Kuzmin [31] studied the effect of the addition of TiO_2 nanoparticles to coal-water fuel on its thermophysical parameters. They suggested that the addition of the TiO_2 nanoparticles in 0.5 to 4 wt.% increases the coal-water fuel thermal conductivity by 9% to 17%. Das et al. [32] noticed that use of TiO_2 nanofluid reduces the wall temperature distribution as well as thermal resistance of thermosyphon and enhances the thermal conductivity compared to deionized water. Therefore, the nanofluids revealed higher thermal conductivity contrasted with base fluid and demonstrated an increase in the effective thermal conductivity with a reduction in particle size and with a growth in particle volume fraction. The present TEP composed of the polymeric nanofluid is capable of generating electromotive force and let-bearing heat dissipation at a temperature difference, and vice versa. Consequently, it is especially favorable for applications in the industrial waste heat and automotive waste heat used for recycling and reusing in order to reduce carbon dioxide emissions. The primary object of the present TEP is to provide a novel device that have high heat conduction performance and relatively good power generation suitability.

2. Materials and Methodology

The section interprets the structural design, thermoelectric function testing, and empirical formula derivation of the thermoelectric performance of the novel TEP, which working principle uses the concepts of heat conduction of the heat pipe and power generation of the electrochemical cell and employs the polymeric nanofluids as electrolysis liquid to improve the thermoelectric performance. Separately, deducing the thermal conductivity of the novel TEP by thermal resistance analysis and measuring the output current and power density of the novel TEP at different temperatures are exploited to derive the empirical formula of the thermoelectric performance via the intelligent dimensional analysis [22] with various experimental data.

2.1. Empirical Formula Derivation of the Novel TEP Thermoelectric Performance

Ordinarily, most of the engineering related to the heat-flow physical mechanics can be analyzed via the motion equations and underlying theories, but there are still many deductions that should be experimentally inspected in order to acquire realistic findings, because the deductions derived from the fundamental theories and motion equations may only be employed for the basic estimations. Units and scales are a manual conception with underlying relevance in the physical world, in which it is a more official way of signifying that kind thought. Accordingly, the dimensional analysis does not frequently render a whole exploration, yet it supplies the beneficial procedures toward an intact comprehension for exploiting the helpful results that are not petty and not distinct. Dimensional analysis is a variable skill and manner that may be accustomed to clarifying and demonstrating the conjunctions between physical quantities, and makes it possible to gather the consequences of estimations and tests in a concise and widespread formula, which can apply forecasts expeditiously. Dimensional analysis is actually adopted to assemble the consequences of experiments in simple and clear modus, so that we can achieve the ordinary fitting from a little number of examinations at a model scale. The present study obtains the empirical formulas of the novel TEP thermoelectric performance, which are derived from the experimental data and the dimensional analysis of factors in Vashy-Buckingham Pi (Π) Theorem. The dimensional analysis with intelligent experiment [22] was introduced, and the application of the empirical formula was searched for the electric charge density output of the novel TEP and waste heat development in the present work. The major ideology of the dimensional analysis with intelligent experiment is that the relationship can continuously be expressed as conjunctions between these Π-dimensional groups. The present study aims to illustrate that the dimensional analysis is a formidable means and covers extended, evident, and new achievements. The analysis procedure is performed to find out all the variables of the novel TEP thermoelectric performance through the repeating variable method resulting from the basic dimensional qualifications. For effective thermal conductivity and power generation empirical formulas of the novel TEP, the dimensional analysis procedure [22] was as follows:

$$K_{tp} = Function\left\{ K_{nf}, C_{nf}, F_{tp},\ T_{tp}, P_{tp}, \mu_{nf},\ \rho_{nf} \right\} \tag{1}$$

$$\overline{P}_{tp} = Function\left\{ V_n, K_{nf}, F_{tp},\ \rho_{nf},\ V_e, T_{tp}, \overline{P}_{nf}, C_{nf},\ P_{tp} \right\} \tag{2}$$

Definitions for the correlated variables of thermoelectric values include the thermal conductivity of the novel TEP, K_{tp}, the thermal conductivity of nanofluid, K_{nf}, the nanofluid specific heat, C_{nf}, the nanofluid viscosity, μ_{nf}, the nanofluid density, ρ_{nf}, the temperature of novel TEP, T_{tp}, the filling amount of novel TEP, F_{tp}, the pressure of novel TEP, P_{tp}, the zeta potential of nanofluid, V_n, the electric charge density output of the novel TEP with nanofluid as electrolyte, $\overline{P}_{tp}$, the standard electric potential of the novel TEP electrode, V_e, and the electric charge density output of the copper-aluminum battery cell with nanofluid as electrolyte, $\overline{P}_{nf}$. We determined the relevant physical quantities and expressed the variables as the basic physical quantities, then selected the required variables to represent

each Π term and repeated variables. We then calculated through repeated variables and multiplied each Π term to find the dimensionless parameters of each Π term. The obtained Π term is expressed as a functional relationship. Equation (1) reveals the K_{tp} function, which was defined via the other seven variables, four of which were independent physical quantities, namely, mass (M), length (L), time (T), and temperature (Θ). $\overline{P}_{tp}$ was decided by the other nine variables, five of which were independent physical quantities consisting of M, L, T, Θ, and voltage (V). These can be employed as in Equation (2). Expressions of all variables were adopted through the M, L, T, Θ, and V, as follows: they are $K_{tp} = \left[\mathrm{MLT^{-3}\theta^{-1}} \right]$, $K_{nf} = \left[\mathrm{MLT^{-3}\theta^{-1}} \right]$, $C_{nf} = \left[\mathrm{L^2T^{-2}\theta^{-1}} \right]$, $\mu_{nf} = \left[\mathrm{ML^{-1}T^{-1}} \right]$, $\rho_{nf} = \left[\mathrm{ML^{-3}} \right]$, $\overline{P}_{nf} = \left[\mathrm{MT^{-3}} \right]$, $T_{tp} = \left[\theta \right]$, $F_{tp} = \left[\mathrm{L^3} \right]$, $P_{tp} = \left[\mathrm{ML^{-1}T^{-2}} \right]$, $V_n = \left[\mathrm{V} \right]$, and $\overline{P}_{tp} = \left[\mathrm{MT^{-3}} \right]$. Regarding the effective thermal conductivity of the novel TEP, there are four dimensionless Π numbers for the K_{tp}. This study chose four repeating variables, K_{nf}, ρ_{nf}, F_{tp}, and C_{nf} for extrapolations. These four repeating variables are multiplied through other non-repeating variables to gain the dimensionless Π parameters. The four Π groups are shown in Equation (3). For the electric charge density of the novel TEP, $\overline{P}_{tp}$, five dimensionless Π number groups are determined separately and five repeated variables ($\overline{P}_{nf}$, V_e, F_{tp}, ρ_{nf}, and C_{nf}) are chosen. The analysis procedure is the same as the empirical formula of Equation (3). Equation (2) displayed the electric charge density output functional equation. The five Π groups are exhibited in Equation (4). The known attributes of the novel TEP acquired from the thermoelectric experiment and experimental data are substituted into Equations (3) and (4) to obtain the indeterminate values of α, β, γ, λ, and τ. After simplification, the thermoelectric empirical formula of the novel TEP are derived in the present study.

$$\frac{\mathrm{K}_{tp}}{\mathrm{K}_{nf}} = \alpha \left\{ \frac{\mu_{nf} \cdot \mathrm{F}_{tp}^{\frac{4}{3}} \cdot \mathrm{C}_{nf}}{\mathrm{K}_{nf}} \right\}^{\beta} \left\{ \frac{\mathrm{T}_{tp} \cdot \rho_{nf}^{2} \cdot \mathrm{F}_{tp}^{\frac{2}{3}} \cdot \mathrm{C}_{nf}^{3}}{\mathrm{K}_{nf}^{2}} \right\}^{\gamma} \left\{ \frac{\mathrm{P}_{tp} \cdot \rho_{nf} \cdot \mathrm{F}_{tp}^{\frac{2}{3}} \cdot \mathrm{C}_{nf}^{2}}{\mathrm{K}_{nf}^{2}} \right\}^{\lambda} \quad (3)$$

$$\frac{\overline{\mathrm{P}}_{tp}}{\overline{\mathrm{P}}_{nf}} = \alpha \left\{ \frac{\mathrm{V}_n}{\mathrm{V}_t} \right\}^{\beta} \left\{ \frac{\mu_{nf}}{\overline{\mathrm{P}}_{nf}^{\frac{1}{3}} \cdot \mathrm{F}_{tp}^{\frac{1}{3}} \cdot \rho_{nf}^{\frac{2}{3}}} \right\}^{\gamma} \left\{ \frac{\mathrm{T}_{tp} \cdot \rho_{nf}^{\frac{2}{3}} \cdot \mathrm{C}_{nf}}{\overline{\mathrm{P}}_{nf}^{\frac{2}{3}}} \right\}^{\lambda} \left\{ \frac{\mathrm{P}_{tp} \cdot \mathrm{F}_{tp}^{\frac{1}{3}}}{\overline{\mathrm{P}}_{nf}^{\frac{2}{3}} \cdot \rho_{nf}^{\frac{1}{3}}} \right\}^{\tau} \quad (4)$$

This research reports the intelligent dimensional analysis methods [22] to be used to find the effective thermal conductivity values and the electric charge density output values of the novel TEP. Consequently, inevitable errors certainly exist among the real values owing to the artificial operation, the restriction of preciseness of the experimental instrument, the measured data during experiment, and the values deriving from experimental data. It is essential to premeditate the trial errors so as to find the experimental reliance before resolving the experimental results based on this, where the notion of the error propagation is employed to appraise the experimental errors and basic functionary relations. Many items of effective thermal conductivities and electric charge density outputs are applied separately to survey the effective thermal conductivity values and the electric charge density output values of the novel TEP during the thermoelectric experiments. The effective thermal conductivity values and electric charge density output values respectively pertain to derived variables consisting of K_{tp}, K_{nf}, C_{nf}, μ_{nf}, ρ_{nf}, T_{tp}, F_{tp}, P_{tp}, V_n, $\overline{P}_{tp}$, V_e, and $\overline{P}_{nf}$ which are measured with experimental apparatus. The error of experimental apparatus is propagated to the consequence during deduction, and thereby transforms the errors of effective thermal conductivities and electric charge density output values. The experimental error is indicated with a relative error, and the maximum relative errors of effective thermal conductivities and electric charge density outputs are within $\pm 5.5\%$ and $\pm 10\%$, respectively. The experimental results are exploited in dimensional analysis to derive the empirical formulas of the novel TEP.

2.2. Structural Design of the Novel TEP and Experimental Apparatus

Figure 1 demonstrates that the novel TEP adopts materials including polytetrafluoroethylene (PTFE), Viton rubber (Gasket), carbon, and aluminum. The carbon rod and the aluminum tube with good thermal conductivities are respectively used as the cathode and the anode. In the insight design, the aluminum and carbon are insulated with PTFE and gaskets to avoid short circuits. Afterwards, the ionic compounds and the nanofluids possessing good thermal conductivity were filled into the tube as the electrolytes, which had four types, involving titanium oxide nanofluid, deionized water, surface seawater, and polymeric nanofluids composed of nanoparticles added to sodium hydroxide (NaOH). When the tubular electrode (aluminum tube) and the core rod (carbon rod) electrode have a temperature difference, thermal energy can be directly converted into electric energy by the redox reaction of the electrolytes (four kinds), and the electrodes can generate electromotive force. In particular, the novel PET device may use the structural design between the tubular electrode and the core rod electrode to provide a greater contact area with a heat source, and may be directly immersed in a heat source.
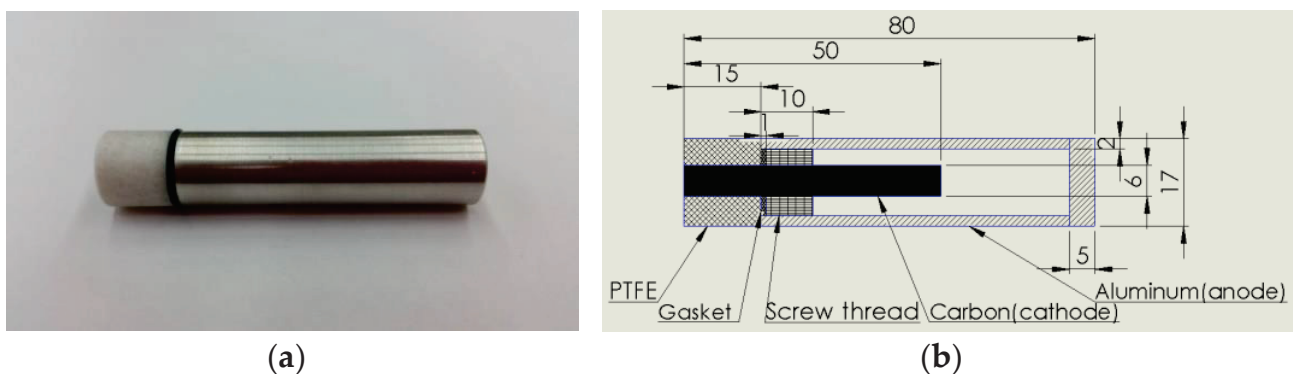
Figure 1. The Novel TEP device. (**a**) Entity photo, (**b**) dimensions and materials.

The principal design of the TEP is based on the energy conservation theorem. Thermal energy increased the rate of the redox reaction, which affected the current density and transferred the energy through electrons to generate electrical energy. The novel TEP is currently devised as a cylinder with a diameter of 17 mm and a length of 80 mm, as shown in the Figure 1b. The operating principle is that the heat energy generated by the machine tool or heat source was transferred to the novel TEP and then the temperature of the nanofluid inside the tube was raised in order to increase the redox reaction rate of the novel TEP, thereby generating additional output power and transferring the power to the carrier for heat recycling.

The experimental framework of the present study is shown in Figure 2. The low-vacuum heating system used in the experiment was manufactured by the thermal-fluid illumination laboratory of National Taiwan Ocean University (NTOU) from Keelung in Taiwan, for which the operating temperature was between 25 and 120 °C and the operating pressure was 300 to 760 torr. The novel TEP was fixed on the heating platform and the operation control panel regulated the time and heating temperature. The low-vacuum glove operation box was employed to fill the electrolytes into the novel TEP, which was from Hoyu Technology Co., Taipei, Taiwan. The oil-free vacuum pump was utilized for low vacuum pressure with a voltage of 100 to 115 V, a motor power of 560 W, and an exhaust speed of 100 l/min. Experimental temperatures were measured by the T-type copper-nickel thermocouples with a wire diameter of 0.32 mm, occupying a measuring range between –200 and 350 °C and an error range of ±0.5 °C. The data logger of the GL-800 was made by Graphtec Co., Yokohama, Japan, which had 40 measuring items containing temperature, voltage, and humidity, etc., with a sampling time of 0.1 ms and a measurement error of ±1%. In the present experiment, the temperature data of the thermocouple can be captured

and recorded on the hard disk and output as a Microsoft Office Excel table. The digital electric meter of TM-8155 with the measurement accuracy of $\pm$ (0.05% reading + 5 digits) used in the experiment was produced by Twintex Instrument Co., New Taipei City, Taiwan, which had the functions of measuring voltage, current, resistance, capacitance, and so on. The generated power density of the novel TEP was determined by the TM-8155. Eventually, the maximum measuring error for the thermoelectric performances of the novel TEP device was thus within $\pm$ 3%.
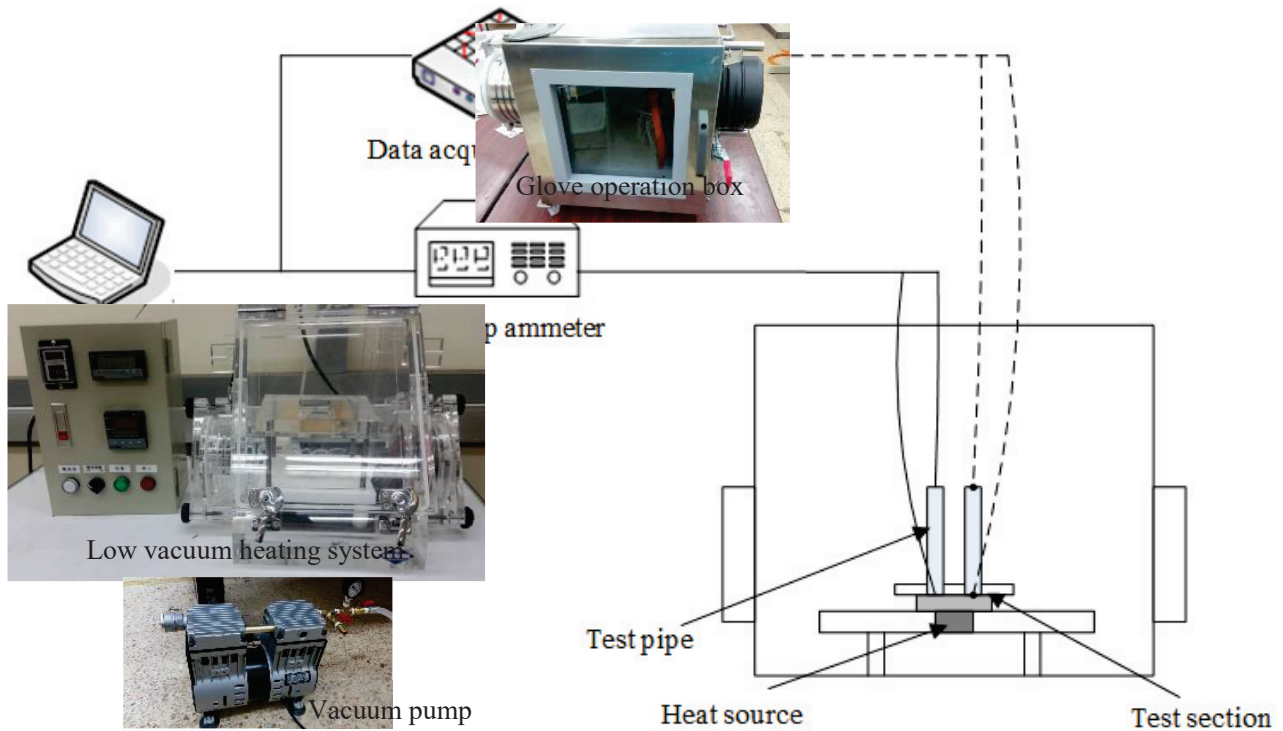

Figure 2. Thermoelectric performance experiment framework of the TEP.

2.3. Thermoelectric Function Testing of the Novel TEP

The performance test of the novel TEP was mainly divided into two parts. The first was to discuss the thermoelectric performance test of the novel TEP using the titanium dioxide nanofluid as the electrolyte under different filling amounts and pressures. Afterwards, the thermoelectric function test of four different electrolytes, including nanofluid, seawater, deionized water, and polymeric nanofluids, composed of nanoparticles added to sodium hydroxide filled into the novel TEP at different temperatures, was investigated. The experimental process of thermoelectric performance is shown in Figure 3.
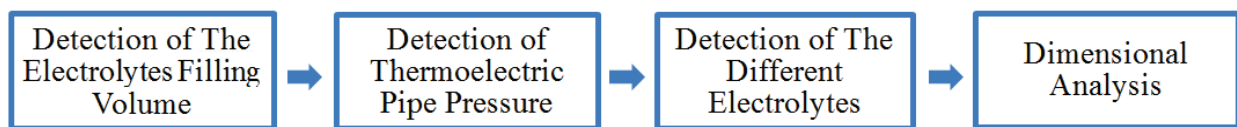

Figure 3. Thermoelectric function testing process of the novel TEP.

The present research mainly exploits the one-dimensional thermal resistance model [22] to evaluate the heat dissipation characteristics of the novel TEP, and the thermal resistance was used to judge the heat dissipation capacity. The larger the thermal resistance value was, the worse the heat dissipation effect was. The thermal resistance of the interface between the heat source and TEP was controlled between 0.05 and 0.09 °C/W. In addition, the thermal conductivity of the novel TEP was derived through the one-dimensional

Fourier heat conduction equation. Thermoelectric performance experiments were carried out in different filling ratios of the novel TEP electrolyte, tube pressures, and electrolyte compositions, and thermocouples were employed to detect the heat transfer of the novel TEP under different temperatures. The temperature difference between the bottom and the top of the novel TEP was adopted to calculate the thermal resistance of the TEP, and then the thermal conductivity of the novel TEP was derived. The thermocouple measurement temperature points and thermal resistance analysis are shown in Figure 4. T_A is the top surface temperature of TEP, T_B is the side surface temperature of TEP, T_C is the bottom surface temperature of TEP, and T_D is the heating source temperature.
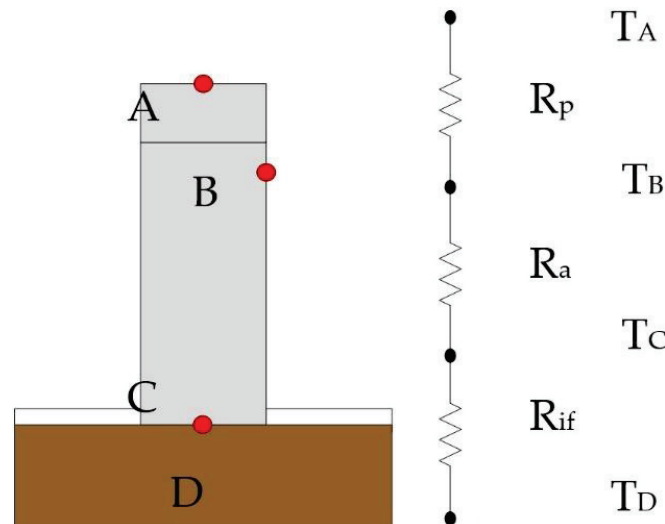
**Figure 4.** Thermal resistance network of the novel TEP.

The effects of filling ratio and vacuum pressure for the novel TEP are major parameters on the thermal performance. In the low-vacuum glove operation box, the oil-free pump was used to evacuate the pressure to the experimental test. The electrical property experiments of the novel TEP with four different solutions involving seawater, deionized water, nanofluid, and polymeric nanofluid are the output current density and power density between 25 and 100 °C. The filling electrolyte processes of the novel TEP are as follows: firstly, fix the TEP in the low-vacuum glove operation box and open the tube cover. When the vacuum pressure reaches the experimental pressure via vacuum pump, close the suction valve. Use the operating gloves to tighten the tube and the cap of the novel TEP. Open the suction valve to make the box pressure reach normal pressure. Then, fix the TEP on the heating platform of the low-vacuum heating system with a downward force of 14.7 N through the baffle plate. The filling ratio experiment was inspected at 400 torr vacuum pressure, at 7 mL (100%), 5.6 mL (80 %), 4.2 mL (60%), 2.8 mL (40%), and 0 mL (0%), and the vacuum pressure tests were 400, 500, 600, and 760 torr, respectively. The experimental processes of the thermoelectric performance were as follows. First, fix the TEP tube on the heating platform, and apply heat dissipation paste on the bottom to make the heat transfer uniform. Connect to the anode of the aluminum tube and cathode of the carbon rod respectively, and connect a desktop electric meter. Power on the operating platform and set the heat source temperature, and start the heating device and set the heating time to 40 min. When the temperature, current, and voltage of the heat source stabilize and reach the experimental temperature, record the temperatures, output current, and voltage. Finally, adjust the heat source to the experimental temperature of 25 to 100 °C, and reset the heating time. Repeat the above the steps and measure temperature, current, and voltage of the novel TEP for different vacuum pressures and filling ratios under four different electrolytes.

3. Results

The thermoelectric performances of the novel TEP under different conditions involving the temperatures, pressures, and better nanofluids as electrolytes are investigated in the present work. Through intelligent experiments, obtained data can be utilized to summarize the empirical formulas of the novel TEP thermoelectric performances by the dimensional analysis method [22].

3.1. Effect of Adding Ionic Compounds on Nanofluids

To explore the effect of adding different concentrations of sodium hydroxide (NaOH) on the particle size and suspension of the polymeric nanofluids, this study appended a better concentration of NaOH to the 2 wt.% titanium dioxide (TiO_2) nanofluid to improve the electrical properties of the novel TEP device. NaOH is an ionic compound that will completely dissociate into sodium ions (Na^+) and hydroxide ions (OH^-) in an aqueous solution, which increases the number of ions that react with the cathode of aluminum in the solution to raise the amount of current. Figure 5a exhibits the effect of adding 0.1 to 0.5 wt.% NaOH on the particle size of nanofluid in 2 wt.% TiO_2 nanofluid. The average size of nanoparticle of polymeric nanofluids was less than 100 nm when adding lower concentrations of 0.1 to 0.2 wt.% NaOH. When 0.3 wt.% NaOH was appended, the particle size was 211 nm, and the particle sizes were 488 and 1050 nm respectively, when 0.4 to 0.5 wt.% NaOH was added. NaOH will erode the surface of nanoparticles inside the metallic nanofluids as it reaches a certain concentration, resulting in an agglomeration phenomenon. Therefore, for the stability and suspension of polymeric nanofluids, we chose to add a lower concentration of NaOH to reduce the impact on nanoparticles. In Figure 5b, comparing the effect of adding 0.2 wt.% NaOH on the particle size, the overall increase in the particle size of the TiO_2 nanofluid with 0.2 wt.% NaOH was about 39%. Adding ionic compounds into the titanium dioxide nanofluids in this experiment, 0.2 wt.% NaOH has tiny effects on the stability of nanoparticles and suspension by detecting particle size and concentration of the polymeric nanofluids, resulting in improving the electrical properties of the present novel TEP.

(**a**) (**b**)
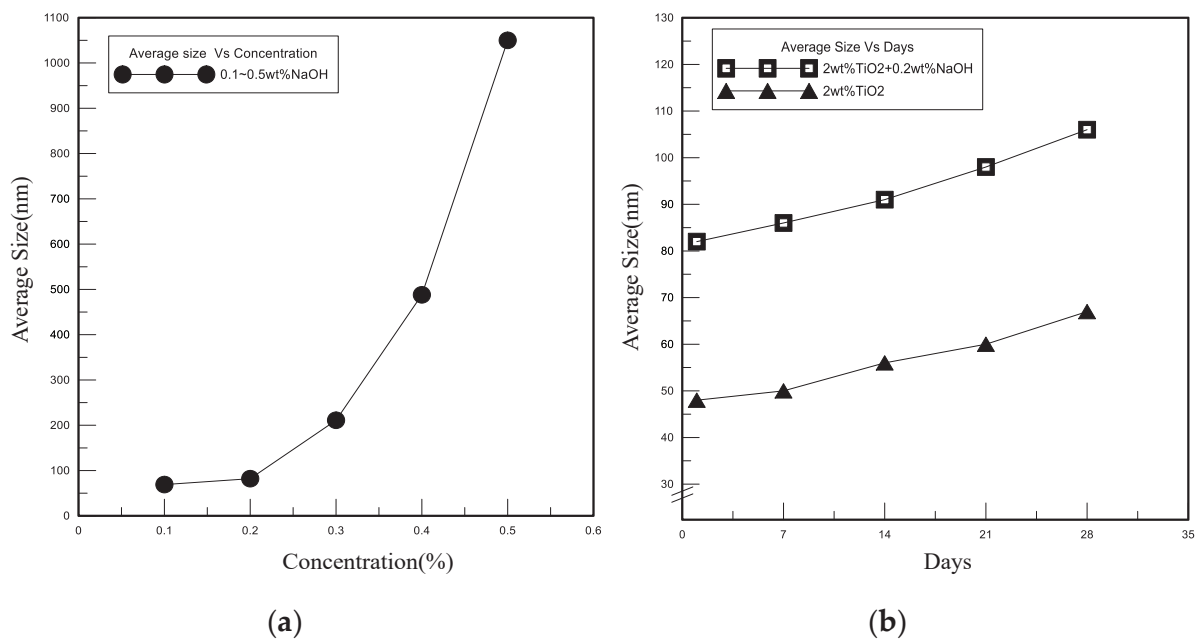
Figure 5. The effect of sodium hydroxide (NaOH) on titanium dioxide (TiO_2) nanofluid. (**a**) Different concentrations of NaOH, (**b**) particle size.

3.2. Effect of Filling Quantity on Thermoelectric Performance of the Novel TEP

As shown in Figure 6, the heat transfer coefficients of the novel TEP tended to increase as the polymeric nanofluid filling amount increased under the pressure of 400 torr in the tube. The thermal conductivity of the novel TEP is derived through the one-dimensional Fourier heat conduction equation and one-dimensional thermal resistance model. We controlled the experimental temperature of the heat source between 25 and 100 °C and let it operate at heating time until steady state. Between 50 and 60 °C, for the filling ratio in the tube of 100% and 80%, the difference in the thermal conductivity was a small increase of about 2%. However, the difference in the coefficient of thermal conductivity of the filling ratio of 100% and 80% in the tube is about 5% above 80 °C. Consequently, the phase change of the fluid increases as the temperature rises. At high temperature, the novel TEP with 80% filling ratio has more space for phase change and takes away more thermal energy, resulting in high thermal conductivity. The current and power of the novel TEP tended to increase as the temperature and filling ratio increased, as shown in Figure 7. When the solution was heated, the evaporation rate of liquid increased to take away more thermal energy, resulting in increasing the thermal conductivity of the novel TEP. Nevertheless, the distinction of the current and power of the novel TEP between 100% and 80% filling ratios was slight because of the novel TEP structural design factors, in which the difference in the electrode reaction area contacted by the filling ratios of 80% and 100% was not large. The electrode reaction surface area of the filling ratio of 100% was only 3.2 cm^2 larger than that of the filling ratio of 80%. The positive reaction was conducive to gas generation. The higher amount of space is conducive to the generation of redox reaction gas of the novel TEP for the filling ratio of 80%, so that the temperature of the polymeric nanofluid in the tube is higher and the electrical energy is increased.
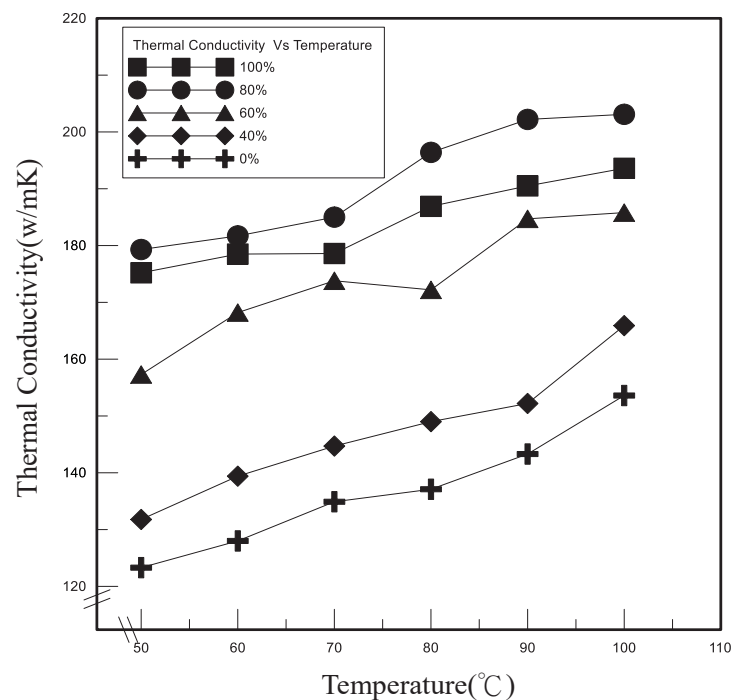

Figure 6. Relationship between thermal conductivity and temperature of TEP.
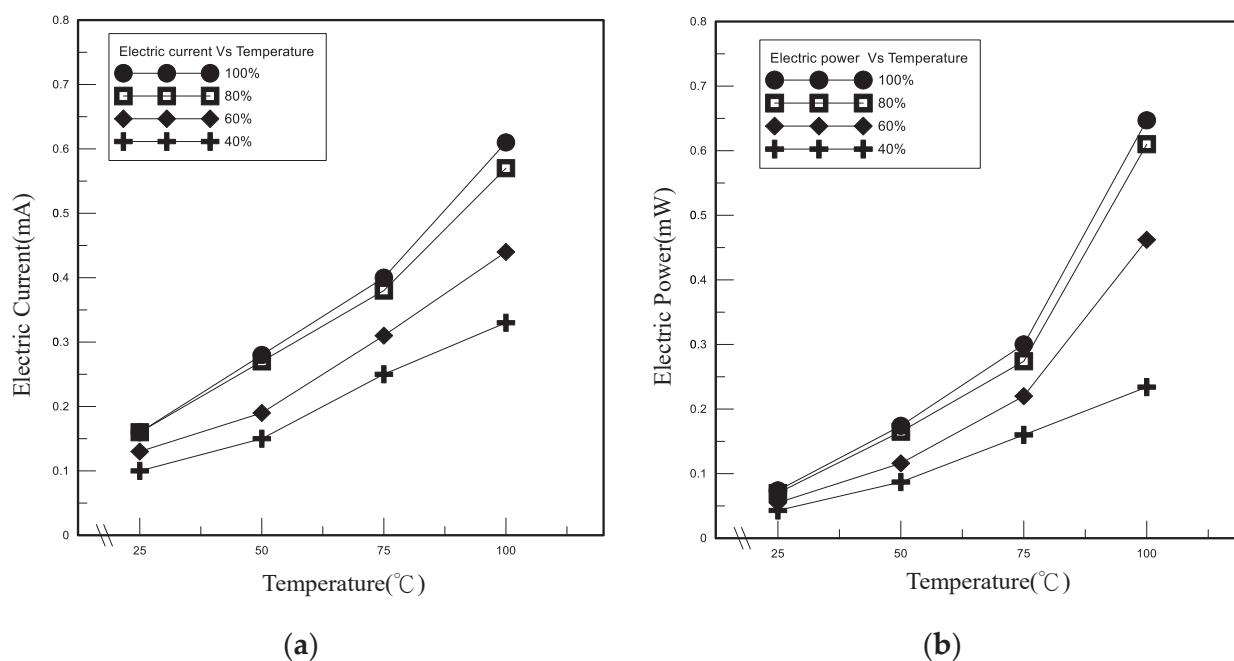
Figure 7. Electric performances of TEP under different filling ratios. (**a**) Current, (**b**) power.

3.3. Effect of Vacuum Pressure on Thermoelectric Performance of the Novel TEP

Table 1 displayed that the thermal conductivities of the novel TEP tended to rise as the vacuum pressure decreased, resulting from the increase in phase change phenomena of the polymeric nanofluid. The overall increment of the thermal conductivity coefficient was about 10% under the vacuum pressure in the TEP tube decreasing from 760 to 400 torr. The relationships between electric performances and temperatures of the novel TEP at different vacuum pressures are shown in Table 2. The power density increased while reducing the vacuum pressure and increasing the thermal conductivity during the heating processes, and the overall temperature of the internal fluid increased, resulting in increasing the power density. These electric performances were current density and power density based on the electrode reaction surface area of the novel TEP, of 24.76 cm^2. Table 2 exhibited that the current and power densities were not greatly affected by vacuum pressure at 25 °C. However, with the increase in temperature and the decrease in vacuum pressure of the novel TEP, the current and power densities had an increasing trend. As the vacuum pressure decreased, the boiling point of the solution inside the tube decreased and the power density tended to increase. Since the reduced vacuum pressure was conducive to the formation of positive electrochemical reactions and the reduction of the thermal resistance inside the tube, the temperature of the polymeric nanofluid inside the tube increased, so that the overall current and power densities rose. In addition, more ions were transported to the electrodes through the auxiliary driving forces of the chemical gradient and potential activity. Reducing the vacuum pressure of the tube increased the rate of the redox reaction, thereby improving the electrical performance. Finally, the overall growth rate was respectively about 22% and 28%.

Table 1. Thermal conductivities W/(m·K) of the novel TEP under various pressures.

Temp. (°C)	Pressure (torr)	760	600	500	400
TEP	50	167.6	169.4	171.3	179.3
	60	169.6	171.0	177.0	181.7
	70	170.4	172.7	178.6	185.0
	80	172.3	179.3	185.8	196.4
	90	181.9	184.7	188.5	202.2
	100	184.2	186.7	190.1	203.1

Table 2. Electric performances ($\mu A/cm^2$ and $\mu W/cm^2$) of the novel TEP under various pressures.

Temp. (°C)	Pressure (torr)	760	600	500	400
Current density ($\mu A/cm^2$) of TEP	25	5.25	5.25	5.65	5.65
	50	8.08	8.89	10.10	10.10
	75	11.71	13.33	14.54	14.94
	100	16.96	18.58	21.01	21.81
Power density ($\mu W/cm^2$) of TEP	25	2.30	2.30	2.59	2.67
	50	4.20	4.44	5.25	5.33
	75	8.20	9.21	10.34	10.74
	100	15.11	16.72	19.55	21.16

3.4. Effect of Different Electrolytes on Thermoelectric Performance of the Novel TEP

Figure 8 demonstrates the thermal conductivities with temperatures change of the novel TEP under various electrolytes, including the deionized water, seawater, titanium dioxide nanofluid, and polymeric nanofluid composed of titanium dioxide nanoparticles with sodium hydroxide. The thermal conductivity of TiO_2 nanofluid was the best among these four solutions. The polymeric nanofluid composed of TiO_2 nanoparticles added to NaOH affects the nanoparticle size, resulting in more serious agglomeration between the nanoparticles and the lower thermal conductivity of NaOH, so that its thermal conductivity tended to decrease more than TiO_2 nanofluid. The difference of thermal conductivity coefficient between seawater and deionized water was not much different and their thermal conductivity coefficients were relatively poor. Compared with deionized water, the overall increase of thermal conductivity coefficient of the novel TEP containing TiO_2 nanofluid was about 11%. The relationships between electric performances and temperatures of the novel TEP at different electrolytes are shown in the Figure 9. However, the effects of different electrolytes on the novel TEP could be seen in that the electric performances of the polymeric nanofluid was the highest among them, and the difference between seawater and the polymeric nanofluid was not much different. Compared with deionized water and TiO_2 nanofluid from Figure 9a, the current density was relatively low. The overall increases in current density of TiO_2 nanofluid and the polymeric nanofluid were respectively about 45% and 419%. Compared with deionized water and TiO_2 nanofluid from Figure 9b, the power density was relatively low. The overall increases in power density of TiO_2 nanofluid and the polymeric nanofluid were respectively about 55% and 768%.
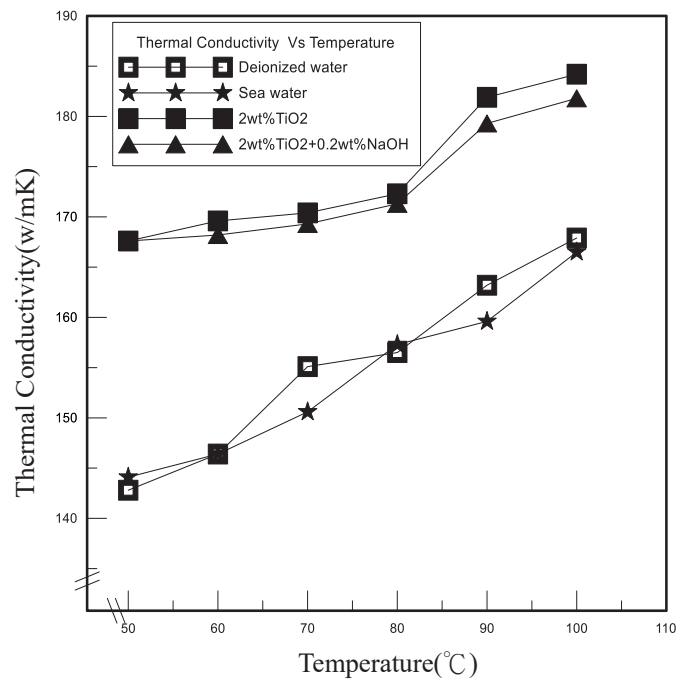
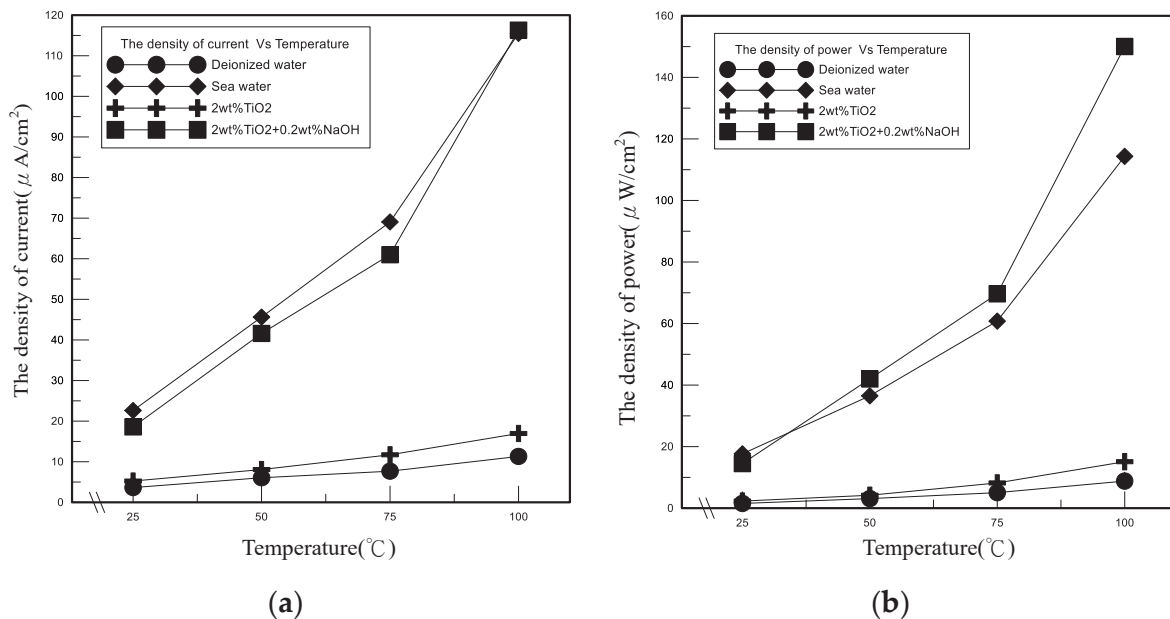**Figure 8.** Relationship between thermal conductivity and temperature of different electrolytes of the novel TEP.

Figure 9. Relationship between electric performances and temperatures of different electrolytes of the novel TEP. (**a**) Current, (**b**) power.

3.5. Thermal Conductivity and Power Density Empirical Formulas of the Novel TEP

In the present study, the purpose of deducing these empirical formulas, including thermal conductivity and power density of the TEP, is to utilize the intelligent dimensional analysis [22] to obtain these values under certain conditions and to enter several basic parameters that did not require instrument measurement. Comprehensive parameters in the empirical formulas were used to forecast the thermoelectric performances of the TEP in the present paper. According to the empirical formulas of the novel TEP derived from the experimental data, they were applicable for 2 wt.% titanium dioxide nanofluids between 25 and 100 °C with vacuum pressure between 400 and 760 torr and with an 80% filling ratio.

Originally, for the thermal conductivity formula of the novel TEP, we substituted the experimental parameters of K_{nf}, ρ_{nf}, F_{tp}, C_{nf}, and μ_{nf} into Equation (3). In order to facilitate a simple calculation, smaller changes of ρ_{nf}, C_{nf}, and μ_{nf} will be substituted into Equation (3) by mean values at different temperatures. As the product of $(C_{nf} \cdot \mu_{nf})$ was a negligible change as vacuum pressure increased, it was ignored because of no impact on the thermal conductivity of TEP and then it was assumed that $\beta = 0$. Therefore, Equation (5) can be briefly acquired as:

$$K_{tp} = 0.62\alpha(50270.55T_{tp})^{\gamma}(13.17P_{tp})^{\lambda} \qquad (5)$$

Equation (5) illustrated that K_{tp} was determined by the temperature and vacuum pressure of the novel TEP. The factor of vacuum pressure was temporarily not pondered. Setting $\lambda = 0$ and taking 400 torr as a benchmark revealed that K_{tp} changed along with temperature at 400 torr. Substituting values from Table 3 into Formula (5), we obtained Equation (6):

$$K_{tp} = 1.2042T_{tp}^{0.866} \qquad (6)$$

Table 3. Parameters substituted into the empirical formulas of the novel TEP.

C_{nf} (J/g-K)		1.45			
ρ_{nf} (kg/m^3)		1084.16			
μ_{nf} (cP)		1.45			
F_{tp} (cm^3)		5.60			
V_t (V)		1.79			
A (cm^2)		24.76			
K_{nf} (W/m-K)		0.62			
$\overline{P}_{nf}$ (μW/cm^2)		2.95			
V_n (mV)		0.47			
	Pressure (torr) / Temp. (°C)	760	600	500	400
$\overline{P}_{tp}$ (μW/cm^2)	25 (298 K)	2.30	2.30	2.59	2.67
	50 (323 K)	4.20	4.44	5.25	5.33
	75 (348 K)	8.20	9.21	10.34	10.74
	100 (373 K)	15.44	16.72	19.55	21.16
K_{tp} (W/m-K)	50 (323 K)	167.6	169.4	171.3	179.3
	60 (333 K)	169.6	171.0	177.0	181.7
	70 (343 K)	170.4	172.7	178.6	185.0
	80 (353 K)	172.3	179.3	185.8	196.4
	90 (363 K)	181.9	184.7	188.5	202.2
	100 (373 K)	184.2	186.7	190.1	203.1

The parameters in Table 3 displayed that the changes in temperature and thermal conductivity of TEP are similar at different vacuum pressures. Consequently, λ value and polynomial function were estimated through the parameters of Table 3 based on 50 °C as the basis under different vacuum pressures. The vacuum pressure was then a function of λ. In summary, the final empirical formula of the novel TEP thermal conductivity is Equation (7):

$$K_{tp} = 1.2042 T_{tp}^{0.866} (13.17 P_{tp})^{\lambda} \lambda = -5.10769 \times 10^{-10} P_{tp}^3 + 9.69923 \times 10^{-7} P_{tp}^2 - 6.1349 \times 10^{-4} P_{tp} + 0.1229 \quad (7)$$

For the power density formula of the novel TEP, the known parameters were substituted into Formula (4). Since the dimensionless parameters were regarded as having little effect on the power density of the novel TEP, the index was assumed to be zero, the same as the processes of deriving the empirical formula of TEP thermal conductivity. Subsequently, the derived results were exhibited in Equation (8), resulting from Equation (4):

$$\overline{P}_{tp} = 0.34\alpha (209.19 T_{tp})^{\lambda} (0.084 P_{tp})^{\tau} \quad (8)$$

Without considering the factor of vacuum pressure first, τ was assumed to be zero when the vacuum pressure of 400 torr was utilized as a benchmark to find the functional relationship of the power density and temperature at this pressure, as shown in Equation (9):

$$\overline{P}_{tp} = \left(2.167 \times 10^{-23}\right) T_{tp}^{9.333} \quad (9)$$

Finally, vacuum pressure was taken into consideration and 50 °C was employed as the benchmark to find the index for τ value. Equation (10) illustrates the power density empirical formula of the novel TEP:

$$\overline{P}_{tp} = \left(2.167 \times 10^{-23}\right) T_{tp}^{9.333} (0.084 P_{tp})^{\tau} \tau = 9.1203 \times 10^{-9} P_{tp}^3 - 1.5595 \times 10^{-5} P_{tp}^2 + 8.4313 \times 10^{-3} P_{tp} - 1.461 \quad (10)$$

As mentioned above, many problems still exist in the present thermoelectric experiments that cause error rates for thermal conductivity and low and unstable current and power output. The calculation method of the error rate is shown in Formulae (11) and (12), where E_K is the error value between the instrument value of $K_{tp,e}$ measured by the equipment and the calculated value of $K_{tp,f}$ calculated by the empirical formula of the thermal conductivity coefficient of the novel TEP. E_P is the error value between the instrument value of $\overline{P}_{tp,e}$ measured by the equipment and the calculated value of $\overline{P}_{tp,f}$ calculated by the empirical formula of the power density of the novel TEP. Tables 4 and 5 illustrate the error rates of E_K and E_P. Initial estimations show that the calculated and measured values were similar. The derived empirical formulas were calculated based on the vacuum pressure of 400 torr and temperature of 50 °C, in which the error rates of the calculated value and the measured value will be lower, and the largest error rate of the thermal conductivity coefficient was 5.06%, indicating that the overall error rates were small. The power density will affect the stabilities of the current and voltage due to the oxidation of the aluminum electrode, and the longer the reaction time, the more the current will decay, and thus the error rate will also be affected. The maximum error rate of power density was 11.27%.

$$E_K = \frac{K_{tp,e} - K_{tp,f}}{K_{tp,e}} \times 100\% \quad (11)$$

$$E_p = \frac{\overline{P}_{tp,e} - \overline{P}_{tp,f}}{\overline{P}_{tp,e}} \times 100\% \quad (12)$$

Table 4. Comparison of measured and calculated thermal conductivities W/(m·K) of TEP and error rates under different vacuum pressures.

Temperature (°C)		50	60	70	80	90	100
760 torr	Equipment	167.60	169.60	170.40	172.30	181.90	184.20
	Formula	167.61	172.10	176.56	181.01	185.44	189.86
	E_K (%)	−0.01	−1.47	−3.62	−5.06	−1.95	−3.07
600 torr	Equipment	169.40	171.00	172.70	179.30	184.70	186.70
	Formula	169.40	173.94	178.45	182.95	187.43	191.89
	E_K (%)	0	−1.72	−3.33	−2.04	−1.48	−2.78
500 torr	Equipment	171.3	177.00	178.60	185.80	188.50	190.10
	Formula	171.3	175.89	180.45	185.00	189.53	194.04
	E_K (%)	−0.01	0.63	−1.04	0.43	−0.55	−2.07
400 torr	Equipment	179.30	181.70	185.00	196.40	202.20	203.10
	Formula	179.33	184.13	188.91	193.67	198.42	203.14
	E_K (%)	−0.02	−1.34	−2.11	1.39	1.87	−0.02

Table 5. Comparison of measured and calculated power densities µW/cm² of TEP and error rates under different vacuum pressures.

Temperature (°C)		25	50	75	100
760 torr	Equipment	2.30	4.20	8.20	15.44
	Formula	2.11	4.48	8.97	17.15
	E_p (%)	8.34	−6.56	−9.46	−11.27
600 torr	Equipment	2.30	4.44	9.21	16.72
	Formula	2.23	4.73	9.49	18.14
	E_p (%)	3.05	−6.54	−3.09	−8.47
500 torr	Equipment	2.59	5.25	10.34	19.55
	Formula	2.64	5.59	11.22	21.43
	E_p (%)	−2.02	−6.54	−8.48	−9.63
400 torr	Equipment	2.67	5.33	10.74	21.16
	Formula	2.68	5.68	11.39	21.76
	E_p (%)	−0.43	−6.52	−5.97	−2.81

4. Conclusions

The empirical formulae including both thermal conductivity and power density for the TEP of TiO_2 nanofluid adopted the dimensional analysis method with thermoelectric experimentation and were applicable to temperatures between 25 and 100 °C and vacuum pressures between 400 and 760 torr in this paper, which were verified and not ordinary expressions. Their error values were separately less than 5.1% and 11.3%. The present empirical equations were not used to forecast the exact values, but instead of portending the thermodynamic activities of the novel TEP under various temperatures and vacuum pressures. For the thermal and electrical performance experiments with different filling volumes, the performances of the novel TEP tended to increase as the filling amount increased. The vacuum pressure inside the tube also affected the electrical and thermal performances of the novel TEP. The results indicated that the novel TEP with a filling ratio of 80% had better performance resulting from the space inside the tube required for the liquid–gas phase conversion to improve heat dissipation and power generation performances.

The thermal performance of titanium dioxide nanofluid of the novel TEP and the electrical performance of the polymeric nanofluid of the novel TEP were respectively better among TiO_2 nanofluid, TiO_2 nanofluid with 0.2 wt.% NaOH, deionized water, and seawater. The temperature and vacuum pressure gradients of chemical and thermodynamic potentials were the driving forces, which had a significant role in the thermoelectric experiment. Finally, the formulas were suitable for an approximate estimation in the present study.

References

1. Zohuri, B. Application of Heat Pipe in Industry. In *Heat Pipe Design and Technology*; Springer: Cham, Switzerland, 2016; pp. 335–394.
2. Wang, J.C. U-and L-shaped heat pipes heat sinks for cooling electronic components employed a least square smoothing method. *Microelectron. Reliab.* **2014**, *54*, 1344–1354. [CrossRef]
3. Wang, R.T.; Lee, Y.W.; Chen, S.L.; Wang, J.C. Performance effects of heat transfer and geometry on heat pipe thermal modules under forced convection. *Int. Commun. Heat Mass Transf.* **2014**, *57*, 140–149. [CrossRef]
4. Zeghari, K.; Louahlia, H.; Le Masson, S. Experimental investigation of flat porous heat pipe for cooling TV box electronic chips. *Appl. Therm. Eng.* **2019**, *163*, 114267. [CrossRef]
5. He, S.; Zhou, P.; Liu, W.; Liu, Z. Experimental study on thermal performance of loop heat pipe with a composite-material evaporator for cooling of electronics. *Appl. Therm. Eng.* **2020**, *168*, 114897. [CrossRef]
6. Bulut, M.; Kandlikar, S.G.; Sozbir, N. A review of vapor chambers. *Heat Transf. Eng.* **2019**, *40*, 1551–1573. [CrossRef]
7. Wang, R.T.; Wang, J.C. Optimization of heat flow analysis for exceeding hundred watts in HI-LEDs projectors. *Int. Commun. Heat Mass Transf.* **2015**, *67*, 153–162. [CrossRef]
8. Wang, R.T.; Wang, J.C. Analysis of thermal conductivity in HI-LEDs lighting materials. *J. Mech. Sci. Technol.* **2017**, *31*, 2911–2921. [CrossRef]
9. Wang, J.C. Thermal investigations on LED vapor chamber-based plates. *Int. Commun. Heat Mass Transf.* **2011**, *38*, 1206–1212. [CrossRef]
10. Wang, J.C. Thermal module design and analysis of a 230 W LED illumination lamp under three incline angles. *Microelectron. J.* **2014**, *45*, 416–423. [CrossRef]
11. Wei, T.; Huang, L.; Qian, J. Study on Application of Aluminous Vapor Chamber in Electronic Module Cooling. In *Proceedings of the Seventh Asia International Symposium on Mechatronics*; Springer: Singapore, 2020; pp. 639–645.
12. Wang, R.T.; Wang, J.C. Analyzing the structural designs and thermal performance of nonmetal lighting devices of LED bulbs. *Int. J. Heat Mass Transf.* **2016**, *99*, 750–761. [CrossRef]
13. Colangelo, G.; Favale, E.; Milanese, M.; de Risi, A.; Laforgia, D. Cooling of electronic devices: Nanofluids contribution. *Appl. Therm. Eng.* **2017**, *127*, 421–435. [CrossRef]
14. Nazari, M.A.; Ghasempour, R.; Ahmadi, M.H. A review on using nanofluids in heat pipes. *J. Therm. Anal. Calorim.* **2019**, *137*, 1847–1855. [CrossRef]
15. Hou, F.; Wang, W.; Zhang, H.; Chen, C.; Chen, C.; Lin, T.; Ferreira, J.A. Experimental evaluation of a compact two-phase cooling system for high heat flux electronic packages. *Appl. Therm. Eng.* **2019**, *163*, 114338. [CrossRef]
16. Wang, R.T.; Wang, J.C.; Chang, T.L. Experimental analysis for thermal performance of a vapor chamber applied to high-performance servers. *J. Mar. Sci. Technol.* **2011**, *19*, 353–360.
17. Wang, J.C.; Wang, R.T. A novel formula for effective thermal conductivity of vapor chamber. *Exp. Tech.* **2011**, *35*, 35. [CrossRef]
18. Wang, J.C.; Chiang, W.C. Researches on thermo-electric properties of seawater and Al_2O_3 nanofluids. In *Applied Mechanics and Materials*; Trans Tech Publications Ltd.: Stafa-Zurich, Switzerland, 2013; Volume 394, pp. 14–19.
19. Tan, M.; Gan, Y.; Liang, J.; He, L.; Li, Y.; Song, S.; Shi, Y. Effect of initial temperature on electrochemical and thermal characteristics of a lithium-ion battery during charging process. *Appl. Therm. Eng.* **2020**, *177*, 115500. [CrossRef]
20. Wang, R.T.; Wang, J.C. Alumina nanofluids as electrolytes comparisons to various neutral aqueous solutions inside battery. *J. Mech.* **2016**, *32*, 369. [CrossRef]

21. Hou, X.R.; Wang, R.T.; Huang, S.W.; Wang, J.C. Thermoelectric Generation and Thermophysical Properties of Metal Oxide Nanofluids. *J. Mar. Sci. Technol.* **2021**, *29*, 8. [CrossRef]

22. Yen, P.H.; Wang, J.C. Power generation and electric charge density with temperature effect of alumina nanofluids using dimensional analysis. *Energy Convers. Manag.* **2019**, *186*, 546–555. [CrossRef]

23. Ambreen, T.; Kim, M.H. Influence of particle size on the effective thermal conductivity of nanofluids: A critical review. *Appl. Energy* **2020**, *264*, 114684. [CrossRef]

24. Poongavanam, G.K.; Duraisamy, S.; Vigneswaran, V.S.; Ramalingam, V. Review on the electrical conductivity of nanofluids: Recent developments. *Mater. Today Proc.* **2020**, *39*, 1532–1537. [CrossRef]

25. Chereches, E.I.; Minea, A.A. Electrical conductivity of new nanoparticle enhanced fluids: An experimental study. *Nanomaterials* **2019**, *9*, 1228. [CrossRef]

26. Mashali, F.; Languri, E.; Mirshekari, G.; Davidson, J.; Kerns, D. Nanodiamond nanofluid microstructural and thermo-electrical characterization. *Int. Commun. Heat Mass Transf.* **2019**, *101*, 82–88. [CrossRef]

27. Barai, D.P.; Chichghare, K.K.; Chawhan, S.S.; Bhanvase, B.A. Synthesis and Characterization of Nanofluids: Thermal Conductivity, Electrical Conductivity and Particle Size Distribution. In *Nanotechnology for Energy and Environmental Engineering*; Springer: Cham, Switzerland, 2020; pp. 1–49.

28. Heyhat, M.M.; Irannezhad, A. Experimental investigation on the competition between enhancement of electrical and thermal conductivities in water-based nanofluids. *J. Mol. Liquids* **2018**, *268*, 169–175. [CrossRef]

29. Geng, Y.; Khodadadi, H.; Karimipour, A.; Safaei, M.R.; Nguyen, T.K. A comprehensive presentation on nanoparticles electrical conductivity of nanofluids: Statistical study concerned effects of temperature, nanoparticles type and solid volume concentration. *Phys. A Stat. Mech. Its Appl.* **2020**, *542*, 123432. [CrossRef]

30. Kim, J.; Park, H. Impact of nanofluidic electrolyte on the energy storage capacity in vanadium redox flow battery. *Energy* **2018**, *160*, 192–199. [CrossRef]

31. Pinchuk, V.A.; Kuzmin, A.V. The effect of the addition of TiO_2 nanoparticles to coal-water fuel on its thermophysical properties and combustion parameters. *Fuel* **2020**, *267*, 117220. [CrossRef]

32. Das, S.; Giri, A.; Samanta, S. Heat transfer enhancement in a thermosyphon using TiO_2 nanofluid through natural convection. *Energy Sources Part A Recovery Util. Environ. Eff.* **2020**, 1–18. [CrossRef]

TD-DFT Simulation and Experimental Studies of a Mirrorless Lasing of Poly[(9,9-dioctylfluorenyl-2,7-diyl)-co-(1,4-diphenylene-vinylene-2-methoxy-5-{2-ethylhexyloxy}-benzene)]

Mamduh J. Aljaafreh [1]**, Saradh Prasad** [1,2] **, Mohamad S. AlSalhi** [1,2,]***, Raya H. Alhandel** [1] **and Reem A. Alsaigh** [1]

[1] Department of Physics and Astronomy, College of Science, King Saud University, Riyadh 11451, Saudi Arabia; maljaafreh@ksu.edu.sa (M.J.A.); srajendra@ksu.edu.sa (S.P.); rhalhandhal@gmail.com (R.H.A.); rsaigh@ksu.edu.sa (R.A.A.)

[2] Research Chair on Laser Diagnosis of Cancers, Department of Physics and Astronomy, College of Science, King Saud University, Riyadh 11451, Saudi Arabia

* Correspondence: malsalhi@ksu.edu.sa; Tel.: +966-50-510-4815

Abstract: In this work, we investigate the TD-DFT simulation, optical, and mirrorless laser properties of conjugated polymer (CP) Poly[(9,9-dioctylfluorenyl-2,7-diyl)-co-(1,4-diphenylene-vinylene-2-methoxy-5-{2-ethylhexyloxy}-benzene)], also known as (PFO-co-PPV-MEHB) or ADS125GE. TD-DFT calculations were performed for three monomer units with truncated tails using time-dependent density functional theory (TD-DFT) calculations. The calculations showed a highest occupied and lowest unoccupied molecular orbital (HOMO-LUMO) structure and a very high oscillator strength of 6.434 for the singlet-singlet transition at 374.43 nm. Experimentally, the absorption and fluorescence spectra were examined at various concentrations in verity of solvents, such as benzene, toluene, and hexane. The experimental results obtained in hexane were comparable with theoretical UV-VIS spectra calculated under vacuum. Amplified spontaneous emission (ASE) spectra peaked at approximately 509 nm for CO PFO-co-PPV-MEHB in solution and were obtained at suitable concentrations and pump energies. Additionally, the photochemical stability of this CP and coumarin (C510) were compared. Time-resolved spectroscopy (TRS) studies with a sub-nanosecond resolution were performed for the CO under various pump energies. These results showed the excited state dynamics and single-pass optical gain of CO PFO-co-PPV-MEHB.

Keywords: CP PFO-co-PPV-MEHB; sub-nanosecond TRS; amplified spontaneous emission (ASE) spectra; green emitter

1. Introduction

Since their discovery [1,2], four decades of research has been performed on conjugated materials (polymers and oligomers) due to their captivating photophysical properties. The properties of these special materials, such as high quantum yield, high chromophore density, large Stokes shift, wavelength tunability, and large optical gain, have been studied in depth [3]. These extraordinary properties make these polymers ideal in many applications, such as in laser-active media [4–8] flexible FET (field-effect transistors) [9], photovoltaic devices [10], and photodiodes, as well as light-emitting diodes (LEDs) [9–11]. Both conjugated polymers (CPs) and conjugated oligomers (COs) are appealing laser materials and can produce lasing at proper concentrations in solid-state, thin-film, and liquid forms [12–16]. ASE is produced when the active medium is optically excited by an intense laser source. Moreover, the ASE feedback can be converted to a laser when an optical cavity is combined with the system [17]. In general, materials that can achieve ASE can produce lasing under an optical cavity. However, some materials produce lasing in the cavity but cannot produce ASE without a cavity.

Many CPs exhibit amplified spontaneous emission (ASE), mirrorless lasing with high intensity, spatial coherence, and low temporal coherence. CPs as active gain media have

produced ASE and lasing, which could be tunable over a wide range in the visible spectrum [18–20]. Broadband ASE is used as a light source, which benefits many applications such as fiber sensing and telecommunications. These polymers are highly efficient in energy transfer to other polymers, oligomers, and perovskite quantum dots.

The first report on ASE from CPs was presented by Moses et al. MEH-PPV produced ASE via optical pumping in solution and film. The quantum efficiency of MEH-PPV was compared to that of the conventional dye rhodamine 6G [21]. Another group reported laser emission from TOP-PPV in solution [22]. Another CP, poly(9,9-dioctylfluorene) (PFO), was also well studied and found to produce ASE at different wavelengths depending on the concentration in solution. Thin films of PFO produce ASE from the β-phase.

In 2007, Redmond's team studied the first incidence of single-nanowire lasing under optical pumping for CO PFO, in which nanowires were formed through the template wetting method and exhibited a single Fabry–Pérot mode [23]. The threshold energy was 100 nJ. Moreover, the M. S. AlSalhi group investigated the properties of a CP as an active laser medium and proved the presence of excimeric and dimeric states of the CP. They studied the spectral temporal profile as well as ASE from the CP under different concentrations, solvent types, temperatures, and laser energy excitations using a Princeton Instruments PI-MAX 4 ultrafast-gated emCCD with an Acton picosecond spectrograph [24]. R. H. Friend and his team organized an intensive research work on CP blend laser systems, especially with the Forster energy transfer (FRET) mechanism [25,26].

Copolymerization is a technique that enables existing monomers to be combined to achieve new bandgaps and emission properties. The ASE properties of copolymer PFO-co-pX were studied by S.A Alfahd et al. There have only been minimal studies carried out on copolymers with a combination of PFO and PPV derivatives.

However, in general, DFT simulation, optical, and laser studies of conjugated polymers are rare [27–31] and in particular, none are about PFO-co-PPV-MEHB. To the best of our knowledge, this work could be the first work on the TD-DFT calculation of CP PFO-co-PPV-MEHB. We calculated electronic properties such as structure optimization; the E_{HOMO}, E_{LUMO}, E_{Gap}; the dipole moment; and the oscillator strength of PFO-co-PPV-MEHB for structures optimized under the three-monomer truncated-tail oligomer model using the DFT/Coulomb-attenuated method at the B3LYP (CAM-B3LYP)/6-31G(d,p) level by Gaussian 16 and other software. Furthermore, experimental studies of PFO-co-PPV-MEHB spectral and mirrorless laser properties in toluene under transverse excitation were performed. The pump source was the Nd: YAG laser of 355 nm. We demonstrate that under a suitable concentration and a low pump energy, CO PFO-co-PPV-MEHB can produce ASE at 508 in toluene. TRS studies display the ASE in 3D features, with the wavelength, spectral amplitude, and time as the X-, Y-, and Z-axes, correspondingly.

2. Materials and Methods

The molecular structure of CP PFO-co-PPV-MEHB could be explained as a group of bridged structures. The molecule (A) 1-methyl-4-[(1E)-prop-1-en-1-yl] benzene shown in Seg. A is connected to both sides of the familiar CP poly[(9,9-dioctylfluorenyl-2,7-diyl)] (PFO) shown in Seg. B. Molecular segment A is connected to another polymer (1,4-diphenylene-vinylene-2-methoxy-5-{2-ethylhexyloxy}-benzene) resembling the MEH-PPV structure, as shown in Seg. C. The cumulative structure becomes [(A)-(B)-(A)-(C)] n. This approach is taken to modify the HOMO-LUMO gap. The calculated dipole moment is 1.4334525 Debye for n = 3, which is for the structure optimized using the DFT/Coulomb-attenuating method (Becke-3 Parameter-Lee-Yang-Parr) CAM-B3LYP/6-31G(d,p) basis set and the augmented structure is shown in Supplementary Figure S1. We used a workstation that consisted of an Intel i7 processor, 64 GB RAM, and 1 TB SSD hard disk for all our simulations.

The CP has 65,000 ± 35,000 g mol^{-1} as its molecular weight (Mw). American Dye Source, Inc. (Baie-D'Urfé, Montreal, QC, Canada) provided the CP material. (ADS125GE) The Coumarin 510 has an Mw of 318.4 g/mol and was precured from Exciton Luxottica. A

Perkin Elmer Lambda 950 spectrophotometer (Llantrisant, UK) was utilized to record the absorption spectra. The fluorescence spectra at an excitation wavelength of 355 nm from a xenon flash lamp were investigated utilizing a spectrofluorometer (LS 55, Llantrisant, UK). To achieve transverse pumping, the tripled frequency (355 nm) of a 5 ns Nd:YAG laser was focused by a quartz cylindrical lens (5 cm focal length). The cylindrical lens focused the pulse onto a horizontal strip of 1 cm × 2 mm (length × width). One fiber was linked to an Ocean Optics spectrograph (Maybachstrasse, Ostfildern, Germany) to record the spectra. Another fiber was linked to a Princeton Instruments PI-MAX 4 ultrafast-gated emICCD, which had a gate delay of less than 500 ps. The camera had a high-speed electrically controlled shutter that allowed events to be recorded with a sub-nanosecond time resolutions (please see [32]).

The monomer of PF-co-MEH-PPV is very large and requires significant computational resources. The full-scale simulation of the complete polymer structure with many monomers could be challenging. However, an oligomer structure with three connected monomers is accepted in practice for simulating polymer properties; hence, we adopted the n = 3 oligomer approach. To further reduce the computational burden, we cut short the tail of PFO and MEH-PPV segments, as shown in Figure 1b, since its contribution to optical properties is insignificant. However, practically, the long tail offers a higher solubility in many common solvents [33]. The TD-DFT calculations were performed via the following steps. The molecular structure was created using the Gaussian View 6 software. The structure was optimized with Gaussian 16 using the DFT/CAM-B3LYP/6-31G(d,p) basis set [34]. Next, the UV-VIS spectra, HOMO–LUMO structure, and dipole moment were calculated using the CAM-B3LYP/6-31G(d,p) basis set. Other calculations, such as acceptor-donor sites, polarizability, and charge distribution, were calculated using molecular dynamics (HFF) in the MarvinSketch software, as shown in Figure S2a–c. The charge distribution showed that the central ring structure was negative, more negative charges were found at oxygen sites and the edge of the ring was mostly positive. The CP polarizability was calculated for n = 3 was 229.15 A^3, which shows that CP has a high polarizability for external electric fields, such as optical pumping. The H bond acceptor and donor site were calculated and it was found that each monomer contained 2 acceptor and 4 acceptor sites at oxygen; hence, the CPs have more solubility in a medium polar solvent.


(**a**)

(**b**)
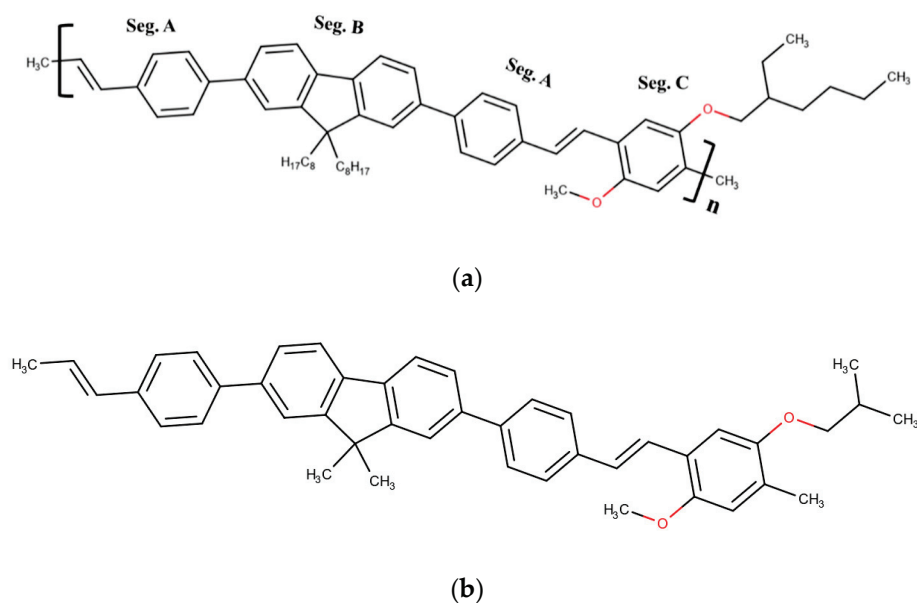
Figure 1. (**a**) Molecular structure of CP poly[(9,9-dioctylfluorenyl-2,7-diyl)-co-(1,4-diphenylene-vinylene-2-methoxy-5-{2-ethylhexyloxy}-benzene)] (i.e., PFO-co-PPV-MEHB). (**b**) Tail-truncated molecular structure utilized for the DFT calculation of PFO-co-PPV-MEHB.

3. Results and Discussion

3.1. DFT Calculation

CPs consist of a large number of atoms; hence, the simulation of CPs is considered to be challenging. Thus, many studies have adopted an oligomeric model of the compound [35–37]. The absorption spectra and energy gap of the PF-co-MEH-PPV were simulated with three monomer units (n = 3) based on the HOMO-LUMO energy gap calculations. Figure 2 shows the HOMO-LUMO structure of the three-monomer model. The HOMO (Frontier orbital) densities are aligned vertically in the major part of the ring structure; however, the density diminishes in the last monomer at one end (left). The LUMO densities are highly delocalized and align horizontally along the molecular backbone. The LUMO density is higher at the end of the oligomer model where the HOMO density is diminished. The movement of the orbital densities upon excitation significantly improves the optical and electronic properties of the CP. The calculated bandgap is 2.91 eV. The HOMO lies at -6.83 and the LUMO lies at -3.92 eV. In the same manner, the structural and optoelectronic properties of CPs and CO (PCDTBT) have been examined by DFT and TD-DFT [38].
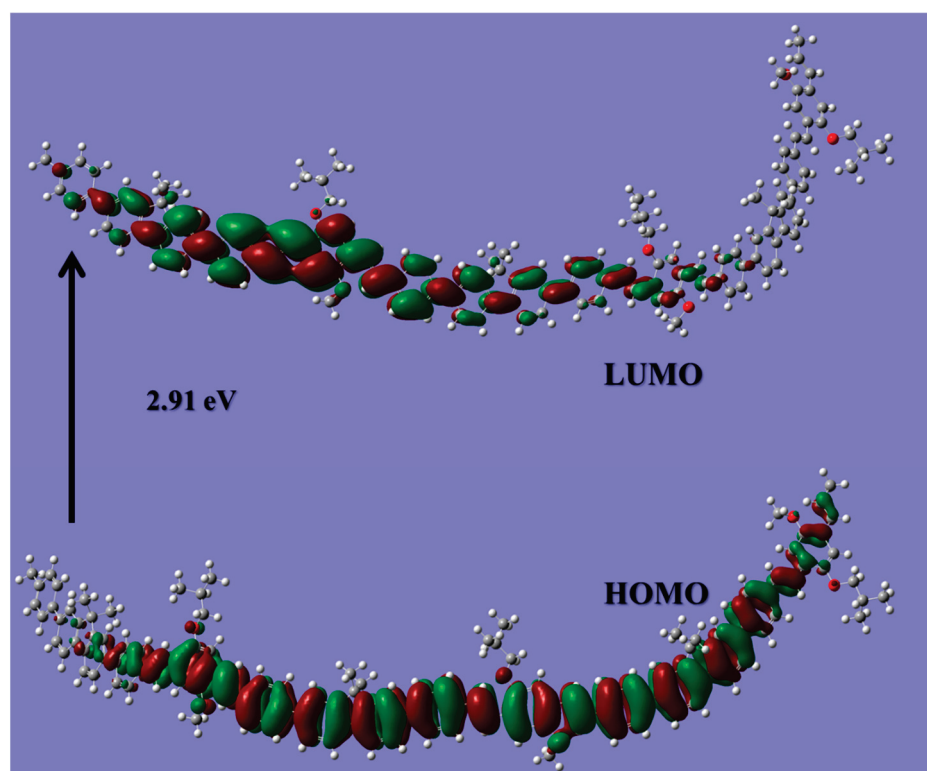
Figure 2. Frontier molecular orbital (HOMO-LUMO) structure of PFO-co-PPV-MEHB (tail-truncated and n = 3 model) calculated using the CAM-B3LYP/6-31G(d,p) basis set.

The UV-VIS spectrum for PFO-co-PPV-MEHB (n = 3) in vacuum was simulated using the DFT/CAM-B3LYP/6-31G(d,p) basis set, as shown in Figure 3a. The results show three singlet oscillator strengths at wavelengths of 341.66, 361.38, and 374.51 nm with high values of f = 0.633, 1.8254, and 6.8762, respectively.

Hexane has a very low dielectric contestant and is a nonpolar solvent; hence, its effect on any molecule (solute) is much less than that of most solvents. Hence, it is optimal for comparison with the results simulated in vacuum. The difference between the simulated and experimental absorption spectra ($\lambda_{Exp} - \lambda_{sim}$) is 30 nm, as presented in Figure 3b. This difference could be attributed to the solvent dielectric constant and concentration of the CP in hexane. However, the simulated singlet oscillator strengths matched the peaks and shoulder of the hexane absorption spectra.
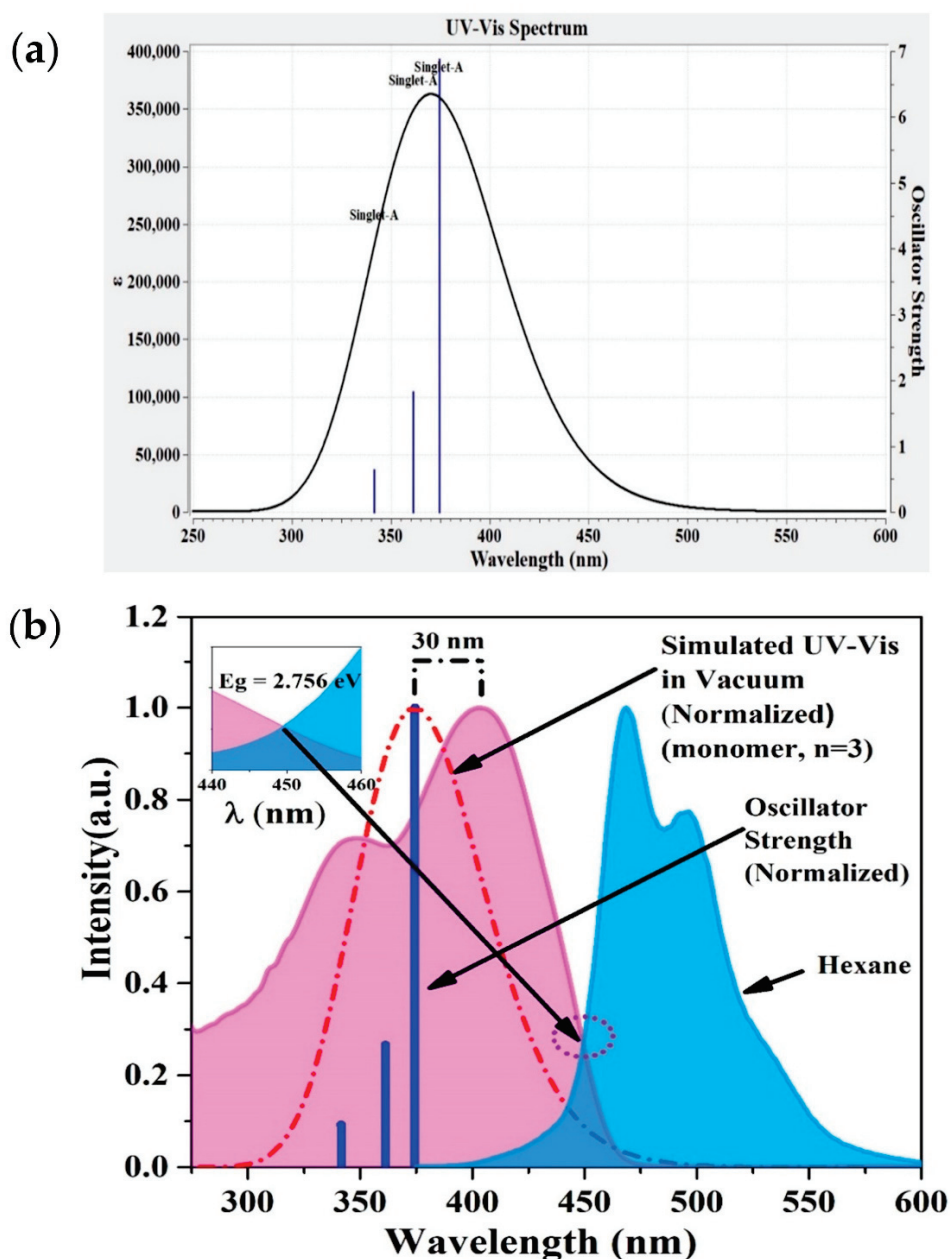
Figure 3. (**a**) UV-VIS and oscillator strength profile of PFO-co-PPV-MEHB (tail-truncated and n = 3 model). (**b**) Absorption of the low-concentration CP in hexane to identify the bandgap using the intersection principle and comparison with the stimulated spectrum.

Figure 3b shows that the bandgap calculated using the absorption and fluorescence intersection method is 2.756 eV. The purple dotted circle highlights the intersection of the absorption and fluorescence spectra, which is zoomed in on and shown in an inset of Figure 3b. This result is in good conformity with the simulated bandgap of 2.91 eV (in hexane). The disturbance could be due to the approximation of the polymer structure and repetition units (n = 3) and a change in the dielectric constant of the solvent. However, the experimental results show two distinctive bands that correlate with the simulated singlet oscillator strengths. Additionally, the experimental results contain three features, two peaks and a shoulder, which could be attributed to the three singlet oscillator strengths found using the simulation methods. The electronic circular dichroism (ECD) result is shown in Figure S3.

Figure S4 shows an estimation of the HOMO−LUMO gaps for PFO-co-PPV-MEHB using the bandgap extrapolation of oligomers (n = 1 to 5). The calculation was performed

using the same TD-DFT method for all repetitive monomer units (n = 1 to 5), but the figures show only n = 3 for a clear presentation of the HOMO LUMO structure. The linear fitting gives the equation E_g (eV) = 2.7667 + 0.3408 × (1/n). When the value of n is large, the second term tends to become negligible. Thus, the calculated bandgap value of the polymer is 2.7667 eV using the extrapolation method. This value is comparable with the experimentally measured bandgap of 2.756 eV.

3.2. Absorption and Fluorescence Spectra of the CP in Toluene

Figure 4 presents the absorption spectra of the CP in toluene and benzene at different concentrations from 195×10^{-4}–12.17×10^{-4} mg/mL. It was found that there are three diverse features. The first is a peak at approximately 355 nm and the second is the main peak at 425 nm, with the third being a shoulder at 370 nm. The optical density decreased from a high value to a low value as the concentration decreased. The absorption spectral profile remained the same, and the full width at half maximum (FWHM) of the maximum peak at 425 nm decreased with the decreasing PFO-co-PPV-MEHB concentration. The absorption spectra in benzene are very close to those of PFO-co-PPV-MEHB in toluene. Figure 4b shows the absorption features in benzene.

(a)

(b)
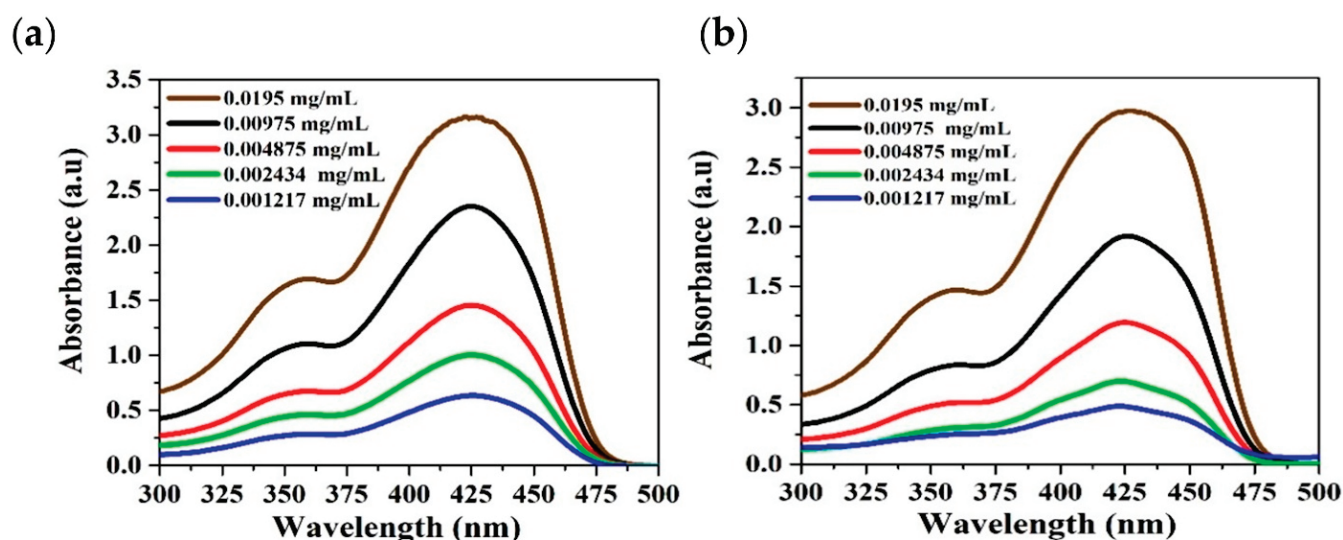
Figure 4. (**a**,**b**) Absorption spectra of PFO-co-PPV-MEHB in (**a**) toluene and (**b**) benzene at various concentrations.

Figure 5a demonstrates the emission spectra of PFO-co-PPV-MEHB in toluene for different concentrations ranging from 2.5 mg/mL to 195×10^{-4} mg/mL. At low concentrations, fluorescence peaks occur at 485 nm and 510 nm, with a tail at 550 nm. Up to a concentration of 0.078 mg/mL, the fluorescence increases; after that, when the concentration (0.156 mg/mL) is further increased, the fluorescence intensity redshifts and the spectral profile shifts toward red. At higher concentrations, the primary peak of the fluorescence spectrum becomes a shoulder and the 515.5 nm peak becomes dominant with reduced intensity. This behavior is common to fluorescent organic molecules. At low concentrations, the fluorescence output is low because the number of molecules is low in a unit area of solution. As the concentration increases, the intensity also increases up to an optimal concentration. Beyond this concentration, the fluorescence output intensity starts decreasing due to the proximity of molecules, which suppress the certain singlet vibration and increase the reabsorption. Figure 5b shows a spectral shift of the singlet peak at around 515.5 at higher concentrations, and the shift is due to reabsorption.
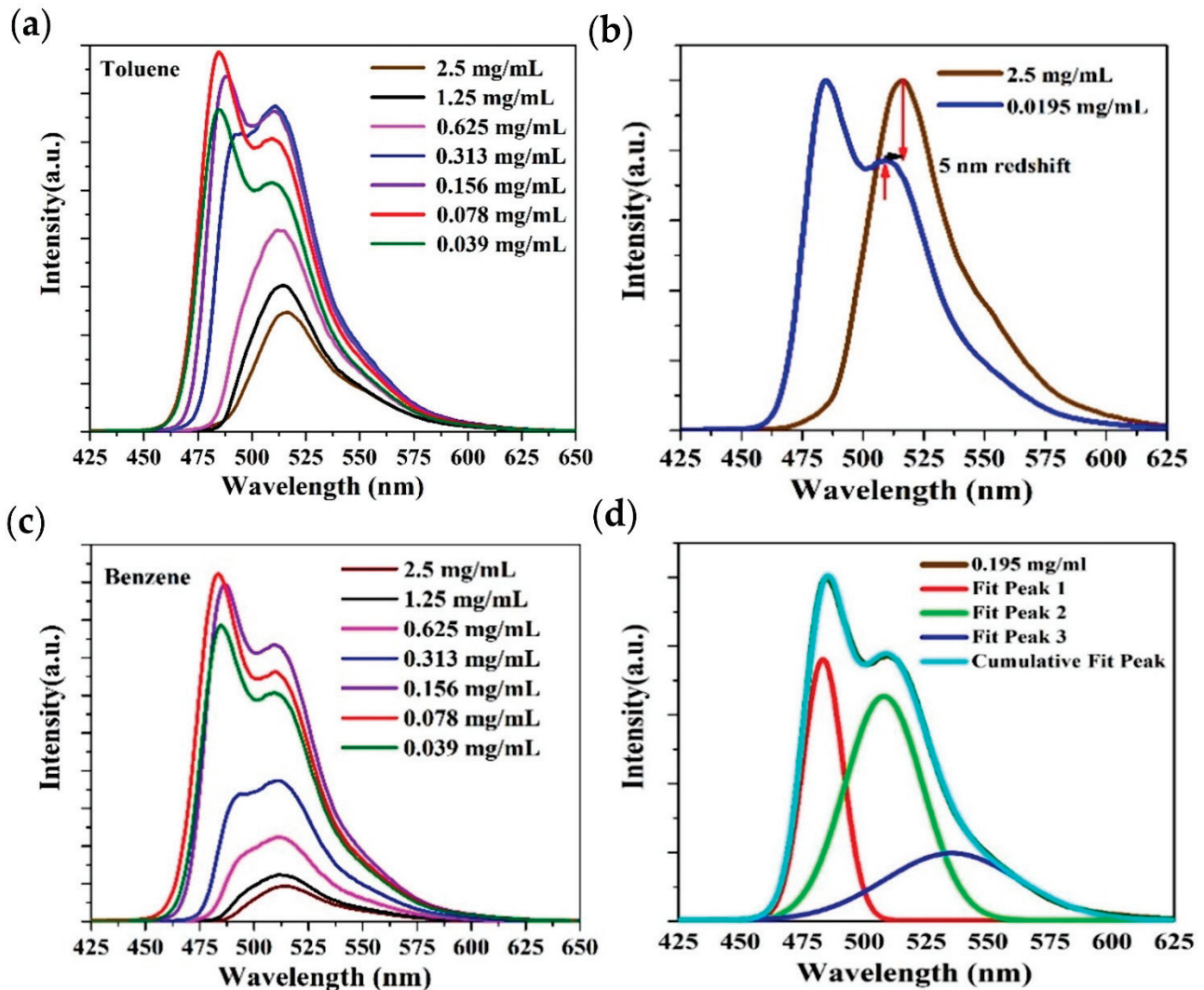
Figure 5. (**a**) Emission spectra of PFO-co-PPV-MEHB for various concentrations in toluene. (**b**) Redshift of the peak fluorescence spectra of PFO-co-PPV-MEHB in toluene. (**c**) Fluorescence spectra in benzene from high to low concentrations. (**d**) Deconvolution of the fluorescence spectrum of PFO-co-PPV-MEHB at 0.0195 mg/mL.

The solvent effect was studied in benzene and the trends of the fluorescence intensity and spectral profile were very similar, with a 4 nm redshift in the peak wavelengths at approximately 483 and 508 nm, as displayed in Figure 5c. This shift is due to the change in the solvent dielectric constant.

Figure 5d shows the deconvolution fitting of the PFO-co-PPV-MEHB fluorescence spectral profile using Gaussian functions. The peak positions are 483.3, 508, and 535.4 nm, and the linewidths are approximately 19, 38, and 60 nm, correspondingly. These peaks can be ascribed to the fluorescence counterparts of the singlet oscillators in the simulated UV-VIS spectra. The Stokes shift was calculated in toluene and benzene and it was 98 nm and 97 nm, respectively. The large Stokes shift could be useful to reduce light scattering and self-absorption in optical materials [39].

3.3. ASE (Mirrorless Lasing) from CO PFO-co-PPV-MEHB in Toluene

Amplified spontaneous emission occurs due to the stimulated emission and amplification of spontaneously emitted photons under a high population inversion with the single-pass gain of the laser media. ASE without feedback can be considered mirrorless lasing, since most of the features are laser features [40]. Many CPs and COs are capable of producing optically pumped ASE [41,42].

PFO-co-PPV-MEHB in toluene at a concentration of 2.5 mg/mL was transversely excited with a 355 nm Nd: YAG laser. At a minimal pump energy density (3.2 mJ/cm^2), the laser-induced fluorescence (LIF) was verified and had two peaks at 507 and 481 nm, as shown in Figure 6. After the pump energy density was increased to 4.5 mJ/cm^2, the spectrum became narrower and peaked at 508 nm with an FWHM of 20 nm. When the pump energy density was 7.75 mJ/cm^2, ASE was obtained with an FWHM of 8.75 nm and a peak at approximately 508 nm, as presented in Figure 6.
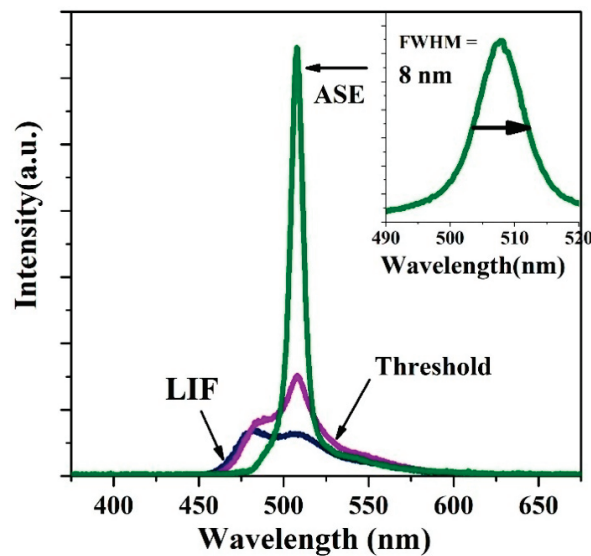
Figure 6. LIF, threshold, and ASE spectra of PFO-co-PPV-MEHB in toluene.

Figure 7 shows the spectral narrowing and increasing of emission intensity of the CP in toluene as a function of the input pump energy density. At 4.5 mJ/cm^2, the FWHM of the spectrum reduced from 60 to 8.4 nm and the surge of intensity was linear. A additional rise in the input energy density boosted the output strength, however the spectral bandwidth (nm) of ASE was sustained. The reduction in bandwidth (nm) occurred due the net gain maximization near the vibronic transition peaks of the fluorescence spectrum; so, the spectrum displayed intensity surge as the pump energy density raised.
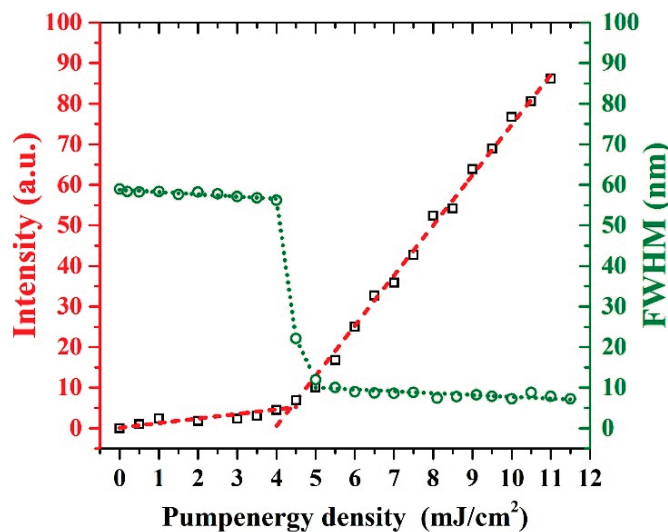
Figure 7. Spectral narrowing and rapid output intensity increase in the CP in toluene as a function of the input pump energy density.

Commonly, photostability is estimated by recording the total ASE intensity emitted under a constant pump energy as a function number of pulses or time. The photodegradation is predictable when a decline in the total ASE output intensity is detected [43]. The ASE stabilities of PFO-co-PPV-MEHB (CP) and the laser dye Coumarin 510 (C510) in its best solvent (methanol) were examined and related, as displayed in Figure 8. Both the CP and C510 were kept at a concentration of 2.5 mg/mL, and the pump energy density was 12.75 mJ/cm^2. The C510 shows signs of degradation, even though the output was high. On the other hand, both the stability and high output of CP did not change much; this shows that CP is a very stable laser material. The CP output was not significantly reduced even after twenty thousand (20×10^3) shots. The CP output was almost maintained, as presented in Figure 8.
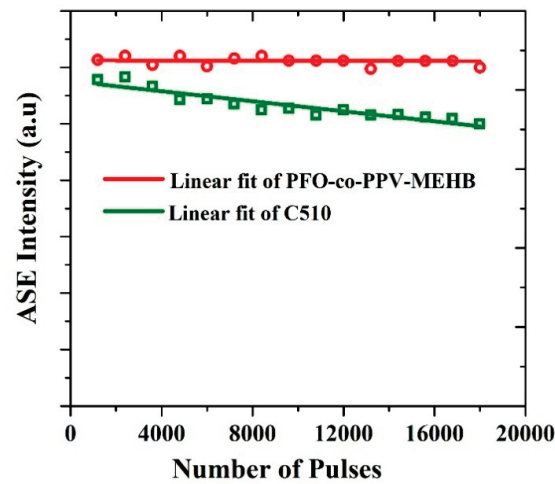
Figure 8. Photochemical stability of the PFO-co-PPV-MEHB ASE in toluene and C510 in methanol at a pump energy density of 12.75 mJ/cm^2.

4. Picosecond Time-Resolved Spectra of ASE in Toluene

We began the TRS studies with a PFO-co-PPV-MEHB solution at a concentration of 2.5 mg/mL and a pump energy density of 850 µJ/cm^2, as shown in Figure 9. The solution produced only laser-induced fluorescence (LIF) of the CP in the three dimensions when the pump energy density was 3.2 mJ/cm^2. The CP started fluorescing at 18 ns and maintained this fluorescence until 69.8 ns. The LIF had two peaks at 507 and 481 nm, and the intensity was unstable, fluctuated unsteadily, and reached a maximum value at 48.19 ns.
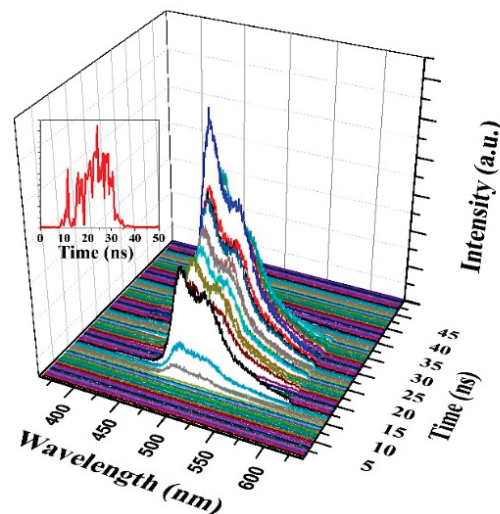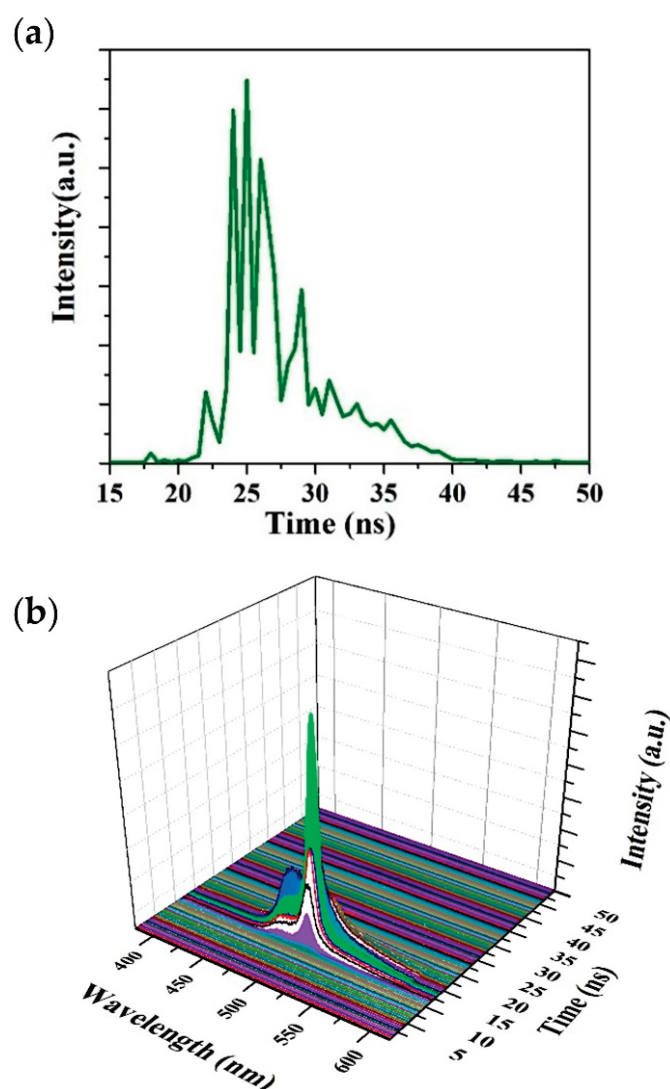

Figure 9. Three-dimensional profiles of LIF, with the inset showing the temporal profile of LIF for a pump energy density of 850 µJ/cm^2.

Figure 10a shows a few frames of the spectral profile from 20 ns after the Q-switch trigger. The peak acquired was very broad, with an FWHM of 55 nm. As the photon flux increased, the band at approximately 509 nm gained intensity due to the large stimulated emission and single-pass optical gain. The FWHM was 21 nm at 22 ns. Threshold spectral narrowing occurred in 2 ns. The full profile of the spectral narrowing spectra over time is shown in Figure 10b. We can compare Figure 6 with Figure 10; the former gives the transition from fluorescence to ASE as a function of pump energy, while the TRS study shows that the transition from fluorescence to spectral narrowing and the onset of ASE takes 2.5 ns at the same pump energy.
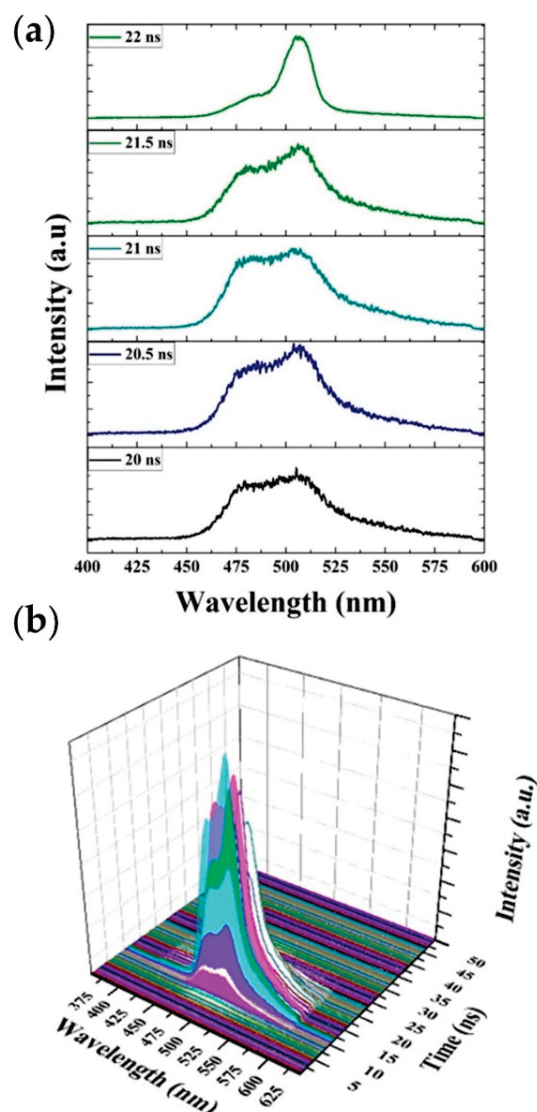
Figure 10. (**a**) Time evolution of the CP threshold spectrum at different time. (**b**) Three-dimensional profiles of the CP solution threshold spectrum for a pump energy density of 4.25 mJ/cm^2.

The ASE of the CP became intense for pump energy densities above the threshold and was recorded using a picomax spectrometer. Figure 11a shows a Z-slice of the ASE of the CP in toluene at a concentration of 2.5 mg/mL under transverse excitation for a pump energy density of 7.75 mJ/cm^2. The CP started fluorescing at 24 ns, and the intensity increased with time. The CP produced ASE at 22 ns and reached a maximum intensity at 25 ns. After 25 ns, the ASE intensity decayed up to 34.5 ns and stopped at 35 ns, as displayed in Figure 11a. The ASE peaked at 508 nm with an FWHM of 8 nm, as shown in Figure 11b.

Figure 11. (**a**) Temporal profile of CP ASE for a pump energy density of 7.75 mJ/cm². (**b**) Three-dimensional profiles of CP ASE (1.55 mJ/cm²).

Figure 11b shows the temporal dynamics of the CP in toluene at the aforementioned concentration, but the pump energy density was increased to above 7 mJ/cm². When the pump energy density was 7.75 mJ/cm², ASE was obtained at 520 nm with an FWHM of 8 nm. The entire ASE event became short due to rapid excitation, population inversion, and stimulated emission. The ASE attained the peak in a rapid phase and lasted for only 4 ns. In the pump pulse tailing phase, the photon flux was lower and produced fluorescence at the vibrational band around 480 nm, producing LIF along with weak ASE 2 ns after the maximum ASE peak intensity.

5. Conclusions

This report investigated the theoretical, optical, and mirrorless laser properties of CP PFO-co-PPV-MEHB. The calculation showed a HOMO-LUMO structure and a very high oscillator strength of 6.434 (a.u.) for the singlet-singlet transition at 374.43 nm. The experimental UV-Vis spectra obtained for the nonpolar solvent hexane were analogous to the simulated HOMO–LUMO structure. The simulation showed three oscillator strengths that matched the two peaks and shoulder manifested in experimental UV-VIS spectra, indicating that highly efficient fluorescence properties arise from singlet vibrational transitions. Under an optimal solution concentration and pump energy, CP spectral narrowing was achieved at 508 nm with an FWHM of 8.75 nm. The photochemical stability under

pulsed laser excitation was excellent, without deuteration for up to 20 k pulses. TRS studies showed a rapid intensity increase and spectral narrowing within 2 ns of fluorescence.

References

1. Chénais, S.; Forget, S. Recent advances in solid-state organic lasers. *Polym. Int.* **2012**, *61*, 390–406. [CrossRef]
2. Scherf, U.; Riechel, S.; Lemmer, U.; Mahrt, R.F. Conjugated polymers: Lasing and stimulated emission. *Curr. Opin. Solid State Mater. Sci.* **2001**, *5*, 143–154. [CrossRef]
3. Mcgehee, M.; Heeger, A. Semiconducting (Conjugated) Polymers as Materials for Solid-State Lasers. *Adv. Mater.* **2000**, *12*, 1655–1668. [CrossRef]
4. Ibnaouf, K.H. Photodynamic properties of poly [2-methoxy-5-(3′, 7′-dimethyloctyloxy)-1, 4-phenylenevinylene] under pulsed laser excitation. *Opt. Laser Technol.* **2020**, *130*, 106369. [CrossRef]
5. AlSalhi, M.S.; Almotiri, A.R.; Prasad, S.; Aljaafreh, M.J.; Othman, A.H.S.; Masilamai, V. A temperature-tunable thiophene polymer laser. *Polymers* **2018**, *10*, 470. [CrossRef] [PubMed]
6. McNeill, C.R.; Greenham, N.C. Conjugated-polymer blends for optoelectronics. *Adv. Mater.* **2009**, *38–39*, 3840–3850. [CrossRef]
7. Lin, Y.; Zhan, X. Oligomer Molecules for Efficient Organic Photovoltaics. *Acc. Chem. Res.* **2016**, *49*, 175–183. [CrossRef]
8. Aljaafreh, M.J.; Prasad, S.; AlSalhi, M.S.; Alahmed, Z.A. Ultrafast dynamics of laser from green conjugated-oligomer in solution. *Polymer* **2019**, *169*, 106–114. [CrossRef]
9. Sirringhaus, H.; Bird, M.; Zhao, N. Charge transport physics of conjugated polymer field-effect transistors. *Adv. Mater.* **2010**, *22*, 3893–3898. [CrossRef]
10. Brabec, C.J.; Dyakonov, V.; Parisi, J.; Sariciftci, N.S. *Organic Photovoltaics: Concepts and Realization*; Springer: New York, NY, USA, 2003.
11. AlSalhi, M.S.; Alam, J.; Dass, L.A.; Raja, M. Recent advances in conjugated polymers for light emitting devices. *Int. J. Mol. Sci.* **2011**, *12*, 2036–2054. [CrossRef]
12. Son, D.I.; Kim, H.H.; Cho, S.; Hwang, D.K.; Seo, J.W.; Choi, W.K. Carrier transport of inverted quantum dot LED with PEIE polymer. *Org. Electron. Phys. Mater. Appl.* **2014**, *15*, 886–892. [CrossRef]
13. Prasad, S.; Ibnaouf, K.H.; Alsalhi, M.S.; Masilamani, V. Laser from the dimer state of a conjugated polymer (PFO) in solution. *Polymer* **2014**, *55*, 727–732. [CrossRef]
14. Murphy, E. The semiconductor laser: Enabling optical communication. *Nat. Photonics* **2010**, *4*, 287. [CrossRef]
15. Prasad, S.; Ibnaouf, K.H.; Alsalhi, M.S.; Devaraj, D.; Masilamani, V. High power amplified spontaneous emission from an oligomer in solution. *J. Lumin.* **2015**, *168*, 109–113. [CrossRef]
16. Pisignano, D.; Anni, M.; Gigli, G.; Cingolani, R.; Zavelani-Rossi, M.; Lanzani, G.; Barbarella, G.; Favaretto, L. Amplified spontaneous emission and efficient tunable laser emission from a substituted thiophene-based oligomer. *Appl. Phys. Lett.* **2002**, *81*, 3534. [CrossRef]

17. Aljaafreh, M.J.; AlSalhi, M.S.; Prasad, S. Design of tunable liquid laser based on presence of the conjugated-polymer counter influencing the spectral properties of the oligomer. *Opt. Mater.* **2021**, *111*, 110575. [CrossRef]

18. Holzer, W.; Penzkofer, A.; Pertsch, T.; Danz, N.; Bräuer, A.; Kley, E.B.; Tillmann, H.; Bader, C.; Hörhold, H.H. Corrugated neat thin-film conjugated polymer distributed-feedback lasers. *Appl. Phys. B Lasers Opt.* **2002**, *74*, 333–342. [CrossRef]

19. Bauer, C.; Giessen, H.; Schnabel, B.; Kley, E.B.; Schmitt, C.; Scherf, U.; Mahrt, R.F. A surface-emitting circular grating polymer laser. *Adv. Mater.* **2001**, *13*, 1161–1164. [CrossRef]

20. Jory, M.J.; Barnes, W.L.; Samuel, I.D.W.; Turnbull, G.A.; Andrew, P. Relationship between photonic band structure and emission characteristics of a polymer distributed feedback laser. *Phys. Rev. B Condens. Matter Mater. Phys.* **2001**, *64*, 1–6. [CrossRef]

21. Moses, D. High quantum efficiency luminescence from a conducting polymer in solution: A novel polymer laser dye. *Appl. Phys. Lett.* **1992**, *60*, 3215–3216. [CrossRef]

22. Brouwer, H.; Krasnikov, V.V.; Hilberer, A.; Wildeman, J.; Hadziioannou, G. Novel high efficiency copolymer laser dye in the blue wavelength region. *Appl. Phys. Lett.* **1995**, *66*, 3404–3406. [CrossRef]

23. O'carroll, D.; Lieberwirth, I.; Redmond, G. Microcavity effects and optically pumped lasing in single conjugated polymer nanowires. *Nat. Nanotechnol.* **2007**, *2*, 180–184. [CrossRef]

24. Mujamammi, W.M.; Prasad, S.; AlSalhi, M.S.; Masilamani, V. Relaxation oscillation with picosecond spikes in a conjugated polymer laser. *Polymers* **2016**, *8*, 364. [CrossRef]

25. Hassan, M.U.; Liu, Y.C.; Butt, H.; Hasan, K.U.; Chang, J.F.; Olawoyin, A.A.; Friend, R.H. Low thresholds for a nonconventional polymer blend—Amplified spontaneous emission and lasing in F81-x:SYx system. *J. Polym. Sci. Part B Polym. Phys.* **2016**, *54*, 15–21. [CrossRef]

26. Oki, O.; Kushida, S.; Mikosch, A.; Hatanaka, K.; Takeda, Y.; Minakata, S.; Kuwabara, J.; Kanbara, T.; Dao, T.D.; Ishii, S.; et al. FRET-mediated near infrared whispering gallery modes: Studies on the relevance of intracavity energy transfer with Q-factors. *Mater. Chem. Front.* **2018**, *2*, 270–274. [CrossRef]

27. Chilukuri, B.; Mazur, U.; Hipps, K.W. Structure, Properties, and Reactivity of Porphyrins on Surfaces and Nanostructures with Periodic DFT Calculations. *Appl. Sci.* **2020**, *10*, 740. [CrossRef]

28. Han, D.; Li, J.; Zhang, Q.; He, Z.; Wu, Z.; Chu, J.; Lu, Y. Synthesis of π-Conjugated Polymers Containing Benzotriazole Units via Palladium-Catalyzed Direct CH Cross-Coupling Polycondensation for OLEDs Applications. *Polymers* **2021**, *13*, 254. [CrossRef]

29. Aljaafreh, M.J.; Prasad, S.; AlSalhi, M.S.; Alahmed, Z.A.; Al-Mogren, M.M. Optically pumped intensive light amplification from a blue oligomer. *Polymers* **2019**, *11*, 1534. [CrossRef]

30. Zou, X.; Wen, G.; Hu, R.; Dong, G.; Zhang, C.; Zhang, W.; Huang, H.; Dang, W. An Insight into the Excitation States of Small Molecular Semiconductor Y6. *Molecules* **2020**, *25*, 4118. [CrossRef] [PubMed]

31. Reyes, Y.I.A.; Ting, L.-Y.; Tu, X.; Chen, H.-Y.T.; Chou, H.-H.; Coluccini, C. Mechanistic Studies of Hydrogen Evolution Reaction on Donor-Acceptor Conjugated Polymer Photocatalysts. *Appl. Sci.* **2020**, *10*, 7017. [CrossRef]

32. Why Must I Have an emICCD? Available online: https://www.princetoninstruments.com/products/pi-max-family/pi-max/tech-notes/why-must-i-have-an-emiccd (accessed on 28 April 2021).

33. Wang, Y.; Tsiminis, G.; Yang, Y.; Ruseckas, A.; Kanibolotsky, A.L.; Perepichka, I.F.; Skabara, P.J.; Turnbull, G.A.; Samuel, I.D.W. Broadly tunable deep blue laser based on a star-shaped oligofluorene truxene. *Synth. Met.* **2010**. [CrossRef]

34. Frisch, M.J.; Trucks, G.W.; Schlegel, H.B.; Scuseria, G.E.; Robb, M.A.; Cheeseman, J.R.; Scalmani, G.; Barone, V.; Petersson, G.A.; Nakatsuji, H.; et al. Gaussian 16 C.01. 2016. Available online: https://gaussian.com/relnotes/ (accessed on 28 April 2021).

35. Chattopadhyaya, M.; Sen, S.; Alam, M.M.; Chakrabarti, S. The role of relativity and dispersion controlled inter-chain interaction on the band gap of thiophene, selenophene, and tellurophene oligomers. *J. Chem. Phys.* **2012**, *136*, 94904. [CrossRef]

36. Peach, M.J.G.; Tellgren, E.I.; Sałek, P.; Helgaker, T.; Tozer, D.J. Structural and electronic properties of polyacetylene and polyyne from hybrid and coulomb-attenuated density functionals. *J. Phys. Chem. A* **2007**, *111*, 11930–11935. [CrossRef] [PubMed]

37. Zade, S.S.; Bendikov, M. From oligomers to polymer: Convergence in the HOMO−LUMO gaps of conjugated oligomers. *Org. Lett.* **2006**, *8*, 5243–5246. [CrossRef]

38. Franco, F.C., Jr.; Padama, A.A.B. DFT and TD-DFT study on the structural and optoelectronic characteristics of chemically modified donor-acceptor conjugated oligomers for organic polymer solar cells. *Polymer* **2016**, *97*, 55–62. [CrossRef]

39. Dutta, T.; Woody, K.B.; Parkin, S.R.; Watson, M.D.; Gierschner, J. Conjugated polymers with large effective stokes shift: Benzobisdioxole-based poly (phenylene ethynylene)s. *J. Am. Chem. Soc.* **2009**, *131*, 17321–17327. [CrossRef]

40. Keppler, S.; Sävert, A.; Körner, J.; Hornung, M.; Liebetrau, H.; Hein, J.; Kaluza, M.C. The generation of amplified spontaneous emission in high-power CPA laser systems. *Laser Photon. Rev.* **2016**, *10*, 264–277. [CrossRef] [PubMed]

41. Lin, Z.; Zhang, Y.; Chen, W.; George, T.F.; Li, S. Transient Aspects and Ultrafast Dynamical Processes of Amplified Spontaneous Emission in Conjugated Polymers. *J. Phys. Chem. B* **2018**, *122*, 10762–10766. [CrossRef]

42. Jiang, Y.; Fang, M.; Chang, S.; Huang, J.; Chu, S.; Hu, S.; Liu, C.; Lai, W.; Huang, W. Towards Monodisperse Star-Shaped Ladder-Type Conjugated Systems: Design, Synthesis, Stabilized Blue Electroluminescence, and Amplified Spontaneous Emission. *Chem. Eur. J.* **2017**, *23*, 5448–5458. [CrossRef]

43. Calzado, E.M.; Boj, P.G.; Díaz-García, M.A. Amplified spontaneous emission properties of semiconducting organic materials. *Int. J. Mol. Sci.* **2010**, *11*, 2546–2565. [CrossRef]

New Polyporphyrin Arrays with Controlled Fluorescence Obtained by Diaxial Sn(IV)-Porphyrin Phenolates Chelation with Cu^{2+} Cation

Galina M. Mamardashvili, Dmitriy A. Lazovskiy, Ilya A. Khodov [ID]**, Artem E. Efimov and Nugzar Z. Mamardashvili ***

G.A. Krestov Institute of Solution Chemistry of Russian Academy of Sciences, Akademicheskaya st. 1, 153045 Ivanovo, Russia; gmm@isc-ras.ru (G.M.M.); lazolvo@mail.ru (D.A.L.); ilya.khodov@gmail.com (I.A.K.); artem.efimov.1995@list.ru (A.E.E.)

* Correspondence: nugzarstrasburg@mail.ru; Tel.: +7-90388934

Abstract: New coordination oligomers and polymers of Sn(IV)-tetra(4-sulfonatophenyl)porphyrin have been constructed by the chelation reaction of its diaxialphenolates with Cu^{2+}. The structure and properties of the synthesized polyporphyrin arrays were investigated by ^{1}H Nuclear Magnetic Resonance (^{1}H NMR), Infra Red (IR), Ultra Violet - Visible (UV-Vis) and fluorescence spectroscopy, mass spectrometry, Powder X-Rays Diffraction (PXRD), Electron Paramagnetic Resonance (EPR), thermal gravimetric, elemental analysis, and quantum chemical calculations. The results show that the diaxial coordination of bidentate organic ligands (L-tyrazine and diaminohydroquinone) leads to the quenching of the tetrapyrrole chromophore fluorescence, while the chelation of the porphyrinate diaxial complexes with Cu^{2+} is accompanied by an increase in the fluorescence in the organo-inorganic hybrid polymers formed. The obtained results are of particular interest to those involved in creating new 'chemo-responsive' (i.e., selectively interacting with other chemical species as receptors, sensors, or photocatalysts) materials, the optoelectronic properties of which can be controlled by varying the number and connection type of monomeric fragments in the polyporphyrin arrays.

Keywords: polyporphyrin arrays; chelation; fluorescence; hybrid materials

1. Introduction

Metal-coordination polymers are hybrid materials consisting of metal ions or clusters interconnected by rigid organic molecules (tectons) [1,2]. The ordering of the components in three dimensions, the possibility to use tectons of different natures and sizes, and the dynamic properties of the frameworks provide coordination polymers with unique luminescent, nonlinear optical, redox, magnetic, sorption, catalytic, ion exchange, sensory, and other properties [3–10] Due to their structure and unique physicochemical and photophysical characteristics, particularlytheir photoactivity, optoelectronic, and electrochemical properties, tetrapyrrole molecules are extremely promising objects for the construction of metal-coordination polymers for various purposes [11–19]. It is known that metal complexes of porphyrins and porphyrinoids are capable of selective reversible binding of substrate molecules and, thus, can be used to construct simple and complex supramolecular systems of various dimensions and architecture [20–27].

The aim of this work was to obtain new hybrid coordination oligomers and 1D-polymers with chelating binding of Sn(IV)-porphyrindiaxial complexes (*bis*-thyrazine-Sn(IV)-5,10,15,20-(4-sulfonatophenyl)porphyrin (I) and *bis*-diaminohydroquinone-Sn(IV)-5,10,15,20-(4-sulfonatophenyl)porphyrin (II)) with Cu^{2+} cations. Structures of the complexes I and II are depicted in Figure 1.
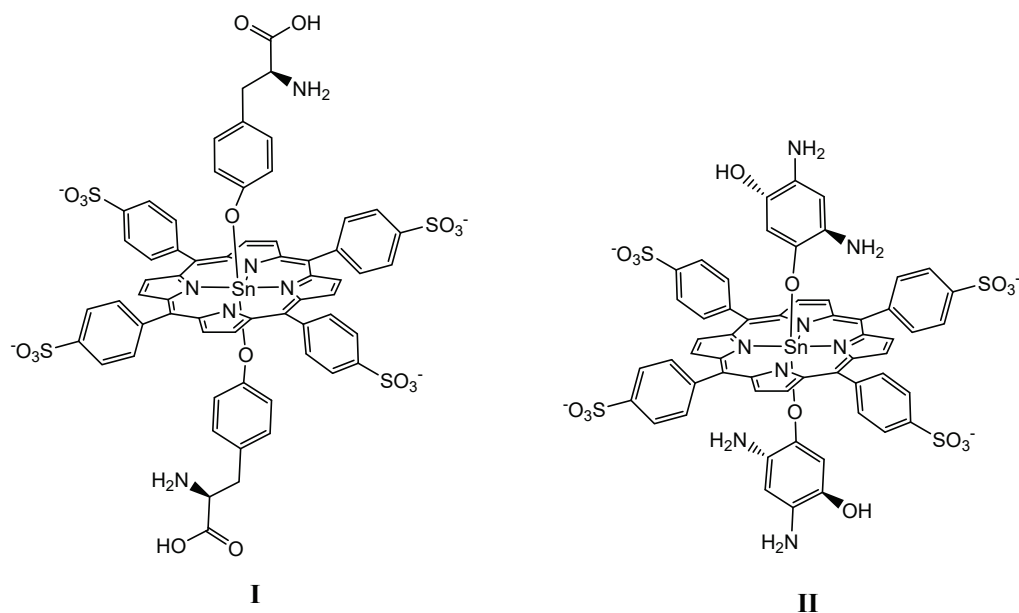
Figure 1. Structures of the complexes I and II.

Complexes I and II were used as tectons coordinating through Cu^{2+} cations. Such ligands have the ability to form stable chelate cycles with *d*-metal cations due to the simultaneous interaction of the metal cation with the ligand reaction centers of different natures(the hydroxyl group oxygen and amino group nitrogen) [28]. Chain oligomerization of the Sn(IV)-porphyrindiaxial complexes (SnP(L)$_2$) via Cu^{2+} cations is ensured by one copper cation forming two stable five-membered chelate rings, with the axial ligands belonging to the neighboring porphyrinates. The result of this oligomerization is the formation of stable nanoparticles (in comparison with less stable oligomers, which can be formed by four- or six-membered chelate rings based on copper cations), the sizes and properties of which depend on the nature of the axial ligands and the concentration ratio of the Sn(IV)-porphyrin axial complexes and *d*-metal cations. Coordination oligomers or polymers of this type are of particular interest to those involved in creating new 'chemo-responsive' (i.e., selectively interacting with other chemical species as receptors, sensors, or photocatalysts) or 'size-responsive' (i.e., capable of separating, storing, and transporting aggressive, toxic or explosive chemical species of different nature) materials, with their functional properties controlled by the number of monomeric fragments in the polyporphyrin arrays.

2. Materials and Methods

2.1. Materials

The high purity reagents were purchased commercially from PorphyChem (5,10,15,20-tetra(4-sulfonatophenyl)porphyrin tetraammonium), and Sigma Aldrich (St. Petersburg, Russia) (2,5-diaminohy droquinone dihydrochloride, L-tyrosine).

2.2. Equipment

All the ^{1}H NMR (500.17) experiments were performed on a Bruker Avance III 500 NMR spectrometer (Bruker Biospin, Karlsruhe, Baden-Württemberg, Germany) with 256 or 512 scans and spectral windows of 20 ppm. The inaccuracy of the ^{1}H NMR chemical shift measurement relative to the solvents (D$_2$O and DMSO) was found to be ±0.01 ppm. The UV-Vis spectra were recorded in the range of 190–1200 nm on a JASCO V-770 spectrophotometer (Tokyo, Japan). The fluorescence spectra were recorded in the range of 430–770 nm on a Shimadzu RF 5301PC Spectrofluorimeter (Kyoto, Japan). The quantum-chemical calculations were performed using v.4.2.1 of the ORCA program system [29]. The Density-functional Theory (DFT) method with the CAM-B3LYP hybrid functional and 3–21 basis set was used to optimize the compound ground state. The pH was monitored

by an Electroanalytical Analyzer (Type OP-300, Radelkis) ion meter. Elemental analyses were performed on a Flash EA 1112 analyzer. The mass spectra were obtained on a Shimadzu Biotech Axima Confidence Maldi TOF mass spectrometer of Kratos Analytical Limited-Great Britain, Manchester (with methanol as the solvent). The infrared analysis of the solid porphyrins was done on a VERTEX 80 V infrared Fourier-spectrophotometer (Ettlingen, Germany) with KBr pellets in the range of 4000–400 cm^{-1}. The thermogravimetric analysis (TG) and differential thermal analysis (DTA) were recorded on a TG 209 F1 Iris thermomicrobalance (Netzsch, Germany) with dry samples at the heating rate of 10 C min^{-1} in an argon atmosphere in the range from room temperature to 900 °C. The Electron Paramagnetic Resonance (EPR) spectra of solutions in water were recorded on an EPR 10-MINI spectrometer (St. Petersburg) with an operating frequency of 9.45 GHz. The magnetic field was calibrated using a standard DPPH (diphenylpicrylhydrazyl) sample.

2.3. Synthesis

Bis-thyrazine-Sn(IV)-5,10,15,20-tetra(4-sulfonatophenyl)porphyrin (I) was obtained according to the procedure described by us previously in [30] from the bis-hydroxy-Sn(IV)-5,10,15,20-tetra(4-sulfonatophenyl)porphyrin (III). Mass-spectrum (MALDI-TOF): (m/z):[M+H]$^+$ 1407.17; molecular formula $C_{62}H_{46}N_6O_{18}S_4Sn$-requires [M]$^+$1406.01;UV-Vis (H$_2$O), λ_{nm} (lgε): 594 (4.06), 555 (3.57), 421 (5.04), ^{1}HNMR (500 MHz, D$_2$O), ppm: 9.41 (s, 8H, Hβ-pyr.), 8.72 (s, 4H, NH$_2$-L), 8.36 (d, J = 7.8, 8H, ortho-C6H4), 8.14 (d, J = 7.8, 8H, meta-C6H4), 5.51 (d, 4H, ortho-Ar-L), 4.37 (t, 2H, CH-L),3.19(m, 4H, CH$_2$-L), 2.28 (d, 4H, meta-Ar-L);IR-spectrum, (KBr), ν, cm^{-1}:3420 (sb)ν (OH), 3143 (b) ν (NH^{3+}str.), 2939(w),ν(C-H, Ar), 2814(w),ν(C-H, Ar), 1680 (b)ν(C=C, Ar), 1655 (b) ν (NH^{3+}deg. def.), 1607 (s)ν (COO- assym.), 1561(b)ν(C=C, Ph), 1517 (m)νNH^{3+}sym. def.),1384 (s) ν (COO-sym.), 1367 bν(C=N), 1337 (w)ν (C-N, Por), 1246–45 (m) (NH^{3+}rocking,),ν(C-N), 1200(w), (C-N, Pr), 1197 (m), 1128 (m), 1116(m)δ(C-H), 1045(m)ν(S-C), 1015(m) δ(C-H), 998 (m) ν(C-C),842–41, 744 (w)γ(C-H, Pyr), 706(w)γ(C-H, Ph), 706(w)γ(C-H, Ph), 646 (m) (COO-wagging), 580m(COO- rocking), 562 (m) ν(Sn-O).

Bis-diaminohydroquinone-Sn(IV)−5,10,15,20-tetra(4-sulfonatophenyl)porphyrin (II) was synthesized similarly to (I): 7.38 mg of III (0.0068 mmol) and 3.62 mg of 2,5-diaminohydroquinone dihydrochloride (0.017 mmol) were dissolved in 20 mL of distilled water. The resulting solution was boiled for 5 h, cooled, and then evaporated to dryness in a vacuum. The product was purified by column chromatography on neutral alumina using an ethanol-water mixture (1:2) as the eluent. The product yield after recrystallization was equal to 93%.Mass-spectrum (MALDI-TOF): (m/z):[M+H]$^+$ 1325.39; molecular formula $C_{56}H_{38}N_8O_{16}S_4Sn$-requires [M]$^+$ 1324.01; UV-Vis (H$_2$O), λ_{max} (logε) nm:419 (5.11),554 (4.10), 593 (3.61);^{1}H NMR, (500 MHz, D$_2$O): 9.10 (s, 8H,β-pyrr.), 8.45 (d, J = 7.8 Hz, 4H, ortho-C$_6$H$_5$), 8.25 (d, J = 7.7 Hz, 8H, meta-C6H5), 8.59 (s, br, 2H, NH$_2$ (L)), 5.32 (s, br, 2H, NH$_2$ (L)), 5.97(t, J = 8.0 Hz, 2H, Ar(L)), 4,90 (s, 2H, OH(L)), 2.92 (t, J = 2.0 Hz, 2H (L)).IR-spectrum, (KBr), ν, cm^{-1}:3357 (sb)ν (N-H), 3244 (sb)ν (O-H) ν, 3052,2930-ν (C-H, Ar) 1695(b)ν(C=C, Ar), 1619(N-H)δ, 1582(b)ν(C=C, Ph), 1601, 1501, 1478 (C-C, Ar) ν, 1381 bν(C=N, Por), 1359 (w)ν (C-N, Por), 1152 (C-O)ν, 1045(m)ν(S-C), 1015(m) δ(C-H), 998 (m) ν(C-C), 821, 7 50 (C-H) γ, 784 (N-H) γ$_w$, 699 (C-C)γ, 566 (m) ν(Sn-O).

Bis-hydroxy-Sn(IV)-5,10,15,20-tetra(4-sulfonatophenyl)porphyrin (III) was synthesized according to the method described by the authors of [31]. Mass-spectrum (MALDI-TOF): (m/z):[M+H]$^+$ 1081.23; molecular formula $C_{44}H_{26}N_4O_{14}S_4Sn$-requires [M]$^+$ 1080.02;UV-Vis (H$_2$O), λ_{max}(logε) nm: 593 (4.10), 554 (3.60), 419 (5.40), ^{1}H NMR, (500 MHz, D$_2$O): 9.10 (s, 8H,β-pyrr.), 8.45 (d, J = 7.8 Hz, 4H, ortho-C$_6$H$_5$), 8.25 (d, J = 7.7 Hz, 8H, meta-C$_6$H$_5$). −7.02 (2H, OH).

The synthesis of dimeric (I-Cu-I, II-Cu-II), oligomeric (Cu-[I-Cu]$_6$ and Cu-[II-Cu]$_6$) and polymers ([I-Cu]$_n$ and [II-Cu]$_n$) porphyrins was carried out by heating an aqueous solution of the corresponding axial complex I or II and copper chloride. The concentration of the complexes was at least 5×10^{-4} mol/L.

Synthesis of I-Cu-I, Cu-[I-Cu]₆ and [I-Cu]ₙ: 13.5 mg (0.0096 mmol) of complex I was dissolved in 10 mL of distilled water. Then, 1.63 mg (0.0096 mmol) or 8.2 mg (0.0480 mmol) of copper chloride dihydrate was added to the resulting solution to obtain a molar ratio of I-Cu^{2+} equal to 1:1 or 1:5, respectively. To suppress hydrolysis, the reaction mixture was acidified with several drops of diluted hydrochloric acid. The resulting reaction mixtures were heated for 24 h at a temperature of 85–90 °C. After the reaction was completed, the soluble and insoluble reaction products were separated by filtration at atmospheric pressure. The insoluble reaction product ([I-Cu]ₙ) was repeatedly washed with distilled water on a filter.

Synthesis of II-Cu-II, Cu-[II-Cu]₆,and [II-Cu]ₙ: 12.5 mg (0.0094 mmol) of complex II was dissolved in 10 mL of distilled water. Then, 1.6 mg (0.0094 mmol) or 8.0 mg (0.0471 mmol) of copper chloride dihydrate was added to the resulting solution to obtain a molar ratio of II-Cu^{2+} equal to 1:1 or 1:5, respectively. The rest of the procedure was similar to the synthesis of polymers and oligomers of I with Cu^{2+}.

3. Results and Discussion

3.1. Synthesis and Structure

It is well known that when amino acids, such as some other polydentate ligands, interact with *d*-metal cations, they form stable compounds with one or two chelate rings [28]. The higher stability of such compounds is the result of each polydentate ligand binding to the complexing cation by at least two bonds (-M-O, M $\leftarrow$ NH$_2$ or M $\leftarrow$ NH). The products of the amino acid interaction with *d*-metal cations can be mono- and bis-ligand particles. In the latter case, bicyclic chelating of the copper cations occurs with formation of 4-coordinate square planar geometry of the coordination center [32,33].

Depending on the self-assembly conditions, the products of the interaction of *bis*-axial complexes I and II with the Cu^{2+} cations can be both porphyrin dimers ([I-Cu-I] and [II-Cu-II]) and oligomers ([Iₙ-Cuₙ±₁] and [IIₙ-Cuₙ±₁]) consisting of several porphyrin fragments and copper cations (Figure 2).

$$\text{NSnP(L)}_2 + (n \pm 1)\text{Cu}^{2+} \xrightarrow{t} [\text{SnP(L)}_2]_n - [\text{Cu}]_{n\pm1} \tag{1}$$
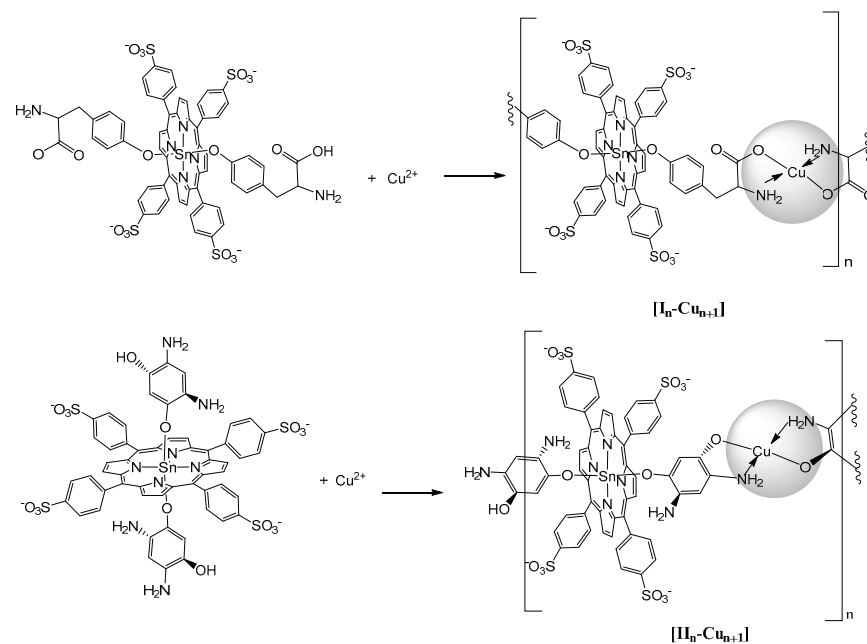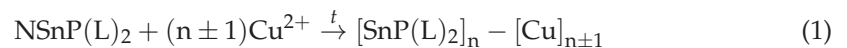
Figure 2. Proposed structures of products of the of the Sn(IV)-porphyrin axial complexes I and II interaction with Cu^{2+} cations.

The structures of *bis*-axial complexes I and II and products of their self-assembly (porphyrin dimers (I-Cu-I and II-Cu-II)), obtained by simultaneous interaction of Cu^{2+} with the hydroxy and amino groups of axial ligands belonging to two different porphyrinate molecules, were optimized by the DFT method with the CAM-B3LYP hybrid functional and 3–21 basis set. The data obtained are shown in Figure 3 and Table 1.

Table 1. Geometric parameters of the studied compounds obtained by quantum-chemical calculations using the Density-functional Theory DFT/CAM-B3LYP hybrid functional and 3–21 g basis.

| Compounds	I	I-Cu-I	II	II-Cu-II
The maximum distance from the upper point of the ligand to the porphyrin core, Å	7.061	10.39314	6.560	7.3955
r(Sn-O), Å	2.0517	2.0517	2.0517	1.9902
r(Sn-N), Å	4.238	4.1662	4.2244	4.1778
r(Cu-O), Å	-	1.81772	-	1.8220
r(Cu-N), Å	-	1.92909	-	1.9377
<L-O-O-L(Ligand rotation angle)	98°	13° and 97°	159°	25° and 149°
<Sn-O-L (The bridge angle)	122°	145°	131°	172°
The angle between porphyrin end aromatic ligand planes	41°	41° 70°	50 °	50° 87°
The angle between the porphyrin planesin the dimer	-	9°	-	9°

As seen from Figure 3 and Table 1, complexes I and II had similar Sn-O and Sn-N bond lengths. A distinctive feature of I wasthe presence of additional points of binding between the axial ligands and the porphyrin macrocycle due to the formation of intramolecular hydrogen bonds, which could potentially prevent the formation of oligomeric and polymer structures. The inclination angle of the axial ligand aromatic part of the axial ligand to the porphyrin plane in complex I was 41°, whereas in complex II, it was 50°.

The formation of dimeric structures increased the inclination angle of the ligand phenolate fragment relative to the porphyrin plane, probably due to the repulsion of the aromatic fragments from each other. The functional groups involved in the chelation with Cu^{2+} werelocated in the dimeric structures at the maximum possible distance from the porphyrin plane. Obviously, in the case of a two-center interaction of the axial fragments with Cu^{2+}, such a structure is the most favorable energetically. In the case of I-Cu-I, the formation of a chelate bond between the tyrosine and the copper cation destroys the hydrogen bonds between the tyrosine and sulfophenyl moieties.

A significant increase in the Sn-O-L angle can be observed in the II-Cu-II structure optimized by quantum chemical calculations. This increase is associated with the fact that the amino group of the diaminohydroquinone fragment approached the pyrrole nitrogen atom of the porphyrin macrocycle. Since there can be a significant electrostatic interaction between the porphyrinate nitrogen atom and the amino group protons, such a structure distortion can be energetically favorable.

Since the axial ligands in complexes I and II were of different sizes, the distance between the porphyrin fragments in the I-Cu-I and II-Cu-II dimers differed significantly and amounted to 21.3 and 17.6 Å, respectively. At the same time, the porphyrin fragments in the dimeric systems were almost parallel to each other (Figure 3). The structures of the porphyrin oligomers linked through Cu^{2+} werenot optimized. However, based on the data about the dimeric structures, it can be assumed that the longer porphyrin oligomers were almost linear, and the porphyrin polymers consisted of fragments similar to those shown in Figure 3.
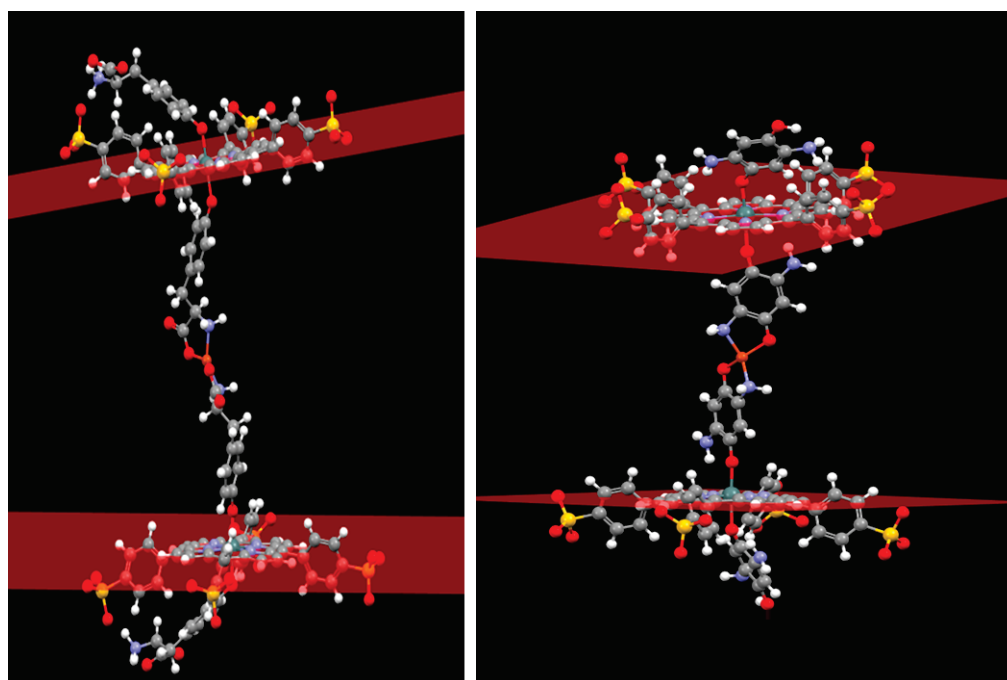
I-Cu-I II-Cu-II

Figure 3. Structures of the dimers I-Cu-I and II-Cu-II optimized by the DFT/CAM-B3LYP hybrid functional and 3–21 g basis.

According to the experimental data, the result of these self-assembly of Sn(IV)-porphyrinates (I-II) in the presence of Cu^{2+} in aqueous solutions depends on the concentration ratio of the starting reagents, reaction time, and temperature. Table 2 shows the empirical formula, molecular weight, and elemental analysis data of the reaction (1) products at different concentrations of the starting compounds. Oligomerization was achieved by heating compounds I and II for several hours at 90 °C. The self-assembly of the porphyrinate fragments was monitored by changes in the UV-Vis spectra.

The self-assembly of the porphyrinate macrocycles into larger aggregates led to a decrease in their solubility. The larger the oligomer, the lower its solubility. Upon reaching a certain size, the resulting oligomers precipitated. The proportions of soluble and insoluble self-assembly products in the studied systems are also presented in Table 2.

An analysis of the molecular weights of the substances presented in Table 2 shows that the soluble products of the interaction of I or II with Cu^{2+} at an equivalent quantitative ratio of the reagents were mainly porphyrin dimers (I-Cu-I and II-Cu-II). Under the conditions of a five-fold excess of copper cations and prolonged heating of the reaction mixture (up to 24 h), oligomers with a large number of macrocycles were formed. The maximum number of porphyrin fragments in soluble oligomers didnot exceed six. Chain oligomers with more than six Sn(IV)-porphyrin units (polymers) precipitated during reaction (1). The formation of porphyrin oligomers and polymers through strong bis-chelate binding with the formation of a flat coordination center (Figure 2) was confirmed by UV-vis, IR, ^{1}H NMR, EPR spectroscopy, and thermogravimetric analysis. The composition of oligomeric chains was estimated from the data of elemental analysis, mass spectrometry, and 2D NMR.

Table 2. Empirical formula, molecular weight, and elemental analysis data of the reaction (1) products with the ratio of reagents (1:1 and 1:5).

Compounds	Yield,%	Formula	Found/Calcd			
			Cu	C	H	N
I	-	$C_{62}H_{44}N_6O_{18}S_4Sn$ 1407.01	-	52.89	3.15	5.97
II	-	$C_{56}H_{38}N_8O_{16}S_4Sn$ 1325.91	-	50.73	2.89	8.45
I: Cu (1:1)	94%	$C_{62}H_{44}N_6O_{18}S_4SnCu_{0.5}$ I-Cu-I 2877.57	2.19/ 2.21	51.67/ 51.72	3.06/ 3.08	5.81/ 5.84
II: Cu (1:1)	96%	$C_{56}H_{38}N_8O_{16}S_4SnCu_{0.5}$ II-Cu-II 2715.38	2.32/ 2.34	49.40/ 49.54	2.80/ 2.82	8.22/ 8.25
I: Cu (1:5) [a]	78%	$C_{62}H_{44}N_6O_{18}S_4SnCu_{1.17}$ Cu-[I-Cu]$_6$ 8892.89	4.98/ 5.00	50.48/ 50.24	2.96/ 2.99	5.64/ 5.67
II: Cu (1:5) [a]	84%	$C_{56}H_{38}N_8O_{16}S_4SnCu_{1.17}$ Cu-[II-Cu]$_6$ 8400.31	5.27/ 5.30	47.98/ 48.04	2.72/ 2.74	7.97/ 8.00
I: Cu (1:5) [b]	22%	$C_{62}H_{44}N_6O_{18}S_4SnCu$ [I-Cu]$_n$ n× [1471.56]	4.27/ 4.32	50.62/ 50.60	3.00/ 3.014	5.68/ 5.71
II: Cu (1:5) [b]	16%	$C_{56}H_{38}N_8O_{16}S_4SnCu$ [II-Cu]$_n$ n× [1389.46]	4.54/ 4.57	48.37/ 48.41	2.74/ 2.76	8.05/ 8.07

Soluble ([a]) and insoluble ([b]) products of the reaction (1).

The mass spectrometry confirmed the formation of dimeric forms of complexes I and II in the products of reaction (1). In addition to the peaks with m/z 1406.01 and 1470.51, corresponding to the [I-H]$^−$ and ([I-Cu]-H)$^−$ ions, the mass spectrum of the product of the complex I interaction with Cu^{2+} (Figure 4) at a 1:1 molar ratio of the reagents hada peak with m/z 2877.03 corresponding to the [I-Cu-I] dimer. It was not possible to confirm the formation of larger (containing six macrocyclic fragments)porphyrin oligomers by the mass spectrometry method, which was probably due to the oligomer instability in the conditions of the mass spectral studies of the samples. Similar behavior wasobserved in the mass spectra of the products of the complex II interaction with Cu^{2+} at 1:1 and 1:5 molar ratios of the reagents.
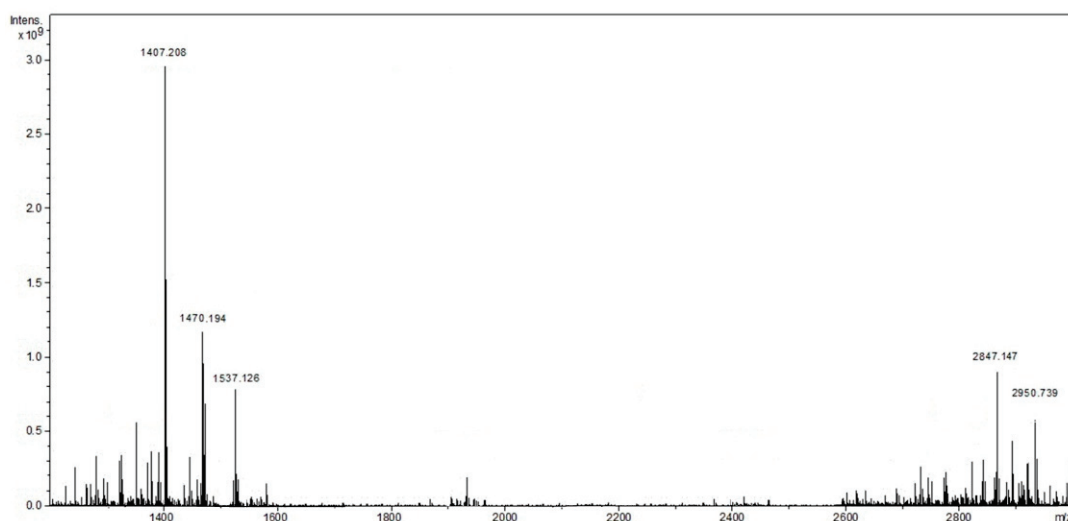
Figure 4. Mass spectrum of the I-Cu-I.

3.2. Thermogravimetric Analysis and Powder XRD

All the products of reaction (1) were thermally stable solids, indicating a strong metal–ligand bonding. Figure 5 shows DTA and TG curves with endo- and exothermic peaks of complex I and the oligomer based on it. The thermal behavior of the free molecules of aminoacids, including tyrazine, has been well studied. According to the results found by the authors of [34,35], the first endothermic stage of tyrazine decomposition occurs in the temperature range of 276–322 °C and corresponds to the reactions of its decarboxylation and deamination. Further, in the temperature range of 322–350 °C, the resulting intermediate product is relatively stable. The second stage of tyrazine decomposition occurs at 350–355 °C and involves oxidation of the phenolic fragment. At the same time, the porphyrin macrocycles in the general case [36], particularly the Sn(IV)-porphyrins [37], are highly resistant to thermal oxidative destruction.

As Figure 4 shows, the decomposition of complex I consisted of four stages. At the first stage, in the temperature range up to 100 °C, the complex thermal dehydration occurred. The loss of 9.45% of the sample mass corresponded to water evaporation as the sample itself was not subjected to preliminary drying. At the second stage, in the temperature range of 217–441 °C, the loss of 15.8% of the sample mass indicates partial axial ligand decomposition. The third stage, in the temperature range of 518–727 °C, the loss of 29.2% of the sample mass corresponded to the detaching of four sulfo groups from the porphyrin aryl fragments. The fourth stage consisted of the removal of the phenyl fragments, both of the porphyrin and axial ligands (15.5% of the sample mass). The residue mass (30% of the sample mass) indicates that the tetrapyrrole macrocycle containing the Sn(IV) cation in the coordination center was not destroyed. Similar data on the thermal decomposition of Sn(IV)-porphyrins have been described by the authors of [37]. The first stage of decomposition of the tyrazine fragments in porphyrin complex I begins at lower temperatures than that of the free aminoacid ligand, whereas the second stage (phenyl fragment oxidation), on the contrary, occurs at a higher temperature.
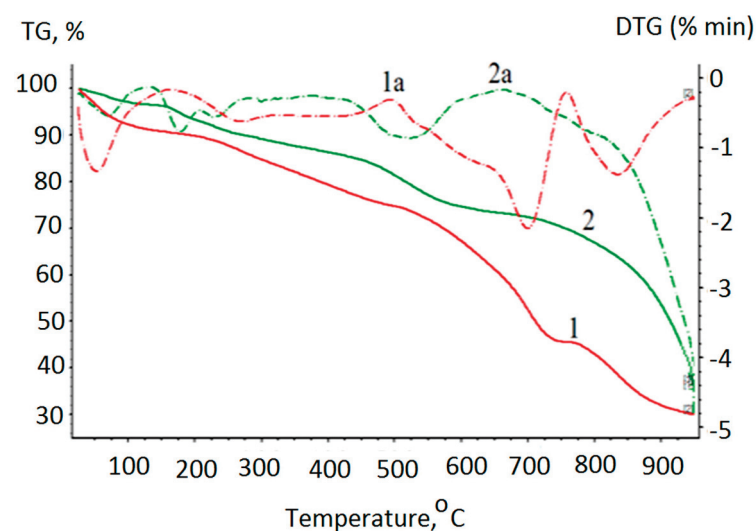
Figure 5. Differential thermal analysis (dashed line, DTA) and thermogravimetric analysis (solid line, TG) curves with endo- and exothermic peaks for thermal decomposition of I (red line) and Cu-[I-Cu]$_6$ (green line).

A thermal analysis of the hexamers shows that decomposition of this compound consists of more stages. The first stage (up to 100 °C), as in the case of monomeric complex I, was associated with thermal dehydration. The second stage, in the temperature range of 100–136 °C, consisted of the dehydration of the water molecules located in the coordination bis-chelate center of Cu^{2+}. The third stage of destruction, in the temperature range of 213–351 °C, corresponded to the destruction stage of the tyrazine fragments of the chelate

cycles. At the next stage, in the temperature range of 434–605 °C, the porphyrin macrocycle sulfo groups were eliminated. The last stage, in the temperature range of 736−925 °C, was probably associated with the processes of removal of the phenyl fragments of the porphyrin macrocycle and axial ligands. The residue mass (33% of the initial sample mass) indicates that the residue contains Sn(IV)-porphyrin and CuO. Similar results were obtained for the [I-Cu]$_n$ polymer. The data for the II and its hexamers are depicted in Table 3.

Table 3. Thermogravimetric analysis data of the II and its hexamer.

Compound	Temperature Range (°C)	DTG Peak (°C)	TG Weight Loss (%)		Assignment
			Calcul.	Experim.	
II	20–200	110	2.64	2.78	uncoordinated water (2 mole)
	200–500	320.9	7.20	8.32	dehydroxylation and deamination
		425.2	23.51	23.07	destruction of sulfo groups
	500–800	690.1	22.35	20.80	oxidation of the Ph-fragment of porphyrins
		820.9	10.88	12.02	oxidation of the Ph- fragment of ligands
	>900		33.41	33.01	(SnC20H12N4O2 rest)
[II-Cu]$_n$	20–200	100	2.46	2.32	uncoordinated water (2 mole)
		180	2.46	2.56	coordinated water (2 mole)
	200–500	352.9	6.71	7.23	dehydroxylation and deamination
		425.2	21.91	18.47	destruction of sulfo groups
	500–800	694.5	20.83	22.30	oxidation of the Ph-fragment of porphyrins
		870.2	10.14	8.69	oxidation of the Ph- fragment of ligands
	>900		36.57	38.43	SnC$_{20}$H$_{12}$N$_4$O$_2$, CuO rest

Powder X-ray diffraction (PXRD) was performed to verify the purity of [I-Cu]$_n$ and [II-Cu]$_n$. The PXRD curve of [II-Cu]$_n$, shown in Figure 6 as an example, indicates a diffuse large steam bun peak. The PXRD curve of [I-Cu]$_n$ looks similar. The absence of other obvious sharp peaks in the corresponding curves indicates that the polymers wereamorphous, with random growth during the self-assembly [38].

(a)

(b)
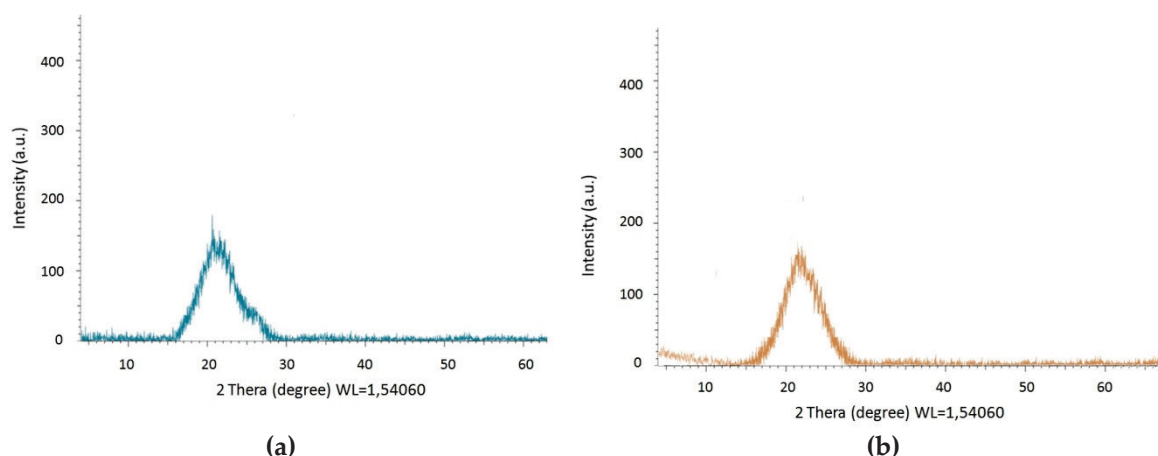
Figure 6. Powder X-ray diffraction XRD (PXRD) of the [I-Cu]$_n$ (**a**) and [II-Cu]$_n$ (**b**).

3.3. UV-Vis and IR-Spectral Studies

The UV-Vis spectra of the water-soluble products of reaction (1) were recorded in the UV-visible region (Figure 7 and Table 4). The spectra for the investigated copper(II) complexes displayed bands at 610 nm and 661nm, assigned to $^2B_{1g} \rightarrow {}^2E_g$ and $^2E_g \rightarrow 2A_{1g}$ *d-d* transitions. According to the authors of [39–41], this indicates that the investigated complexes weremononuclear complexes with four-coordinate square planar geometry.
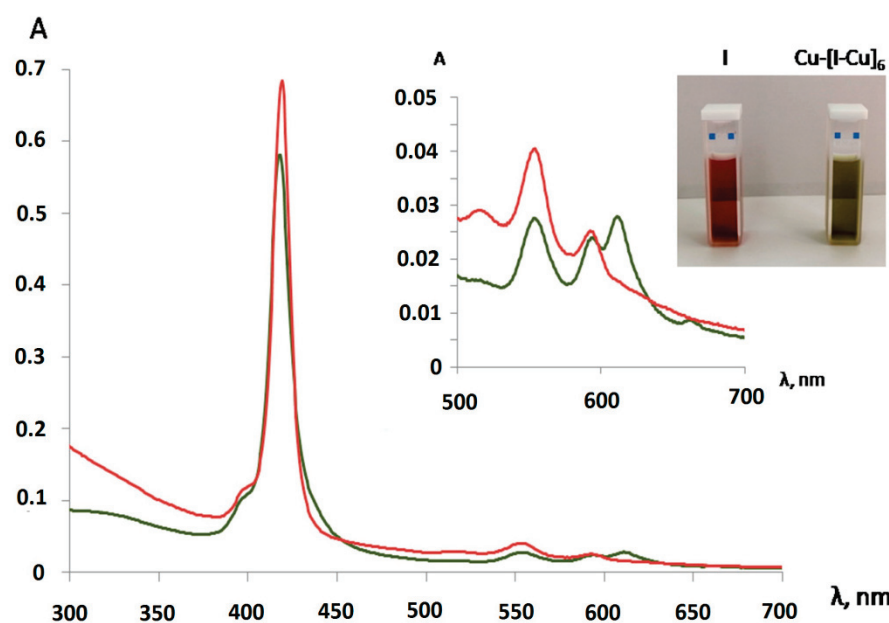
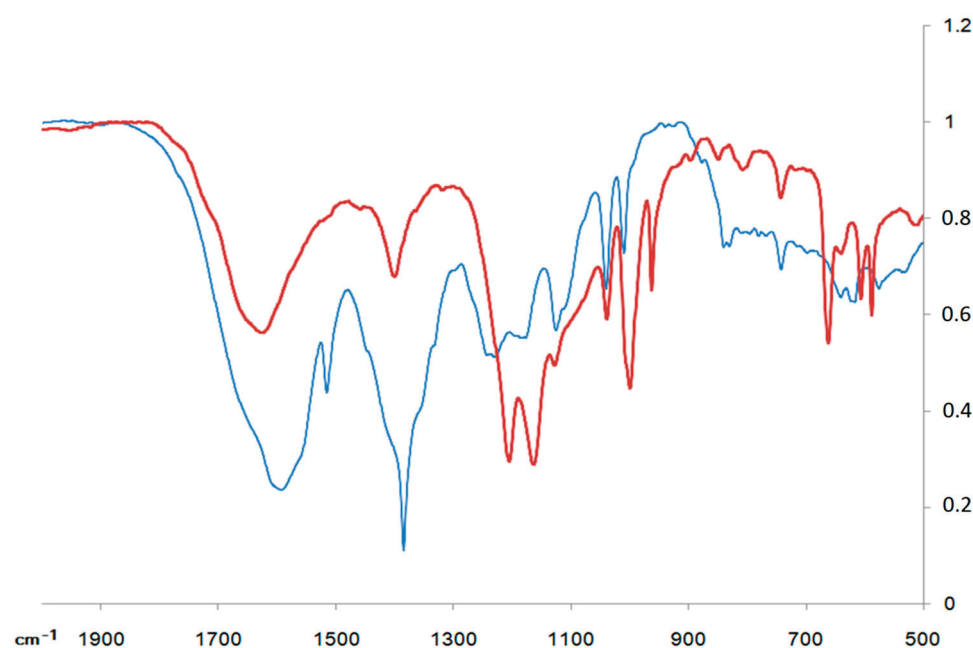**Figure 7.** UV-Vis spectra of complex I (red line) and hexamers Cu-[I-Cu]$_6$ (green line) in water.

Table 4. UV-Vis spectra of the studied compounds (I, II, Cu-[I-Cu]$_6$, and Cu-[II-Cu]$_6$).

Compounds	UV-Vis Spectra, λ_{nm}(lgε)
I	419 (5.04), 555 (4.06), 594 (3.57)
I-Cu-I	418 (5.00), 554 (3.87), 595 (3.45), 610 (3.33)
Cu-[I-Cu]$_6$	418 (4.98), 554 (3.78), 595 (3.40), 610 (3.89)
II	419 (5.11), 554 (4.10), 593 (3.61)
II-Cu-II	418 (5.05), 553 (4.07), 592 (3.48), 609 (3.29)
Cu-[II-Cu]$_6$	418 (5.03), 553 (4.07), 592 (3.35), 609 (3.54)

The Fourier Transform Infrared (FTIR) spectra of the metal complexes were recorded in KBr discs over the range of 4000–400 cm^{-1}. The data of the IR studies (Table 5 and Figure 8) of the corresponding samples provide valuable information on how axial complexes I and II bind to Cu^{2+} during the formation of chelate complexes. Based on the analysis of the spectra of the reaction (1) products, it can be concluded that the amino and carboxyl groups were simultaneously involved in the chelate complex formation. The IR spectra of the oligomers now have new bands caused by the bending vibrations of the bonds formed due to the coordination with Cu^{2+}. The frequency ranges expected for these vibrations are well known [42]. In addition to the vibrations of the amino and carboxyl groups, the processes of chelation were also confirmed by the vibrations of the N-M and O-M bonds.

Table 5. Relevant IR bands for the compounds I and Cu-[I-Cu]$_6$.

| I	Cu-[I-Cu]$_6$	I	Cu-[I-Cu]$_6$	II	Cu-[II-Cu]$_6$	II	Cu-[II-Cu]$_6$
NH^{3+}	NH$_2$	COO-	COO-	N-H	N-H	O-H	O-H
3188ν	3201ν					3244ν	-
3299ν	3230ν	1607ν_{as}	1660ν_{as}			1378δ_d	-
1655δ_d	1668δ_d	1384ν_s	1405ν_s	3357ν	3430ν	C-O	C-O
1517δ_s	1534 δ	646δ_{as}	606δ	1619δ	1638δ		
1246γ_r	1200γ	580δ_s	588δ	764γ_w	747γ	1152ν	1114ν
1181γ_r	1166γ						
Cu-N	Cu-N	Cu-O	Cu-O	Cu-N	Cu-N	Cu-O	Cu-O
-	633ν	-	472ν	-	620ν	-	480ν

Figure 8. IR spectra of complex I (blue line) and Cu-[I-Cu]$_6$ (red line) in KBr discs.

The IR spectra of the aminoacid fragments with a bipolar structure contained characteristic bands of the NH^{3+}-group corresponding to symmetric stretching (in the region of 3200–3400 cm^{-1}) and bending (in the region of 1550–1600 cm^{-1}) vibrations. In the chelate complexes, the stretching vibrations of the bound NH$_2$ group were shifted to longer wavelengths. Such a decrease in the frequency and increase in the intensity of the amino-group stretching vibrations can be interpreted by coordination interactions between the metal cation and the nitrogen atom of the amino-group, which increased the dipole moment value. Also characteristic of chelation is the band at 1160 cm^{-1}, which was related to the deformation vibrations of the NH$_2$ group but was not observed in the bipolar compound.

A vibration band typical of the free carboxylate anion appeared at 1607 cm^{-1} and 1384 cm^{-1}. The carboxyl group transition to the non ionized state caused this band to disappear, and the vibration appeared in the longer wavelength region as ν(C=O) in the carboxyl group. For the investigated complexes, the COO−asymmetric stretching frequencies were shifted to lower values compared with those of the ligand. The bands in the region of 480 cm^{-1} indicate the formation of a Cu–O bond and further confirm the ligand coordination to the central metal ion via the oxygen atom of the carboxylate group [42]. Hypsochromic shifts were observed for the –NH$_2$ frequencies during coordination. This indicates bond elongation during the coordination, therefore suggesting probable square planar geometry of the complexes. The new bands in the spectra of the complexes at 535–552 cm^{-1} were assigned to the (M–N) stretching frequency. The participation of the lone pairs of electrons on the N atom of the amino group in the ligand in the coordination was confirmed by these band frequencies [43].

3.4. EPR Studies

The conclusions about the planar-square structure of the obtained Cu(II) complexes based on the results of the IR spectra were additionally confirmed by EPR spectroscopy data [44–47]. In the EPR spectra of the studied compounds (Figure 9) at room temperature, the hyperfine lines from the magnetic interaction of the unpaired electron spin with the copper atom nuclear spin were well resolved. The isotropic EPR spectra are described by a symmetric spin Hamiltonian and had four hyperfine lines of equidistant components of different intensities and widths for nuclear spin projections, which is explained by the McConnell relaxation mechanism [47]. The spectra were a superposition of the spectra from the ^{63}Cu nuclei, with the trans-N$_2$O$_2$ coordination environment of the Cu(II) ion.
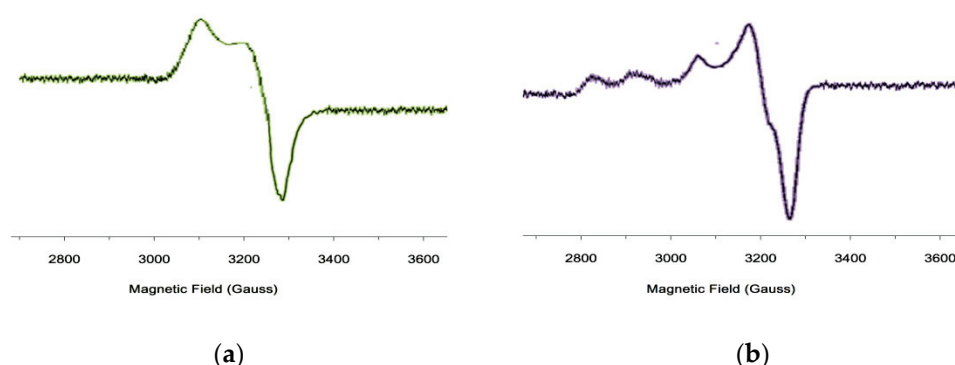
Figure 9. Powder Electron Paramagnetic Resonance (EPR) spectrum of Cu-[I-Cu]$_6$ (**a**) and [I-Cu]$_n$ (**b**).

The presence of two five-membered metallocycles in complex compounds, regardless of the nature of the coordinated atoms, led to a planar conformation. The coordination center in oligomers based on II increased the electron-donating properties of the nitrogen and oxygen atoms. These conclusions were confirmed by the calculated parameters of the EPR spectra. The EPR parameters for the Cu- [I-Cu]$_6$ hexamer with tyrazine fragments (L1), had the following values: g = 2.119, a$_{cu}$ = 89.6 E, α^2 = 0.81, whereas for the oligomer with aminoresorcinol ligands, these values were within the following range: g = 2.108, a$_{Cu}$ = 95.84 E, α^2 = 0.89. The αparameter calculated from the isotropic EPR parameters using Formula (2) [48]:

$$\alpha^2 = \frac{1}{0.43}\left(\frac{\alpha_{Cu}}{0.036} + g - 2\right) + 0.02 \qquad (2)$$

characterizes the degree of covalence of the copper-ligand bond. If the oligomer based on II had α^2 = 0.89, then the oligomer based on I was somewhat lower (0.81).

3.5. NMR Spectroscopy Studies

The NMR spectroscopy is a very important tool for the investigation of the structure of an unknown compound in solutions. Data of two-dimensional ^{1}H NMR make it possible not only to obtain information confirming the presence of chelate binding in the products of reaction (1), but also to determine the number of porphyrinate fragments in the resulting porphyrin oligomers. The formation of chelating bonds of porphyrinate axial ligands with Cu^{2+} is evidenced by characteristic shifts in the signals of the ligand protons located in close proximity to the inner coordination sphere of the copper cations. The NMR study results are presented in Table 6.The absence of signals of protons of the -COOH and -OH groups indicates the formation of the corresponding Cu(II)-complexes (due to the replacement of H$^+$ with the metal ion). The signal of the protons at the carbon atom, which was closer to the NH$_2$ group, was significantly shifted (by 0.5 ppm) in a strong field.

Diffusion-ordered spectroscopy (DOSY) was used to determine the composition of the reaction (1) products between Sn(IV)-porphyrin axial complexes and Cu^{2+}. It has been reported in recent works [30,49–54] that this method is among the most effective in the analysis of supramolecular complexes of macrocyclic compounds. This method makes it possible to confirm the structures of the formed supramolecular complexes by comparing the diffusion coefficients of the systems obtained by self-assembly with the diffusion coefficients of the initial compounds (before the self-assembly) taken as objects of comparison. In our case, diaxial complexes I and II were employed as the reference compounds. The diffusion coefficients (D) of complexes I and II and the products of their interaction with Cu^{2+} (in 1:1 and 1:5 ratios) were measured by the stimulated echo method, with a bipolar gradient and a WATERGATE pulsed water suppression unit [55] in an H$_2$O/D$_2$O mixture (in a 90:10 ratio) at 298 K. The results are presented in Table 7 and Figure 10.

Table 6. Relevant ^{1}H-NMR signals for studied compounds.

Type of Protons	Chemical Shifts of Signals			Type of Protons	Chemical Shifts of Signals		
	I	I-Cu-I	Cu[I-Cu]$_6$		II	II-Cu-II	Cu[II-Cu]$_6$
-COOH	11.37 (s, 2H)	11.35 (s, H)	-	-OH	10.7 (s, 2H)	10.6 (s, H)	-
-NH$_2$	6.72 (s, 4H)	6.71 (s, 2H), 6.91(brs, 2H)	6.93 (brs, 2H)	-NH$_2$	8.59 (s, 4H)		8.79 (brs, 2H)
-CH(L)	4.37 (t, 2H)	4.36 (t, H) 3.81 (t, H)	3.78 (t, 2H)	-NH$_2$	5.32 (s, 4H)	5.35 (s, 4H)	5.36 (s, 4H)
-CH$_2$-	3.19 (m, 4H)	3.15 (m, 4H)	3.11 (m, 4H)	Ph(L)	5.97 (t, 2H)	5.99(m, 2H)	6.03 (t, 2H)
2-Ph (L)	5.51 (d, 4H)	5.64 (m, 4H)	5.82 (d, 4H)	Ph(L)	2.92 (t, 2H)	2.92 (t, 2H)	2.91 (t, 2H)
3-Ph (L)	2.28 (d, 4H)	2.30 (d, 4H)	2.35 (d, 4H)	2-Ph(Porph.)	8.45 (d, 8H)	8.46 (d, 8H)	8.44 (d, 8H)
2-Ph(Porph)	8.36 (d, 8H)	8.37 (d, 8H)	8.38 (d, 8H)	3-Ph(Porph.)	8.25 (d, 8H)	8.24(d, 8H)	8.23 (d, 8H)
3-Ph(Porph)	8.14 (d, 8H)	8.17 (d, 8H)	8.15 (d, 8H)	β-Por	9.10 (s, 8H)	9.13 (s, 8H)	9.12 (s, 8H)
β-Porph.	9.41(s, 8H)	9.43 (s, 8H)	9.42 (s, 8H)				

Table 7. Diffusion coefficients (D$\times 10^{-10}$, m^{2}s^{-1}) of the complexes I and II and the products of their interaction with Cu^{2+} at the 1:1 and 1:5 concentration ratios of the reagents.

I	I-Cu-I	I-[Cu-I]$_n$
2.96	2.26	1.55
II	II-Cu-II	II-[Cu-II]$_n$
2.80	2.13	1.32

The measurement error is equal to $\pm 0.04 \div 0.09 \times 10^{-10}$, m^{2}s^{-1}.

(a) (b)
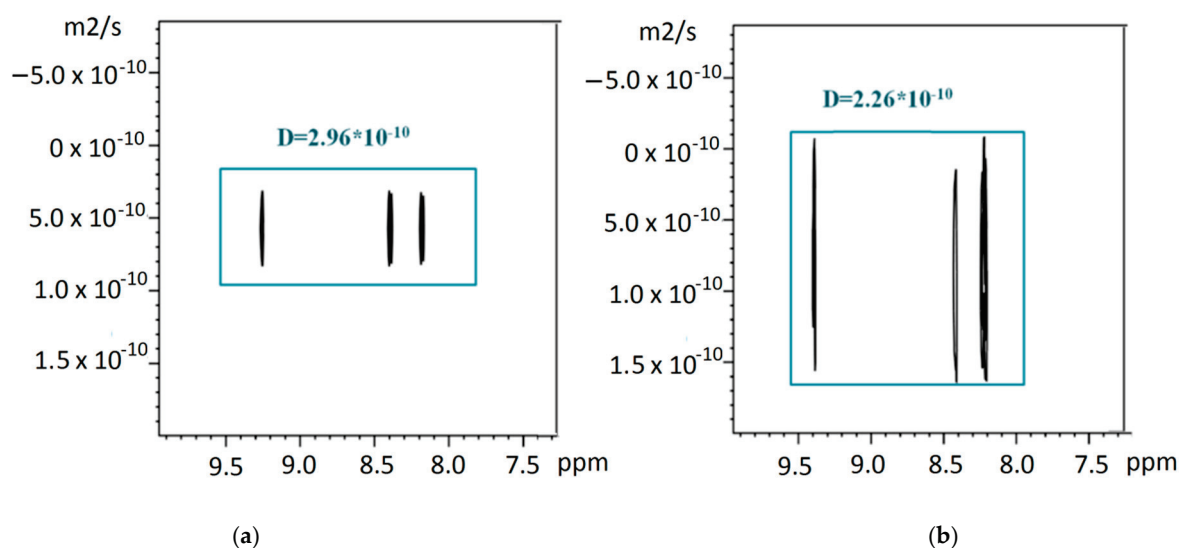
Figure 10. ^{1}H NMR diffusion-ordered spectroscopy (DOSY) spectra of products of interaction the complex I (**a**) and porphyrin dimers with Cu^{2+}I-Cu-I (**b**).

The high accuracy of these measurements clearly indicates that the DOSY method is sensitive enough for us to speak with confidence about the difference between the complexes of the monomeric porphyrinates and oligomeric porphyrin systems and to confirm the complexation process in the studied systems.

For the sake of simplicity of interpretation of the DOSY experiments, we conducted a graphical analysis, which has been successfully applied to related/similar molecular

systems earlier [56–58]. This graphical analysis is based on a model of a mass dependence on the coefficient of translational diffusion, obtained from the Einstein–Smoluchowski relation [59,60]. Thus, it is shown that the ratio of the diffusion coefficients for two different molecular particles (D_i/D_j) is inversely proportional to the square root or cubic root of the ratio of their molecular masses (M_j/M_i) for rod-like and spherical forms of molecules, and can be calculated by the formula:

$$\sqrt[2]{\frac{M_j}{M_i}} \geq \frac{D_i}{D_j} \geq \sqrt[3]{\frac{M_j}{M_i}} \tag{3}$$

This ratio can be used to calculate a set of theoretical diffusion coefficients (upper and lower limits) for each supramolecular complex based on the diffusion coefficients of starting complexes I and II (monomers). As shown by Cabrita and Berger [61], the use of a reference compound is effective for solving problems associated with qualitative and quantitative analysis of intermolecular interactions. For graphical analysis, in addition to the theoretical curves of the solvent diffusion coefficients shown in Figure 11 (the black line refers to the simulated theoretical dependence for rod-shaped oligomeric particles, the dotted line refers to the simulated theoretical dependence for spherical oligomeric particles), we indicated the experimental values of the self-diffusion coefficients determined both for initial complexes I and II and the products of their interaction with Cu^{2+}. The performed graphical analysis showed that the experimental values of the diffusion coefficients of the reaction (1) products at 1:1 and 1:5 ratios of the starting compounds fit well in the range of the calculated theoretical curves. The data obtained indicate that the products of reaction (1), with an equivalent ratio of reactants in the case of both complex I and complex II, were most likely dimers with molecular weights of 2877.57 g/mol (I-Cu-I) and 2715.37 g/mol (II-Cu-II). The systems formed with a five-fold excess of copper cations were characterized by the formation of Cu-[I-Cu-]$_6$ oligomers with molecular weights of 8892.89 g/mol and Cu-[II-Cu-]$_6$ oligomers with molecular weights of 8400.3 g/mol.

(**a**)   (**b**)
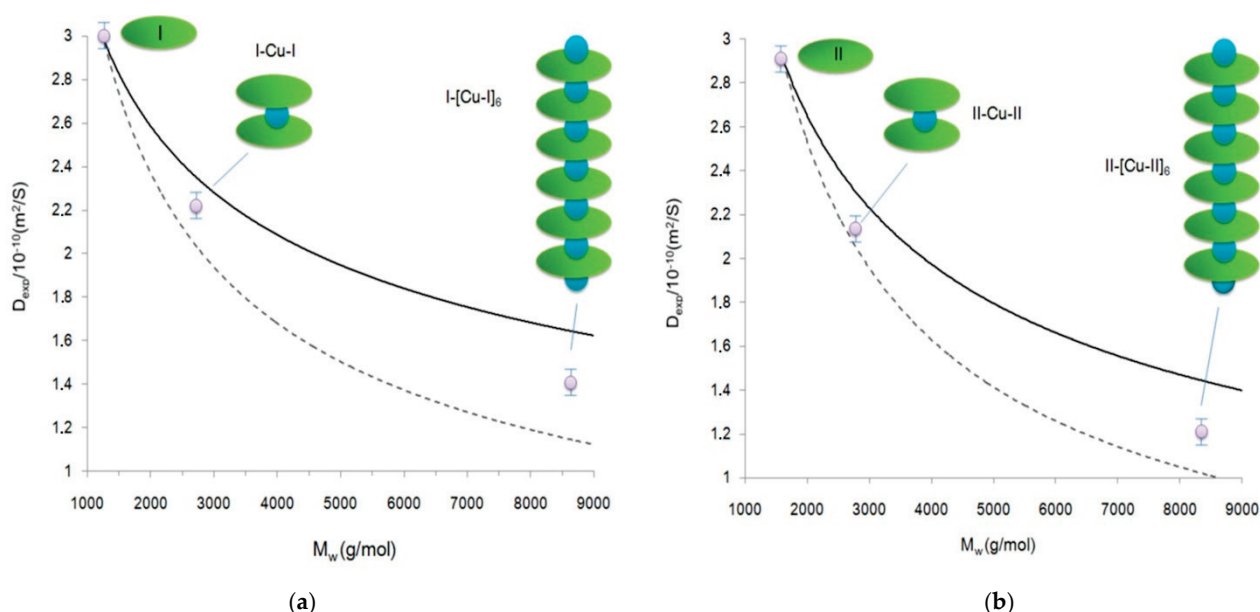
Figure 11. Graphical analysis of self-diffusion coefficients of the products of SnP(L)$_2$ interaction with Cu^{2+} cations at the 1:1 and 1:5 ratios with monomer complexes taken as the reference standard: (**a**)-I, (**b**)-II. The solid lines represent the theoretical values calculated by the Formula (3).

3.6. Fluorescent Properties Studies

Figure 12 shows the change in the fluorescent properties of complexes I and II as the corresponding dimers and oligomers were formed from them. The distinguishing feature of the presented spectra was an additional peak in the region of 620–625 nm as the corresponding porphyrin arrays with different numbers of tetrapyrrole chromophores (n = 2, 6) were formed from the porphyrin monomers (complexes I and II). Such a peak probably appeared because the porphyrin dimers and oligomers formed during the chelation had an additional energy level, enabling an emitting transition to the ground state.
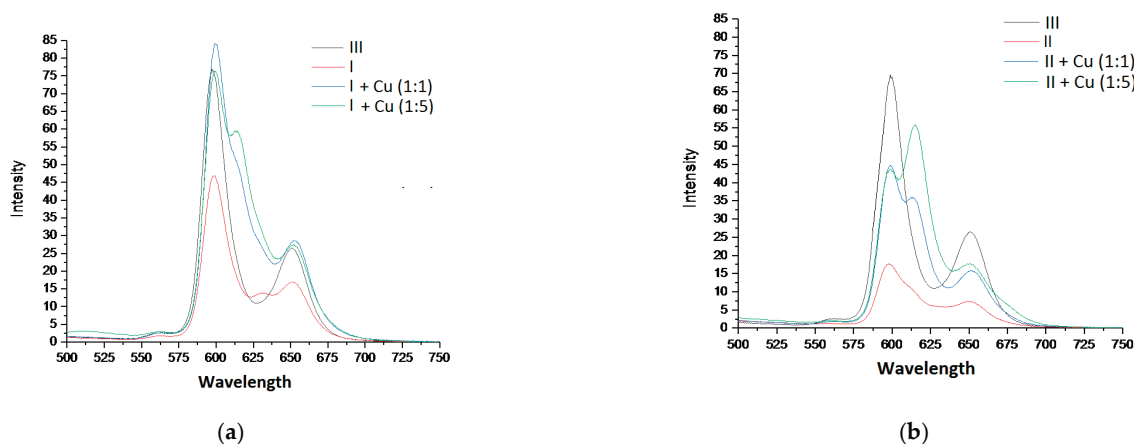

Figure 12. Fluorescence spectra of the studied systems with different concentration ratios of the reagents, λ_{ex} = 416 nm (I-(**a**), II-(**b**)).

Strong quenching of the fluorescence (Figure 11) of complexes I and II in comparison with bis-hydroxy-5,10,15,20-tetra-(4-sulfonatophenyl)porphyrin-Sn(IV) (III), according to the literature data [62,63] and the results of our own studies [64,65], is caused by the interaction of the closely spaced aromatic systems of the ligand and porphyrin macrocycle (in complex I, the inclination angle of the axial ligand aromatic part to the porphyrin plane was 31°, while in complex II, it was 50°). The results of the quantum chemical calculations show (Figure 2, Table 1) that as dimeric structures were formed, the inclination angle of the phenolate fragment of the ligands relative to the porphyrin plane increased (the angle became close to 90°). The functional groups involved in the chelation with Cu^{2+} cations in the dimeric structures were located at the maximum possible distance from the porphyrin plane. It is logical to assume that the structural changes accompanying the formation of dimeric and oligomeric systems weakened the mutual influence of the aromatic systems of the ligand and macrocycles in them. This is in good agreement with the data presented in Figure 13. In the case of complex I, the quantum yield of the systems formed at different ratios of the reagents (1:1 or 1:5) increased by about two-fold. In the case of complex II, at a 1:5 molar ratio of the reagents, the quantum yield of fluorescence increased by about four-fold. The difference in the quantum yields of the dimeric and oligomeric systems obtained on the basis of complexes I and II could probably be explained by the different sizes of the axial ligands in the corresponding complexes. The importance of spatial effects was confirmed by the data in Tabl. 1, according to which the distance between the porphyrin fragments in the I-Cu-I and II-Cu-II dimers differed significantly and amounted to 21.3 and 17.6 Å, respectively.

It should be also noted that some of the products of reaction (1) precipitated. It is logical to assume that the polymer products of the reaction of the Cu^{2+} cation chelate complex formation with the studied axial complexes of Sn(IV)-porphyrin were precipitated. Currently, our laboratory is conducting research related to the establishment of their structure and properties. According to the preliminary studies, these porphyrin polymers are characterized by high porosity and capacity to selectively adsorb organic solvent molecules. This suggests that coordination polymers of this type could be promising

"size-responsive" materials (i.e., capable of separating, storing, and transporting aggressive, toxic, or explosive chemical species of different natures).

(a)   (b)
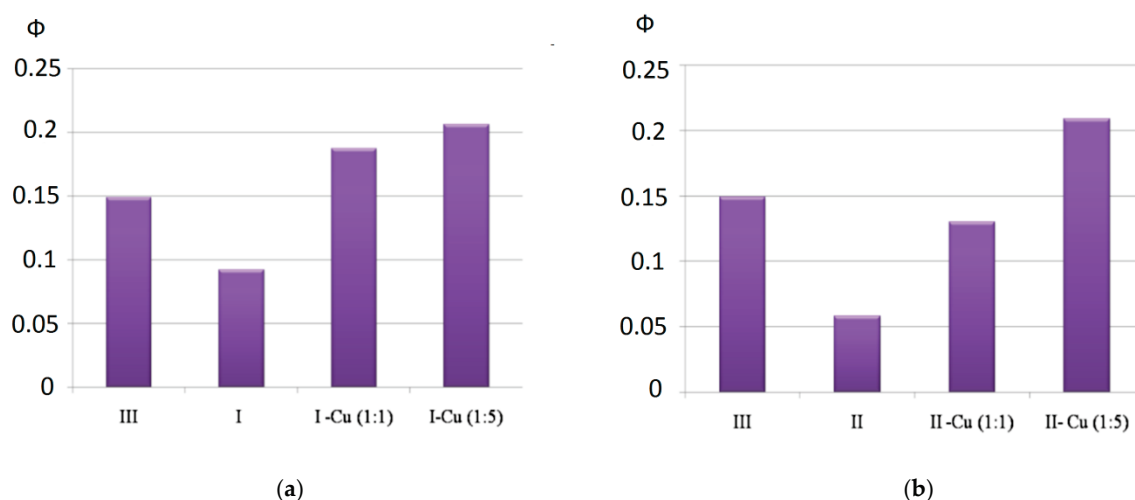
Figure 13. (**a**) Fluorescence quantum yields of complexes III and I and products of their interaction with Cu^{2+} depending on the concentration ratio of the reagents; (**b**) fluorescence quantum yields of complexes III and II and products of their interaction with Cu^{2+} depending on the concentration ratio of the reagents.

4. Conclusions

Thus, the obtained porphyrin oligomers and polymers in solid state and in solution are compounds in which the porphyrin fragments with tyrosine and diaminoresorcinol axial ligands form stable coordination compounds with two five-membered square planar metallocycles. Soluble products of the chelation of Sn(IV)-tetra(sulfonatophenyl)porphyrin diaxial complexes with Cu^{2+} are porphyrin coordination oligomers with different numbers of tetrapyrrole fragments (from two to six). The specific composition of the interaction products depends on the concentration ratio of the reagents. If, at an equivalent concentration ratio of the reagents, the main products are porphyrin dimers, then an excess of Cu^{2+} leads to the formation of larger oligomeric porphyrin arrays. The obtained porphyrin oligomers formed by five-membered chelate rings with Cu^{2+} are stable compounds (in comparison with oligomers, which can be formed by four- or six-membered chelate rings based on copper cations). The results show that chelation of Sn(IV)-porphyrin diaxial complexes with Cu^{2+} is accompanied by an increase in the fluorescence of the resulting hybrid organic-inorganic oligomers. The results obtained are of particular interest to those involved in creating of new 'chemo-responsive' (i.e., selectively interacting with other chemical species as receptors, sensors, or photocatalysts) materials, the optoelectronic properties of which could be controlled by varying the number of monomeric fragments in the polyporphyrin arrays.

Institutional Review Board Statement: Not applicable.

Informed Consent Statement: Not applicable.

Data Availability Statement: Samples of the compounds are available from the authors.

References

1. Batten, S.R.; Champness, N.R.; Chen, X.-M.; Garcia-Martinez, J.; Kitagawa, S.; Öhrström, L.; O'Keeffe, M.; Suh, M.P.; Reedijk, J. Terminology of metal–organic frameworks and coordination polymers (IUPAC Recommendations 2013). *Pure Appl. Chem.* **2013**, *85*, 1715–1724. [CrossRef]
2. Chui, S.S. A Chemically Functionalizable Nanoporous Material [Cu3(TMA)2(H2O)3]n. *Science* **1999**, *283*, 1148–1150. [CrossRef]
3. Czaja, A.U.; Trukhan, N.; Müller, U. Industrial applications of metal–organic frameworks. *Chem. Soc. Rev.* **2009**, *38*, 1284–1293. [CrossRef]
4. Henschel, A.; Gedrich, K.; Kraehnert, R.; Kaskel, S. Catalytic properties of MIL-101. *Chem. Commun.* **2008**, *35*, 4192–4194. [CrossRef]
5. Furukawa, H.; Cordova, K.E.; O'Keeffe, M.; Yaghi, O.M. The Chemistry and Applications of Metal-Organic Frameworks. *Science* **2013**, *341*, 1230444. [CrossRef] [PubMed]
6. Peng, Y.; Li, Y.; Ban, Y.; Jin, H.; Jiao, W.; Liu, X.; Yang, W. Metal-organic framework nanosheets as building blocks for molecular sieving membranes. *Science* **2014**, *346*, 1356–1359. [CrossRef] [PubMed]
7. Falcaro, P.; Ricco, R.; Doherty, C.M.; Liang, K.; Hill, A.J.; Styles, M.J. MOF positioning technology and device fabrication. *Chem. Soc. Rev.* **2014**, *43*, 5513–5560. [CrossRef]
8. Li, Y.-N.; Wang, S.; Zhou, Y.; Bai, X.-J.; Song, G.-S.; Zhao, X.-Y.; Wang, T.-Q.; Qi, X.; Zhang, X.-M.; Fu, Y. Fabrication of Metal–Organic Framework and Infinite Coordination Polymer Nanosheets by the Spray Technique. *Langmuir* **2017**, *33*, 1060–1065. [CrossRef] [PubMed]
9. Liu, J.; Chen, L.; Cui, H.; Zhang, J.; Zhang, L.; Su, C.-Y. Applications of metal–organic frameworks in heterogeneous supramolecular catalysis. *Chem. Soc. Rev.* **2014**, *43*, 6011–6061. [CrossRef]
10. Ravon, U.; Domine, M.E.; Gaudillere, C.; Desmartin-Chomel, A.; Farrusseng, D. MOFs as acid catalysts with shape selectivity properties. *New J. Chem.* **2008**, *32*, 937–940. [CrossRef]
11. Paille, G.; Gomez-Mingot, M.; Roch-Marchal, C.; Lassalle-Kaiser, B.; Mialane, P.; Fontecave, M.; Mellot-Draznieks, C.; Dolbecq, A. A Fully Noble Metal-Free Photosystem Based on Cobalt-Polyoxometalates Immobilized in a Porphyrinic Metal–Organic Framework for Water Oxidation. *J. Am. Chem. Soc.* **2018**, *140*, 3613–3618. [CrossRef]
12. Kucheryavy, P.; Lahanas, N.; Lockard, J.V. Spectroscopic Evidence of Pore Geometry Effect on Axial Coordination of Guest Molecules in Metalloporphyrin-Based Metal Organic Frameworks. *Inorg. Chem.* **2018**, *57*, 3339–3347. [CrossRef]
13. Pereira, C.F.; Figueira, F.; Mendes, R.F.; Rocha, J.; Hupp, J.T.; Farha, O.K.; Simões, M.M.Q.; Tomé, J.P.C.; Paz, F.A.A. Bifunctional Porphyrin-Based Nano-Metal–Organic Frameworks: Catalytic and Chemosensing Studies. *Inorg. Chem.* **2018**, *57*, 3855–3864. [CrossRef]
14. Stassen, I.; Burtch, N.; Talin, A.; Falcaro, P.; Allendorf, M.; Ameloot, R. An updated roadmap for the integration of metal–organic frameworks with electronic devices and chemical sensors. *Chem. Soc. Rev.* **2017**, *46*, 3185–3241. [CrossRef]
15. Gao, W.-Y.; Chrzanowski, M.; Ma, S. Metal–metalloporphyrin frameworks: A resurging class of functional materials. *Chem. Soc. Rev.* **2014**, *43*, 5841–5866. [CrossRef]
16. Huh, S.; Kim, S.-J.; Kim, Y. Porphyrinic metal–organic frameworks from custom-designed porphyrins. *CrystEngComm* **2016**, *18*, 345–368. [CrossRef]
17. Day, N.U.; Wamser, C.C.; Walter, M.G. Porphyrin polymers and organic frameworks. *Polym. Int.* **2015**, *64*, 833–857. [CrossRef]
18. Ermakova, E.V.; Enakieva, Y.Y.; Meshkov, I.N.; Baranchikov, A.E.; Zvyagina, A.I.; Gorbunova, Y.G.; Tsivadze, A.Y.; Kalinina, M.A.; Arslanov, V.V. Bilayer Porphyrin-Graphene Templates for Self-Assembly of Metal-Organic Frameworks on the Surface. *Macroheterocycles* **2017**, *10*, 496–504. [CrossRef]
19. Zvyagina, A.I.; Shiryaev, A.A.; Baranchikov, A.E.; Chernyshev, V.V.; Enakieva, Y.Y.; Raitman, O.A.; Ezhov, A.A.; Meshkov, I.N.; Grishanov, D.A.; Ivanova, O.S.; et al. Layer-by-layer assembly of porphyrin-based metal–organic frameworks on solids decorated with graphene oxide. *New J. Chem.* **2016**, *41*, 948–957. [CrossRef]
20. Imai, H.; Misawa, K.; Munakata, H.; Uemori, Y. Water-soluble zinc porphyrins as artificial receptors for amino acids. *Chem. Pharm. Bull.* **2008**, *56*, 1470–1472. [CrossRef]
21. Noworyta, K.; Kutner, W.; Wijesinghe, C.A.; Srour, S.G.; D'Souza, F. Nicotine, Cotinine, and Myosmine Determination Using Polymer Films of Tailor-Designed Zinc Porphyrins as Recognition Units for Piezoelectric Microgravimetry Chemosensors. *Anal. Chem.* **2012**, *84*, 2154–2163. [CrossRef] [PubMed]
22. Yoon, H.; Lee, C.-H.; Jeong, Y.-H.; Gee, H.-C.; Jang, W.-D. A zinc porphyrin-based molecular probe for the determination of contamination in commercial acetonitrile. *Chem. Commun.* **2012**, *48*, 5109–5111. [CrossRef]
23. Gilday, L.C.; White, N.; Beer, P.D. Halogen- and hydrogen-bonding triazole-functionalised porphyrin-based receptors for anion recognition. *Dalton Trans.* **2013**, *42*, 15766. [CrossRef]

24. Nguyen, N.T.; Mamardashvili, G.M.; Kulikova, O.M.; Scheblykin, I.G.; Mamardashvili, N.Z.; Dehaen, W. Binding ability of first and second generation/carbazolylphenyl dendrimers with Zn(ii) tetraphenylporphyrin core towards small heterocyclic substrates. *RSC Adv.* **2014**, *4*, 19703–19709. [CrossRef]

25. Mamardashvili, G.M.; Mamardashvili, N.Z.; Koifman, O. Self-assembling systems based on porphirins. *Russ. Chem. Rev.* **2008**, *77*, 59–75. [CrossRef]

26. Mamardashvili, G.M.; Mamardashvili, N.Z. Self-organization of zinc(II) and tin(IV) porphyrinates into supramolecular trimers. *Russ. J. Gen. Chem.* **2013**, *83*, 1424–1428. [CrossRef]

27. Sun, H.; Guo, K.; Gan, H.; Li, X.; Hunter, C.A. Influence of receptor flexibility on intramolecular H-bonding interactions. *Org. Biomol. Chem.* **2015**, *13*, 8053–8066. [CrossRef]

28. Steed, J.W.; Atwood, J.L. *Supramolecular Chemistry*, 2nd ed.; John Wiley& Sons, Ltd: Chichester, UK, 2009; pp. 1–48.

29. Neese, F. Software update: The ORCA program system, version 4.0. *Wiley Interdiscip. Rev. Comput. Mol. Sci.* **2018**, *8*, 1327. [CrossRef]

30. Mamardashvili, G.M.; Maltceva, O.V.; Lazovskiy, D.A.; Khodov, I.A.; Borovkov, V.; Mamardashvili, N.Z.; Koifman, O.I. Medium viscosity effect on fluorescent properties of Sn(IV)-tetra(4-sulfonatophenyl)porphyrin complexes in buffer solutions. *J. Mol. Liq.* **2019**, *277*, 1047–1053. [CrossRef]

31. Herrmann, O.; Mehdi, S.H.; Corsini, A. Heterogeneous metal-insertion: A novel reaction with porphyrins. *Can. J. Chem.* **1978**, *56*, 1084–1087. [CrossRef]

32. Bâtiu, C.; Jelic, C.; Leopold, N.; Cozar, O.; David, L. Spectroscopic investigations of new Cu(II), Co(II), Ni(II) complexes with γ-l-glutamyl amide as ligand. *J. Mol. Struct.* **2005**, *744-747*, 325–330. [CrossRef]

33. Lewis, E.A.; Tolman, W.B. Reactivity of Dioxygen−Copper Systems. *Chem. Rev.* **2004**, *104*, 1047–1076. [CrossRef]

34. Cabrele, C.; Langer, M.; Beck-Sickinger, A.G. Amino Acid Side Chain Attachment Approach and Its Application to the Synthesis of Tyrosine-Containing Cyclic Peptides. *J. Org. Chem.* **1999**, *64*, 4353–4361. [CrossRef]

35. Rodante, F.; Marrosu, G.; Catalani, G. Thermal analysis of some α-amino acids with similar structures. *Thermochim. Acta* **1992**, *194*, 197–213. [CrossRef]

36. Antina, E.V.; Balantseva, E.V.; Berezin, M.B. Oxidative degradation of porphyrins and metalloporphyrins under polythermal conditions. *Russ. J. Gen. Chem.* **2011**, *81*, 1222–1230. [CrossRef]

37. Katoch, S.; Bajju, G.D.; Devi, G.; Ahmed, A. Synthesis, thermoanalytical and spectroscopic characterization of newly synthesized macrocyclic complexes of thallium(III) and tin(IV). *J. Therm. Anal. Calorim.* **2017**, *130*, 2157–2165. [CrossRef]

38. Xu, Y.; Yu, Q.; Zhao, D.; Zhang, W.; Wang, N.; Li, J. Synthesis and characterization of porphyrin-based porous coordination polymers obtained by supercritical CO2 extraction. *J. Mater. Sci.* **2018**, *53*, 10534–10542. [CrossRef]

39. Rajalakshmi, V.; Vijayaraghavan, V.R.; Varghese, B.; Raghavan, A. Novel Michael Addition Products of Bis(amino acidato)metal(II) Complexes: Synthesis, Characterization, Dye Degradation, and Oxidation Properties. *Inorg. Chem.* **2008**, *47*, 5821–5830. [CrossRef] [PubMed]

40. Yamauchi, O.; Tsujide, K.; Odani, A. Copper(II) complexes of tyrosine-containing dipeptides. Effects of side-chain groups on spectral and solution chemical properties and their structural implication. *J. Am. Chem. Soc.* **1985**, *107*, 659–666. [CrossRef]

41. Sugimori, T.; Shibakawa, K.; Masuda, H.; Odani, A.; Yamauchi, O. Ternary metal(II) complexes with tyrosine-containing dipeptides. Structures of copper(II) and palladium(II) complexes involving L-tyrosylglycine and stabilization of copper(II) complexes due to intramolecular aromatic ring stacking. *Inorg. Chem.* **1993**, *32*, 4951–4959. [CrossRef]

42. Nakamoto, K. (Ed.) *Infrared and Raman Spectra of Inorganic and Coordination Compounds Part B: Applications in Coordination, Organometallic, and Bioinorganic Chemistry*, 6th ed.; John Wiley & Sons, Inc.: New York, NY, USA, 2009; 408p.

43. Srivastava, K.P.; Singh, A. Facile Eco-friendly Synthesis, Spectral and Antimicrobial Activities of Copper—Amino Acid Complexes. *IOSR J. Appl. Chem.* **2016**, *9*, 1–6, e-ISSN 2278-5736. [CrossRef]

44. Pogni, R.; Della Lunga, G.; Basosi, R. Multi-microwave frequency EPR in the structural characterization of copper(II) dipeptide complexes. *J. Am. Chem. Soc.* **1993**, *115*, 1546–1550. [CrossRef]

45. Gala, L.; Lawson, M.; Jomova, K.; Zelenicky, L.; Congradyova, A.; Mazur, M.; Valko, M. EPR Spectroscopy of a Clinically Active (1:2) Copper(II)-Histidine Complex Used in the Treatment of Menkes Disease: A Fourier Transform Analysis of a Fluid CW-EPR Spectrum. *Molecules* **2014**, *19*, 980–991. [CrossRef]

46. Mabbs, F.E.; Colisson, D. *Electron Paramagnetic Resonance of d-Transition Metal Compounds*; Elsevier: Amsterdam, The Netherlands, 1992; p. 102.

47. Krinichnyi, V.I. *2-mm Wave Band EPR Spectroscopy of Condensed Systems*; CRC Press: Boca Raton, FL, USA, 2018; pp. 33–62.

48. Avezov, K.G.; Umarov, B.B.; Tursunov, M.A.; Parpiev, N.A.; Minin, V.V. Copper(II) complexes based on 2-thenoyltrifluoroacetone aroylhydrazones: Synthesis, spectroscopt and X-ray diffraction analysis. *Russ. J. Coord. Chem.* **2016**, *42*, 470–475. [CrossRef]

49. Khodov, I.; Alper, G.; Mamardashvili, G.; Mamardashvili, N. Hybrid multi-porphyrin supramolecular assemblies: Synthesis and structure elucidation by 2D DOSY NMR studies. *J. Mol. Struct.* **2015**, *1099*, 174–180. [CrossRef]

50. Watanabe, H.; Kamatani, Y.; Tamiaki, H. Coordination-Driven Dimerization of Zinc Chlorophyll Derivatives Possessing a Dialkylamino Group. *Chem. Asian J.* **2017**, *12*, 759–767. [CrossRef] [PubMed]

51. Efimov, S.V.; Zgadzay, Y.O.; Tarasova, N.B.; Klochkov, V.V. Evidence of oligomerization of bovine insulin in solution given by NMR. *Eur. Biophys. J.* **2018**, *47*, 881–889. [CrossRef] [PubMed]

52. Nikitina, L.E.; Pavelyev, R.S.; Startseva, V.A.; Kiselev, S.V.; Galiullina, L.F.; Aganova, O.V.; Timerova, A.F.; Boichuk, S.V.; Azizova, Z.R.; Klochkov, V.V.; et al. Structural details on the interaction of biologically active sulfur-containing monoterpenoids with lipid membranes. *J. Mol. Liq.* **2020**, *301*, 112366. [CrossRef]

53. Mamardashvili, G.M.; Kaigorodova, E.Y.; Khodov, I.A.; Scheblykin, I.; Mamardashvili, N.Z.; Koifman, O.I.; Sheblykin, I. Micelles encapsulated Co(III)-tetra(4-sulfophenyl)porphyrin in aqueous CTAB solutions: Micelle formation, imidazole binding and redox Co(III)/Co(II) processes. *J. Mol. Liq.* **2019**, *293*, 111471. [CrossRef]

54. Maltceva, O.; Mamardashvili, G.; Khodov, I.; Lazovskiy, D.; Khodova, V.; Krest'Yaninov, M.; Mamardashvili, N.; Dehaen, W. Molecular recognition of nitrogen-containing bases by Zn[5,15-bis-(2,6-dodecyloxyphenyl)]porphyrin. *Supramol. Chem.* **2017**, *29*, 360–369. [CrossRef]

55. Zheng, G.; Stait-Gardner, T.; Kumar, P.A.; Torres, A.M.; Price, W.S. PGSTE-WATERGATE: An STE-based PGSE NMR sequence with excellent solvent suppression. *J. Magn. Reson.* **2008**, *191*, 159–163. [CrossRef]

56. Oliva, A.I.; Gómez, K.; González, G.; Ballester, P. Diffusion-ordered spectroscopy (1H-DOSY) of Zn-porphyrin assemblies induced by coordination with DABCO. *New J. Chem.* **2008**, *32*, 2159–2163. [CrossRef]

57. Timmerman, P.; Weidmann, J.-L.; Jolliffe, K.A.; Prins, L.J.; Reinhoudt, D.N.; Shinkai, S.; Frish, L.; Cohen, Y. NMR diffusion spectroscopy for the characterization of multicomponent hydrogen-bonded assemblies in solution. *J. Chem. Soc. Perkin Trans. 2* **2000**, *2*, 2077–2089. [CrossRef]

58. Ksenofontov, A.A.; Stupikova, S.A.; Bocharov, P.S.; Lukanov, M.M.; Ksenofontova, K.V.; Khodov, I.A.; Antina, E.V. Novel fluorescent sensors based on zinc(II) bis(dipyrromethenate)s for furosemide detection in organic media. *J. Photochem. Photobiol. A Chem.* **2019**, *382*, 111899. [CrossRef]

59. Holz, M.; Mao, X.; Seiferling, D.; Sacco, A. Experimental study of dynamic isotope effects in molecular liquids: Detection of translation-rotation coupling. *J. Chem. Phys.* **1996**, *104*, 669–679. [CrossRef]

60. Waldeck, A.; Kuchel, P.W.; Lennon, A.J.; Chapman, B.E. NMR diffusion measurements to characterise membrane transport and solute binding. *Prog. Nucl. Magn. Reson. Spectrosc.* **1997**, *30*, 39–68. [CrossRef]

61. Cabrita, E.J.; Berger, S. DOSY studies of hydrogen bond association: Tetramethylsilane as a reference compound for diffusion studies. *Magn. Reson. Chem.* **2001**, *39*, S142–S148. [CrossRef]

62. Reddy, D.R.; Maiya, B.G. Bis(aryloxo) derivatives of tin(IV) porphyrins: Synthesis, spectroscopy and redox activity. *J. Porphyrins Phthalocyanines* **2002**, *6*, 3–11. [CrossRef]

63. Bhosale, S.V.; Chong, C.; Forsyth, C.; Langford, S.J.; Woodward, C.P. Investigations of rotamers in diaxial Sn(IV)porphyrin phenolates—towards a molecular timepiece. *Tetrahedron* **2008**, *64*, 8394–8401. [CrossRef]

64. Mamardashvili, G.M.; Lazovskiy, D.A.; Maltceva, O.V.; Mamardashvili, N.Z.; Koifman, O.I. The Sn(IV)-tetra(4-sulfonatophenyl) porphyrin complexes with antioxidants: Synthesis, structure, properties. *Inorganica Chim. Acta* **2019**, *486*, 468–475. [CrossRef]

65. Lazovskiy, D.A.; Mamardashvili, G.M.; Khodov, I.A.; Mamardashvili, N.Z. Water soluble porphyrin-fluorescein triads: Design, DFT calculation and pH-change-triggered fluorescence response. *J. Photochem. Photobiol. A Chem.* **2020**, *402*, 112832. [CrossRef]